THE UNIVERSITY OF QUEENSLAND

AUSTRALIA

Transportation and Deposition of Particles in Metal Foam Heat Exchanger

Fadhilah Shikh Anuar

B. M.E. (Hons), M. Eng.

A thesis submitted for the degree of Doctor of Philosophy at

The University of Queensland in 2018

School of Mechanical & Mining Engineering

Abstract

Open-cell metal foams have been investigated extensively as a potential heat exchanger in many applications due to their unique microstructures, made of interconnected pore-ligament constructions. Many studies have proved their excellent heat transfer performances. However, excessive pressure drop becomes one of its major drawbacks. In addition, fluid flow structures induced by the metal foam are always associated with various instabilities. For established thermohydraulics properties of the metal foam heat exchangers in clean and fouled conditions, more experimental works are called for. Until recently, the fouled condition has received relatively little attention among researchers. It is understandable as there are still many unsolved issues in the clean condition due to various geometrical considerations such as annulus pipe, duct, baffle, porous sandwich, including the trade-off analyses between pressure drop and thermal performances for both fully and partially filled configurations at different operating conditions.

This present study conducted a series of experiments to investigate the thermohydraulic properties of (1) a metal foam-filled annulus and (2) a partially filled channel with metal foam. The latter configuration was also subjected to a fouled condition to gain insight of underlying mechanisms of particle transport and deposition processes in the metal foam structure. The experiments were conducted using Particle Image Velocimetry (PIV), Laser Doppler Anemometry (LDA), Hot-Wire Anemometry (HWA), Phantom high-speed camera and infrared radiation (IR) camera, depending on the experimental purposes. The PIV measurement provides instantaneous whole flow-field velocity, and the LDA and HWA offer local flow velocity in non-porous regions. The investigation of flow behaviours inside the porous structure of the metal foam was conducted based on the temperature distributions from the IR images. Meanwhile, in-situ observation of particles movement and deposition was performed using the high-speed camera, where the particle trajectories in a region of interest (ROI) could be determined.

The result shows that the pressure drop of the metal foam-filled annulus is increasing with the airflow rates (20, 85, and 150 SLPM) and foam length. However, a significant amount of heat transfer takes place only in the first half of the foam, suggesting a need for an effective length for this kind of metal foam heat exchanger. For a certain case, for example, 20 PPI at 20 SLPM, a longer metal foam than 0.05 to 0.06 m would be unnecessary since it will only increase the pressure drop. The temperature distributions inside the porous structure are non-linear with a developed flow could be only seen at the lower half of the annulus of 20 PPI at 150 SLPM.

For the partially filled channel, a part of the incoming airflows would enter the porous structure of the metal foam block, while the rest is going into the free stream region (a non-porous region that located on the top of the foam block). The free stream velocity is increasing with the blockage ratio (a ratio of foam height to channel height) and a formation of recirculation zone could be seen at the downstream region of a high enough blockage ratio. Interestingly, this phenomenon did not occur with the low pore density, e.g., 10 PPI foam but the 30 PPI foam and solid block. The flow inside the foam block also tends to leave into the free stream region through the fluid/foam interface for a certain foam length, pore density and blockage ratio. While the pressure drop is expected to be increased with the pore density in a fully filled channel, it is not necessarily always true for the partially filled channel. The fluctuating velocity and changes of the flow direction at the interface, as well as the formation of a recirculation zone would affect the total pressure drop and resistance coefficient.

Furthermore, the metal foam causes a higher pressure drop than the solid block of the same size, indicating the substantial effects of porous structure on the total pressure drop. Our proposed friction factor model for the partially filled channel agrees with the experimental data with ±16% deviation. The result from the fouling experiment shows that the particle size has a significant influence on the particle transport and deposition processes. The large particles tend to keep their inertia, while the fine particles would follow the fluid streamlines. For the high blockage ratio, more particles tend to deposit on the frontal area of the foam block and the deposition is building up in the upstream region. When the blockage ratio is low, more deposited particles could be observed on the top surface of the foam block. As expected, the deposition causes an increase in the pressure drop performance. However, fluctuated pressure drop values could be seen at the beginning of the fouling process before reaching a similar value over time, regardless of pore density.

Declaration by author

This thesis is composed of my original work, and contains no material previously published or written by another person except where due reference has been made in the text. I have clearly stated the contribution by others to jointly-authored works that I have included in my thesis.

I have clearly stated the contribution of others to my thesis as a whole, including statistical assistance, survey design, data analysis, significant technical procedures, professional editorial advice, financial support and any other original research work used or reported in my thesis. The content of my thesis is the result of work I have carried out since the commencement of my higher degree by research candidature and does not include a substantial part of work that has been submitted to qualify for the award of any other degree or diploma in any university or other tertiary institution. I have clearly stated which parts of my thesis, if any, have been submitted to qualify for another award.

I acknowledge that an electronic copy of my thesis must be lodged with the University Library and, subject to the policy and procedures of The University of Queensland, the thesis be made available for research and study in accordance with the Copyright Act 1968 unless a period of embargo has been approved by the Dean of the Graduate School.

I acknowledge that copyright of all material contained in my thesis resides with the copyright holder(s) of that material. Where appropriate I have obtained copyright permission from the copyright holder to reproduce material in this thesis and have sought permission from co-authors for any jointly authored works included in the thesis.

Publications during candidature

Peer-reviewed journal papers

1. **F. Shikh Anuar**, M. R. Malayeri, & Kamel Hooman. “Particulate fouling and challenges of metal foam heat exchangers”, *Heat Transfer Engineering*, 38, 7-8, pp. 730 – 742, 2017.
2. M. P. Orihuela, **F. Shikh Anuar,** I. A. Abdi, M. Odabaee, and K. Hooman, “Thermohydraulics of a metal foam-filled annulus”, *International Journal of Heat and Mass Transfer*, 117, pp. 95–106, 2018.
3. **F. Shikh Anuar**, I. A. Abdi, M.Odabaee and K. Hooman, “Experimental study of fluid flow behaviour and pressure drop in channels partially filled with metal foams”, *Experimental Thermal and Fluid Science*, 99, pp. 117-128, 2018.
4. **F. Shikh Anuar**, I. A. Abdi, and K. Hooman, “Flow Visualization Study of Partially filled Channel with Aluminium Foam Block”, *International Journal of Heat and Mass Transfer*, 127, pp. 1197–1211, 2018.

Conference presentations

1. **F. Shikh Anuar**, M. R. Malayeri, & Kamel Hooman. “A review of particulate fouling and challenges of metal foam heat exchanger”, *Heat Exchanger Fouling and Cleaning Conference*, Ireland, 7-12 June (2015).

Publications included in this thesis

1. **F. Shikh Anuar**, M. R. Malayeri, & Kamel Hooman. “Particulate fouling and challenges of metal foam heat exchangers”, *Heat Transfer Engineering*, 38, 7-8, pp. 730 – 742, 2017. – incorporated as Chapter 2.

Contributor	Statement of contribution
Author Fadhilah Shikh Anuar (Candidate)	Drafting and wrote the paper (70%)
Author Mohamad Reza Malayeri	Reviewed and edited the paper (15%)
Author Kamel Hooman	Reviewed and edited the paper (15%)

2. M. P. Orihuela, **F. Shikh Anuar,** I. A. Abdi, M. Odabaee, and K. Hooman, “Thermohydraulics of a metal foam-filled annulus”, *International Journal of Heat and Mass Transfer*, 117, pp. 95–106, 2018. – incorporated as Chapter 3.

Contributor	Statement of contribution
Author Fadhilah Shikh Anuar (Candidate)	Conducted the experiment, analysed the results and wrote the paper (30%)
Author Maria Pilar Orihuela	Conducted the experiment, analysed the results and wrote the paper (30%)
Author Iman Ashtianti Abdi	Analysed the results and wrote the paper (15%)
Author Mostafa Odabaee	Designed experiment, analysed the results and wrote the paper (15%)
Author Kamel Hooman	Reviewed and edited the paper (10%)

3. **F. Shikh Anuar**, I. A. Abdi, M.Odabaee and K. Hooman, “Experimental study of fluid flow behaviour and pressure drop in channels partially filled with metal foams”, *Experimental Thermal and Fluid Science*, 99, pp. 117-128, 2018. – incorporated as Chapter 4.

Contributor	Statement of contribution
Author Fadhilah Shikh Anuar (Candidate)	Conducted the experiment, analysed the results, developed the mathematical model and wrote the paper (35%)
Author Iman Ashtianti Abdi	Conducted the experiment, analysed the results and wrote the paper (35%)
Author Mostafa Odabaee	Analysed the sample properties (20%)
Author Kamel Hooman	Wrote and edited the paper (10%)

4. **F. Shikh Anuar**, I. A. Abdi, M.Odabaee and K. Hooman, “Flow Visualization Study of Partially filled Channel with Aluminium Foam Block”, *International Journal of Heat and Mass Transfer*, 127, pp. 1197–1211, 2018. – incorporated as Chapter 5.

Contributor	Statement of contribution
Author Fadhilah Shikh Anuar (Candidate)	Experimental design, conducted the experiment, analysed the results, and wrote the paper (45%)
Author Iman Ashtianti Abdi	Conducted the experiment, analysed the results and edited the paper (45%)
Author Kamel Hooman	Reviewed and edited the paper (10%)

Contributions by others to the thesis

This thesis consists of several papers, which involve the contribution by others as mentioned in the previous section. The significant inputs came from the first co-authors; Dr. I. Ashtianti Abdi, who provided the raw data and data interpretation of one of the test facility (WT-2), and M.P. Orihuela who contributed in analysing and interpreting some of the research data from the metal foam-filled annulus experiment.

Statement of parts of the thesis submitted to qualify for the award of another degree

None.

Research Involving Human or Animal Subjects

No animal or human subjects were involved in this research.

Acknowledgements

I would like to express my sincere gratitude to my advisors, Assoc. Prof. Kamel Hooman and Prof. M. Reza Malayeri for their continuous support of my Ph.D. research. For their patience, motivation, enthusiasm, and immense knowledge. Their guidance helped me to go through my research journey until the end. No words can describe how thankfully I am for their understandings and supports.

I also would like to thank my thesis committee, Dr. Anand Veeraragavan and Dr. Yuanshen Lu for their encouragement and insightful comments. My sincere thanks also go to my colleagues; Dr. Iman Ashtianti Abdi, Mostafa Odabaee, Maria Pilar Orihuela, Berto Di Pasquale, and the members of research groups; QGECE and RECCE. Also, I'm really grateful for continuous supports and financial assistance from Universiti Teknikal Malaysia Melaka (UTeM), Ministry of Education (Malaysia), School of Mechanical and Mining Engineering (SoMME) and Graduate School, The University of Queensland (UQ). Without their funding, it was impossible to complete this journey.

And finally, I would like to thank my husband, Ahmad Fitri Azhar for his love, concerns and great support while we are far away from home. Thanks for being there when I needed you. Also, to my son, Abdul Rahman Fathi who is always waiting for me, every day and night, showing patience and understanding to my hectic day. I'm truly blessed to have you both while enduring this journey. Special thanks to my siblings, parents, parents, parents-in-law, and friends who are always supporting me all the ways, morally and emotionally.

Thanks for all your encouragement!

Financial support

This research was supported financially by Ministry of Education, (MoeE), Malaysia, Universiti Teknikal Malaysia Melaka (UTeM), and The University of Queensland, Australia.

Keywords

Metal foam, fouling, thermohydraulic properties, particle image velocimetry, laser Doppler anemometry, flow behaviours, pressure drop, partially filled channel

Australian and New Zealand Standard Research Classifications (ANZSRC)

ANZSRC code: 091504 Fluidisation and Fluid Mechanics, 60%

ANZSRC code: 091505 Heat and Mass Transfer Operations, 40%

Fields of Research (FoR) Classification

FoR code: 0913, Mechanical Engineering, 80%

FoR code: 0915, Interdisciplinary Engineering, 20%

Table of Contents

List of Figures

List of Tables

Chapter 1: Introduction

1.1 Research Background and Motivation

Open-cell metal foam heat exchangers have been studied for diverse applications such as automotive [1], electronic cooling [2], air conditioning and refrigeration system [3], geothermal power plants [4], solar energy [5], and many others. The metal foams show superior thermal performances because of its interconnected pore-ligament construction that offers a tortuous flow path, large specific surface area and light-weight [6]. Despite numerous findings on their promising thermal capabilities, past studies also found significant pressure drop effects because of their complicated microstructure [1]. To date, there are still inconclusive findings on their thermohydraulic performance in a clean condition, furthermore under a fouled condition. This is not a surprising fact due to the existence of numerous heat exchanger designs, operating conditions as well as various foam properties from different manufacturing methods and manufacturers. Further optimization studies and validation tests are required for different configurations such as fully filled and partially filled configurations. Note that the former configuration has its entire cross-section filled with the metal foam, while the latter is only partly filled with the foam structure, where an optimum foam height (thickness) and arrangement are crucial for a trade-off between heat transfer and pressure drop performances.

In recent years, many studies [5, 7-9] have considered the partially filled configurations as an alternative to reduce the pressure drop effects. Unlike the fully filled configuration, the reasons for the increase of pressure drop in the partially filled configurations are still not yet well-addressed, where the effects of internal and external flows (of the porous region) should be taken into account. Besides, there exist only a few experimental studies on the partially filled channel [10, 11]. Common issues of the partially filled configuration also revolve around its interfacial properties such as shear stress and slip velocity, which is difficult to be determined experimentally. Moreover, the interface condition of fluid/foam could not be modelled accurately [12], yet the established interface theories of porous media [13, 14] are commonly adopted in the metal foam studies. Indeed, there is disagreement between one of the pioneering theoretical studies on a partially filled channel with porous medium [15] and experimental findings using an open-cell metal foam [16] despite their similar

configurations. Interestingly, the flow behaviours in the partially channel with metal foam are rarely discussed and validated with experimental studies, even though it is crucial in understanding the pressure drop effects and the possibility of using the metal foam under a fouled condition.

There are different opinions on the application of metal foam under the fouled condition. For example, Muley et al. [1] stated that the use of open-cell metal foam as an exhaust gas recirculation (EGR) cooler could be inappropriate since its porous structure is prone to fouling. However, Hooman and Malayeri [17] positively stated that a proper foam design could enhance the heat transfer rate at an acceptable pressure drop effects. There exists mathematical model [18] and numerical studies [19-22] on this topic, but lack of experimental studies to describe the effects of the complicated foam structure. Previous experimental studies [23, 24] have focused on bulk-scale fouling, with the analyses on the fouling layer were conducted through the naked eyes. The exact circumstances that susceptible to fouling are not well described in their studies, suggesting the needs for thorough investigations. Considering this premature research stage, the compatibility of the open-cell metal foam under a fouled condition is still indecisive.

1.2 Problem Statement

The underlying mechanisms of solid particle (foulant) transports are close-related to flow behaviours in a metal foam heat exchanger, suggesting a requirement for a depth understanding of this topic under a clean condition. Additionally, more experimental studies are required to validate the thermohydraulic properties of a fully/partially filled configuration with metal foam that involve a thorough measurement inside the porous structure of the foam. The processes of particle transport and deposition should be fully understood for a proper foam design and the use of metal foam under a fouled condition. This includes the determination of particle preferential deposition area, which usually involves stagnant and exposed regions to the incoming particle-laden flow.

1.3 Research Objectives

There are four objectives in the present study which related to the thermohydraulic properties and fouling of open-cell metal foams, which stated as below:

- Identify the effects of metal foam properties and operating conditions on the thermohydraulic of a metal foam-filled annulus.
- Develop a mathematical model in determining the pressure drop of a channel partially filled with metal foam blocks.
- Investigate the fluid flow behaviours in the partially filled channel with metal foam blocks.
- Describe the particle transport and deposition processes in the partially filled channel and determine the particles preferential deposition area.

1.4 Thesis Structure

Chapter 1 Introduction

This chapter contents a motivation of research, problem statement and research objectives.

Chapter 2 Literature review

The content of this chapter is from a published paper, which is a review of the metal foam microstructural properties and its potential as a high-performance heat exchanger. Previous literature on the metal foam heat exchangers has been reviewed in this chapter. It also includes a description of particulate fouling with several established solutions to reduce the fouling effects. Possible challenges in implementing the metal foam heat exchangers are also discussed, with several research gaps in the field of interest have been pointed out. A part of the research gaps become the main focuses of this study.

Paper 1:

F. Shikh Anuar, M. R. Malayeri, & K. Hooman. “Particulate fouling and challenges of metal foam heat exchangers”, *Heat Transfer Engineering*, 38, 7-8, pp. 730– 742, 2017.

Chapter 3 Fully filled configuration with open-cell metal foam

This chapter contents a published paper on a fully filled configuration – a metal foam-filled annulus. It has been pointed out in the previous chapter that the complicated structure of the metal foam required additional experimental studies, especially in understanding the thermohydraulic properties and the local effects within

the porous region. Thus, an extensive measurement was conducted to obtain a temperature distribution inside the porous microstructure of the metal foam. Results proved that the pore-ligament randomness is complicated and could not be accurately modelled. Conventional measurement technique using a thermocouple could be considered as exhaustive and time-consuming experiments.

Paper 2:

M. P. Orihuela, F. Shikh Anuar, I. A. Abdi, M. Odabaee, and K. Hooman, “Thermohydraulics of a metal foam-filled annulus”, *International Journal of Heat and Mass Transfer,* 117, pp. 95–106, 2018.

Chapter 4 Partially filled channel with open-cell metal foam – Part I: Point-wise Measurement using Laser Doppler and Hot-Wire Anemometers

A partially filled channel with clear windows has been considered to study the fouling of metal foam, in which a direct observation of the particle transport and deposition processes is possible. However, the flow characteristics for that kind of setup should be fully understood. This chapter presents the flow behaviours in the partially filled channel, including the pressure drop effects. A solid block of the same size is used as a reference case to investigate the significant influence of the porous structure of the metal foam. The content of this chapter is from the following paper,

Paper 3:

F. Shikh Anuar, I. A. Abdi, M.Odabaee and K. Hooman, “Experimental study of fluid flow behaviour and pressure drop in channels partially filled with metal foams”, *Experimental Thermal and Fluid Science*, 99, pp. 117-128, 2018.

Chapter 5 Partially filled channel with open-cell metal foam – Part II: Global-wise Measurement using Particle Image Velocimetry

This chapter is the extension of chapter 4 since the use of point-wise equipment could not explain the complicated flows induced by the metal foam. Additionally, there is an unexplainable result of pressure drop in the partially channel, which required a further investigation. Hence, this chapter presents global-wise measurement techniques to visualize the flow behaviours in both regions: (1) free stream region (outside of a porous foam block) and (2) porous foam block with different pore density

(pores per inch) and foam heights. The content of this chapter is from the following paper,

Paper 4:

F. Shikh Anuar, I. A. Abdi, and K. Hooman, "Flow visualization study of partially filled channel with aluminium foam block", *International Journal of Heat and Mass Transfer*, 127, pp. 1197–1211, 2018.

Chapter 6 Experimental study of particulate fouling in the partially filled channel

This chapter presents an extended study from Chapters 4 and 5, with the addition of solid particle into the partially filled channel. The particle trajectories and pressure drop performances are investigated. The results of the clean condition (chapter 4 and 5) were considered as the baseline cases in this study. This chapter includes both qualitative and quantitative data, where the particle preferential deposition area and deposition mechanisms were also discussed.

Chapter 7 Conclusion and suggestions for future work

References

[1] A. Muley, C. Kiser, B. Sundén, and R. K. Shah, "Foam Heat Exchangers: A Technology Assessment", *Heat Transfer Engineering*, 33, pp. 42–51, 2012.

[2] O. Bagcl, N. Dukhan, M. Ozdemir, and L. A. Kavurmacloglu, "Experimental heat transfer due to oscillating water flow in open-cell metal foam," *International Journal of Thermal Science*, 101, pp. 48–58, 2016.

[3] H. Hu, X. Weng, D. Zhuang, G. Ding, Z. Lai, and X. Xu, "Heat transfer and pressure drop characteristics of wet air flow in metal foam under dehumidifying conditions," *Applied Thermal Engineering*, 93, pp. 1124–1134, 2016.

[4] M. Odabaee and K. Hooman, "Application of metal foams in air-cooled condensers for geothermal power plants: An optimization study", *International Communications in Heat and Mass Transfer*, 38, 7, pp. 838–843, 2011.

[5] M. Tajik Jamal-Abad, S. Saedodin, and M. Aminy, "Experimental investigation on the effect of partially metal foam inside the absorber of parabolic trough solar collector", *International Journal of Engineering*, 30, pp. 281–287, 2017.

[6] F. S. Anuar, M. R. Malayeri, and K. Hooman, "Particulate Fouling and Challenges of Metal Foam Heat Exchangers", *Heat Transfer Eng.*, 38, 7–8, pp. 730–742, 2017.

[7] W. Lu, T. Zhang, and M. Yang, “Analytical solution of forced convective heat transfer in parallel-plate channel partially filled with metallic foams”, *International Journal of Heat and Mass Transfer*, 100, pp. 718–727, 2016.

[8] M. G. Ghorab, “Modeling mixing convection analysis of discrete partially filled porous channel for optimum design”, *Alexandria Engineering Journal*, 54, 4, pp. 853–869, 2015.

[9] B. Buonomo, A. Diana, O. Manca, and S. Nardini, “Numerical investigation on natural convection in horizontal channel partially filled with aluminium foam and heated from above”, *Journal of Physics: Conference Series*, 923, 012049, 2017.

[10] M. Sener, A. Yataganbaba, and I. Kurtbas, “Forchheimer forced convection in a rectangular channel partially filled with aluminum foam”, *Experimental Thermal and Fluid Science*, 75, pp. 162–172, 2016.

[11] B. Buonomo, G. Ferraro, O. Manca, and L. Marinelli, “Mixed convection in horizontal channels partially filled with aluminium foam heated from below and with external heat losses on upper plate Mixed convection in horizontal channels partially filled with aluminium foam heated from below and with external heat losses on upper plate”, *Journal of Physics: Conference Series* , 501, 012005, 2014.

[12] K. Hooman, “Thermohydraulics of porous heat exchangers: full or partial blockage?”, in *Proceedings of the 5th International Conference on Porous Media and its Applications in Science and Engineering (ICPM5)*, Kona, Hawaii, 2014.

[13] G. S. Beavers and D. D. Joseph, “Boundary conditions at a naturally permeable wall”, *Journal of Fluid Mechanics*, 30, 01, pp. 197-207, 1967.

[14] J. A. Ochoa-Tapia and S. Whitaker, “Momentum transfer at the boundary between a porous medium and a homogenous fluid-I. Theoretical development”, *International Journal Heat Mass Transfer*, 38, pp. 2635–2646, 1995.

[15] K. Vafai, *Handbook of Porous Media - Chapter 6: Analytical Studies of Frorced Convection in Partly Porous Configuration*, CRC Press, 2000.

[16] E. Sauret, I. Abdi, and K. Hooman, “Fouling of waste heat recovery: Numerical and experimental results”, in *19th Australasian Fluid Mechanics Conference*, Melbourne, Australia, 2014.

[17] K. Hooman and M. R. Malayeri, “Metal foams as gas coolers for exhaust gas recirculation systems subjected to particulate fouling”, *Energy Conversion and Management*, 117, pp. 475–481, 2016.

[18] K. Hooman, A. Tamayol, and M. R. Malayeri, “Impact of Particulate Deposition on the Thermohydraulic Performance of Metal Foam Heat Exchangers: A Simplified Theoretical Model”, *Journal of Heat Transfer*, 134, 9, pp. 092601-1, 2012.

[19] E. Sauret, S. C. Saha, and Y. Gu, “Numerical Simulations of Particle Deposition in Metal Foam Heat Exchangers”, *International Journal of Computational Materials Science and Engineering*, 02, 3&4, pp. 1350016, 2013.

[20] E. Sauret and K. Hooman, “Particle size distribution effects on preferential deposition areas in metal foam wrapped tube bundle”, *International Journal of Heat and Mass Transfer*, 79, pp. 905–915, 2014.

[21] M. Odabaee, M. De Paepe, P. De Jaeger, C. T’Joen, and K. Hooman, “Particle deposition effects on heat transfer from a metal foam-wrapped tube bundle”, *International Journal of Numerical Methods for Heat and Fluid Flow*, 23, 1, pp. 74–87, 2013.

[22] S. T. W. Kuruneru, E. Sauret, S. C. Saha, and Y. T. Gu, “Numerical investigation of the temporal evolution of particulate fouling in metal foams for air-cooled heat exchangers”, *Applied Energy*, 184, pp. 531–547, 2016.

[23] J. Kahle, “Experimental investigation of deposit formation in foam structured EGR coolers”, ITW-Thesis, University of Stuttgart, Germany, 2012.

[24] H. D. Ackermann, “Experimental Investigation of Fouling in various Exhaust Gas Recirculation Coolers”, ITW-Thesis, University of Stuttgart, Germany, 2012.

[25] V. T. Morgan, “The overall convective heat transfer from smooth circular cylinders”, *Advances in Heat Transfer*, 11, pp. 199–264, 1975.

[26] F. W. Dittus and B. M. K., *Heat transfer in automobile radiator of the tubular type*. 1930.

Chapter 2: Literature Review

In this chapter, previous studies on the open-cell metal foams as potential heat exchangers is reviewed. The main benefits imposed by their unique microstructures are discussed, by including significant findings from other literature. This chapter also focuses on particulate fouling, involving an exhaust gas recirculation (EGR) system. The metal foams have been considered to be used under a similar (fouled) condition, yet there are also still unsolved issues under a clean condition. The literature review is extended by identifying current challenges of the metal foam heat exchangers, whereas several research gaps in the field of interest are pointed out.
The content of this chapter is from a published paper as stated below:

Paper 1**:**
F. Shikh Anuar, M. R. Malayeri, & K. Hooman. "**Particulate fouling and challenges of metal foam heat exchangers**", *Heat Transfer Engineering*, 38, 7-8, pp. 730 – 742, 2017.

Particulate Fouling and Challenges of Metal Foam Heat Exchangers

Fadhilah Shikh Anuar[a,d], M. Reza Malayeri[b,c], and Kamel Hooman[d]

[a]Centre for Advanced Research on Energy (CARe), Fakulti Kejuruteraan Mekanikal, Universiti Teknikal Malaysia Melaka, Hang Tuah Jaya, 76100 Durian Tunggal, Melaka, Malaysia; [b]School of Chemical and Petroleum Engineering, Shiraz University, Shiraz, Iran; [c]Institute for Process Technology and Environment (IVU), Technische Universität Dresden, Dresden, Germany; [d]School of Mechanical and Mining Engineering, The University of Queensland, Queensland, Australia

Abstract

In recent years, open-cell metal foam has gained attention for utilization for exhaust gas recirculation coolers due to its large surface area and porous structure. Theoretically, the porous foam structure would have better transfer heat through conduction and convection processes. However, the exhaust gases that enter the cooler would carry particulate matter, which may deposit within the foam structure. The existing fouling studies cannot explain the underlying mechanisms of particulate deposition thoroughly within the foam structure. This study reviews the particulate fouling of heat exchangers, particularly in the exhaust gas recirculation system. Some past approaches to investigate fouling, particle transport, and deposition in the metal foam heat exchangers for many different applications are also included. In addition, this study also includes the challenges that lie ahead in implementing the metal foam heat exchangers in the industries.

Nomenclature

A	heat transfer area (m^2)
BMEP	brake mean effective pressure (Pa)
C	heat capacity rate ($W.K^{-1}$)
C^*	ratio of minimum and maximum capacity rates
CFD	Computational fluid dynamics
C_p	specific heat at constant pressure ($J.kg^{-1}\ K^{-1}$)
EGR	exhaust gas recirculation
HC	hydrocarbon

LMTD	logarithmic mean temperature difference
$\dot{m}$	mass flow rate ($kg.s^{-1}$)
NTU	number of transfer units
PPI	pore per inch
PM	particulate matter
Q	heat transfer rate (W)
R	thermal resistances ($m^2K.W^{-1}$)
Re	Reynolds number, dimensionless
SOF	soluble organic fraction
T	temperature (K)
U	overall heat transfer coefficient ($W.m^{-2}K^{-1}$)
Q	heat transfer rate (W)
Subscripts	
c	cold surface
f	fouling
FL,O	outer fouling layer
in	inlet
max	maximum
min	minimum
o	overall
out	outlet
p	pore
th	thermal
Greek Symbols	
ε	heat exchanger effectiveness
ϕ	particle diameter (m)

2.1 Introduction

2.1.1 Metal foam microstructural and thermophysical properties

Metal foams are classified into two categories; (1) open-cell or closed-cell structure and (2) cell arrangement either stochastic or periodic [1, 2]. The metal foams have been used in many industries such as the biomedical industry because of their bio-compatibility, in the automotive, aerospace, ship, and railway industries for their light-weight, crash energy absorption, and noise control properties, besides being proposed for heat exchanger industries due to its highly conductive and porous structure [3]. The

open-cell metal foam consists of interconnected cells like dodecahedron shape which allow fluids to flow and the closed-cell metal foam has individual enclosure within the material as shown in **Figure 2.1**. The dodecahedron shape of open-cell foam is usually modeled as a cubic unit cell model or tetrakaidecahedron in numerical or mathematical studies [4-6]. The metallic material of foam prospered the heat transfer performance through conduction processes. An aluminum metal foam has been widely considered for heat exchangers due to its low density, high thermal conductivity and relatively low in price [7].

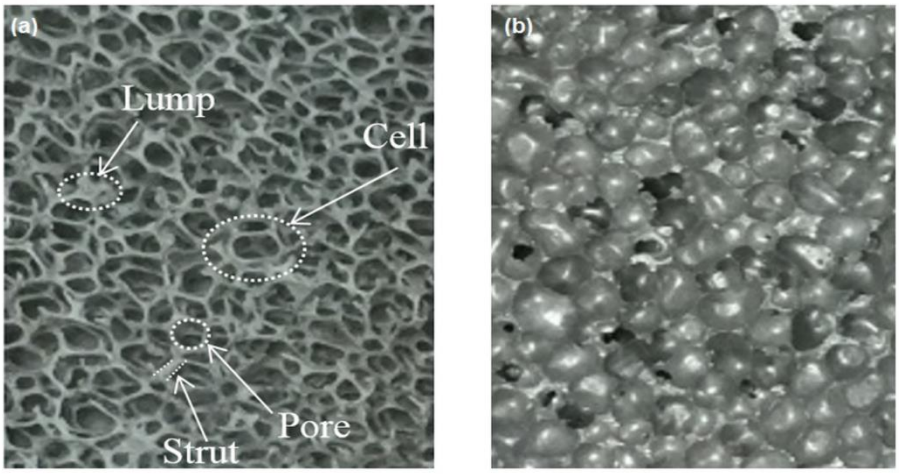

Figure 2.1 (a) 10 PPI open-cell metal foam (b) Closed-cell metal foam

The open-cell metal foams have considerable advantages in thermal management [8] and heat recovery [9, 10]. The thermo-physical properties of high porous metal foams have been investigated aggressively for the last 15 years [4, 11–13]. Manufacturers usually have classified the microstructure of open-cell metal foams based on porosity and pore density. The porosity can be estimated by using the weight of a given volume of the sample and the density of the metal, meanwhile the pore density is the number of pores per unit length of the material specified as PPI (pores per inch), which usually being supplied by the manufacturer [14]. The relative density of metal foam which is defined as the volume of solid foam material relative to the total volume of metal foam significantly influences the heat transfer performance. The open-cell metal foam with low relative densities and large surface area per unit volume promotes eddies for better thermal management, and compactness. While the porous structure (low relative density) foam offers high convective heat transfer by thermal dispersion and permeability, the high relative density one offers high thermal

conductivity [2]. By increasing the porosity and pore diameter, the permeability can be increased significantly. However, only the metal foam porosity has influenced the effective thermal conductivity [4, 15]. In addition, the increased porosity reduces the ligament (also known as strut or fiber) diameter, which consequently affects the conduction and the overall heat transfer coefficient significantly [16].

In terms of heat transfer performance, the complex structure of open-cell metal foam induces two different modes of heat transfer; convection and conduction which vary significantly based on the foam microstructure and operating condition. The effective thermal conductivity, the permeability, and the inertial impaction could be influenced by the foam microstructural properties such as the pore density (PPI), mean pore diameter, and surface-area to volume ratio [15–17]. Consequently, the microstructural properties of metal foams may also affect the overall heat transfer performance [15, 18]. The convective heat transfer within a porous structure metal foam is more dominant than conduction since its thermal conductivity is one order of magnitude lower than their parent material [1]. By increasing the foam thickness, the air side convective resistance could be reduced as the air penetrated within the foam structure up to 3–5 mm into the foam [2]. Chumpia and Hooman [18] proved that the thermal performance and pressure drop of 20 PPI metal foam wrapped on an aluminum cylinder could be increased with foam thickness of 5 – 20 mm. But, when comparing the foam to a finned tube at the same pressure drop of 25 Pa, the foam with 15 mm thickness has a higher heat transfer up to 37%. The study also claimed that the same foam thickness could have different thermal resistances due to other factors such as bonding method, air velocity, porosity and surface material. Generally, the overall thermal resistances of a heat exchanger include the convective and fouling resistances for both free stream fluids as well as the wall (surface) conductive resistance. For a metal foam heat exchanger, some additional thermal resistances are expected if the fouling layer is insignificant or did not clog the porous structure completely due to its bonding (contact) method [2, 5] and the ligaments layout (convective and conduction resistances). **Figure 2.2** shows a descriptive comparison of thermal resistances between a flat surface and a brazed metal foam based on the heat transfer mediums.

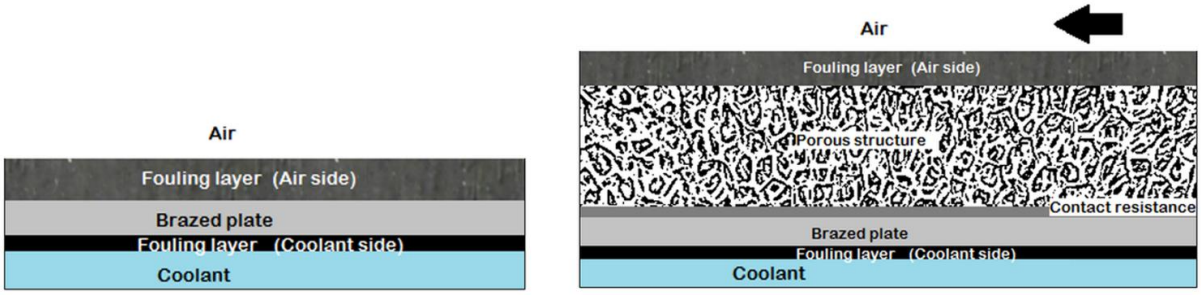

Figure 2.2 Heat transfer mediums for a flat surface (left) and a metal foam (right) – No deposition within the porous structure

The foam ligaments show similar concepts of corrugated fins or vortex generators which increase the heat transfer rate by imposing higher mixing flow, especially, at high Reynolds numbers (*Re*) [9, 19]. Furthermore, the ligament diameter and the interfacial velocity, which is calculated as Darcy velocity have been proven to influence the Reynolds number [19]. The open-cell metal foam heat exchangers show advantages in term of physical and mechanical properties as follows [1, 2, 19]: Light weight as composed about 90% of air; large specific surface area, i.e. 500 to 10,000 m^2/m^3; high gas permeability and thermal conductivity; resistive to high temperatures, humidity and thermal cycling; and excellent fluid mixing as it offers a tortuous flow path. Due to the promising foam properties, many studies have been conducted in different heat exchanger application, e.g., exhaust gas recirculation (EGR) cooler [15, 20, 21], air-cooled condenser [18, 22], and waste heat recovery [10]. A good review on the heat exchanger and heat sink using metal foam and metal matrix composites can be found from Han et al. [1]. As overall, the review supported the benefits of metal foam with better thermal conductivity, lighter in weight, higher surface-area to volume ratio, and convective heat transfer compared to the other conventional heat exchanger. However, the study also stated that no mass and cheap production are available for the metal foam, and there are lacks of open literatures on the thermo-hydraulic characterization based on a full scale testing for diverse application, which required more information for system integration and design optimization. Especially, to implement metal foam as a heat exchanger in diverse industries. Therefore, this study reviewed the metal foams as a potential heat exchanger to reduce particulate fouling and enhance the heat transfer performance. In addition, the particle transport and deposition process within different types of heat exchangers, configurations and

operating condition are also included, mainly for an exhaust gas recirculation (EGR) cooler application. The possible challenges related to the metal foam heat exchangers are also identified which should be solved in the near future.

2.1.2 Exhaust gas recirculation (EGR) system

Modern diesel engines have been installed with the EGR system to reduce nitrogen oxides (NO_x) emission by recirculating a fraction of the exhaust gas into an engine combustion chamber. The exhaust gas contains a lower oxygen concentration, but it has a higher heat capacity compared to the fresh air. The recirculation process reduces the combustion temperature through a dilution of fresh air (oxygen concentration) which allows higher mass concentration of the exhaust gas in the combustion chamber [23, 24]. Zheng et al. [24] determined the EGR rate by subtracting the measured fresh intake air (using a mass air flow sensor) from the estimated mass flow of a cylinder charge and attempted to reduce the combustion temperature in their study. Their result showed that an enhanced cooled EGR reduced about 200 ppm of NO_x at 20% EGR rate as compared to a hot raw EGR at 2100 rpm and brake mean effective pressure of 900 kPa bar as shown in **Figure 2.3**. Therefore, the cooled EGR is preferred in attaining much lower NO_x emission. Principally, the operation between the hot EGR and cooled EGR systems are different due to several additional components like EGR cooler (a heat exchanger), EGR valve, etc. The hot EGR system recycles the exhaust gas directly to the combustion chamber, meanwhile the cooled EGR system will reduce the exhaust gas temperature at the first hand before entering the chamber [24, 25]. The details literature on the EGR system could be found from Zheng et al. [24]. Even though, the cooled EGR showed greater reduction of NO_x by lowering the combustion temperature using a heat exchanger, a very low combustion temperature may cause incomplete combustion process which consequently, may produce more soot particles [26]. Therefore, a trade-off design between the soot particle deposition and NO_x reduction is critical in designing the EGR system. The first EGR cooler design was a shell and smooth tube type, and it is commonly used in many heavy-vehicles. The EGR cooler development is continued with corrugated tubes, and rectangular corrugated tubes with housing to attain EURO 5 standard, and later, the internal fins are considered to be attached to different geometries, e.g., tubes or plates to attain EURO 6 standard [27].

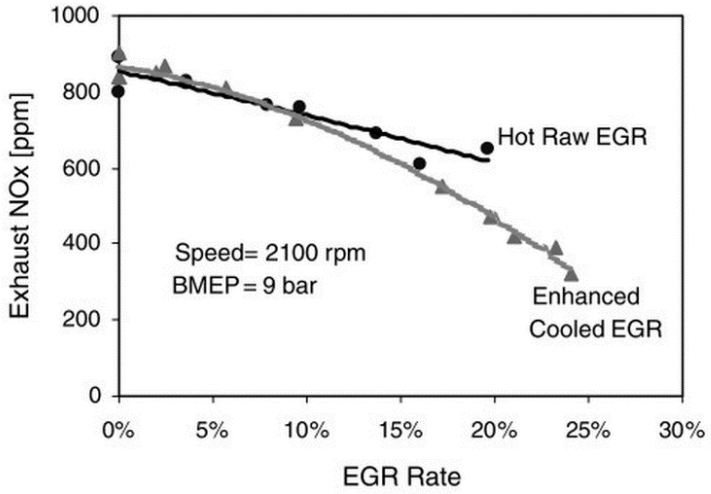

Figure 2.3 Exhaust nitrogen oxides, (NO_x) versus EGR rate [24]

2.2 Particulate Fouling

2.2.1 Particulate fouling in EGR coolers

Fouling in EGR coolers is a combination of chemical reaction, corrosion fouling, or particulate fouling. The condensation of unburned hydrocarbon (HC), water and acid as suggested by Kahle [21] and Abarham et al. [28] may initiate corrosion on the heat transfer surfaces. Meanwhile, biofuel as an alternative fuel could produce different chemical properties of a fouling layer [29]. However, the particulate fouling is a dominant fouling type in the EGR system. It is always related to one of the main exhaust gas composition, Particulate Matter (PM) which is a combination of soot particles, soluble organic fraction (SOF), sulfates and unburned hydrocarbon [30–32]. Additionally, the condensed HC was also considered as the main constituent of the fouling layer due to its significant effects on fouling growth [33]. Storey et al. [29] investigated fouling using two different fuels: ultra-low sulfur diesel and biodiesel blends, B20. The study proved the insignificant difference in the fouling rate based on the different fuels, HC level, or surface treatment and concluded that the fouling layer is porous with the thermal conductivity was approximate to 0.04 W/m K. Thus, the very low thermal conductivity of the fouling layer is considered as a barrier to heat transfer process.

Different types of heat exchanger exhibit dissimilar heat transfer characteristics due to the different fluid flow pattern, total heat transfer surface areas and surface material. For a smooth surface such as a shell and tube heat exchanger, the deposited

particles forms a layer and subsequently, reduces the cross-sectional area of the tubes. However, a process of particle removal is expected after some time, since the reduced cross-sectional area could induce high shear forces to drag or roll the particles before an asymptotic fouling condition is achieved. Furthermore, the temperature-dependent fouling in a heat exchanger becomes insignificant at that condition. The temperature of the outer layer deposit is close to the hot gas temperature. This in turn causes the temperature gradient as well as the particle deposition rate to decrease as shown in **Figure 2.4**.The fine particles deposited on the heat transfer surface at high deposition rate at the beginning of the deposition process prior to coarse particles, as they have higher sticking velocity compared to the coarse particles [30, 35, 36].

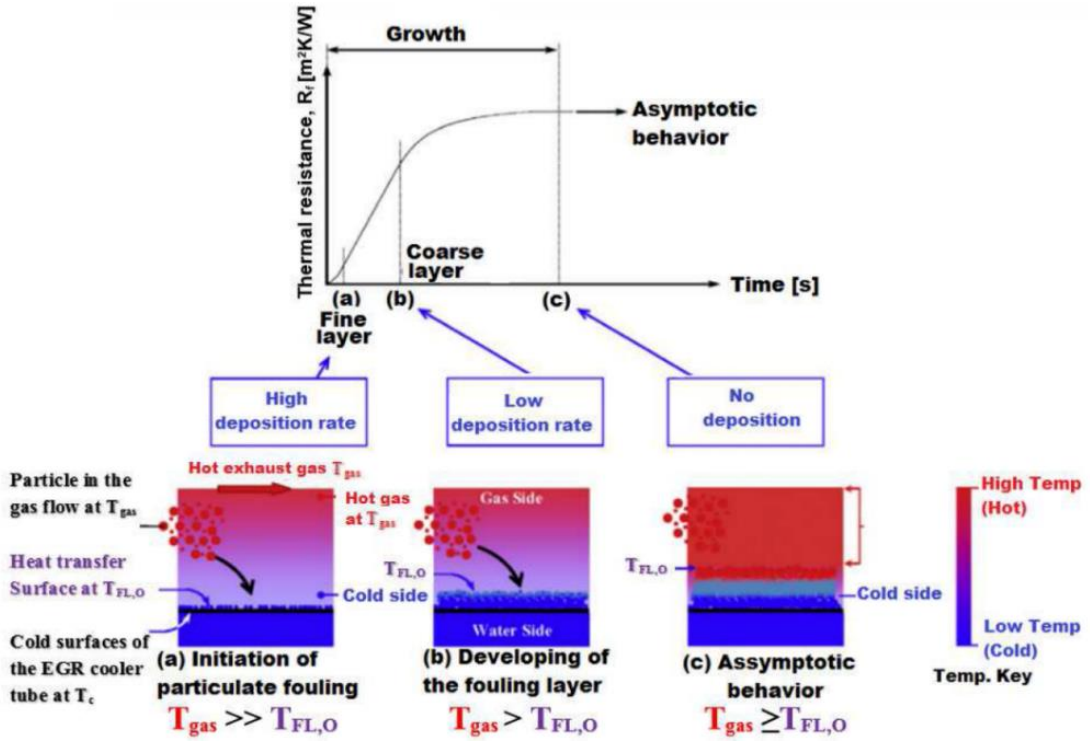

Figure 2.4 Stage of particulate fouling [34]

The deposit layer increased the pressure drop thus, affecting the thermo-hydraulic performance of the heat exchanger [21, 34, 37]. The high pressure drop may increase the NOx as affecting the engine operation, but low pressure drop could be handled by the EGR valve by modifying the position of the actuator [27]. The increased pressure drop across the EGR cooler may increase the pumping power [32]. In addition, the exit gas temperature is higher than initial EGR cooler design, thus reducing the EGR efficiency [27]. Moreover, the condensation of unburned HC of the diesel exhaust gas

[25, 38], excessive fuel consumption in the engine chamber [27], fouled EGR cooler design, operating mode based on the engine load and corrosion by SOF and PM [31] as well as carbon monoxide [25] would intensify the fouling problem. **Table 2.1** shows the typical soot particles and operating conditions in investigating the fouling problem in the EGR cooler [34, 39].

Table 2.1 Typical particle properties and operating conditions for EGR cooler fouling test

Properties	Values	References
Soot particle size	10-300 nm	Abd-Elhady and Malayeri [34]
Soot particle mass	100 mg/m^3	
Exhaust gas temperature	300-400°C (depends on the load and speed)	
Exhaust gas velocity	30 m/s	
Coolant temperature	80°C	
Coolant flow rate	>1 LPM	Lance et al. [39]

2.2.2 Fouling mechanisms and particle deposition on metal foam heat exchanger

Fouling mechanisms in EGR coolers include thermophoresis, electrostatic, eddy diffusion, turbulent impaction and gravitational force [23, 32] which depend on the operating mode and the particle properties. Any particle size smaller than 1 μm could be transported through thermophoresis, while the larger particles may experience inertial impaction for flowing exhaust gas in the EGR cooler at 400°C and 30 m/s [34]. However, the thermophoresis is the dominant fouling mechanism for the EGR cooler due to fine particle size and high temperature gradient [21, 32, 34]. In the meantime, van der Waals forces initiated opposite charges and forced the particles to move toward each other [29]. Thus, particle agglomeration occurs and the bigger particles deposit on the EGR cooler surface due to gravitational forces (sedimentation). The diffusion occurs as the EGR cooler surface temperature is lower than the material dew point temperature at local pressure, which then, initiates the SOF and HC condensation [31, 38]. According Abd-Elhady & Malayeri [34], the shear forces exerted by the gas flow can dislodge the deposited particles either by rolling or sliding the particles over the surface. The adhesion force and weight could be overwhelmed by

higher rolling moment, meanwhile, the drag force may slide (drag) the particles if it is higher than the friction force. **Figure 2.5** shows the acting forces on a particle on a flat plate surface.

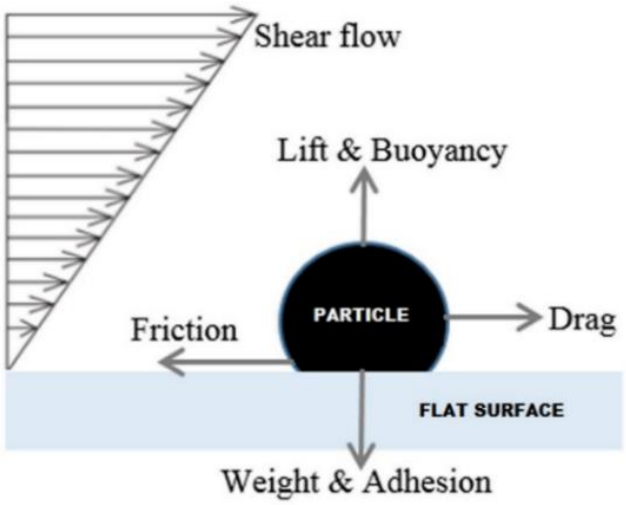

Figure 2.5 Forces acting on a resting particle

In addition to the operating conditions, the fouling in structurally various types of heat exchangers could be different, especially for the unique structure likes metal foam. Most numerical studies on fouling of metal foam have considered T'Joen et al. [2] experimental work for their geometry consideration [5, 40] and validation [40]. Earlier, T'Joen et al. [2] investigated the thermo-hydraulic performance of metal foams with different thickness, 4, 6 and 8 mm glued on aluminum tubes (0.01 m internal diameter and 0.012 outer diameter) and different dimensionless transversal tube pitch of 2.38, 2.68, 3.06 and 3.57 under diverse inlet air velocity of 0.75 – 7.7 m/s. The past numerical studies have considered no slip condition as assuming the particles have the same velocity as the continuous fluid flow [5, 40, 41]. However, the slip velocity depends significantly on the geometrical parameters of the foam which influence the sharp gradient at the interface of fluid and porous structure [42, 43]. Odabaee et al. [5] looked into the effect of dust deposition thickness in the range of 0.01 - 0.2 mm on metal foam thermo-hydraulic properties using computational fluid dynamics (CFD) simulation. Based on the contours of normalized velocity for both clean and fouled foam with the inlet velocity of 3 m/s, the study has concluded that the air velocity reduced to the lowest values at the forward and backward stagnation point of the foam tube inside the porous region, meanwhile a large recirculation zone appeared at the downstream, right after the tube. Sauret et al. [41] investigated the preferential areas

of particulate deposition in one row tube bundle wrapped with metal foam by injecting 5000 particles (mean diameter of 50 µm, standard deviation of 50 µm) into the air stream which developed 4 mm deposition thickness. The injected particles were about 3 orders of magnitude larger than those encountered in the EGR cooler work, as indicated in **Table 2.1**. The results showed that the backward velocity is noticeably smaller, about -0.6 m/s (no particle movement) compared to the main jet velocity of 10 m/s. Their results on the backward velocity is similar to another numerical study by Sauret and Hooman [40].

Both studies from Sauret et al. [41], and Sauret & Hooman [40] set the top, bottom and side surfaces of the domain to symmetry and atmospheric pressure at the outlet, but the former study set the wall temperature at 353 K and the inlet axial velocity of 3 m/s meanwhile, the latter has used 353 K and 450 K as the wall temperature and 1 – 7 m/s as the inlet axial velocity. However, the ligaments inside the porous medium in the between of foam and tube radius and tube radius were not modeled due to the complexity of real foam microstructure. By adding more particles up to 7500, the results showed no significant difference as compared to 5000 particles, but reducing the particles amount to 2500 showed significant effects on the deposition process [40]. The high deposition rate occurred mostly at the front tube which involved large particles with higher momentum, whereas for the tube rear region was subjected to large recirculation zone thus moving the particles back to the tube wall especially for particles < 20 µm [40, 41]. **Figure 2.6** shows the recirculation and dead zones of metal foam at the rear of the tube, marked as ‘x’ and **Figure 2.7** shows the preferential particulate deposition area which relates the particle size and particle volume fraction. The stagnant and recirculation zones exist behind the ligaments [1] possibly increased the particle deposition within the porous structure, which contradicts the ligaments function to increase the shear force to remove the deposited particles.

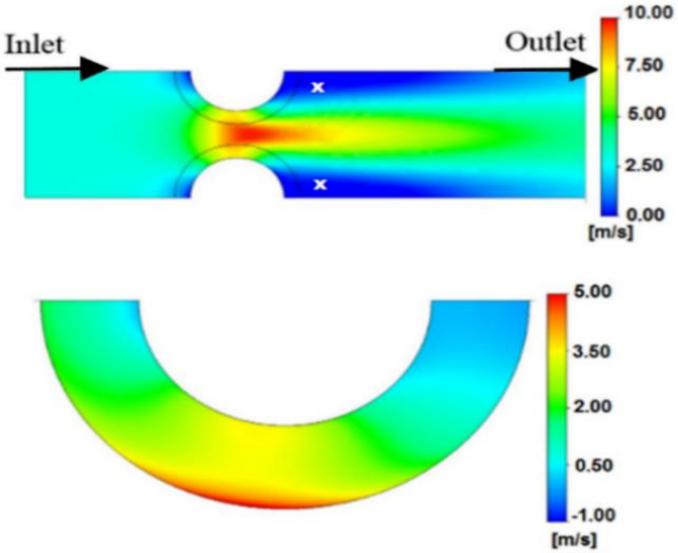

Figure 2.6 Axial velocity distribution with 3 m/s inlet air velocity (top) and axial velocity profile in the metal foam (below) [40]

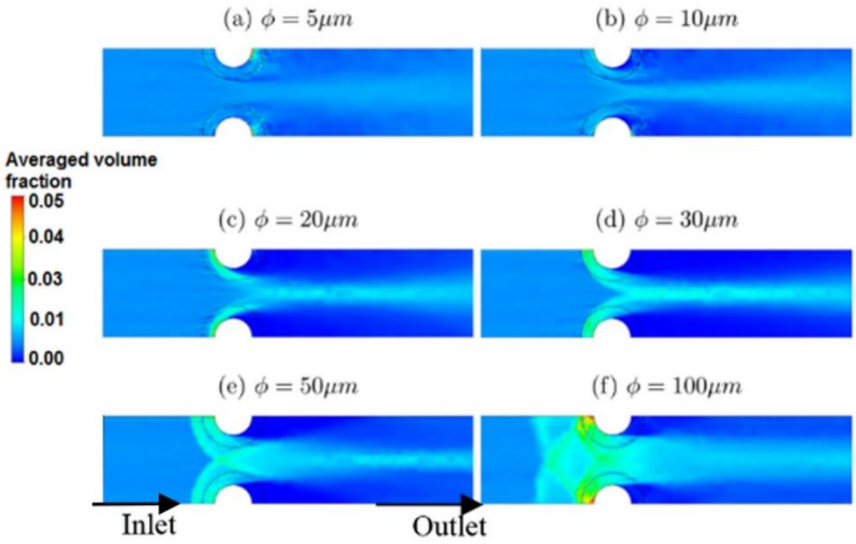

Figure 2.7 Average volume fraction of particle with particle size distribution [40]

Also, the ligaments may block the particle motion, accumulate the particles and develop a fouling layer. The fouling severity depends on the particle size, the pore size and the heat transfer characteristics [17]. By considering 60 - 130 nm soot particle, stated that the top layer of a foam plate was fully blocked, but partial blockage for underneath area within the ligaments structure and higher PPI clogged faster in a duration of 100 minutes. The clogged porous structure consequently increased the pressure drop [5, 21]. At high velocities, the metal foam area goodness factor reduced significantly due to the increased drag component of the pressure while the skin friction

is dominant on the pressure drop at low velocity [16]. In general, three factors in estimating the propensity of particulate fouling in the gas - side of metal foam are (1) particle volume fraction, (2) particle velocity, and (3) particle travelling time [40].

2.2.3 Metal foam fluid flow, solid-fluid interface and boundary layer

Sauret et al. [40] investigated the interface boundary condition between the gas and porous layer of metal foam with different pore density, foam height and gas inlet velocity. The study stated that at a low gas velocity, the disagreement between numerical and experimental studies occurred due to high uncertainties in the experimental data for low pressure drop condition and the model inaccuracy in predicting the fluid behavior at foam-fluid interface. Ashtiani Abdi et al. [9, 44] worked on 10 PPI metal foam, and claimed that a double wake size appeared behind the foam cylinder with 10% higher shedding frequency compared to a bare tube due to its rougher surface. In addition, the experimental work has shown no wake region within field of view at Re = 8000, compared to Re = 2000 which proved the relationship between swirl strength and Reynolds number. Meanwhile, the geometrical effects in their study could be observed only at high gas velocity. Furthermore, Hooman [45] stated that a fluid flow within a porous layer was leaving earlier before reaching the end because of a recirculation region exits at the downstream of the porous medium. Meanwhile, Sauret et al. [40] also agreed that gas velocity was already fully developed at a quarter of a channel length of porous structure. The porous structures of a metal foam heat exchanger may create tortuous flows and boundary layer disruption all the time. Therefore, the particle deposition seems likely to be influenced by the foam geometrical and microstructural aspects. Moreover, the flow regimes are also classified based on the pore-based Reynolds number, Re_p, which stated as follows [46]: Darcy dominated laminar flow region, Re_p <1; Forchheimer dominated laminar flow region, 1–10 < Re_p <150; Post-Forchheimer, unsteady laminar flow regime, 150 < Re_p < 300; and fully turbulent flow, Re_p > 300.

2.2.4 Effect of particles, operating conditions, and heat exchanger design

Abd-Elhady et al. [35] stated that the irregular size of particles reduced the critical flow velocity as some of the larger particles could roll the fine particles and the particle deposition likely to occur at the rear end of the tube due to lower shear force presented at that region. Storey et al. [29] proved that different fuel types, HC level, and surface

treatment had insignificant effects on the fouling process as their results showed similar particle deposition rates. Besides, the study also questioned the fact of increasing shear force as building up the fouling layer as the effect seems insignificant due to the porous structure of fouling layer. In addition, a part of the fouling layer microstructure and thermal conductivity are inconsistent throughout the fouling process due to an ageing process, a sintering process [47]. The fouling layer starts to harden gradually and under a hot gas stream, the layer become denser and stronger [35, 48]. Therefore, the fouling layer could be divided into two different layers called as coke (an aged deposit with higher thermal conductivity) and gel (a fresh deposited particle with low thermal conductivity) [47]. Meanwhile, Salvi [49] who investigated the nano-particulate layers in the engine exhaust gas heat exchangers using a visualization rig and in-situ measurement proved that the particulate layer thickness has insignificant effects on thermal conductivity. Since, the layer densification which influenced the layer porosity did not occur with deposition. Nevertheless, the thermal resistance, fouling layer thickness and fouling rate could be reduced by increasing the gas velocity [30]. Particularly, Abd-Elhady & Malayeri [34] stated that if the gas velocity is higher than the critical flow velocity (at maximum based on particle size), the fouling layer formation could be avoided. However, the study also claimed the gas velocity in the current EGR cooler is very small, about 10 - 30 m/s as compared to the required critical flow velocity of 40- 280 m/s for typical size of soot particles in between 10 - 300 nm. Despite, the low gas velocity had increased the radial and circumferential growth of fouling layer [35], but a very high gas velocity may cause pressure drop and required an alteration of the existing EGR system [50].

Thus, improving the geometrical aspect of a heat exchanger is preferred rather than considering the particle (foulant) chemical properties and diverse operating condition. A stack-type heat exchanger exhibited 25 – 50% higher effectiveness compared to a shell & tube heat exchanger [51, 52] and an oval spiral type had less particle deposition than a spiral EGR cooler [53] due to two main reasons (1) better mixing flows and (2) larger surface area. Meanwhile, the effectiveness of finned EGR coolers reduced gradually under different cycles [54] and the EGR cooler with a higher fin pitch of 4 mm had similar effectiveness with 2.5 mm fin pitch, but showing a lower pressure drop [55]. The effectiveness of a metal foam EGR cooler was higher than a flat plate after 4.5 hours under a fouling condition at 10 m/s gas velocity, but 40 PPI

foam has more deposited particles than 20 PPI [21]. Meanwhile, as comparing the same foam size of 30 mm (width), 195 mm (length) and different thickness of 3 mm and 4 mm, Ackermann [20] has agreed with Kahle [21] that lower PPI (e.g., 20 PPI) had better performance and the pressure drop could be decreased by reducing the foam thickness. Like the metal foam which acts as a turbulence inducer, other studies on fouling have attempted to improve the EGR cooler surface by creating inducers [56] or using a corrugated tube [27]. Meanwhile, an oval type EGR cooler with 4 mm fin pitch had better efficiency than 6 mm fin pitch since its wavy finned had created turbulence flow for self-purity [31].

2.2.5 Mathematical equation for fouling measurement

This study includes some common mathematical equations in determining the heat exchanger effectiveness, heat transfer rate, and thermal resistances. The effectiveness of a heat exchanger could be calculated by using (1) effectiveness-NTU method and (2) EGR cooler (heat exchanger) temperature ratio. The former has been used widely to compare various types of heat exchangers in order to determine the best-suited type of heat exchanger in a certain application [53–55]. It is defined as a ratio of the actual heat transfer rate (Q) and maximum possible heat transfer rate (Q_{max}) in a system, with the equation is written as [53]:

$$\varepsilon = 1 - \exp\left[\frac{\exp(-NTU \times C^{*} n) - 1}{C^{*} n}\right] \quad \textbf{(2.1)}$$

where $n = NTU^{-0.22}$ and number of transfer units (NTU) to represent the size of EGR cooler is equal to $UA/C_{\min}$. Meanwhile, C_{min} and C_{max} are the minimum and maximum capacity rates, and C^* is the ratio of C_{min} and C_{max}. Meanwhile, **Equation (2.2)** shows the effectiveness by describing the actual changes in the EGR gas temperature to the maximum change in the EGR gas temperature being cooled by the coolant temperature [29, 31, 57].

$$\varepsilon = \left(\frac{T_{gas,in} - T_{gas,out}}{T_{gas,in} - T_{coolant,in}}\right) \times 100 \quad \textbf{(2.2)}$$

The overall thermal resistance, R_{th} of an EGR cooler could be calculated by using **Equation (2.3)** [32]. As shown in **Equations (2.3**) and **(2.4)**, LMTD is an

abbreviation for logarithmic mean temperature difference, defined as an average temperature difference of the hot gas temperature and can be written as [21, 58]:

$$R_{th} = \frac{A_o \times LMTD}{Q} \quad \textbf{(2.3)}$$

$$LMTD = \frac{(T_{gas,in} - T_{coolant,out}) - (T_{gas,out} - T_{coolant,in})}{\ln\left(\frac{T_{gas,in} - T_{coolant,out}}{T_{gas,out} - T_{coolant,in}}\right)} \quad \textbf{(2.4)}$$

Equation (2.5) is used to determine the heat transfer rate, which involved the gas mass flow rate, $\dot{m}$ and heat capacity, c_p [21]:

$$Q = \dot{m} c_p (T_{gas,in} - T_{gas,out}) \quad \textbf{(2.5)}$$

The fouling thermal resistances, R_f can be determined using **Equation (2.6)**, which is the difference of the thermal resistance between a clean condition and a fouling condition at a certain time [32, 47]:

$$R_f = R_{th,(fouled)} - R_{th,(clean)} \quad \textbf{(2.6)}$$

Commonly, the fouling resistances are obtained by considering the process is a thermal steady state which assumed that the temperature profiles through fouling layer are lines, the heat flux through fouling layer is constant and the duration of heat transfer through the fouling layer is so much faster than the fouling layer growth [47].

2.3 Challenges of Metal Foam Heat Exchangers

2.3.1 Complex structure of Open-Cell Metal Foam

In general, the metal foam heat exchanger challenges included the accurate characterization of foam geometrical parameters, prophecy and validation of thermo-hydraulic performance, finding alternative measures and design improvement for excessive pressure drop and fouling [15]. Besides, a very limited published literatures on fouling of metal foam heat exchangers, current studies on the porous structure metal foam could not explain the insight of fouling phenomenon due to its complex structure. Previously, the numerical studies were conducted to explain the propensity of fouling within the foam structure and fluid-solid interface with some assumptions as follows [5]: Uniform deposition of particle within foam structure; uniform free stream velocity; constant temperature across the foam structure; and constant local thermal

equilibrium through porous medium by using thermal conductivity effectiveness from another experimental study on the heat transfer performance of a metal foam. However, the fluid velocity varies within the foam structure and it causes uneven particle deposition on the ligaments surface [41]. Kahle [21] also showed different severity of fouling in bulk within the ligaments and interfaces. However, no reference to local scales is made which seems to be controlling the overall performance of heat exchanger. Besides, the numerical studies and mathematical modeling used a cubic cell unit to represent the porous structure of metal foam. In real practice, the foam ligament diameter/shape, porosity and thickness affect the thermo-hydraulic properties significantly, which require experimental studies to explain the fouling process within the metal foam heat exchangers.

2.3.2 Range of operating condition, metal foam geometry and foulant properties

Due to diverse heat exchanger operating conditions in many industries, the optimization of metal foam geometrical parameters are not well established to match a particular application, especially the trade-off design between heat transfer and pressure drop performances. In addition to that, the particle removal and mitigation techniques from the foam microstructure are unclear and fall behind compared to other types of heat exchanger. Furthermore, as the deposited particles are subjected to the ageing process [47], more experimental and numerical studies are required as it may affect the thermal performance as well as the particle removal process. In addition to that, the effects of foam geometrical on the fouling propensity are not well established due to small parameter ranges [20, 21] and no foulant was involved physically in the past experimental study, even though the effect on velocity profile and flow separation were identified to increase the understanding on porous and non-porous interface [10]. Moreover, there are some conflicting results on the fouling effects with nano-sized particles on metal foam regardless of the particle chemical properties, such as 40 nm Al_2O_3 nanoparticles showed no deposition or the effects was insignificant for flowing fluid to block the porous cylinder with 0.249 porosity [59]. The nanofluids (based-fluid suspended with nano-size particles) have discrepancies in results probably due to the foam porosity or particle size effects, since 100-nm Al_2O_3 particles had deposited on the higher porosity (0.98) copper and nickel foams [60].

An optimum pore diameter is required so that more particles can pass through the foam microstructure to reduce fouling, without deteriorating the heat transfer performance. However, the interconnected ligaments can act like the barriers and to be considered as the nearby walls for the flowing fluid. Thus, the particle deposition may happen either partially or fully blocked the pores due to the ligament construction. Practically, it is difficult to obtain the exact fouling rates and resistances at every point of the EGR cooler surface due inconsistent thermo-physical properties [47], moreover within a complex porous foam. Besides, the reliable dominant fouling mechanism in the metal foam heat exchanger is unknown, which requires the manipulation of foam geometry, foulant properties, as well as the fluid velocities under both non-isothermal and isothermal condition. The partial and fully blocked metal foam heat exchanger [45] may also possibly have different effects on the particle deposition because of the fluid flow disturbance. Furthermore, the foam thickness showed significant effects on the pressure drop [61], even though the fouling effects are not being considered at all.

2.3.3 Free flow region, interface and porous structure

Sauret et al. [10] have suggested further fouling studies to explain the particle deposition across the interface of the porous and non-porous regions (transverse direction) as well as the particle motion along the foam length (streamwise direction). Particularly, as their results could not identify any sharp gradient at the porous and non-porous interface as assuming a continuous shear stress has appeared in that specific region. Moreover, the idea of particles to move from the fluid-foam interface to the tube wall in building-up fouling layer could not be true if considering the rebound and impaction velocities of the particles [40]. Besides, the numerical simulation of an interface boundary condition between the fluid and porous region in their study hardly simulates the experimental studies or represent real condition. More studies on slip velocity preferred through mathematical modeling [62–64], instead of the experimental work. For example, Xu, et al. [64] investigated on velocity slip, thermal slip, local thermal non-equilibrium effect, and asymmetric heat fluxes in two-parallel plate sandwiched with microfoams. The study derived an explicit expression for velocity and temperature of solid and fluid where their analytical solutions for wide ranges of Knudsen number and heat flux showed in agreement with existing references. In terms of fouling, the process of particle transport near the interface (boundary layer) could not be explained thoroughly. It shows the needs of experimental studies with a slip

condition in investigating the fouling and the thermo-hydraulic properties effects at the free fluid-porous interface. The thermo-hydraulic properties of fluid flow affect the fouling process which required more explanation as the deposition process varied based on the surface roughness, surface area to volume ratio, pore size, and pore distribution over the time [17].

2.3.4 Bonding method and overall thermal resistance

An appropriate bonding method of the metal foam heat exchanger could reduce the thermal resistances [19]. The manufacturing of metal foam should be improved in producing uniform ligaments throughout the foam structure. Hence, the lumps at the ligaments intersection and the irregularity of the ligament diameter could be avoided. Past fouling studies assumed that the thermal resistances in the EGR cooler were constant, as assuming a uniform fouling layer formation, but truthfully, they are changing with time [50]. Specifically for metal foam heat exchangers, the net radiation between the foam surface and surroundings was neglected from the overall thermal resistance as it was insignificant [18, 22]. The prediction of radiative heat transfer of metal foams is difficult due to the foam architecture, inherent complexity and transport mechanism within the ligaments layout [6]. However, the radiation effects can be significant for high temperature heat exchanger applications. One of the early attempts to consider the radiative heat transfer of metal foam was done by Contento et al. [6] who used a tetrakaidecahedron model as the basic unit cell to represent the foam microstructure. By combining the numerical simulations and analytical models based on ray-tracing Monte Carlo method and an iterative procedure, their model showed in agreement with experimental results from the past literatures. They have suggested to prepare an accurate foam morphological characteristics for a reliable model in considering the radiative conductivity.

2.3.5 Fouled Foam Cleaning Methods

Due to limited past literatures on fouling of the metal foam heat exchangers, there is no established fouling cleaning measure for that kind of heat exchanger. However, Kahle [21] has compared three different off-line cleaning method for a fouled metal foam by using a brush, an ultrasonic device and an oxidization method. The study concluded that the best cleaning procedure for soot particle deposition on the porous structure metal foam was when combining two methods using the brush and the

ultrasonic device together. To the best authors' knowledge, no studies or published literatures have considered the effects of corrosion fouling or other types of fouling on the metal foam heat exchanger which specifically may influence the cleaning measures. Current mitigation and cleaning strategies for the other types of heat exchanger reviewed by Müller-Steinhagen et al. [65] could also be considered for the metal foam heat exchanger, as long as, the cleaning process does not deteriorate the foam microstructure – ligament layout.

2.4 Summary and Future Work

The underlying knowledge of metal foam heat exchangers is important, especially the thermohydraulic properties and the fouling effects. At least to be accepted as a potential heat exchanger, the metal foam heat transfer performance should be superior compared to other types of heat exchangers at an identical pressure drop. The optimization of foam geometry and operating conditions should be determined for diverse heat exchanger applications. For further studies in the fouling aspect, the future work will be aimed to gain the insight of fouling on a porous foam block and identifying the preferential deposition areas through a visualization technique. The study will investigate the propensity of particulate fouling by considering the effects of foam microstructural and geometrical properties. Prior to that, the thermohydraulic properties under a clean condition should be fully understood. Ultimately, all regions along the metal foam as well as the upstream and downstream regions will be considered as the main points of flow visualization.

References

[1] X. H. Han, Q. Wang, Y.-G. Park, C. T'Joen, A. Sommers and A. Jacobi, "A review of metal foam and metal matrix composites for heat exchangers and heat sinks", *Heat Transfer Engineering*, 33, 12, pp. 991–1009, 2012.

[2] C. T'Joen, P. De Jaeger, H. Huisseune, S. Van Herzeele, N. Vorst and M. De Paepe, "Thermo-hydraulic study of a single row heat exchanger consisting of metal foam covered round tubes", *International Journal of Heat and Mass Transfer*, 53, 15–16, pp. 3262–3274, 2010.

[3] J. Banhart, "Manufacture, Characterisation and application of cellular metals and metal foams", *Progress in Material Science*, 46, 6, pp. 559–632, 2001.

[4] A. Bhattacharya, V. V. Calmidi and R. L. Mahajan, “Thermophysical properties of high porosity metal foams”, *International Journal of Heat and Mass Transfer*, 45, pp. 1017–1031, 2002.

[5] M. Odabaee, M. De Paepe, P. De Jaeger, C. T’Joen and K. Hooman, “Particle deposition effects on heat transfer from a metal foam-wrapped tube bundle”, *International Journal of Numerical Methods for Heat and Fluid Flow*, 23, 1, pp. 74–87, 2013.

[6] G. Contento, M. Oliviero, N. Bianco and V. Naso, “The prediction of radiation heat transfer in open cell metal foams by a model based on the lord kelvin representation”, *International Journal of Heat and Mass Transfer*, 76, pp. 499–508, 2014.

[7] N. Dukhan, “Correlations for the pressure drop for flow through metal foam”, *Experiments in Fluids*, 41, pp. 665–672, 2006.

[8] M. Odabaee, S. Mancin and K. Hooman, “Metal foam heat exchangers for thermal management of fuel cell systems–An experimental study”, *Experimental Thermal and Fluid Science*, 51, pp. 214–219, 2013.

[9] I. Ashtiani Abdi, K. Hooman and M. A. Khashehchi, “Comparison between the separated flow structures near the wake of a bare and a foam-covered circular cylinder”, *Journal of Fluids Engineering*, 136, 12, pp. 121203-1–121203-8, 2014.

[10] E. Sauret, I. Ashtiani Abdi and K. Hooman, “Fouling of waste heat recovery: numerical and experimental results”, *19th Australasian Fluid Mechanics Conference*, Melbourne, Australia, December 2014.

[11] V. V. Calmidi, “Transport phenomena in high porosity fibrous metal foams”, Thesis, University of Colorado, Boulder, CO, 1998.

[12] J. Paek, B. Kang, S. Kim and J. Hyun, “Effective thermal conductivity and permeability of aluminum foam materials”, *International Journal of Thermophysics*, 21, 2, pp. 453–464, 2000.

[13] D. Poulikakos and K. Boomsma, “On the effective thermal conductivity of a three-dimensionally structured fluid-saturated metal foam”, *International Journal of Heat and Mass Transfer*, 44, 4, pp. 827–836, 2001.

[14] S. Mahjoob and K. Vafai, “A synthesis of fluid and thermal transport models for metal foam heat exchangers”, *International Journal of Heat and Mass Transfer*, 51, 15–16, pp. 3701–3711, 2008.

[15] A. Muley, C. Kiser, B. Sundén and R. K. Shah, “Foam heat exchangers: A technology assessment”, *Heat Transfer Engineering*, 33, 1, pp. 42–51, 2012.

[16] I. Ghosh, “How Good Is Open-Cell Metal Foam as Heat Transfer Surface?”, *Journal of Heat Transfer*, 131, 10, pp. 101004, 2009.

[17] K. Hooman, A. Tamayol and M. R. Malayeri, “Impact of particulate deposition on the thermohydraulic performance of metal foam heat exchangers: A simplified theoretical model”, *Journal of Heat Transfer*, 134, 9, pp. 092601, 2012.

[18] A. Chumpia, and K. Hooman, “Performance evaluation of single tubular aluminium foam heat exchangers”, *Applied Thermal Engineering*, 66, pp. 266–273, 2014.

[19] S. De Schampheleire, P. De Jaeger, H. Huisseune, B. Ameel, C. T’Joen, K. De Kerpel and M. De Paepe, “Thermal hydraulic performance of 10 PPI aluminium foam as alternative for louvered fins in an HVAC heat exchanger”, *Applied Thermal Engineering*, 51, pp. 371–382, 2013.

[20] H. D. Ackermann, “Experimental Investigation of fouling in various exhaust gas recirculation coolers”, ITW Thesis, University of Stuttgart, Stuttgart, Germany, 2012.

[21] J. Kahle, “Experimental investigation of deposit formation in foam structured EGR coolers”, ITW Thesis, University of Stuttgart, Stuttgart, Germany, 2012.

[22] A. Chumpia and K. Hooman, “Quantification of contact resistance of metal foam heat exchangers for improved air-cooled condensers in geothermal power application”, *18th Australasian Fluid Mechanics Conference*, Launceston, Australia, December 2012.

[23] A. Mirsadraee and M. R. Malayeri, “Prediction of fouling in EGR coolers with radial basis function neural networks”, *Proceedings of International Conference on Heat Exchanger Fouling and Cleaning*, Budapest, Hungary, June 2013.

[24] M. Zheng, G. T. Reader and J. G. Hawley, “Diesel engine exhaust gas recirculation—A review on advanced and novel concepts”, *Energy Conversion Management*, 45, 6, pp. 883–900, 2004.

[25] H. Wei, T. Zhu, G. Shu, L. Tan and Y. Wang, “Gasoline engine exhaust gas recirculation—A Review”, *Applied Energy*, 99, pp. 534–544, 2012.

[26] D. Agarwal, S. Kumar Singh and A. Kumar Agarwal, “Effect of exhaust gas recirculation (EGR) on performance, emissions, deposits, and durability of a constant speed compression ignition engine”, *Applied Energy*, 88, pp. 2900–2907, 2011.

[27] Y. Bravo, C. Larrosa, C. Arnal, M. Alfè and R. Bilbao, “Effects of soot deposition on EGR coolers: dependency on heat exchanger technology and engine conditions”, *Proceedings of International Conference on Heat Exchanger Fouling and Cleaning*, Budapest, Hungary, June 2013.

[28] M. Abarham, T. Chafekar, J. W. Hoard, A. Salvi, D. J. Styles, C. Scott Sluder and D. Assanis, “In-situ visualization of exhaust soot particle deposition and removal in Channel Flows”, *Chemical Engineering Science*, vol. 87, pp. 359–370, 2013.

[29] J.M. E. Storey, C. S. Sluder, M. J. Lance, D. J. Styles and S. J. Simko, “Exhaust Gas Recirculation cooler fouling in diesel applications: Fundamental studies of deposit properties and microstructure”, *Heat Transfer Engineering*, 34, 8–9, pp. 655–664, 2013.

[30] M. S. Abd-Elhady, M. R. Malayeri and H. Müller-Steinhagen, “Fouling problems in exhaust gas recirculation coolers in the automotive industry”, *Heat Transfer Engineering*, 32, 3–4, pp. 248–257, 2011.

[31] J. Lee and K. Min, “A study of the fouling characteristics of EGR coolers in diesel engines”, *Journal of Mechanical Science and Technology*, 28, 8, pp. 3395–3401, 2014.

[32] A. Warey, S. Balestrino, P. Szymkowicz and M. R. Malayeri, “A one-dimensional model for particulate deposition and hydrocarbon condensation in exhaust gas recirculation coolers”, *Aerosol Science and Technology*, 46, 2, pp. 198–213, 2012.

[33] A. Warey, A. S. Bika, D. Long, S. Balestrino and P. Szymkowicz, “Influence of water vapor condensation on exhaust gas recirculation cooler fouling”, *International Journal of Heat and Mass Transfer*, 65, pp. 807–816, 2013.

[34] M. S. Abd-Elhady and M. R. Malayeri, “Asymptotic characteristics of particulate deposit formation in exhaust gas recirculation (EGR) coolers”, *Applied Therm. Engineering*, 60, pp. 96–104, 2013.

[35] M. S. Abd-Elhady, C. C. M. Rindt, J.G. Wijers, A. A. van Steenhoven, E. A. Bramer and T. H. van der Meer, “Minimum gas speed in heat exchangers to avoid particulate fouling”, *International Journal of Heat and Mass Transfer*, 47, 17–18, pp. 3943–3955, 2004.

[36] K. K. Santhyanarayanarao Subbarao, C. C. M. Rindt and A. A. van Steenhoven, “Growth rates of dry particulate fouling under variable process”, *Proceedings of International Conference on Heat Exchanger Fouling and Cleaning*, Crete, Greece, June 2011.

[37] T. R. Bott, *Fouling notebook*, Institution of Chemical Engineers, England, 1990.

[38] K. S. Hong, K. S. Lee, S. Song, K. M. Chun, D. Chung and S. Min, “Parametric study on particle size and SOF effects on EGR cooler fouling”, *Atmospheric Environment*, 45, pp. 5677–5683, 2011.

[39] M. J. Lance, C. S. Sluder, H. Wang and J. M. E. Storey, “Direct measurement of EGR cooler deposit thermal properties for improved understanding of cooler fouling”, *SAE International*, 2009. DOI: 10.4271/2009-01-1461

[40] E. Sauret and K. Hooman, “Particle size distribution effects on preferential deposition areas in metal foam wrapped tube bundle”, *International Journal of Heat and Mass Transfer*, 79, pp. 905–915, 2014.

[41] E. Sauret, S. C. Saha and Y. Gu, “Numerical simulations of particle deposition in metal foam heat exchangers”, *International Journal of Computational Materials Science and Engineering*, 2, 3&4, pp. 1350016, 2013.

[42] G. S. Beavers and D. D. Joseph, “Boundary conditions at a naturally permeable wall”, *Journal of Fluid Mechanics*, 30, 1, pp. 197-207, 1967.

[43] E. Sauret, K. Hooman and S. C. Saha, “CFD simulations of flow and heat transfer through the porous interface of a metal foam heat exchanger”, *Proceeding of the ASME 2014 Power Conference*, Baltimore, Maryland, USA, July 2014.

[44] I. Ashtiani Abdi, M. Khashehci and K. Hooman, “A comparison between the separated flow structured near the wake of a bare and a foam-covered circular cylinder”, *Proceeding of the ASME 2013 Fluids Engineering Summer Meeting (FEDSM2013)*, Incline Village, Nevada, USA, July 2013.

[45] K. Hooman, “Thermohydraulics of porous heat exchangers: Full or partial blockage?”, *Proceedings of the 5th International Conference on Porous Media and its Applications in Science and Engineering (ICPM5)*, Kona, HI, June 2014.

[46] N. Dukhan, “*Metal foams; Fundamentals and applications”*, DEStech Pubs., Inc., Lancaster, PA, USA, 2013.

[47] V. Y. Lister, J. F. Davidson and D. I., Wilson, “When is fouling too fast to measure thermally?”, *Proceeding of International Conference on Heat Exchanger Fouling and Cleaning*, Budapest, Hungary, June 2013.

[48] M. S. Abd-Elhady, S. H. Clevers, T. N. G. Adriaans, C. C. M. Rindt, J. G. Wijers and A. A. van Steenhoven, “Influence of sintering on the growth rate of particulate fouling Layers”, *International Journal of Heat and Mass Transfer*, 50, 1–2, pp. 196–207, 2007.

[49] A. Salvi, “In-situ determination of the thermo-physical properties of nano-particulate layers developed in engine exhaust gas heat exchangers and opportunities for heat exchanger effectiveness recovery”, Ph.D. Thesis, University of Michigan, Ann Arbor, MI, 2013.

[50] M. S. Abd-Elhady, T. Zornek, M. R. Malayeri, S. Balestrino, P. G. Szymkowicz and H. Müller-Steinhagen, “Influence of gas velocity on particulate fouling of exhaust gas recirculation coolers”, *International Journal of Heat and Mass Transfer*, 54, 4, pp. 838–846, 2011.

[51] S. Jang, S. Park, K. Choi and H. Kim, “Experimental investigation of the influences of shape and surface area on the EGR cooler efficiency”, *Heat and Mass Transfer*, 47, 6, pp. 621–628, 2010.

[52] H.-M. Kim, D.-H. Lee, S.-K. Park, K.-S. Choi and H.-M. Wang, “An experimental study on heat exchange effectiveness in the diesel engine EGR coolers”, *Journal of Mechanical Science and Technology*, 22, 2, pp. 361–366, 2008.

[53] S. K. Park, J. Lee and H. M. Kim, “Experimental study on the spiral and oval spiral EGR cooler efficiencies in a diesel engine”, *Heat and Mass Transfer*, 50, 12, pp. 1783–1789, 2014.

[54] S. Park, K. Choi, H. Kim and K. Lee, “Influence of pm fouling on effectiveness of heat exchanges in a diesel engine with fin-type EGR coolers of different sizes”, *Heat and Mass Transfer*, 46, pp. 1221–1227, 2010.

[55] S. H. Jang, S. J. Hwang, S. K. Park, K. S. Choi and H.M. Kim, “Effects of pm fouling on the heat exchange effectiveness of wave fin type EGR cooler for diesel engine use”, *Heat and Mass Transfer*, 48, 6, pp. 1081–1087, 2011.

[56] K. Mohammadi and M. R. Malayeri, “CFD study of turbulence induced structures in EGR coolers”, *Proceedings of International Conference on Heat Exchanger Fouling and Cleaning*, Budapest, Hungary, June 2013.

[57] K. S. Hong, J. S. Park and K. S. Lee, “Experimental evaluation of SOF effects on EGR cooler fouling under various flow conditions”, *International Journal of Automotive Technology*, 12, 6, pp. 813–821, 2011.

[58] M. Hatami, D. D. Ganji and M. Gorji-Bandpy, “A review of different heat exchangers designs for increasing the diesel exhaust waste heat recovery”, *Renewable & Sustainable Energy Reviews*, 37, pp. 168–181, 2014.

[59] A. F. Miguel, “Experimental study on nanofluid flow in a porous cylinder: Viscosity, permeability and inertial factor”, *Trans. Technical Publications*, 362, pp. 47–57, 2015.

[60] Z. G. Xu and C. Y. Zhao,” Influences of nanoparticles on pool boiling heat transfer in porous metals”, *Applied Thermal Engineering*, 65, pp. 34–41, 2014.

[61] N. Dukhan and K. Patel, “Effect of sample’s length on flow properties of open-cell metal foam and pressure-drop correlations”, *Journal of Porous Material*, 18, pp. 655–665, 2011.

[62] K. Hooman, A. Tamayol, M. Dahari, M. R. Safaei, H. Togun and R. Sadri, “A Theoretical model to predict gas permeability for slip flow through a porous medium”, *Applied Thermal Engineering*, 70, 1, pp. 71–76, 2014.

[63] Q. Zheng, B. Yu, Y. Duan and Q. Fang, “A fractal model for gas slippage factor in porous media in the slip flow regime”, *Chemical Engineering Science,* 87, pp. 209–215, 2013.

[64] H. J. Xu, C. Y. Zhao and Z. G. Xu, “Analytical considerations of slip flow and heat transfer through microfoams in mini/microchannels with asymmetric wall heat fluxes”, *Applied Thermal Engineering*, 93, pp. 15–26, 2016.

[65] H. Müller-Steinhagen, M. R. Malayeri and A. P. Watkinson, “Heat exchanger fouling: mitigation and cleaning strategies”, *Heat Transfer Engineering*, 32, pp. 189–196, 2011.

Chapter 3: Fully Filled Configuration with Open-Cell Metal Foam

From the literature review, there are notably significant gaps in the metal foam heat exchanger because of its complicated microstructural properties. Besides, the arrangement of the metal foam itself has influences on the thermal and pressure drop performances. Since last decades, a fully field configuration has been extensively studied. However, it is quite challenging to understand the microscopic contribution as the pore-level effects in real practice is rather complicated and could be different when comparing to the existing numerical and analytical results. Thus, this research includes the investigation of a fully filled configuration, where a series of experiments were conducted and the collected data were compared numerically. The temperature measurements have covered almost the entire foam structure. These long and exhaustive experiments were performed by measuring the temperature distribution throughout the complicated structure of the metal foam. Through this, the intricate metal foam structure was studied and acknowledged. Specifically, this chapter presents the investigation of forced convection through a vertical foam-filled annular heat exchanger. Temperature distributions within the porous foam were investigated experimentally and numerically, where an optimal thermal entrance length for each case is presented here. Also, the pressure drop effects were also determined based on different pore density and flow rates. A numerical model is also applied to analyse the improvement with the presence of the foam against a bare tube heat exchanger. Difficulties in taking measurements are undisputable due to the randomness of pore-ligaments layout, suggesting a non-invasive technique and an exact model to avoid time-consuming experiments. The content of this chapter from a published paper as follows:

Paper 2:

M. P. Orihuela, **F. Shikh Anuar**, I. A. Abdi, M. Odabaee, and K. Hooman, "**Thermohydraulics of a metal foam-filled annulus**", *International Journal of Heat and Mass Transfer*, 117, pp. 95–106, 2018.

Thermohydraulics of a Metal Foam-Filled Annulus

M.P. Orihuela [a,1], F. Shikh Anuar [b,c,1], I. Ashtiani Abdi [b,*,2], M. Odabaee [b,2], K. Hooman[b]

[a]Dpto. de Ingeniería Energética, Escuela Técnica Superior de Ingenieros, Universidad de Sevilla, Camino de los Descubrimientos, s/n, 41092 Sevilla, Spain; [b]School of Mechanical and Mining Engineering, The University of Queensland, Queensland, Australia; [c]Centre for Advanced Research on Energy (CARe), Fakulti Kejuruteraan Mekanikal, Universiti Teknikal Malaysia Melaka, Hang Tuah Jaya, Durian Tunggal, 76100, Melaka, Malaysia

Abstract

This paper offers numerical and experimental analysis of forced convection through an annulus filled with aluminium foam. Effects of flow rate and foam pore density on the performance of the heat exchanger were investigated. Specifically, 5 and 20 pore per inch (PPI) aluminium metal foams were tested at three different airflow rates; 20, 85 and 150 standard litre per minute. In parallel, the problem has been simulated numerically. Once validated against experimental data, numerical simulations were conducted to add to the level of details obtained from experiments. The thermal study was done by analysing the temperature field throughout the porous volume and determining the thermal entrance length. This parameter, the thermal entrance length, establishes a reliable design criteria for metal foam-filled heat exchangers, since it marks the length beyond which heat transfer does not significantly increase while the pressure drop keeps growing.

Nomenclature

A	area (m^2)
cd	cell density (equiv. to PPI, pores per inch) (1/m)
C_p	specific heat capacity (J/kg K)
d	diameter (m)
e	error (%)
E	total energy (J)
f	inertia coefficient (–)
g	gravitational acceleration (m/s^2)
h	heat transfer coefficient (W/m^2 K)
h_i	enthalpy of species i (J/kg)

J_i	diffusion flux of species i (kg/m^2 s)
k	thermal conductivity (W/m K)
k_1	Darcian permeability (m^2)
k_2	inertia resistance (m^{-1})
L	length (m)
LMTD	logarithmic mean temperature difference (K)
$\dot{m}$	mass flow rate (kg/s)
P	pressure (Pa)
ΔP	pressure drop (Pa)
Q	heat transfer rate (W)
S_f^h	fluid enthalpy source term (W/m^3)
S_s^h	solid enthalpy source term (W/m^3)
SLPM	standard litre per minute
ΔT	temperature difference (K)
t	thickness (m)
T	temperature (K)
U	overall heat transfer coefficient (W/m^2 K)
v	velocity (m/s)
z	axial direction (m)
$\partial\eta/\delta z$	efficiency gradient (m^{-1})

Subscripts

a	air
ai	air inlet
EA	external air
eff	effective
EW	external wall
f	fluid
F	foam
fs	fluid/solid interface
fx	fixed
i	inlet
IW	internal wall
l	ligament (struts in the foam)
m	mean
o	outlet
p	pore

r	random
s	solid
T	total
TA	air temperature
te	thermal entrance
∞	ambient
w	water
wi	water inlet
Greek symbols	
β	Forchheimer coefficient (inertia resistance) (1/m)
	$= f/\sqrt{k_1} = k_2$
ε	porosity
δ	uncertainty
∅	non-dimensional temperature
η	efficiency
ρ	density (kg/m3)
θ	angle (degrees)
μ	viscosity (kg/s.m)

3.1 Introduction

Open-cell metal foams have been investigated extensively for heat exchanger applications due to their promising properties such as lightweight, high surface area, high thermal conductivity, tortuous flow paths and good mechanical strength and stiffness [1–4]. Many studies have proved that the metal foams can augment the heat transfer compared to an identical heat exchanger with no foams or even different surface extension techniques [1]. Accordingly, a great deal of information is available in the literature addressing metal-foam filled tubes [5, 6], metal-foam wrapped tubes [7–10], fully-filled channels [11–18], partially filled channels [19, 20] and other constructions [21, 22] in order to match different applications. Due to significant improvement in heat transfer at the expense of higher pressure drop, many studies [9, 10, 21] have investigated the trade-off between the heat transfer and pressure drop increase. Odabaee et al. [9] numerically investigated a metal foam-wrapped tube with different foam thickness by varying the ratio of porous medium radius and surface radius from 1.025 to 2. Their results showed that the pressure drop and the heat

transfer rate were increasing with the foam thickness. Odabaee and Hooman [23] extended their investigation on the same samples through an optimization study based on the first and second law of thermodynamics and concluded that the metal foam heat exchangers would have 2–6 times higher performance factor than finned-tubes in the air-cooled condenser application. Chumpia and Hooman [10] experimentally studied the thermo-hydraulic of five foam wrapped heat exchangers with different thickness (5–20 mm). They showed that an optimum thickness of metal foam that provide a similar level of pressure drop to a finned tube will have better heat transfer performances. Mao et al. [24] also proved that the foam thickness of metal foam-wrapped tube has significant effects on the pressure drop and heat transfer performances. The study also claimed that only porosity has significant influence on the form coefficient, neither the pore size nor the pore shape. However, Hu et al. [3] demonstrated that a metal foam heat exchanger exhibited higher pressure drop and heat transfer rate as compared to a fin-and-tube heat exchanger when increasing the pore density and the relative humidity of the inlet air. Jin and Leong [25] also reported that the pressure drop was increasing with the pore density based on their study on steady and oscillating flows within 10, 20 and 40 PPI foams. Huisseune et al. [21] numerically designed two tube rows in a staggered tube layout inside a metal foam block which was a comparable design to a louvered finned heat exchanger. The study showed that the high pore density metal foam (>40 PPI) would have better performance than the finned heat exchanger and six times higher heat transfer compared to the bare tube.

In addition to the effects of foam thickness and its microstructural properties, there are also studies of heat transfer due to oscillating flow [26], as well as the thermal development in the flow directions [27, 28]. Iasiello et al. [27] investigated the developing thermal airflow through an open-cell metal foam based on the Kelvin's tetrakaidecahedron foam model. They stated that the presented correlation agreed with the existing results, within 20% and 30%, for interfacial and volumetric heat transfer coefficients, respectively. They also identified three regions in the foam along the flow direction; an impingement region, a thermally developing region and a thermally developed region, where the impingement effects were dominants at the inlet section. Dukhan et al. [28] stated that the thermal entrance regions must be considered based on their findings on the heat transfer of water run inside a metal

foam-filled tube. They identified two thermal behaviours based on the local Nusselt number, which then classified as thermally-developing and fully-developed conditions. In a similar metal foam construction, Bagci et al. [26] studied the heat transfer of oscillating water flow, as its thermal dispersion could not be neglected, unlike gas in the porous media. Details studies on the thermal dispersion have been conducted in different constructions, e.g., a porous-saturated pipe [29] and parallel plate porous channel [30]. In another interesting study, Dukhan et al. [31] proved that their experimental results on the fluid temperatures inside a heated aluminium foam-filled tube showed unexplainable behaviour when compared to the existing analytical solution. They proposed analytical solution which has been under-predicting fluid temperatures to achieve a comparable result to the experimental data. Meanwhile, some other experimental studies have addressed the difficulties in measuring the temperature within foam microstructures [12, 31].

It is important to note that the fluid temperature measurement within the foam microstructure unveils some uncertainties. When measuring with thermocouples at high temperature, errors may arise from the transient states and the high thermal gradients between the temperature of the solid and the temperature of the fluid [32]. To consider the temperature effects at pore level, Dukhan and Chen [12] measured the temperatures within three metal foam samples with different porosities by inserting thermocouples directly into the drilled holes. They presented the results as a function of the position and predicted an uncertainty in the temperature of about 11.7%, and in the non-dimensional temperature of about 13.9%. Meanwhile, Dukhan et al. [31] designed and fabricated a system to measure the internal temperature by using common thermocouples, but isolating their tips with small perforated aluminium tubes.

In this study, the ambient air is sucked into the porous structure of metal foam fills an annular section. The local temperatures were measured by positioning a thermocouple using a singular and in-house manufactured clamp. The internal temperature measurements have covered almost the entire foam structure to identify the air temperature distribution. Possible errors in the temperature measurements are counteracted with the increase in the number of measuring points, especially at the entrance region where higher temperature gradients are expected. This study also investigated the effects of the cell density (5 and 20 PPI) and the airflow rates on the

pressure drop. A numerical model is also applied to analyse the improvement with the presence of the foam against a bare tube heat exchanger.

3.2 Experimental Work and Simulation

3.2.1 Experimental Setup

This study investigated the pressure drop and the air temperature distribution of 5 and 20 PPI metal foam-wrapped pipes, manufactured by ERG Aerospace Corporation [33]. The microstructural properties of the metal foams and the heat exchanger geometrical description are tabulated in **Table 3.1**. The pore sizes and the ligament diameters were determined from the images obtained using a stereomicroscope (Nikon SMZ-745). The images of the metal foam microstructures with scale of 1 mm shown in **Figure 3.1**.

Table 3.1 Metal foam microstructural properties and heat exchanger geometrical description

Metal foam microstructural properties (Aluminium 6101 T6 Alloy)			Heat exchanger dimensions (m)	
Pore density (PPI)	5	20	Overall length (height)	0.53
Relative density (%)	7.9	7.0	Foam length (height)	0.45
Ligament diameter, d_f (mm)	0.00041	0.00026	Air inlet/outlet diameter	0.015
Pore diameter, d_p (mm)	0.0047	0.00085	*Inner tube - Aluminium*	
Porosity, ε (-)	0.921	0.930	Inner diameter	0.032
Permeability x 10^{-8}, k_1 (m^2)	7.09	2.89	Outer diameter	0.034
Drag coefficient, C_D (m^{-1})	256.43	211.66	*Outer tube (Shell) -*	
Inertia coefficient, *f (-)*	0.07	0.04	*Plexiglass*	0.055
			Inner diameter	0.059
			Outer diameter	

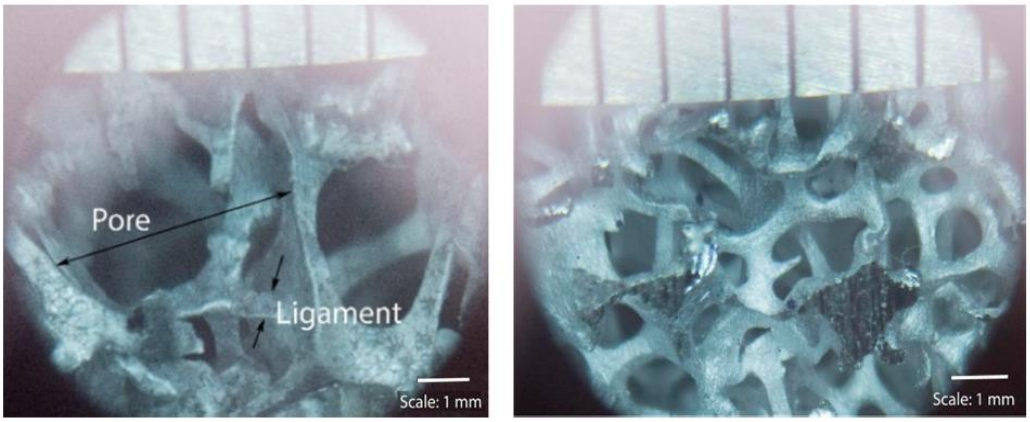

Figure 3.1 Microstructure of open-cell metal foam 5 PPI (left) and 20 PPI (right)

Figure 3.2 shows a schematic diagram of experimental setup which consists of three main components; the metal foam wrapped single pipe heat exchanger, a heating circulator (Julabo unit F25-ME), and a vacuum pump (ELMO-G; 1.1 kW). The heating circulator run the water through the inner pipe at a constant temperature of 60°C in a closed loop. The water flow rate was set at 5 l/min by using a manual valve and that constant value has been monitored using a digital flow sensor (SM 6000-Efector 300; ±2% accuracy) throughout the experiment. The vacuum pump sucked the ambient air to flow across the metal foam-ligament layout construction. The experiments were conducted at three different airflow rates; 20, 85, and 150 SLPM for both 5 and 20 PPI foams. The airflow rates were controlled using a gas mass flow controller (Cole Parmer EW-32907-79; ±0.8% accuracy). The vacuum pump and the heating circulator run idle for 30 min prior to the beginning of each experiment in order to achieve a steady state condition.

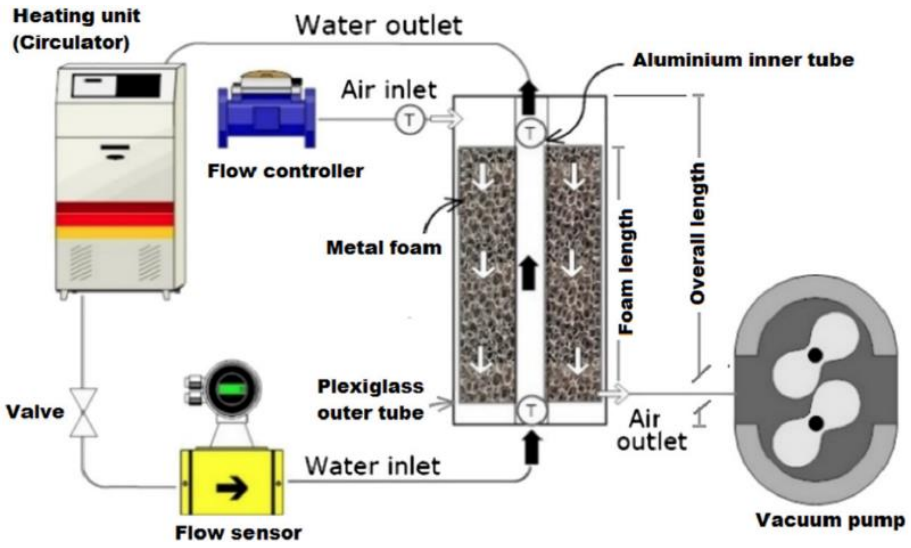

Figure 3.2 Schematic diagram of the experiment setup

Making a total of 40 holes, four holes were drilled radially in each of the 10 selected cross-sections through the plexiglass tube and the metal foam porous structure at different angles (0°, 90°,180° and 270°) and heights as shown in **Figure 3.3**. A thermocouple (K-type) was inserted into each single hole (d_{hole} = 1.8 ± 0.1 mm) to measure the air temperature at different positions; 1, 3, 6, 9 and 12 mm from the outer surface of the aluminium inner tube (**Figure 3.3**). The air temperatures were recorded at each point, by averaging the measured data over a 60s period to satisfy the statistical convergence. A clamp that is equipped with a trail and a millimetre ruler was used to precisely hold the thermocouple at the centre of the hole shown in **Figure**

3.4. Two additional thermocouples were fixed at the top and bottom of the inner pipe to measure the water outlet and inlet temperatures, respectively. All the thermocouples were connected to a data logger (PICO TC-08).

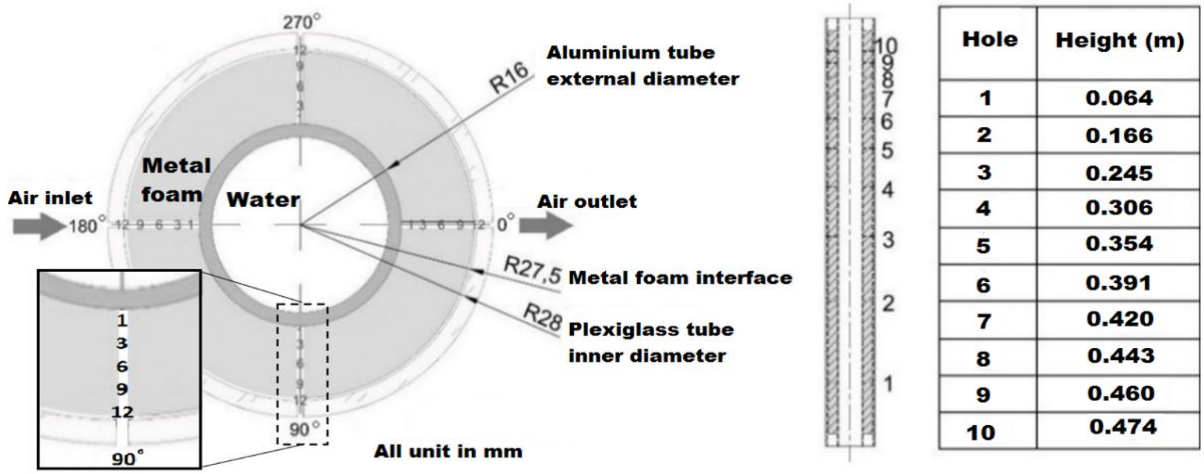

Hole	Height (m)
1	0.064
2	0.166
3	0.245
4	0.306
5	0.354
6	0.391
7	0.420
8	0.443
9	0.460
10	0.474

Figure 3.3 Measurement points in the radial and vertical positions - cross-sectional view

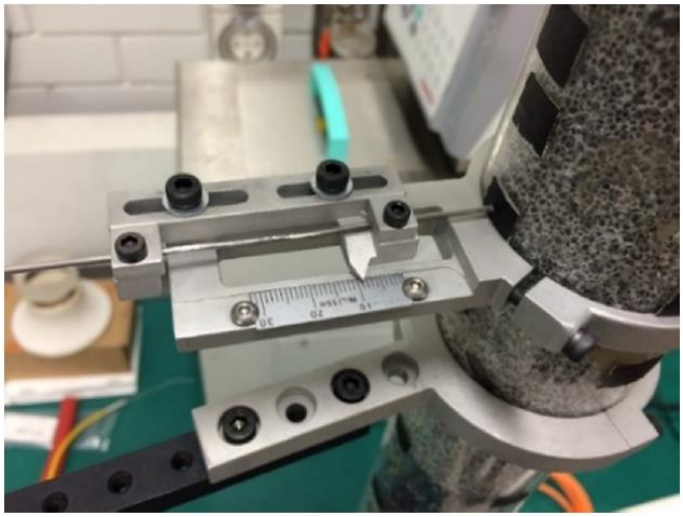

Figure 3.4 In-house manufactured clamp to position the thermocouple at the centre of hole

To measure the pressure drops of the metal foam, two pressure taps and a differential pressure sensor (Sensirion-SDP600 series) were installed at 90° position. One of the pressure taps was fixed into a reference point (a hole labelled as 10 in **Figure 3.3**), while the other pressure tap was moving downwards into each single hole (from hole number 9 to 1) to obtain the pressure difference between those two points. The measurements were also recorded at 0° position to study the effect of angular position on the pressure drop performances. However, the analysis of both,

temperature and pressure, results showed that there is no significant difference moving from one angle to the other along the same longitudinal line.

3.2.1.1 Uncertainty analysis

The uncertainties of the gas mass flow controller, reported by the manufacturer included a fixed error, e_{fx} = ±0.2% of the full scale and a random estimated error, e_r = ±0.8% of the reading. While for the differential pressure sensor, e_{fx} = ±3.0% and e_r = ±0.5%. The total uncertainties in the airflow rate and the pressure were calculated using the root-sum-squares method [31]:

$$\delta_T = \pm\sqrt{e_{fx}{}^2 + e_r{}^2} \quad \textbf{(3.1)}$$

Therefore, the total uncertainties in the airflow rate and the pressure drop in this study are about ±0.8% and ±3.0%, respectively. The diameter, thickness and length of the heat exchanger (metal foam, inner tube, and outer tube) as well as the distance between drilled holes were measured using a vernier caliper with the uncertainties in these readings were, δ_L = ±0.0001 m or by using a reference length of 0.5 m, the relative uncertainty in the length is about ±0.02%. Meanwhile, the uncertainty in the linear pressure drop, $(\Delta P/L)$ was calculated using **Equation (3.2)**:

$$\delta_{(\Delta P/L)} = \pm\sqrt{\left(\frac{\partial(\Delta P/L)}{\partial \Delta P}\right)^2 \delta_P^2 + \left(\frac{\partial(\Delta P/L)}{\partial \Delta L}\right)^2 \delta_L^2} \quad \textbf{(3.2)}$$

Hence, the maximum uncertainty of linear pressure drop in this study is about ±48.5 Pa/m. For the temperature, the manufacturer reported that the PICO-data logger accuracy is about a sum of ±0.2% of reading and ±0.5°C. The uncertainty in the K-type thermocouple is estimated to be within ±0.3°C. Using **Equation (3.1)** and setting the ambient temperature of 21°C as a reference, the relative uncertainty in the air temperature, δ_{TA} is about ±3.0%. A similar relative uncertainty is found in the water temperature, as the fixed error of the heating circulator is relatively small, around ±0.01 °C. The uncertainty propagation in the reported non-dimensional temperatures can be calculated from the corresponding partial derivatives using **Equation (3.3)**:

$$\delta_{(\phi)} = \pm\sqrt{\left(\frac{\partial \phi}{\partial T_a}\right)^2 \delta_{T_a}^2 + \left(\frac{\partial \phi}{\partial T_{ai}}\right)^2 \delta_{T_{ai}}^2 + \left(\frac{\partial \phi}{\partial T_{wi}}\right)^2 \delta_{T_{wi}}^2} \quad \textbf{(3.3)}$$

The term of the partial derivative associated with the air inlet temperature, T_{ai}, is much smaller than the other two terms. For instance, in Dukhan's uncertainty analysis for the non-dimensional temperature [34], T_{ai} is equivalent to an ambient air temperature, T_∞ and its error was not taken into account. In this case, based on **Equation (3.3)**, the estimated uncertainty in the non-dimensional temperature, considering a mean value of / = 0.6 is equal to 9.3%.

3.2.2 CFD Simulation

A numerical model based on the Navier-Stokes conservation equations is proposed to further extend the experimental study. The conservation equations for steady, incompressible flow of air with constant thermophysical properties are applicable at the outside of the porous zone, as well as the inlet and outlet regions. By assuming isotropic porosity, single phase and steady state flow, the equations of volume-averaged mass and momentum conservation in the porous zone are stated as follows (**Table 3.2**).

Table 3.2 Summary of the volume-averaged governing equations in the porous zone

Continuity equation:

$$\nabla \cdot (\rho \boldsymbol{v}) = 0 \quad \textbf{(3.4)}$$

Momentum equation:

$$\nabla \cdot (\rho \boldsymbol{v}\boldsymbol{v}) = -\varepsilon \nabla p + \varepsilon \mu_{eff} \nabla^2 \boldsymbol{v} + \varepsilon \rho \boldsymbol{g} - \frac{\mu}{k_1} \boldsymbol{v} - \frac{1}{2} k_2 \rho |v| \boldsymbol{v} \quad \textbf{(3.5)}$$

Energy equation:

(i) Fluid zone:

$$\nabla \cdot \left(\boldsymbol{v} \left(\rho_f E_f + p \right) \right) = \nabla \cdot \left(\varepsilon k_f \nabla T_f - \left(\sum_i h_i J_i \right) + \mu_{eff} \, \Delta \boldsymbol{v} \cdot \boldsymbol{v} \right) + S_f^h + h_{fs} A_{fs} \left(T_s - T_f \right) \quad \textbf{(3.6)}$$

(ii) Solid zone:

$$0 = \nabla \cdot \left((1 - \varepsilon) k_s \nabla T_s \right) + S_s^h + h_{fs} A_{fs} \left(T_f - T_s \right) \quad \textbf{(3.7)}$$

It is worth to mention that the porous medium was not modelled at pore-scale with separated-interactive solid and fluid volumes. As shown in **Table 3.2**, the porous model used in this study is similar to that of a normal fluid, but including a sink term in the momentum equation to represent the flow resistance. Consequently, this model is not as accurate as a model at pore-scale, but allows simulating a larger and more complicated geometry without needing much computational cost.

3.2.2.1 Geometry and mesh

A symmetrical 3-D geometry of the metal foam and air sections is created in ANSYS-Geometry based on the heat exchanger dimensions and the metal foam properties that tabulated in **Table 3.1**. Only one-half of the heat exchanger is modelled due to symmetry, as shown in **Figure 3.5**. The numerical model used in this study for the porous zone assumes that the porosity is isotropic and uses a simplified superficial velocity inside the porous medium based on the volumetric flow rate. In absence of radial effects, the geometrical symmetry will lead foreseeably to fluid-mechanic symmetry, with a flat two-dimensional velocity field in the symmetry plane. Under this hypothesis, there is no mass, momentum or energy transport across the symmetry plane. The inner pipe that conveys the hot water was not included as a volume in the model, but its thermal effect was taken into account by using a convective boundary condition in the internal wall of the domain. The geometrical domain is built with one inlet section in the upper side pipe, one outlet section in the lower side pipe, a number of external and internal walls, and six flat surfaces acting as symmetry planes. In order to generate a 3-D mesh for the geometrical domain, ANSYS-Mesh was used. A structured mesh was generated for the foam side while an unstructured mesh was utilized for the air one.

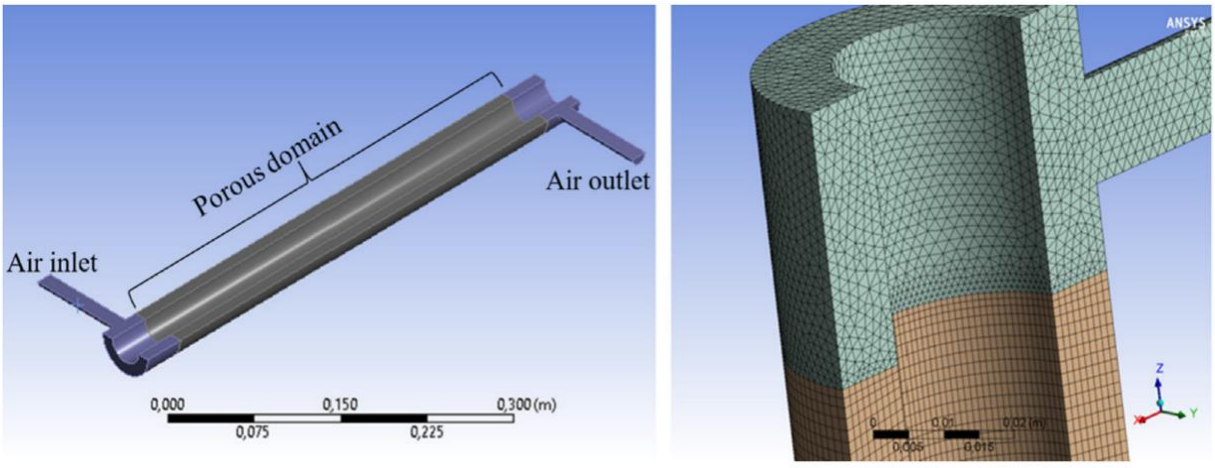

Figure 3.5 Geometrical domain (left) and detail of mesh (right) from CFD simulations

Figure 3.5 shows the aspect of the mesh in the upper zone of the heat exchanger, where the different structures of each part can be seen, and a mesh refinement can be distinguished in the interface between the air-inlet volume and the foam volume. A

growth rate of 1.2 was applied to the interfaces between porous and air volumes. The mesh independency is examined by trying a finer mesh and evaluating *ΔP* and *ΔT* between the 1st and 10th points as dependent variables. **Table 3.3** shows that a reduction in mesh size produces a difference between the variables lower than 2.3%. It could be seen as attaining an asymptotic behaviour in the present numerical model. Therefore, the nominated mesh size applied for CFD results is 0.95 mm.

Table 3.3 Analysis on the mesh independency

Mesh size (mm)	Number of elements	*ΔT* (°C)	*ΔP* (Pa)
1.20	286,560	6.7	27.0
0.95	508,433	8.8	27.8
0.40	21,855,517	9.0	28.0

3.2.2.2 Solver and boundary conditions

The 3-D continuity, momentum and energy equations are solved using the commercial CFD software ANSYS Fluent 17.0. The porous medium and fluid flow are considered to be in local thermal non-equilibrium where a dual cell approach is used to solve two separated equations, for the fluid and the solid phase, as stated in **Equations (3.6)** and **(3.7)**. A steady state, incompressible flow (pressure-based), and absolute velocity formulation (the macroscopic flow is practically one-dimensional) are considered to define the solver. The SIMPLE precision algorithm is used, so that the pressure and the velocity equations are then decoupled. The ANSYS Fluent Least Squares Cell-Based method is used to construct values of a scalar at the cell faces. Finally, a second order spatial discretization scheme is implemented in all the equations.

Two specific materials are implemented to assign accurate physical properties to the model: (a) plexiglass for the outer shell and (b) aluminium 6101 T6 for the foam. The metal foam is assumed to be homogeneous and isotropic with its microstructural properties are shown in **Table 3.1**. Some of the microstructural properties either were measured experimentally or have been provided by the manufacturer. The Darcian permeability, k_1 and the Forchheimer coefficient, $\beta = f/\sqrt{k_1}$ were calculated experimentally in this study by the Forchheimer-extended Darcy equation, as in Ref. [35]. They are presented in **Table 3.1**.

The total heat given by the water stream can be calculated as:

$$Q = \dot{m}_w C_p \Delta T \quad \textbf{(3.8)}$$

where $\dot{m}_w$ is the water mass flow rate, C_p is the water specific heat capacity, and ΔT is the temperature decrease in the water stream along the pipe in the heat exchanger. This heat is transferred to air and can be expressed as:

$$Q = U\ A\ LMTD \quad \textbf{(3.9)}$$

where LMTD is the logarithmic mean temperature difference between the hot and the cold side of the heat exchanger, and *A* is the total contact surface between the solid foam and the air. This latter may be calculated from the total volume and the specific surface of the foam given by the manufacturer.

Table 3.4 Summary of the boundary conditions used in the numerical model for 20 SLPM case, similar for both foam samples, 5 and 20 PPI

Surface	Boundary condition	Parameter	Value
Air inlet	Velocity inlet	v_i [(a)]	1.9 m/s
Air outlet	Pressure outlet (gauge)	P_o	0
External wall	Stationary wall	Wall thickness, t_{EW}	0.001 m
	Conduction across the wall	Thermal conductivity, k_{EW}	0.190 W/m.K
	Convection with the external air	Heat transfer coefficient, h_{EA} [(b)]	20 W/m^2.K
		External temperature	299.0 K
Internal wall	Stationary wall	Wall thickness, t_{IW}	0.002 m
	Conduction across the wall	Thermal conductivity, k_{IW}	202.4 W/m.K
	Convection with the internal water	Heat transfer coefficient, h_{IW} [(c)]	52 W/m^2.K
		Internal temperature	332.2 K
Symmetry surfaces	Symmetry	-	-

[(a)] Calculated from the imposed volumetric flow; 20 SLPM and the surface of the air inlet.
[(b)] Calculated from a correlation for natural convection around a cylinder [25].
[(c)] Calculated from a correlation for turbulent flow inside a circular tube [26].

While the applied boundary conditions are summarized in **Table 3.4** for one particular case, it is worth noting that the walls (internal and external) are modelled with their thickness to take into account the conjugated heat transfer (wall conductions). A convection boundary condition with the corresponding fluid are also included. For the wall of the outer pipe, Morgan's [36] correlation for natural convection around a cylinder is used to calculate the heat transfer coefficient.

3.3 Results and Discussion

The measurements occurred in between point 1 and 10 as shown in **Figure 3.3**. **Figure 3.6** shows that at the lowest flow rate, 20 SLPM, the increase of the pressure drop across the metal foam length is much lower compared to higher flow rates. At higher airflow rates (85 and 150 SLPM), the pressure drop growth is much more noticeable; up to 2.5 times. For example, in the case of 20 PPI foam at 85 SLPM, the pressure drop at point 2 is about 200 Pa. At 150 SLPM, the same foam shows an increase of pressure drop up to 500 Pa. Interestingly, the pressure drop of 20 PPI foam is about 35% higher than the 5 PPI foam at the same air mass flow rate. However, with either of the foams, the pressure drop at 150 SLPM is almost 10 times higher than that at 20 SLPM. In general, the numerical results are in agreement with the experimental counterparts as shown in **Figure 3.6**. Both data follow the same trends and showing similar results. The most significant difference is shown at 85 SLPM and is under 10%.

In **Figure 3.7**, the experimental pressure drop per unit length is plotted against the air mass flow rate over the range 0.0004–0.0030 kg/s. It shows that the pressure gradients across the metal foam (between hole 10 and hole 1) are increasing with the number of pores per inch for both foam samples. Even though the numerical values of porosities are close, ($\varepsilon > 0.90$), the 20 PPI foam shows higher pressure gradients compared to 5 PPI, as expected. The difference between those two values is more significant at higher flow rates. The growth of pressure gradients in this study could be represented by a linear trend similar to [38]. Specifically, the deviation in the linearity is neglected, as the measured pressure gradients are relatively small which mostly due to the low range of airflow rates and the non-uniform pore characteristics.

The thermal analysis of the metal foam-filled annulus began by obtaining the complete temperature field throughout the volume. In order to represent the evolution of temperature along the pipe, the non-dimensional temperature (/) was used. At each measuring length (each height) the non-dimensional temperature can be calculated as shown in **Equation (3.10).**

$$\phi = \frac{T_a - T_{ai}}{T_{wi} - T_{ai}} \qquad \textbf{(3.10)}$$

where T_a was obtained by averaging the temperature data of all the measured points in the cross section of the pipe at a certain height. At the lowest point of the system (air outlet), where the total thermal drop in the heat exchanger was considered, the dimensionless temperature represents the efficiency of the heat exchanger, η (since the air is the cold fluid and $(\dot{m}C_p)_{air} < (\dot{m}C_p)_{water}$, i.e.

$$\eta = \phi_0 \tag{3.11}$$

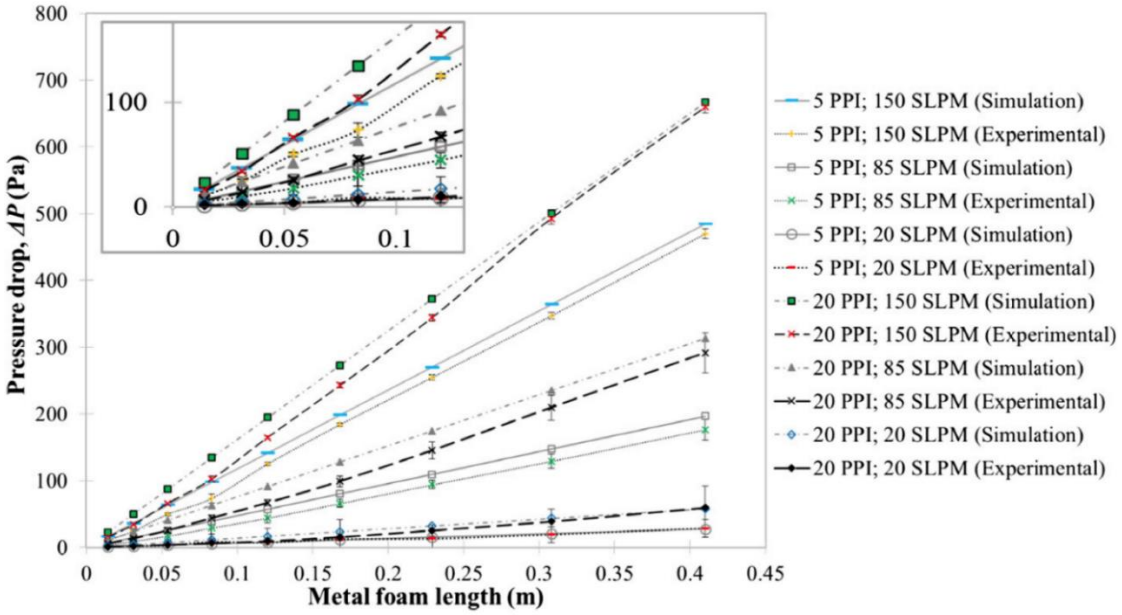

Figure 3.6 Comparison of pressure drop along the 5 PPI and 20 PPI foam at different flow rates

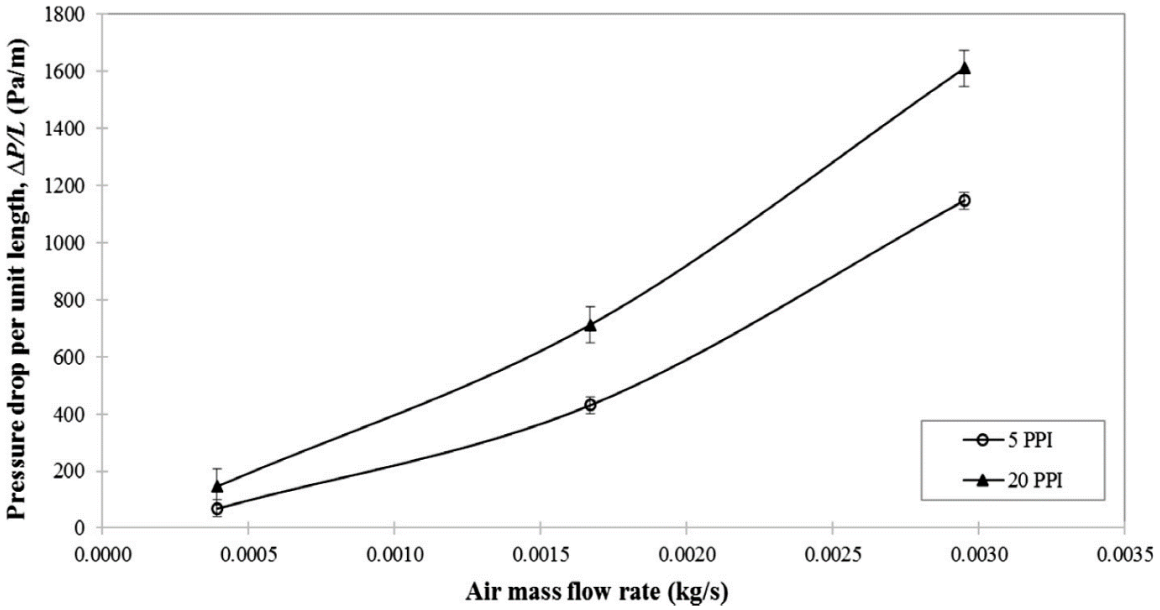

Figure 3.7 Pressure gradient versus flow rate

Thus, the non-dimensional temperature shown in **Equation (3.10)** is also representing the effectiveness of the metal foam heat exchanger at a given length. The non-dimensional temperature for different pore densities at the maximum and minimum flow rates is illustrated in **Figure 3.8**. The trend shows that most of the heat is exchanged in the entrance region where the non-dimensional temperature dramatically increases. The slopes are highest, moving from the air entrance all the way to 0.1 and 0.15 m for 20 and 150 SLPM, respectively. Following this, a less vigorous heat transfer process, compared to the first part of the annulus, is observed. The increment in the non-dimensional temperature is reduced towards an asymptotic value towards the exit.

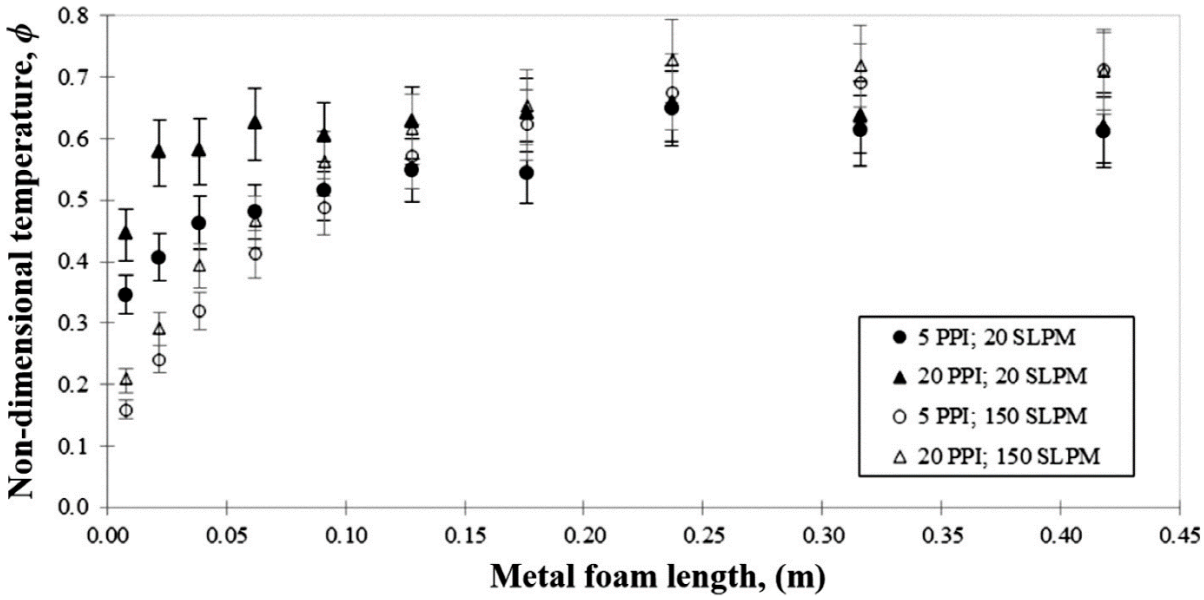

Figure 3.8 Non-dimensional temperature of 5 and 20 PPI at different flow rate

Figure 3.8 also shows that for an identical pore size, the non-dimensional temperature rises sharply in the entry region, especially with lower airflow rates. Even though the heat exchange process is slowed down in the second segment of the annulus, the maximum non-dimensional temperature is obtained at the end of the foam. The experimental results show a higher non-dimensional temperature for 20 SLPM in the first segment of the heat exchanger, but similar final non-dimensional temperature for both flow rates. A possible explanation for this might be the variation in the residence time. When the air flow is slower, it spends more time crossing the foam and collects more heat, especially in the entrance region where the temperature difference is higher. At final stage of heat exchanger, the non-dimensional temperature for 150 SLPM seems higher; nevertheless, the uncertainty at the last points is

considerable and it should not be ruled out that these values were due to a lack of accuracy in the measurement.

Figure 3.9 shows the non-dimensional temperature comparison between the experiment and the simulation on the metal foams and bare tube heat exchanger at 20 SLPM. The non-dimensional temperature from the numerical results are in good agreement with the experimental results for both the 5 PPI and the 20 PPI foams. By using the same model to simulate a bare tube heat exchanger, the increase in the non-dimensional temperature due to the foam construction can be estimated. In that case where there is only a bare tube without foam, a considerable decrease of air temperature is noted. Subsequently, the non-dimensional temperature reduction, which is higher than 50%, should be expected for the total length of the heat exchanger.

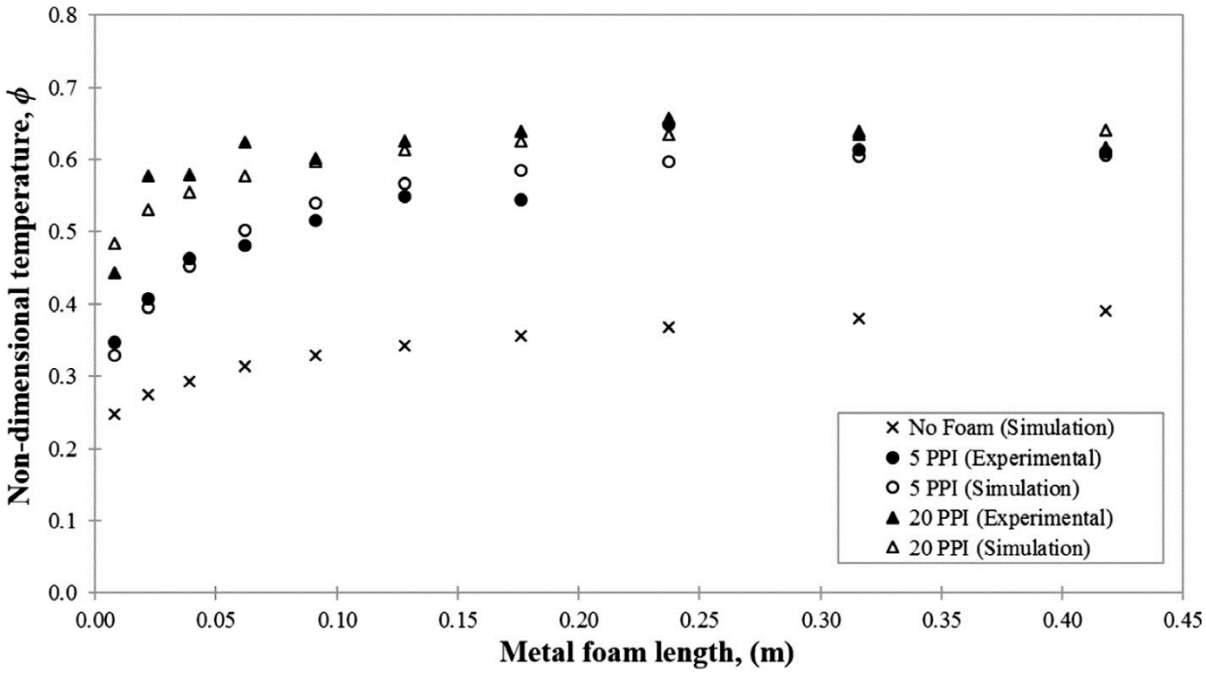

Figure 3.9 Predicted non-dimensional temperature for metal foams and the bare tube heat exchanger at 20 SLPM

In order to set a first design criterion for an optimized compact heat exchanger, the thermal entrance length (L_{te}) was calculated for each case as indicated in **Equation (3.12):**

$$\frac{\partial}{\partial z}\left(\frac{T_a - T_{IW}}{T_m - T_{IW}}\right)\Big|_{z=L_{te}} \geq 0 \qquad \textbf{(3.12)}$$

In each case (for each cell density and each flow rate), T_m is the mean temperature of the air in the complete volume, and it was obtained as the average from all the measured points of the heat exchanger. Thus, the expression in brackets represents the ratio between the thermal drop air-wall in each point and the mean thermal drop. This ratio has been represented in **Figure 3.10** for both foam samples, 5 PPI and 20 PPI, and for two different air flow rates: 20 SLPM and 150 SLPM.

The thermal entrance length is the distance from the entrance needed by the thermal ratio shown in **Equation (3.12)** to reach a constant value (zero gradient). In **Figure 3.10**, L_{te} is the metal foam length (x-axis) needed by the Y-variable to reach the minimum and start rising. As shown in that Figure, L_{te} is shorter than 0.25 m for all the cases considered in this study. The thermal entrance length is shorter for 20 SLPM than for 150 SLPM. Besides, when the flow rate is 20 SLPM, it can be seen that the lowest cell density, 20 PPI, provides with the shortest thermal entrance length. This contribution of the cell density is only noticeable for the 20 SLPM flow rate, since for 150 SLPM no difference can be appreciated. For all the cases studied in this work, the best scenario was found for the 20 PPI foam with 20 SLPM. In that case, the thermal entrance length was equal to 0.1 m.

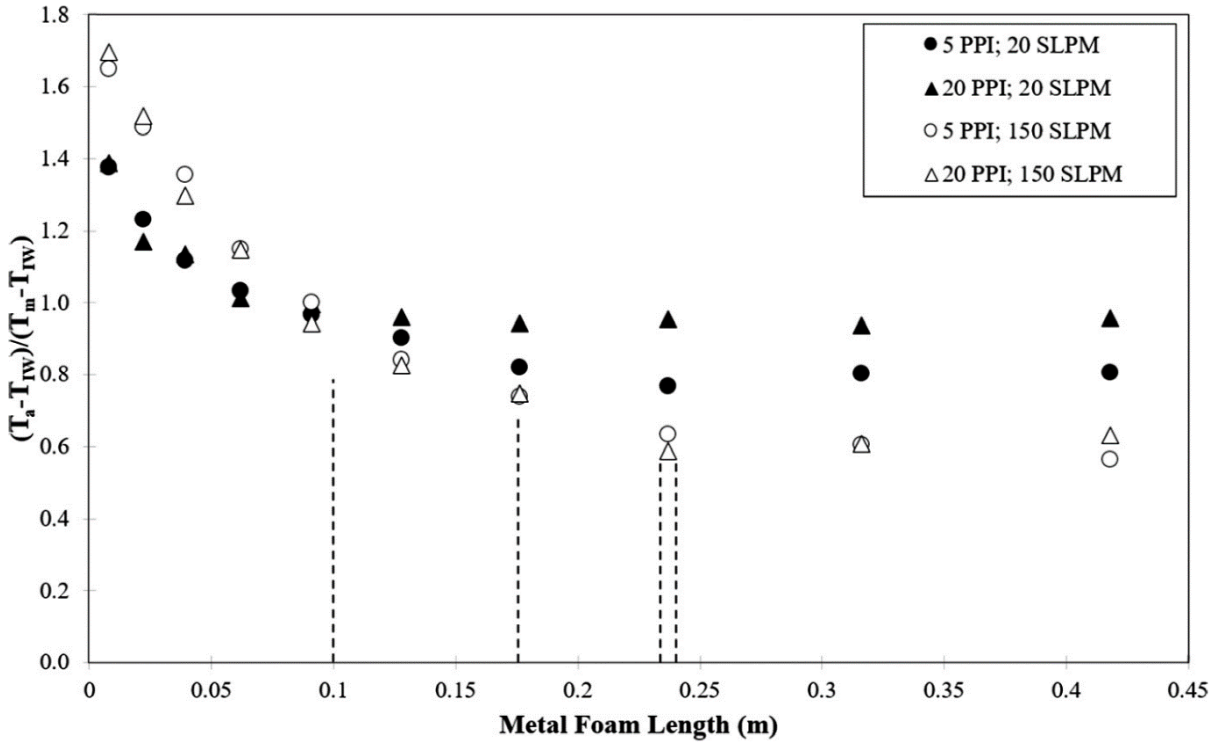

Figure 3.10 Thermal entrance length of 5 and 20 PPI at different flow rate

A similar conclusion can be obtained when examining the non-dimensional temperature or the potential efficiency for a certain length as it was defined in **Equation (3.10)** and **(3.11)**. An interesting parameter of the heat exchanger could be the length of the foam beyond which the gradient of efficiency becomes equal to or smaller than a certain value, for instance 1 m^{-1} as proposed in **Equation (3.13)**:

$$\left.\frac{\partial \eta}{\partial z}\right|_{z=L_{eff}} \leq 1 \qquad \textbf{(3.13)}$$

Since the pressure drop increases linearly with the length and the non-dimensional temperature doesn't, this parameter may represent an effective length beyond which extending the heat exchanger may not be worthy. In particular, in **Equation (3.13)**, this value would represent the point from which the increase in non-dimensional temperature is less than 1% in each 0.01 m of the additional pipe length. The decision criterion (1 m^{-1} or any other) is subjective and may depend on the application. For applications where the space is more restricted, a higher value for the efficiency gradient may be considered.

Table 3.5 Dimensionless effective length for each case

Cell density, cd (PPI)	Airflow rate (SLPM)	Effective length, L_{eff} (m)	Dimensionless effective length
5	20	0.0747	0.166
	85	0.1413	0.314
	150	0.1474	0.328
20	20	0.0413	0.092
	85	0.1042	0.232
	150	0.1578	0.351

This parameter, L_{eff}, reinforces the idea of a heat exchanger with optimal thermal entrance length. For each case, this effective length was calculated according to **Equation (3.13)**, and presented in **Table 3.5**, next to its dimensionless value (a ratio of the effective length to the total foam length, L_{eff}/L_F). The dimensionless effective length is decreasing with the airflow rates for both different PPI values. However, the 5 PPI foam with larger pore sizes requires an additional length to have a good thermal performance at the lowest flow rate. Increasing the flow rates, the dimensionless effective length becomes more PPI independent. The 20 PPI foam has shorter effective length at 20 and 85 SLPM, but showing a similar value to that of the 5 PPI at

the highest flow rate; 150 SLPM. Since all the values of dimensionless effective length are lower than 0.40, it has been proved that the majority of the heat exchange takes places at the first half (initial stage) of the annulus.

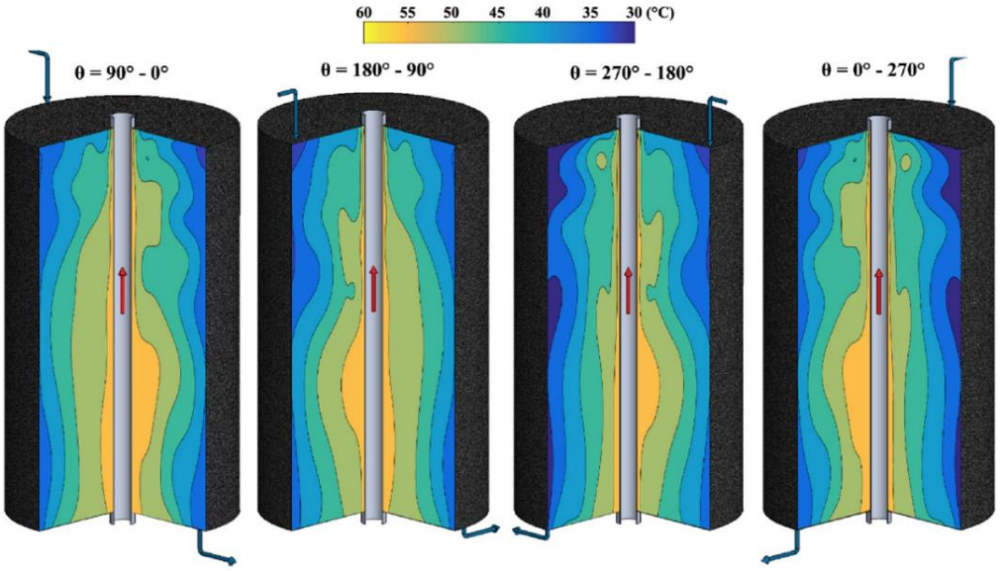

Figure 3.11 Experimental temperature contour (5 PPI, 20 SLPM)

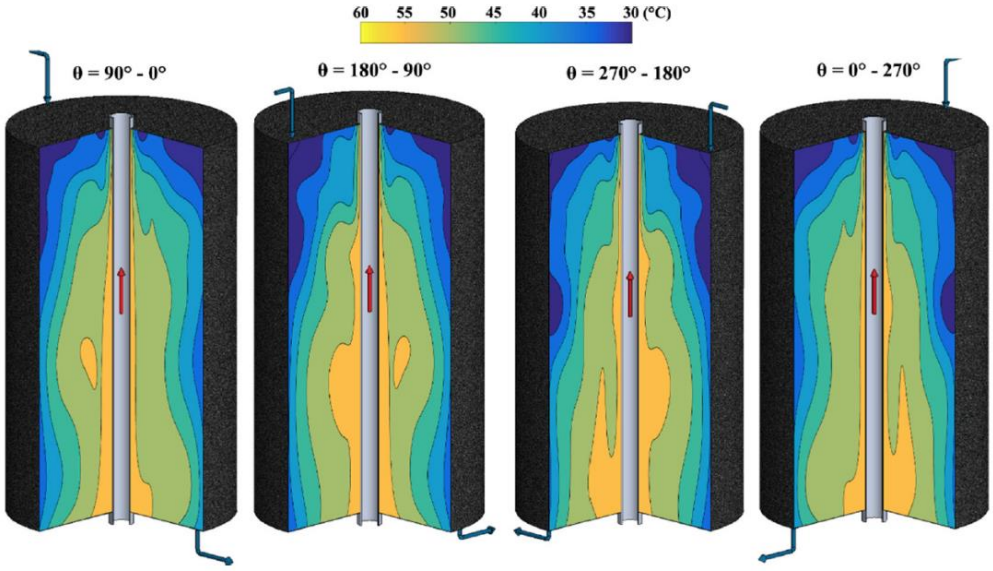

Figure 3.12 Experimental temperature contour (5 PPI, 150 SLPM)

Figures 3.11 – 3.14 demonstrate the temperature distribution along the pipe at four different angles (0, 90, 180 and 270°) for two different airflow rates (20 and 150 SLPM) and different pore sizes (5 and 20 PPI). As expected, the measured temperature on the outer surface of the inner pipe is about 60°C, and the temperature drops as moving to the colder surface. However, the temperature distribution is nonlinear. Evidence of developed flow is

apparent for the foam tube with smaller pore size at higher airflow rate in the lower half of the annulus, but the flow is clearly developing in the rest of figures where the radial temperature profile is non-linear. Another significant observation is the high temperature region that is forming in lower regions of the pipe towards the air flow direction. The region is formed uniformly in the developed regions of the foam obtained with 150 SLPM compared to the lower flow rate of 20 SLPM (**Figures 3.11** and **3.13**).

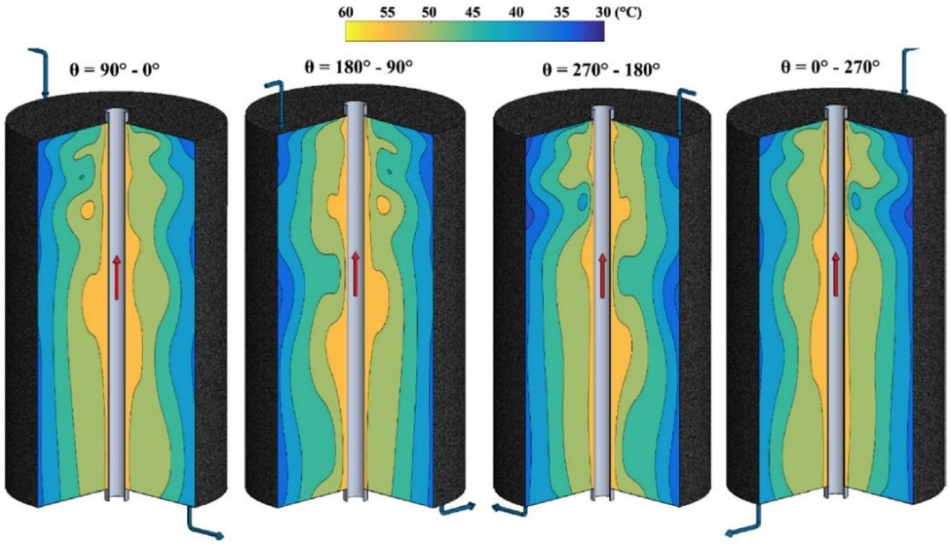

Figure 3.13 Experimental temperature contour (20 PPI, 20 SLPM)

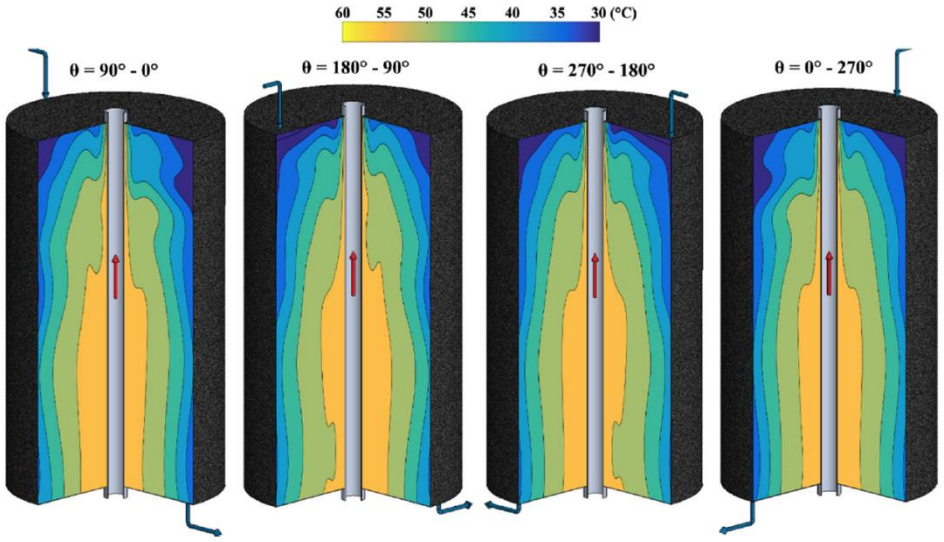

Figure 3.14 Experimental temperature contour (20 PPI, 20 SLPM)

According to **Table 3.5**, the effective length of the samples varies between 0.04 and 0.15 m. Same phenomena can be detected in the temperature distribution contours. For example, comparing the images corresponding to 0–90° in **Figure 3.11** and **Figure 3.12** shows the development of the maximum temperature at about 0.07

m from the foam inlet for lower flow rate; while for the higher flow rate this length is almost doubled. Same phenomenon can be observed for the foam with 20 PPI in **Figure 3.13** and **Figure 3.14**. Regardless of the pore size, one can note that with low air flow rates, air crossovers the inner pipe causing a wavy distribution of temperature, and then exits the plexiglass pipe. This observation is clear by comparing the contour plots at different angles in **Figure 3.11** and **Figure 3.14**. On the contrary, with higher flow rates, the temperature distribution is less wavy partly because the air is more vigorously pushed towards the side walls where there is a clearance of 1 mm between foam and plexiglass.

Figure 3.15 shows the results of three simulation cases: (a) with a 5 PPI foam, (b) with a 20 PPI foam, and (c) without foam; all of them for a fixed flow rate of 20 SLPM. The main purpose of **Figure 3.15** is to compare the numerical results of temperature distribution contours with and without foam, where the foam case has a pore size of 5 PPI, and the flow rate is fixed for both cases at 20 SLPM. An important observation is that, adding foam causes higher heat transfer rate that makes the effective lengths much shorter. Interestingly, in the absence of the foam, the transport in the radial direction becomes more significant. This phenomenon can be seen in 0 – 180° contour **Figure 3.15**, where a shift of the temperature field towards the 0° side is clearly noticeable. In presence of the foam, the numerical simulation cannot predict the same airflow performance.

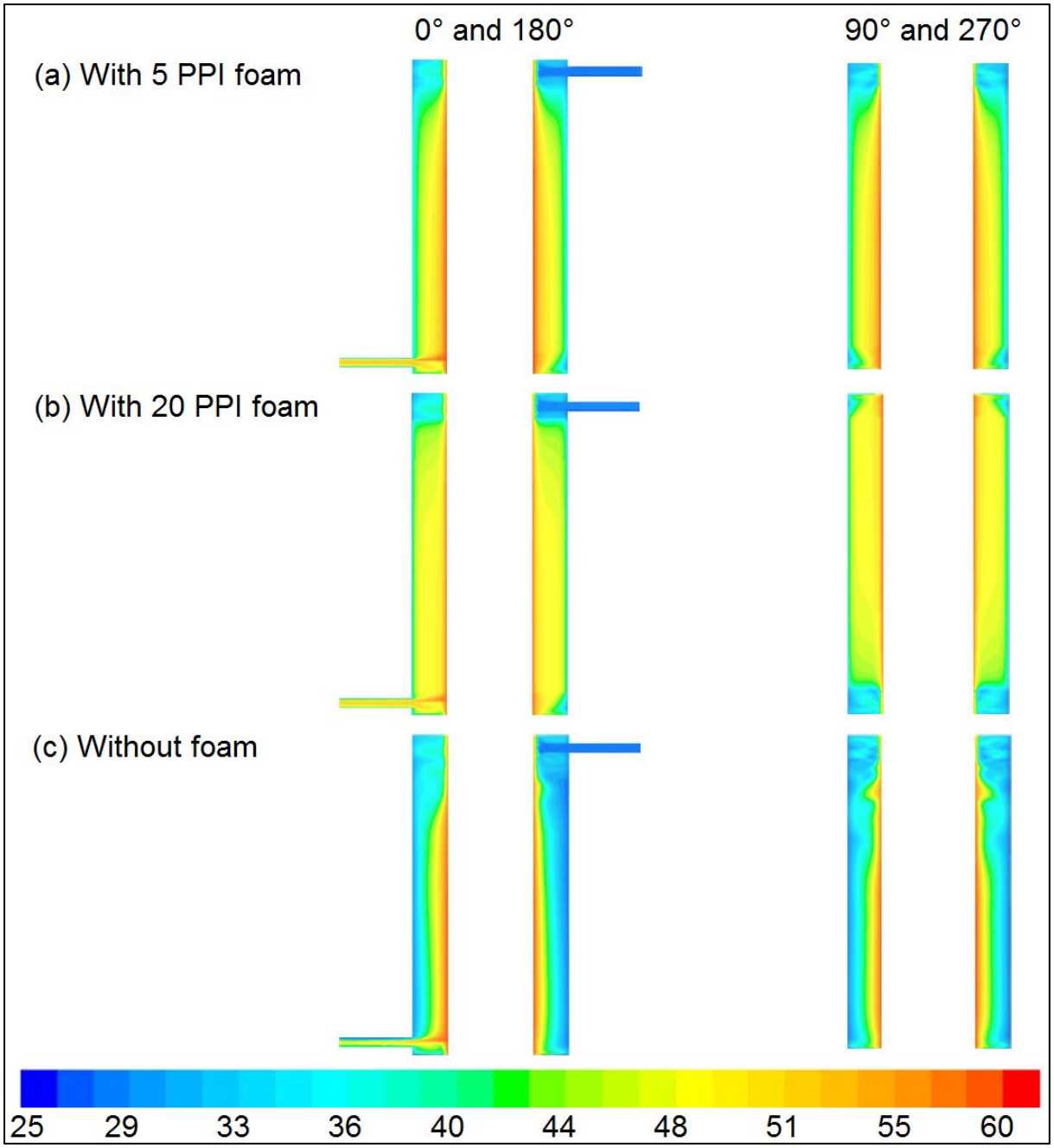

Figure 3.15 Temperature contours in the upper zone of the heat exchanger for the 0, 90, 180 and 270° planes: (a) 5 PPI foam, (b) 20 PPI foam and (c) without foam

3.4 Conclusion

The present work is focused on the accurate measurement of the pressure drop and the temperature fields in the air side of a foam-filled annulus. A considerable number of measuring points were arranged all the way through the foam in different heights, depths and angles, and a special clamp was manufactured to accurately place the

sensors in these points. Besides, two different foam samples (5 and 20 PPI) and three different airflow rates (20, 85 and 150 SLPM) are considered in the experiments to study the metal foam heat exchanger performance. This study shows that, for a vertical foam-filled annular heat exchanger, the pressure drop is proportional to the foam length. However, there is no significant difference in the pressure drop measured at different angles. The airflow rate has more significant effect on the pressure drop than the pore density or the metal foam length. At a higher airflow rate; 150 SLPM, the pressure drop is about three times higher than that of 20 SLPM, regardless of the pore size.

In addition to that, the temperature field shows that a significant amount of heat transfer takes place in the first half of the foam. The 20 PPI foam has a better performance than the 5 PPI one in the entry zone. Specifically, the low airflow rate leads to lower pressure drop with a reasonable heat transfer rate in the first half of the metal foam. In this work, the thermal entrance length was calculated for each case as a first design criterion for a compact metal foam-filled heat exchanger. The best result that is the shortest thermal length, was obtained for the 20 PPI foam and 20 SLPM. In that case, the thermal entrance length is around 0.1 m. A further analysis over the potential efficiency of a short heat exchanger yielded similar results. In this study, it was found that a foam larger than 0.05–0.06 m may be unworthy if using a 20 PPI foam at 20 SLPM airflow rate; from that length on, the pressure drop continues rising considerably whilst no significant improvement in the non-dimensional temperature is expected. Further researches are required to find a useful correlation to estimate the effective length of a heat exchanger based on different parameters. Additionally, different PPI foams should also be investigated to obtain a generalized conclusion. Although a numerical model is used to simulate the actual heat exchanger, a slight deviation is obtained due to the limitations of the porous media model in the Fluent software. This model is useful only for a qualitative analysis yet an improved model would be useful to avoid the time-consuming experimental measurements.

References

[1] F. Shikh Anuar, M. R. Malayeri and K. Hooman. “Particulate fouling and challenges of metal foam heat exchangers”, *Heat Transfer Engineering*, 38, 7 -8, pp. 730 – 742, 2017.

[2] X.-H. Han, Q. Wang, Y.-G. Park, C. T'Joen, A. Sommers and A. Jacobi, "A review of metal foam and metal matrix composites for heat exchangers and heat sinks", *Heat Transfer Engineering*, 33, 12, pp. 991–1009, 2012.

[3] H. Hu, X. Weng, D. Zhuang, G. Ding, Z. Lai and X. Xu, "Heat transfer and pressure drop characteristics of wet air flow in metal foam under dehumidifying conditions", *Applied Thermal Engineering*, 93 , pp.1124–1134, 2016.

[4] S. Mahjoob and K. Vafai, "A synthesis of fluid and thermal transport models for metal foam heat exchangers", *International Journal of Heat and Mass Transfer*, 51, 15–16, pp.3701–3711, 2008.

[5] C.Y. Zhao, W. Lu and S.A. Tassou, "Thermal analysis on metal-foam filled heat exchangers. Part II: Tube heat exchangers", *International Journal of Heat and Mass Transfer,* 49, pp. 2762–2770, 2006.

[6] W. Lu, C.Y. Zhao and S.A. Tassou, "Thermal analysis on metal-foam filled heat exchangers. Part I: Metal-foam filled pipes", *International Journal of Heat and Mass Transfer,* 49, pp. 2751–2761, 2006.

[7] M. Odabaee, M. De Paepe, P. De Jaeger, C. T'Joen and K. Hooman, "Particle deposition effects on heat transfer from a metal foam-wrapped tube bundle, *International Journal of Numerical Methods for Heat and Fluid Flow,* 23, pp.74–87, 2013.

[8] E. Sauret and K. Hooman, "Particle size distribution effects on preferential deposition areas in metal foam wrapped tube bundle", *International Journal of Heat and Mass Transfer,* 79, pp.905–915, 2014.

[9] M. Odabaee, K. Hooman and H. Gurgenci, "Metal foam heat exchangers for heat transfer augmentation from a cylinder in cross-flow", *Transport in Porous Media*, 86, pp. 911–923, 2011.

[10] A. Chumpia and K. Hooman, "Performance evaluation of single tubular aluminium foam heat exchangers", *Applied Thermal Engineering, 66*, pp.266–273, 2014.

[11] S.Y. Kim, B.H. Kang and J.H. Kim, "Forced convection from aluminum foam materials in an asymmetrically heated channel", *International Journal of Heat and Mass Transfer,* 44 pp.1451–1454, 2001.

[12] N. Dukhan and K.-C. Chen, "Heat transfer measurements in metal foam subjected to constant heat flux", *Experimental Thermal and Fluid Science,* 32, pp.624–631, 2007.

[13] A. Cavallini, S. Mancin, L. Rossetto and C. Zilio, "Air flow in aluminum foam: heat transfer and pressure drops measurements", *Experimental Heat Trans*fer, 23, pp.94–105, 2009.

[14] I. Kurtbas and N. Celik, "Experimental investigation of forced and mixed convection heat transfer in a foam-filled horizontal rectangular channel", *International Journal of Heat and Mass Transfer,* 52, pp.1313–1325, 2009.

[15] S. Mancin, C. Zilio, A. Cavallini and L. Rossetto, “Heat transfer during air flow in aluminum foams, *International Journal of Heat and Mass Transfer,* 53, pp. 4976–4984, 2010.

[16] P.T. Garrity, J.F. Klausner and R. Mei, “Performance of aluminum and carbon foams for air side heat transfer augmentation”, *Journal of Heat Transfer,* 132, pp.121901, 2010.

[17] S. Mancin, C. Zilio, A. Diani and L. Rossetto, “Air forced convection through metal foams: experimental results and modelling”, *International Journal of Heat and Mass Transfer,* 62, pp.112–123, 2013.

[18] K. Boomsma, D. Poulikakos and F. Zwick, “Metal foams as compact high performance heat exchangers”, *Mechanics of Material*, 35, pp.1161–1176, 2003.

[19] B. Buonomo M. Oronzio S. Nardini and L. Guy, “Experimental investigation on mixed convection in horizontal channels heated below and partially filled with aluminium foam”, in: *8th World Conference on Experimental Heat Transfer Fluid Mechanics and Thermodynamics*, pp. 1–12, 2013.

[20] M. Sener, A. Yataganbaba and I. Kurtbas, “Forchheimer forced convection in a rectangular channel partially filled with aluminum foam”, *Experimental Thermal and Fluid Science*, 75, pp.162–172, 2016.

[21] H. Huisseune, S. De Schampheleire, B. Ameel and M. De Paepe, Comparison of metal foam heat exchangers to a finned heat exchanger for low Reynolds number applications, *International Journal of Heat and Mass Transfer,* 89, pp.1–9, 2015.

[22] M. Odabaee, S. Mancin and K. Hooman, “Metal foam heat exchangers for thermal management of fuel cell systems – an experimental study”, *Experimental Thermal and Fluid Science*, 51, pp.214–219, 2013.

[23] M. Odabaee and K. Hooman, “Application of metal foams in air-cooled condensers for geothermal power plants: an optimization study”, *International of Communications in Heat and Mass Transfer,* 38, pp. 838–843, 2011.

[24] S. Mao, N. Love, A. Leanos and G. Rodriguez-Melo, “Correlation studies of hydrodynamics and heat transfer in metal foam heat exchangers”, *Applied Thermal Engineering,* 71, pp.104–118, 2014.

[25] L.W. Jin and K.C. Leong, “Pressure drop and friction factor of steady and oscillating flows in open-cell porous media”, *Transport in Porous Media,* 72, pp. 37–52, 2007.

[26] O. Bagcl, N. Dukhan, M. Ozdemir and L.A. Kavurmacloglu, “Experimental heat transfer due to oscillating water flow in open-cell metal foam”, *International Journal of Thermal Sciences,* 101, pp. 48–58, 2016.

[27] M. Iasiello, S. Cunsolo, N. Bianco, W.K.S. Chiu and V. Naso, “Developing thermal flow in open-cell foams”, *International Journal of Thermal Sciences,* 111, pp.129–137, 2017.

[28] N. Dukhan, Ö. Bałci and M. Özdemir, “Thermal development in open-cell metal foam: An experiment with constant wall heat flux”, *International Journal of Heat and Mass Transfer,* 85, pp. 852–859, 2015.

[29] K. Hooman and J. Li, M. Dahari, “Thermal dispersion effects on forced convection in a porous-saturated pipe”, *Thermal Science and Engineering Progress*, 2, pp. 64–70, 2017.

[30] K. Hooman and M. Dahari, Thermal dispersion effects on forced convection in a parallel plate porous channel, *Meccanica* 50, pp. 1971–1976, 2015.

[31] N. Dukhan, M.A. Al-Rammahi and A.S. Suleiman, “Fluid temperature measurements inside metal foam and comparison to Brinkman-Darcy flow convection analysis”, *International Journal of Heat and Mass Transfer,* 67, pp.877–884, 2013.

[32] X. Chen, X.-L. Xia, C. Sun and Y. Li, “Numerical analysis on the transient measurement of gas temperature in porous material using thermocouples at high temperatures”, *International Journal of Heat and Mass Transfer,* 91, pp.1060–1068, 2015.

[33] ERG Aerospace Corporation [Online]. Available: <http://www.ergaerospace.com/index.html>.

[34] N. Dukhan, R. Picón-Feliciano and A.R. Álvarez-Hernández, “Heat transfer analysis in metal foams with low-conductivity fluids”, *International Journal of Heat and Mass Transfer,* 128, pp.784-792, 2006.

[35] N. Dukhan, Ö. Bağci and M. Özdemir, “Metal foam hydrodynamics: flow regimes from pre-Darcy to turbulent”, *International Journal of Heat and Mass Transfer,* 77, pp.114–123, 2014.

[36] V.T. Morgan, The overall convective heat transfer from smooth circular cylinders, *Advances in Heat Transfer,* 11, pp.199–264, 1975.

[37] F.W. Dittus and M.K. Boelter, *Heat Transfer in Automobile Radiator of the Tubular Type*, 1930.

[38] N. Dukhan and M. Ali, “Strong wall and transverse size effects on pressure drop of flow through open-cell metal foam”, *International Journal of Thermal Sciences, 57*, pp. 85–91, 2012.

Chapter 4: Partially Filled Channel with Open-Cell Metal Foam – Part I: Point-wise Measurement using Laser Doppler and Hot-Wire Anemometers

The performances of metal foam are always evaluated in bulk, particularly for a fully filled configuration. In a case where a partly filled with metal foam is involved, other areas need more attention, such as the non-porous region and interface regions, which are completely influenced by the existence of the metal foam in the neighbouring region. It is not a surprising fact that the metal foam ligaments may act as a turbulence inducer at a significant fluid velocity. Thus, the investigation of fluid flow behaviours across the non-porous and interface regions become debated issues. For the partially filled configuration with a metal foam, there is abundant literature that adapted the porous media theory, which allegedly suits the metal foam characteristics. Rather than experiments, most of the metal foam studies in the literature have considered the numerical and analytical approaches. For a successful fouling study, the flow behaviours in the clear region should be fully understood. However, instead of a fully filled configuration, a partially filled configuration would be better to reduce the significant pressure drop effects. Therefore, this chapter investigates flow behaviours in a non-porous region and pressure drop effects. This investigation focuses on two different sizes of a partially filled channel with metal foam (a foam block as a resistance to the flow). The effects of pore density on the flow velocity were investigated using Laser Doppler Anemometry (LDA) or Hot-Wire Anemometer (HWA) in two separate experiments. A solid block with the same size as the metal foam block is considered as a reference case to determine the significance of foam microstructure effects. A correlation of friction factor for a partially filled channel with metal foam is also proposed in this chapter. The content of this chapter is from,

F. Shikh Anuar, I. A. Abdi, M.Odabaee and K. Hooman, "**Experimental study of fluid flow behaviour and pressure drop in channels partially filled with metal foams**", *Experimental Thermal and Fluid Science*, 99, pp. 117-128, 2018.

Experimental Study of Fluid Flow Behaviour and Pressure Drop in Channels Partially Filled with Metal Foams

Fadhilah Shikh Anuar[a, b, 1], Iman Ashtiani Abdi[a, 1], Mostafa Odabaee[a], Kamel Hooman[a]

[a]School of Mechanical and Mining Engineering, The University of Queensland, Queensland, Australia;
[b]Centre for Advanced Research on Energy (CARe), Fakulti Kejuruteraan Mekanikal, Universiti Teknikal Malaysia Melaka, Hang Tuah Jaya, 76100, Durian Tunggal, Melaka, Malaysia

Abstract

This study experimentally investigates the effects of pore density, inlet velocity and blockage ratio on fluid flow behaviour and pressure drop in channels partially filled with a metal foam block. The fluid velocities in the free stream region, which is a clear (from foam) region on the top of foam block, are measured using Laser Doppler Anemometry (LDA) and hot-wire anemometry. The metal foam data are compared to those of solid blocks with the same size. For low blockage ratios, i.e. thin foam layers, the pressure drop caused by a solid block is higher than that of the foam when tested under identical conditions. Interestingly, nonetheless, beyond a threshold blockage ratio value, the pressure drop induced by the metal foam block exceeds that of the solid block of the same height tested at the same air flow rate. This behaviour is best described as the interplay between resistance caused by blockage versus that of the wake forms downstream and over the objects and additional frictional effects within the porous region and on the interface. Furthermore, a correlation, with ±16% deviation, is developed to predict the flow resistance caused by the solid and foam blocks across the partially filled channel.

Nomenclature

A_f	frontal area (m^2)
Da	Darcy number, K/H^2
d_p	pore diameter (m)
d_l	ligament diameter (m)
Dh	hydraulic diameter (m)

e	error
exp	experiment
f	friction factor
FOV	field of view
h	metal foam height (m)
H	channel or test section height (m)
Hf	free stream region height (m)
h/H	blockage ratio
K	permeability (m^2)
L	pressure taps distance (m)
L_C	channel length (m)
Lf	foam length (m)
m	mass (kg)
N	number of sample size
ΔP	pressure drop (Pa)
P	pressure (Pa)
PPI	pore per linear inch
Q	volume flow rate (m^3/s)
Re	Reynolds number
$\bar{u}$	average velocity of partially filled channel (m/s)
u_f	free stream region velocity (m/s)
u_o	inlet velocity (m/s)
u_p	average pore velocity (m/s)
V	volume (m^3)
W	channel width (m)
wf	foam width (m)
WT-1	test facility with *Dh* = 0.088 m
WT-2	test facility with *Dh* = 0.320 m

Subscripts

corr	correlated or predicted
Dh	channel hydraulic diameter
ds	downstream
exp	experimental data
f	free stream region
fx	fixed
h	foam height

H	channel height
pf	partially filled
r	random
T	total
us	upstream
p	pore (porous region)
Greek symbols	
ε	porosity
δ	uncertainty
ρ	density (kg/m^3)
μ	viscosity (kg/(s.m)
λ	laser wavelength (nm)

4.1 Introduction

Metal foam heat exchanger has been considered in numerous applications due to its superior thermal capabilities [1-3]. The foam can be used to fill a channel and increase the heat transfer from the wall (compared to no foam case). However, the metal foam microstructures induce massive pressure drop, which becomes one of the major concerns in design of metal foam heat exchangers. Alternatively, a partially filled configuration is preferred to minimise the excess pressure drop yet at reasonably higher heat transfer rate; compared to no-foam case [4]. Despite that, a proper selection of microstructural properties, e.g., pore density (PPI) is essential to ensure optimum fluid goes into a porous region instead of the non-porous region. Ideally, most of the incoming flows will naturally evade the high pore-ligament restrictions and choose the non-porous region or unobstructed pathway. In that case, the benefits of the complicated foam structures [5] could not be fully utilized. Past studies have investigated the thermo-hydraulic properties of the partially filled configuration analytically [6-9] and numerically [10-11]. In all of these studies one needs to make assumptions to model the interface between a porous medium and the non-porous region. Even though there are established theories of porous medium/fluid interfaces [12-13] that can be used for porous metal foams, the interface condition remains controversy due to the discrepancies in findings and lack of experimental studies.

It is worth to note that many experimental studies have investigated the flow pattern around foamed cylinders, e.g., separation flow, wakes or vortex shedding to

identify the effects of metal foam structure [14-16]. However, to the best of authors' knowledge, only Sauret et al. [17] investigated the velocity profiles in a channel partially filled with a metal foam block. The study considered inlet velocity and foam block height as the variable parameters to measure the velocity profiles at the interface using hot-wire anemometry. The experimental results were in agreement with their numerical model, but they found significant discrepancies when comparing their data with an existing theoretical model. Nevertheless, the difficulty in modelling the exact condition outside (interface) of the porous medium/metal foam has been addressed in Ref. [4]. A boundary layer will form on a non-porous solid-fluid interface but for a porous-clear fluid interface this boundary layer can be continuously disrupted if the momentum exchange at the interface go both ways. This is likely due to tortuous flow with a continuous disruption of the pore level boundary layers [18]. Alternatively, experimental velocity profiles in a free stream region of a partially filled configuration could represent the direct effects of complex foam microstructure, boundary layer and slip velocity (if present).

There exists a few number of experimental studies on the partially filled configuration with porous metal foam in the literature. Sener et al. [19] experimentally investigated 10 and 20 PPI aluminium foams inside a channel with four different configurations; convex, concave and triangular and completely filled channel. Their result showed that the effect of Reynolds number (*Re*) on the pressure drop decreases for a surface curvature parameter larger than zero, regardless of the pore density. Those authors derived empirical correlations for the pressure gradient of laminar and turbulent channel flows, with ±25% deviations from the experimental data. Liu et al. [20] experimentally investigated the thermo-hydraulic properties of a tube partially filled with metal foam to note that by increasing the PPI, the pressure drop would increase first and then decrease. The authors claimed that the fluctuations of the pressure drop in the high PPI foams are due to (1) the high number of ligaments that increase the flow resistances and (2) the reduction of mass flow rate in the low permeability foam, resulting in the smaller flow resistances. Lu et al. [21] described the pressure drop performances of metal foam by employing porous media characteristics such as Brinkman-extended Darcy model. Their analytical results showed that the pressure drop is increasing with PPI, but the substantial increments only occurred with low PPI foams (less than 15 PPI). Besides, the high PPI foam with more restrictions

were found to force the flow into the free stream region, which lessen the effects of porous structure on the overall resistance. Additionally, their study also showed a higher pressure drop could be attained by increasing the foam height and flow velocity, but the former effect is found to be more dominant. Through their numerical study, Forooghi et al. [22] also stated that the pressure drop effects were remarkable once the porous medium has filled more than half of the channel. The study stated that a smaller Darcy number, $Da = 10^{-5}$ would only cause a higher pressure drop, than $Da = 10^{-4}$, when the blockage ratio exceeds 0.4 Similarly, Sung et al. [23] numerically investigated the effects of Darcy number on the flow characteristics of a channel partially filled with a porous block. A larger recirculation zone appeared behind the porous block with a higher Reynolds number, $Re = 500$, as compared to $Re = 100$, at a constant Darcy number, $Da = 10^{-5}$. However, no recirculation zone appears with a higher Darcy number, $Da = 10^{-2}$. The study also found that the pressure drop increases with the porous height but a fully filled channel caused 400 times higher pressure drop compared to a clear channel. Shuja and Yilbas [24] numerically investigated the effects of porosity of a porous block in a vertical channel with different aspect ratios.

A channel partially filled with a solid block could be considered as forward-backward facing step flow, where three recirculation zones appears in the upstream, above the step (solid block), and immediate vicinity of the downstream regions [25]. However, if one replaces the solid block with a permeable one of the same size, the local velocity profiles and, thereby, the pressure drops would be different. Interestingly, Kouidri and Madani [26] qualitatively analysed the roughness of foam surfaces to note that a smooth foam when compared with a highly rough surface has difference effects on the pressure drop and the surface roughness enhances the process of flow regime transition.

The aforementioned experimental studies have considered only the total pressure drop, but no further explanation on the local pressure losses involving the upstream, core (porous region) and downstream regions were offered. This could be because of the presumption that the major part of the flow resistance can be attributed to the core. Thus, this study experimentally investigates the effects of various foam samples, channel blockage ratios and inlet velocities on the velocity profiles of partially filled channels. The total pressure drops are also measured and the results are compared to equivalent solid blocks. This study introduced an appropriate range of

PPIs and blockage ratios for optimum flow at the expense of low-pressure drop effects. The presented results are the direct effects of a real and complicated structure of the metal foam, instead of relying on the assumptions and idealized foam in those above-mentioned numerical and mathematical studies.

4.2 Experimental Work

4.2.1 Experimental setup and measurements

Experiments were conducted in two different channels with cross-sectional areas of 0.008 m^2 and 0.102 m^2. Each channel was partially filled with a metal foam block where various geometrical and microstructural properties are parametrically investigated. Different inlet velocity ranges were also applied in those channels. In addition, the velocity measurements in each channel are discretely performed either using Laser Doppler Anemometry (LDA) or hot wire anemometry. The randomized approaches in this study would be helpful to suit numerous applications as well as generalizing the proposed friction factor model, due to the diverse metal foam microstructure characteristics from different manufacturers. The details of each experimental setup and procedures are presented in the following sections.

The test facility is demonstrated schematically in **Figure 4.1**. The ambient air is sucked into the blower, which then passes through a diffuser, a heater (irrelevant to the present study), and a settling chamber before entering a rectangular test section. The size of the test section is 0.078 m (H) x 0.10 m (W) x 0.35 m (L_c) with clear windows on the top and side walls to provide a better optical access. The airflow into the test section is controlled using a gauge valve. In this experiment, we used the average inlet velocities of 3.9, 5.5 and 6.2 m/s, with the maximum turbulence intensity of 1.7%. The Reynolds number in the empty channel (Re_{Dh}) is in the range of 22,000 to 36,000. This study has considered turbulent flow due to limited data exists on the turbulent flow characteristics through the porous media, especially in a partially filled channel. Also note that flow in the porous media is turbulent in many industrial and heat exchanger applications.

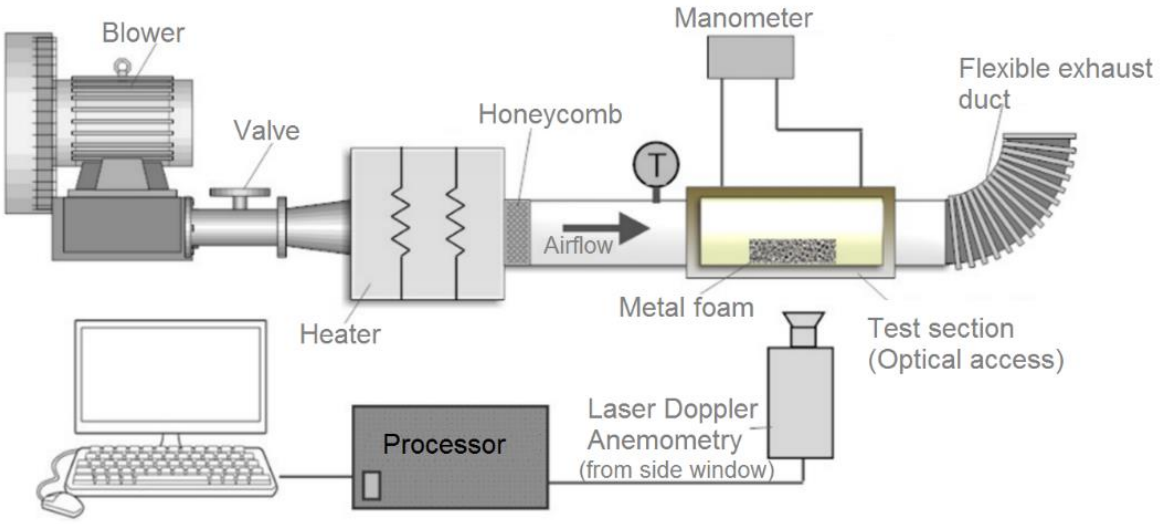

Figure 4.1 Schematic of the experimental setup

A non-intrusive technique, LDA was used to measure the local velocities in the clear region of the partially filled channel (**Figure 4.1**). The LDA system (Dantec Dynamics) consists of three main components: (1) FlowExplorer unit, which consists of an optical probe (2) Burst Spectrum Analyzer (BSA) signal processor (3) Windows software package (BSA Flow Software). The additional components include a seeding generator and a traversing system. The seeding generator was used to inject oil droplets (approximately, 3.0 μm diameter) into the test section. The oil droplets (seeding particles) must be able to accurately follow the flow to represent the fluid velocities. In the FlowExplorer unit, two beams (diameter, ∅ = 2.6 mm) with the same intensity are created by splitting a continuous laser light (λ = 660 nm; 785 nm) using a beam splitter. The parallel exit beams are focused by a lens to intersect in a probe volume. The seeding particles that move through the probe volume would scatter the laser light, and the scattered light is then collected by a receiver lens and focused on a photo-detector. Flow velocity information comes from the scattered light that contains a Doppler frequency, which is proportional to the velocity component perpendicular to the bisector of the two laser beams. The measurement locations in the test section are described schematically in **Figure 4.2**.

The clear region of the partially filled channel can be divided into three sections; (1) upstream, (2) downstream and (3) free stream region (which is a non-porous region on top of the metal foam). The measurement locations in these experiments are located within the free stream or non-porous region (outside of the porous structure). The intersected laser beam is adjusted to be at the middle plane of the test

section/foam width and the laser is moved vertically on the selected locations as shown in **Figure 4.2**. Specifically, numbered labels from 1 to 5 in **Figure 4.2** represent the measurement locations for flow velocities in the y-axis direction. Each location contains of 14 data points 0.005 m apart. The upstream and downstream velocities (labelled as 1 and 5) were measured 0.015 m and 0.030 m from the foam edges, respectively. The latter measurements were taken at a longer distance from the foam edges, due to the possibility of wakes formation in that region. Meanwhile, P_1 and P_2 represent the locations of pressure taps which are 0.25 m apart. The distance between the pressure taps spans over both major and minor losses, since the taps were positioned outside (and away from) the partially filled section. The pressure drop was measured using a pressure sensor (Sensirion SDP600 series), and the measurements were taken at the centre plane of the test section in the z-axis. All data obtained from the smaller test section (**Figure 4.1**) are labelled as WT- 1.

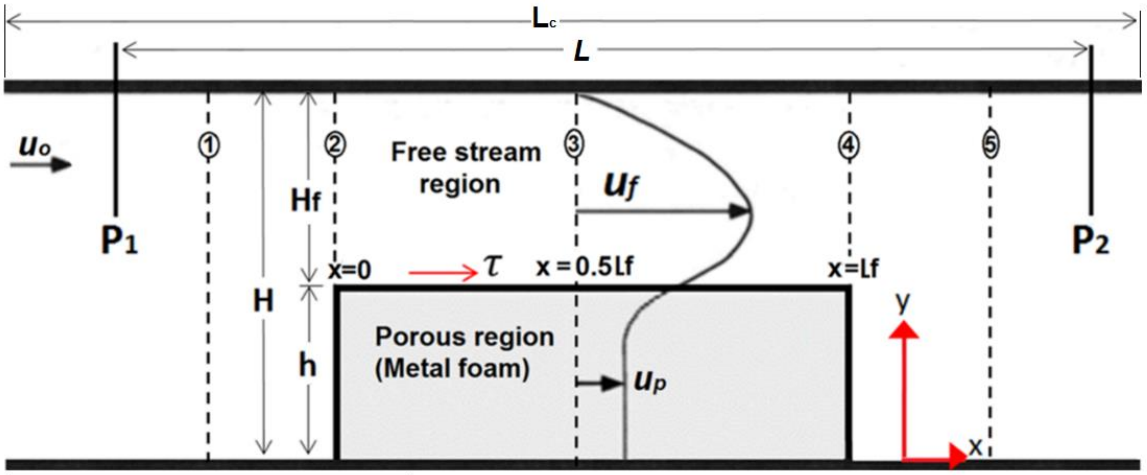

Test section dimension (m)	WT-1	WT-2
Height, H	0.078	0.32
Width, W	0.10	0.32
Length, L_c	0.35	2.00

Note:
Vertical dashed lines represent the velocity measurement locations ① upstream, ② x = 0, ③ x = 0.5Lf, ④ x = Lf, and ⑤ downstream

Figure 4.2 Partially filled channel with metal foam

Another set of experiment was conducted in a larger test section, 0.32 m (H) x 0.32 m (W) x 2.0 m (L_c). The square test section was partially filled with foam blocks of different heights, 0.010, 0.020 and 0.050 m, and three inlet velocities, (6.5, 9.5 and 12.5 m/s), used in this experiment. The test section was installed in a wind tunnel described in Ref. [16], with the Re_{Dh} in range of 135,000 to 265,000 (TI<1%). The same pressure sensor was used to measure the total pressure drop in this wind tunnel. The pressure taps were positioned, L = 0.40 m apart at 0.07 m from the leading and

rear edges of the foam. Meanwhile, the velocities in the free stream region were measured at x = 0, x = 0.5Lf and x = Lf (**Figure 4.2**). The measurements were obtained using the same hot wire anemometry as the one used in Ref. [17]. Details of the equipment will not be repeated in this paper. The obtained data from the experiments conducted in the larger test section are labelled as WT-2. Both experimental datasets (WT-1 and WT-2) are later combined to expand the applicable range of the correlation proposed in this study.

To fully understand the effects of complicated metal foam structures, flow visualization experiments using Particle Image Velocity (PIV) were also conducted in WT-1. The experiments used the highest blockage ratio, h/H = 0.39 of both porous (10 and 30 PPI foams) and solid block. The PIV is also a non-intrusive measuring device, but it involves global measurements that capture the flows in the entire regions, simultaneously. Specifically, the total field of view (FOV) is 68 mm x 178 mm. The main components of the PIV system include a light source (Nd:YAG laser), CCD (charged-couple device) camera, a synchronizer, and seeding particles. The light (double-pulsed laser) from the top of test section illuminated the seeding particles, with two cameras positioned next to the side window to acquire the desired FOV. The time between pulses was set at 100 μs and 2000 images were captured at a constant inlet velocity, u_o of 6.2 m/s. The images were analysed using an adaptive correlation algorithm [27], and the final pass used a 32 x 32 pixels interrogation window with 50% overlap.

4.2.2 Metal foam samples

This study examined commercially available metal foams from two different manufacturers; China Beihai Building Material Co., Ltd. [28] and ELHI Thermal Solution COMM.V [29]. Primarily, the effects of foam height and PPI on the flow behaviour and total pressure drop were investigated in the experiments. Other foam microstructural properties such as the pore diameter and permeability were also considered as main parameters affecting the pressure drop of partially filled channels. A 2D image post-processing was conducted to determine the pore and ligament diameters (**Figure 4.3**). Besides, the structure of the metal foam samples was analysed using a micro-CT scanner and generating a 3D geometry of the metal foam structure in order to increase the measurement accuracy of the pore and ligament diameters. The metal foam properties are presented in **Table 4.1**, with the reading

deviation of ±15%. The porosity of the samples was calculated based on the density of the solid metal using **Equation (4.1)**. The permeability of the samples was also determined using **Equation (4.2)** which is valid for 10 – 40 PPI porous media with porosity ε = 0.75 to 0.97 [30] and for 5 PPI foam, **Equation (4.3)** [31] was used.

$$\varepsilon = 1 - \frac{\mathrm{m}_{\mathrm{solid}} / \rho_{\mathrm{solid}}}{V_{\mathrm{total}}} \tag{4.1}$$

$$K = \frac{d_p d_l \varepsilon}{6} \tag{4.2}$$

$$K = 0.00073 d_p{}^2 (1-\varepsilon)^{-0.224} \left(d_l / d_p\right)^{-1.11} \tag{4.3}$$

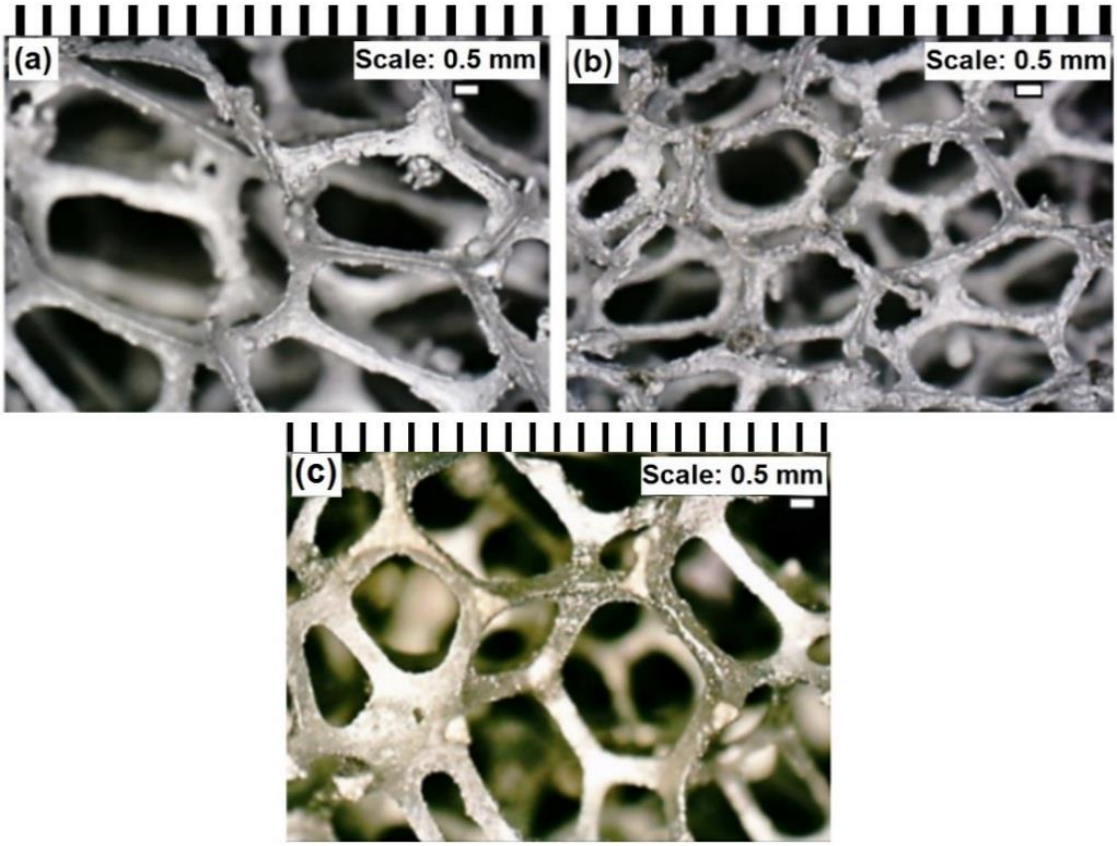

Figure 4.3 Aluminium open-cell metal foam microstructure: (a) 10 PPI (b) 30 PPI (c) 5 PPI

Table 4.1 Geometrical and microstructural properties of foam samples

Metal foam physical properties	China Beihai Building Material (WT-1)		ELHI Thermal Solution (WT-2)
Pore density (PPI)	10	30	5
Ligament diameter, d_l (m)	0.00044	0.00027	0.00113
Pore diameter, d_p (m)	0.00256	0.00087	0.00577
Porosity, ε (-)	0.82 – 0.91	0.88 - 0.94	0.92
Permeability, K x 10^{-7} (m^2)	1.54 - 1.65	0.35 - 0.37	2.61
Foam height, h (m)	0.004, 0.01, 0.03		0.01, 0.02, 0.05
Blockage ratio, h/H	0.05, 0.13, 0.39		0.03, 0.06, 0.16
Foam length, Lf (m)	0.09		0.27
Foam width, wf (m)	0.10		0.32

4.2.3 Uncertainty analysis

The uncertainty of the differential pressure sensor as reported by the manufacturer has included a fixed error, e_{fx} = ±3.0%, and a random estimated error, e_r = ±0.5%. Thus, the total uncertainty can be calculated using the root-sum-square method [32], expressed as below:

$$\delta_T = \pm\sqrt{{e_{fx}}^2 + {e_r}^2} \quad \textbf{(4.4)}$$

The total uncertainty in pressure reading is about ±3.0%. Meanwhile, the pressure taps distance, L, = 0.25 m (WT-1) was measured using a vernier caliper with the uncertainty, δ_L = ± 0.0001 m. The uncertainty in the pressure drop per unit length, $\delta_{(\Delta P/L)}$, can be determined using **Equation (4.5)** [18].

$$\delta_{(\Delta P/L)} = \pm\sqrt{\left(\frac{\partial(\Delta P/L)}{\partial \Delta P}\right)^2 \delta_P^2 + \left(\frac{\partial(\Delta P/L)}{\partial \Delta L}\right)^2 \delta_L^2} \quad \textbf{(4.5)}$$

Similarly, the maximum relative uncertainty of pressure drop per unit length is about ±3.0% due to the small uncertainty in the length measurements. For the LDA measurements, the standard deviation in the mean velocity of a velocity component can be represented by the root mean square [33]. Thus, the uncertainty of mean

velocity in the test section with 95% confidence interval can be determined using the following equation, with the maximum relative uncertainty about ±1.8%.

$$\delta_{(\bar{u})} = \frac{2u_{RMS}}{\sqrt{N}} \tag{4.6}$$

Meanwhile, the uncertainty relative to the maximum velocity using the hot-wire anemometry based on 95% confidence interval is about ±1.3% [17].

4.3 Results and Discussion

4.3.1 Flow behaviour and velocity profiles

For validation of the results, the fully developed velocity profile of the empty channel h/H = 0, together with a similar result from [34], are shown in **Figure 4.4**. An acceptable agreement is found between the present result and those mentioned study. Note that a slight missing data in a region near to the top wall (WT-1) is due to the limitation of our test rig, which will not interfere with our investigation and experimental purposes. This study focus on the flow behaviours affected due to the presence of metal foam block at the bottom wall, instead of the top smooth channel wall.

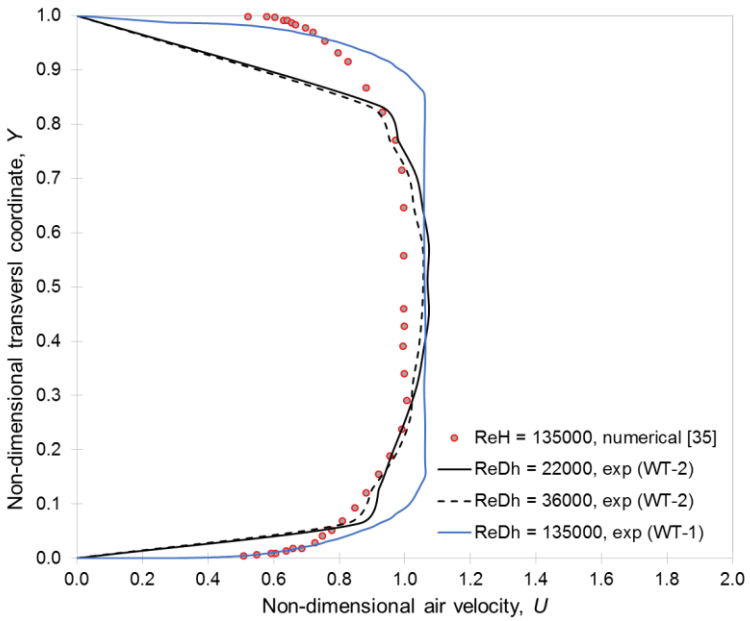

Figure 4.4 Comparison of velocity profiles of empty channels (WT-1) and (WT- 2) with another literature [34].

Figure 4.5 (a) to **(i)** shows the velocity profiles of 10 and 30 PPI with different blockage ratios, h/H = 0.05, 0.13, and 0.39. The inlet velocities are 3.9, 5.5 m/s and 6.2 m/s,

while the non-dimensional air velocity, U on the x-axis is a ratio of the free region velocity, u_f and the inlet velocity, u_o. The u_f was measured at point 1 (upstream), point 2 (x = 0), point 3 (x = 0.5Lf), point 4 (x = Lf) and point 5 (downstream) of the non-porous region, as shown in **Figure 4.2**. The local velocity profiles obtained in this study illustrate the effects of the metal foam block and inlet velocities on the fluid flow behaviour in the clear region. The velocity profiles are nearly flat at the centre in between the top wall and the foam surface. The small velocity fluctuations far from the foam surface contributed to the sensitivity of the LDA in measuring turbulent flow. The maximum velocity occurs near the centreline of the free stream region, except for h/H = 0.39 and h/H = 0.13 at u_o = 3.9 and 5.5 m/s. In the upstream and downstream regions, the velocity decreases towards the top wall as one would expect. Meanwhile, the velocity behaviour near the bottom wall is rather complex, due to the presence of the metal foam block. This will be further explained in the forthcoming discussion.

The results also show that the effects of the lowest blockage ratio (h/H = 0.05) on the average velocities in the partially filled channel is insignificant, regardless of the pore density. The presence of foam is noticeable with h/H = 0.13. The leading-edge velocity profiles (x = 0) of 10 PPI foam with h/H = 0.13 (**Figure 4.5 (d)**) shows velocity fluctuations up to 30% higher than the inlet velocities (u_o = 3.9 m/s) in a region near the bottom wall. There is also some missing data due to inadequate seeding particles at the downstream (**Figure 4.5 (d)**) and near the interface. This suggests a separated region, where recirculation or dead zones (very small velocities) appear in those regions. Furthermore, a reduction in the adjacent velocities in close proximity to the foam surface can be observed. In the free stream region, the velocities are higher than the inlet velocities, and the difference becomes more pronounced with a thicker foam (or higher h/H). It is important to note that an optimum seeding particles must be attained when conducting experiments with high blockage ratio such as h/H = 0.39. Due to the smaller free stream region, the air tends to flow faster carrying more seeding particles. On the other extreme, however, excessive particle density will cancel out the produced signals, causing unavailable velocity data.

The maximum free stream velocities of 30 PPI foam are higher compared to those of the 10 PPI case and this is more pronounced at higher blockage ratios. Smaller pores with the 30 PPI case, compared to the 10 PPI, translate into higher flow resistance hence the air is more prone to avoid the foam and move away with higher

PPI foam. Interestingly, the velocity profile at the middle of the partially filled section (**Figure 4.5 (g) – (i)**) for 10 and 30 PPI; h/H = 0.39) shows increasing velocities as approaching the foam surface. This phenomenon also occurs at the middle and rear edges of the 5 PPI metal foam block in the WT-2 with h/H = 0.16, at u_o = 6.5 and 9.5 m/s, as shown in **Figure 4.6**. The increase in the velocity along the interface, when the blockage is increased, has been already reported by Sauret et al. [17], nevertheless, the reason behind this behaviour has not been discussed yet. This effect is significant with higher blockage ratios. However, as increasing the inlet velocity, this effect is diminished, e.g., u_o = 12.5 m/s in WT- 2.

When one compares the velocities at x = 0, 0.5 Lf & Lf far enough away the foam to ignore the interface effects, it is clear that the velocity at x = 0 is lower than the inlet velocity, and it reaches its minimum somewhere between x = 0 and x = 0.5 Lf, and then increases all the way to x= Lf. Obviously, a portion of the incoming flow tends to enter the foam, as the velocity magnitude is smaller compared to the inlet velocity. The velocity magnitude starts decreasing up to a certain point, which is about 30% of the total length of the foam for this case [16]. At this point, the velocity plunges to its minimal value. This drives home the point that the air that goes into the pores starts losing its momentum to confronting ligaments and the flow does not contain enough energy to continue passing through the pores all the way down the other end of the foam block. As the sides and the bottom faces of the foam are all blocked by the channel surfaces, this leaves only the air with the option to move up to the interface and leave the foam causing additional mixing losses.

This is because the air that leaves the foam is being mixed by the air that flows over the foam. After the incoming flow passes the critical point, since no more upward air component exists on the interface, the velocity magnitude increases. This behaviour is a major point of difference between foam and solid blocks. The critical point can be used to define a practical length of foam beyond which the foam can be considered as a solid block. As one would anticipate, this critical point or location is not fixed and depends on the pore size, PPI, and the blockage ratio.

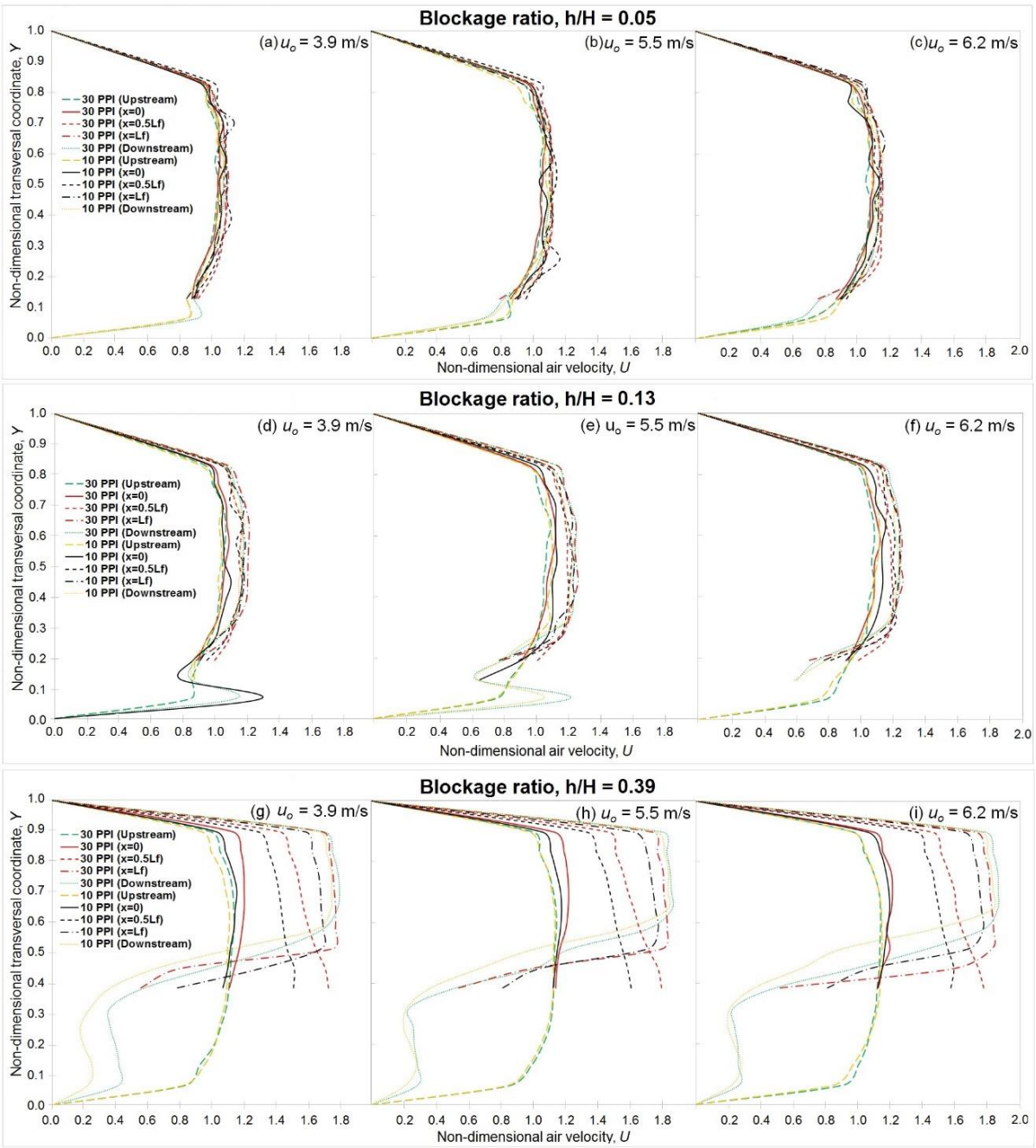

Figure 4.5 Velocity profiles of 10 PPI and 30 PPI foams at u_o = 3.6, 5.5 and 6.2 m/s in WT-1: (a) – (c) h/H = 0.05, (d) – (f) h/H = 0.13 and (g) – (i) h/H = 0.39

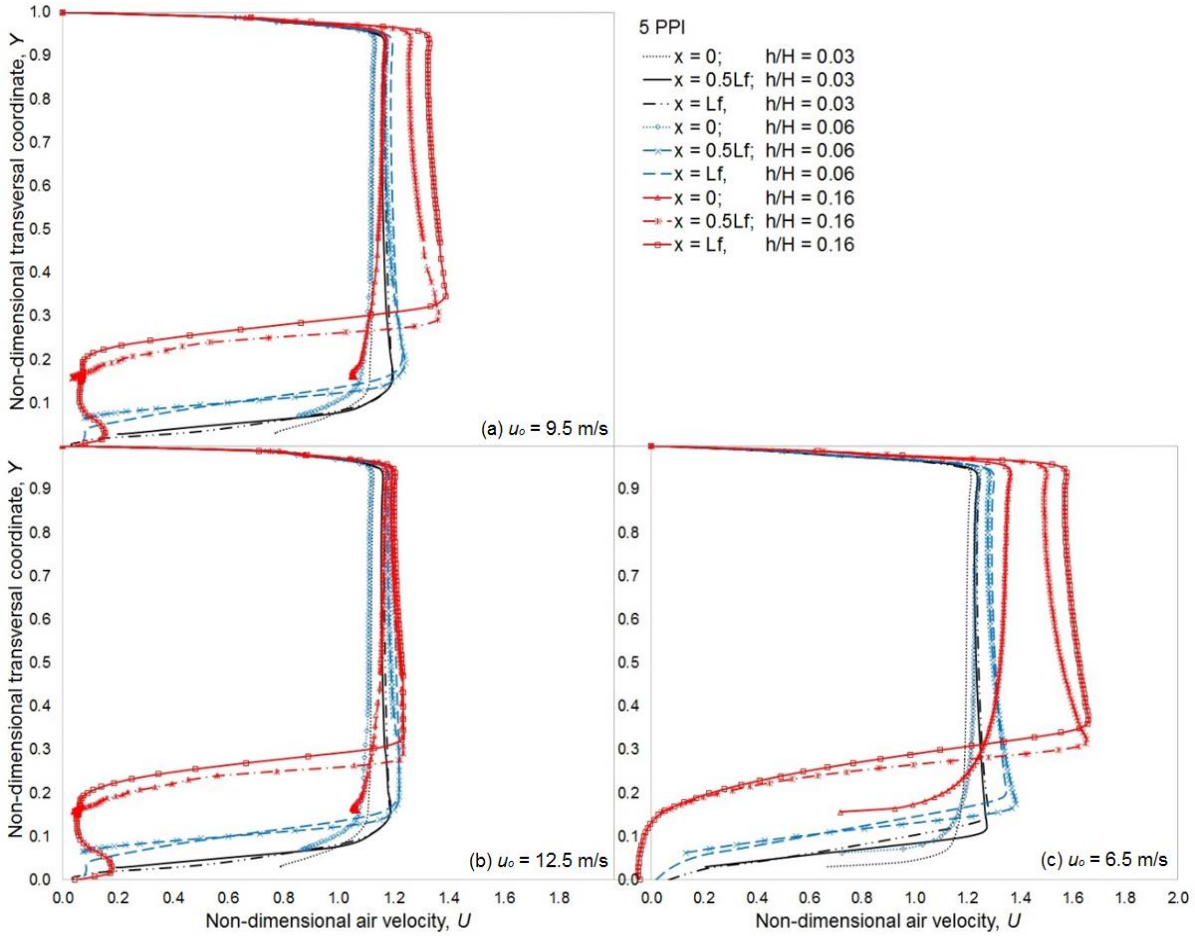

Figure 4.6 Velocity profiles of 5 PPI foams at u_o = 6.5, 9.5 and 12.5 m/s (WT-2)

Figure 4.6 demonstrates non-dimensional velocity profiles of 5 PPI foam in the larger test section (WT-2). The maximum blockage ratio in WT-2 is lower compared to WT-1, which is only about one-fifth of the channel height. Hence, the free stream region velocities are more stable with the reduction of velocities occuring in the regions closer to the foam surface. The velocity trends are almost similar to WT-1, with increasing velocities towards the rear edge of the metal foam block. Similarly, the free stream region velocities are higher compared to the inlet velocities. However, for low blockage ratios the free stream velocity decreases with increasing the inlet velocity. The high inlet velocity up to 12.5 m/s creates large inertial effect, and the flow tends to ignore the presence of the metal foam for that particular blockage ratios (<0.16). In that case, there is a maximum value of inlet velocity for the viscous effects to significantly affect the velocity profiles. The negative values of measured velocities with h/H = 0.16 at u_o = 6.5m/s can be attributed to the measurement locations positioned within a vortex formed downstream of the foam block. The other possible cause of this phenomenon could be the adverse pressure gradient. This effect gets

stronger by increasing the height of the foam block leading to a suction downstream the foam block.

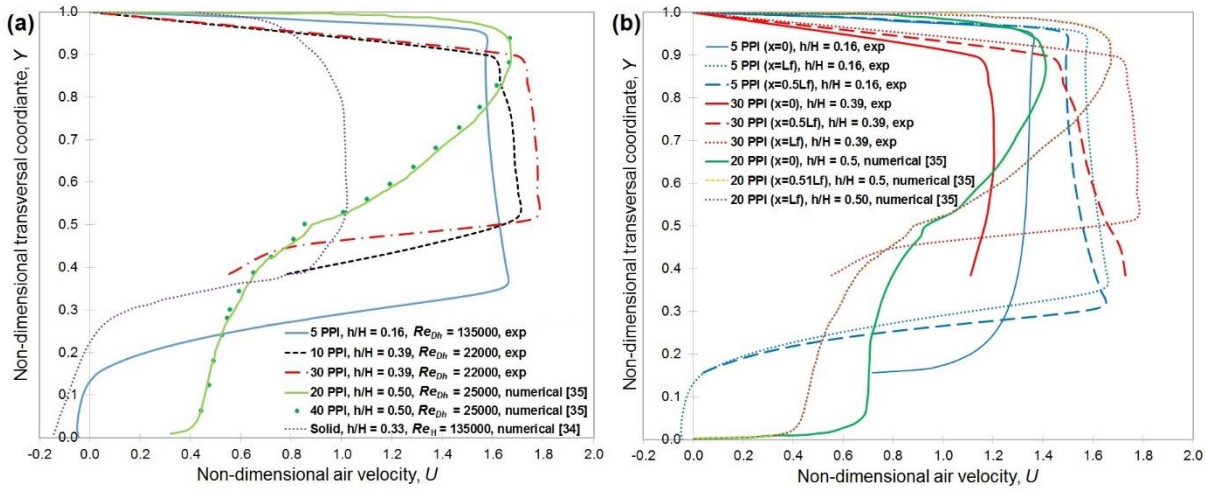

Figure 4.7 (a) Comparison of velocity profiles at x= Lf (b) Comparison of velocity profiles from x = 0 to x = Lf

Figure 4.7 shows a comparison of turbulent flow velocity profiles of a partially filled channel with similar literature; Sauret et al. [35]. The authors numerically investigated the velocity profiles of a partially filled channel with 20 and 40 PPI foams. The foams were modelled as isotropic homogenous porous media using modified Darcy law, and a continuous velocity and shear stress were used at the fluid/foam interface. **Figure 4.7 (a)** shows the velocity profiles at x = Lf, (rear edge), while **Figure 4.7 (b)** depicts the free stream velocity profiles along the foam block from x = 0 to Lf. At a similar Reynolds number, the simulated velocity profiles of 20 and 40 PPI from [35] are more parabolic with the maximum velocities are shifted closer to the top wall as compared to the present experimental results, which have flat profiles at the centre of the free stream region. The numerical study also shows an insignificant difference between PPIs, in contrast to the experimental results, where the profiles could be different, especially at a region close to the fluid/solid interface. Furthermore, the experimental result shows a formation of recirculation zone at x= Lf, based on the negative velocity profile, which is more similar to the profile of a solid block, measured at (Lf+x)/H = 1.33 [34]. At x = Lf, the solid block would have a similar profile as shown in **Figure 4.4**. In this case, the numerical study [35] did not consider the effect of minor loss or flow separation at the downstream region, which may occur in a real practice.

Figure 4.7 (b) shows that the numerical study [35] shows no difference in the profiles along (0.5 Lf = Lf) the foam towards the end of the foam length, except at the inlet, x = 0. However, the experimental results for both high and low PPIs show that the velocity profiles are changing from x = 0 to Lf. Also note that the PPI and the foam length (Lf = 0.195 m) from Sauret et al. [35] are within our parameter ranges, which may dispute any possibility for the source of difference because of those aspects. The use of k-ε turbulence model in the simulation for the non-porous region could not capture these behaviours, which affected due to the existence of a porous medium. The intra-pore level of turbulence within metal foam should be expected in simulating the partially filled channel. Also, the changes of velocity profiles in the streamwise direction suggest a high possibility of a non-uniform flow inside the porous region to obey the law of conservation of mass. Hence, the assumption of uniform flow in the porous media is not always true, for example, the partially filled configuration with a metal foam, when a non-porous region exists.

4.3.2 Pressure drop in partially filled channel

Effects of various parameters such as pore density (5 - 30 PPI), foam height (0.004 – 0.050 m) and inlet velocity (3.9 – 12.5 m/s) on the pressure drop of the partially filled channels are investigated as shown by **Figure 4.8**. The airflow in the channel is obstructed by the presence of metal foam. Basically, the pressure drop is increasing with the inlet velocity, pore density and blockage ratio. However, there is insignificant difference in the pressure drop for a low blockage ratio, e.g., h/H = 0.05, regardless of the pore density at a lower velocity. With a higher blockage ratio, h/H = 0.13, the 30 PPI foam shows a slightly higher pressure drop than that of the 10 PPI foam. The difference between 10 and 30 PPI foams becomes more obvious when the foam height is further increased to h/H = 0.39 when the pressure drop increases rapidly even with the lowest inlet velocity. One would expect that the 30 PPI foams with smaller pores than 5 and 10 PPI foams will cause a higher pressure drop due to the higher ligament restrictions. However, in the partially filled channel, it shows that the effects of pore density comes into play only beyond a certain blockage ratio.

According to **Figure 4.8**, the pressure drop of WT-1 with h/H = 0.13 is similar to h/H = 0.03 in WT-2 at a similar inlet velocity, u_o = 6.2 to 6.5 m/s. Interestingly, WT-2 used 5 PPI foam, while WT-1 used higher pore densities of 10 and 30 PPI. In that case, neither the blockage ratio nor the pore density has significantly influenced the

pressure drop. As seen, at the same velocity range, the effect of pore density on the pressure drop is negligible for blockage ratio less than 0.15. The pressure drop is sensitive to a high blockage ratio because of several factors including (1) flow separations due to sudden contraction and expansion of the channel, (2) flow restrictions in the foam due to the internal microstructure and (3) massive wakes appearing downstream the foam. Regardless of the pore density, the presence of a foam block that partially filled the channel could be considered as an additional component, which contributed to a higher pressure drop. By comparing the experimental data with our proposed model, the results are in good agreement, except for the result of 5 PPI foam at h/H = 0.16. The proposed model is fitted from different set of experimental data: two different channels and various physical and geometrical properties of metal foam blocks. The details of the proposed model could be seen in Section 4.3.3. The under-predicted pressure gradient most probably due its significant tortuous flow path and fluctuated velocities within the porous structure. Also, for that large pore foam, there is a high possibility for the flow to escape into the free stream region, and creating a mixing flow at the interface. These factors may contribute to an additional local pressure loss, hardly captured through different PPIs, and a small number of sample size.

The present experimental results are also compared to a numerical data from Lu et al. [21]. **Figure 4.8** shows that both 10 and 30 PPI foams from the experimental and numerical results of the similar and significant blockage ratio, h/H = 0.4 are in agreement that the higher PPI foam would have a higher pressure drop than the lower PPI foam. However, at a similar inlet velocity, for example, 5.0 to 6.0 m/s, the experimental results vary significantly, as compared to the numerical results [21]. The higher pressure drop in the experimental data is most probably due to the turbulent flow regime in this study, while the numerical study assumed a fully developed laminar flow. The experimental data are also subjected to minor losses at the upstream and downstream regions as the pressure taps are located outside of the partially filled section, discussed in details in the following section.

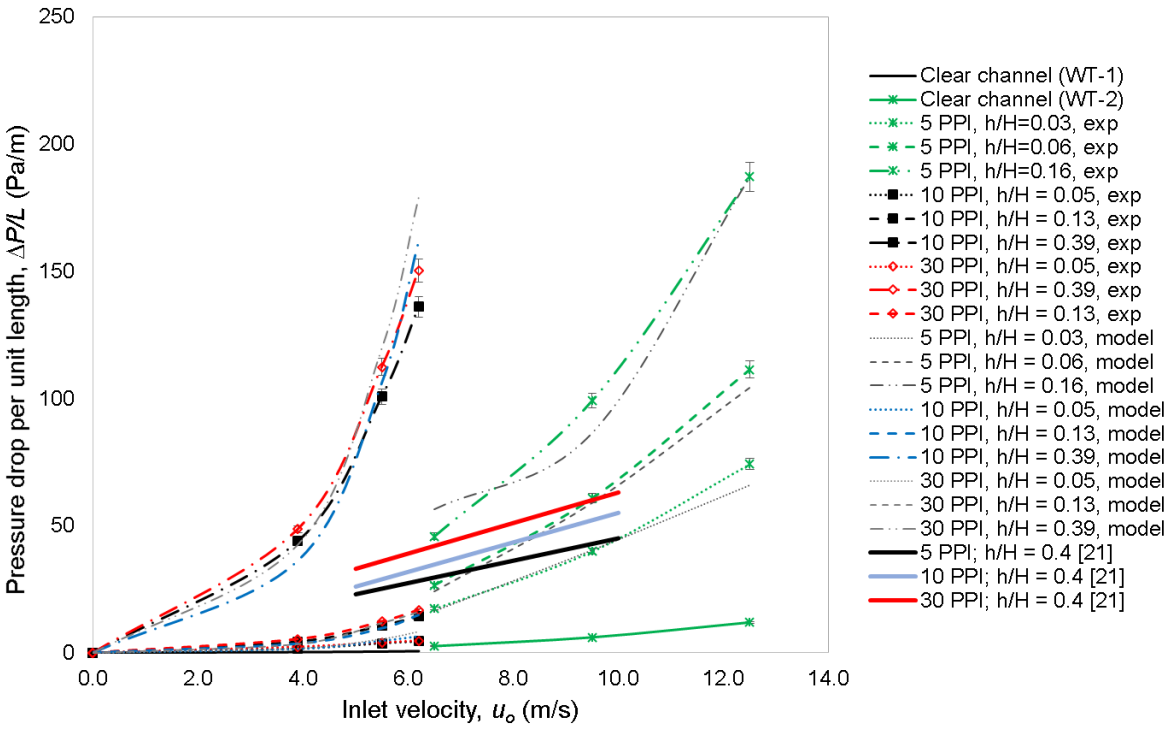

Figure 4.8 Comparison of pressure drop per unit length versus inlet velocity between present experimental data, proposed model and similar literature

Figure 4.9 indicates pressure gradient versus blockage ratio for different types of blockage (foam and solid) at different air flow velocities (channel inlet) and foam PPIs. One notes a consistent behaviour that the pressure drop increases with the air velocity for either (foam or solid) block. Starting with WT-2 results, the pressure drop for the 5 PPI foam is higher than that of the solid block. One might expect a higher pressure drop for a solid block compared to a permeable counterpart under identical test conditions. However, as results indicate, the converse is true. This can be attributed to local losses which are higher with a foam block. For instance, the skin-friction drags due to the complicated foam structures induce massive pressure drops. Moreover, for a partially filled channel with a higher blockage ratio both skin-friction drag at the interface and form drag should be taken into account. It is true that the air velocity through the foam is lower than that of the air inlet to the channel but, as mentioned before, part of the air that enters the foam leaves it half-way through and induces further mixing losses at the interface. This trend is also observed in results obtained in WT-1. Interestingly, the 10 and 30 PPI foams show higher pressure drops compared to an identical solid block, which is even more pronounced with higher blockage ratios (> 0.15). The 30 PPI foam shows a maximum increment in the

pressure drop at u_o = 6.2 m/s, h/H = 0.39, with the value about twice that of the solid block. The pressure drops of 10 and 30 at a lower inlet velocity, u_o = 5.5 m/s are still higher compared to a solid block at a higher inlet velocity, u_o = 6.2 m/s. For a solid block to have the same pressure drop as a foam block, for example 5 PPI, h/H = 0.06 at u_o = 9.5 m/s, it has be stretched by an extra 75% (to its original height of 0.02 m). The additional heights of the solid block was estimated by drawing a horizontal line from the y-axis through the foam data and solid block line, then a vertical line from the intersection point through the x-axis, as shown (dashed lines) in **Figure 4.9**.

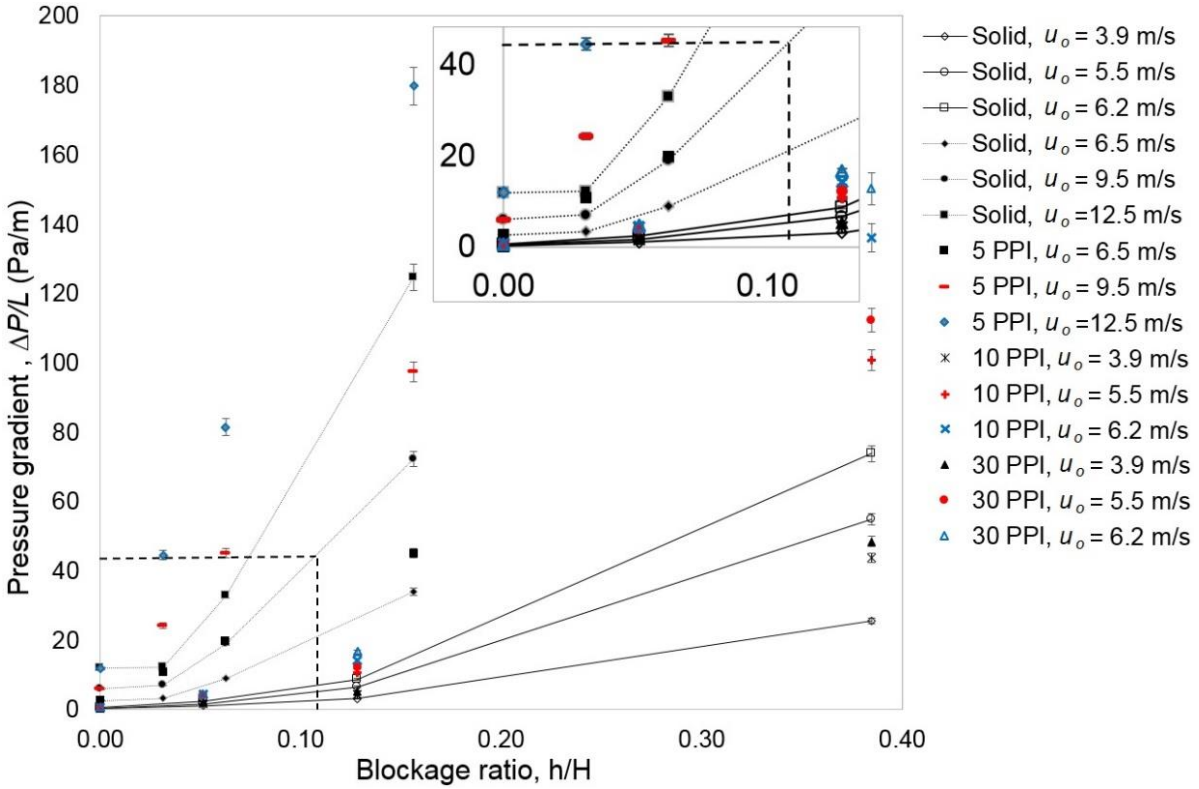

Figure 4.9 Pressure gradient versus blockage ratio – Metal foam and solid blocks

The porous foam would impose flow resistances internally (inside the porous region) and externally (at the interface and through stretched secondary flows downstream). However, the significance of these losses depends on the air flow rate flowing through the porous and free stream regions. Specifically, the pressure losses in the porous region are possibly due to ligaments flow resistance and tortuous flow paths along the pores on top of local expansions and contractions. However, these effects are only significant in more porous foams, like 10 PPI rather than 30 PPI foam, based on the streamlines shown **Figure 4.10 (a)**. As it was discussed in the previous

section, there is a major difference between the flow that passes (through and over) a foam block and that over a solid block with same size. In the case of a foam with large enough pore size, the incoming flow tends to enter the foam and exit through the pores on the interface. The exiting air does not carry enough momentum to stop the incoming air but it will induce losses while mixing with the incoming air that has avoided the foam and moved up to the free stream region. In **Figure 4.10 (a)**, one clearly observes the vortex formation just before the front face of the solid block, as no air can enter the block, but for both foam cases no vortex is formed in that region. Noteworthy, the wake size downstream of the solid block is in order of the block height, and the core of the wake is close to the block. However, for the foam case, not only size of the wake is about two times bigger than the foam height but also the wake core is pushed further downstream that lead to having larger pressure drop. Even though the metal foams impose a higher pressure drop due to wakes and frictional effects, their significances depend on the pore density. Nevertheless, the effects of pore density would only become evident after a certain blockage ratio.

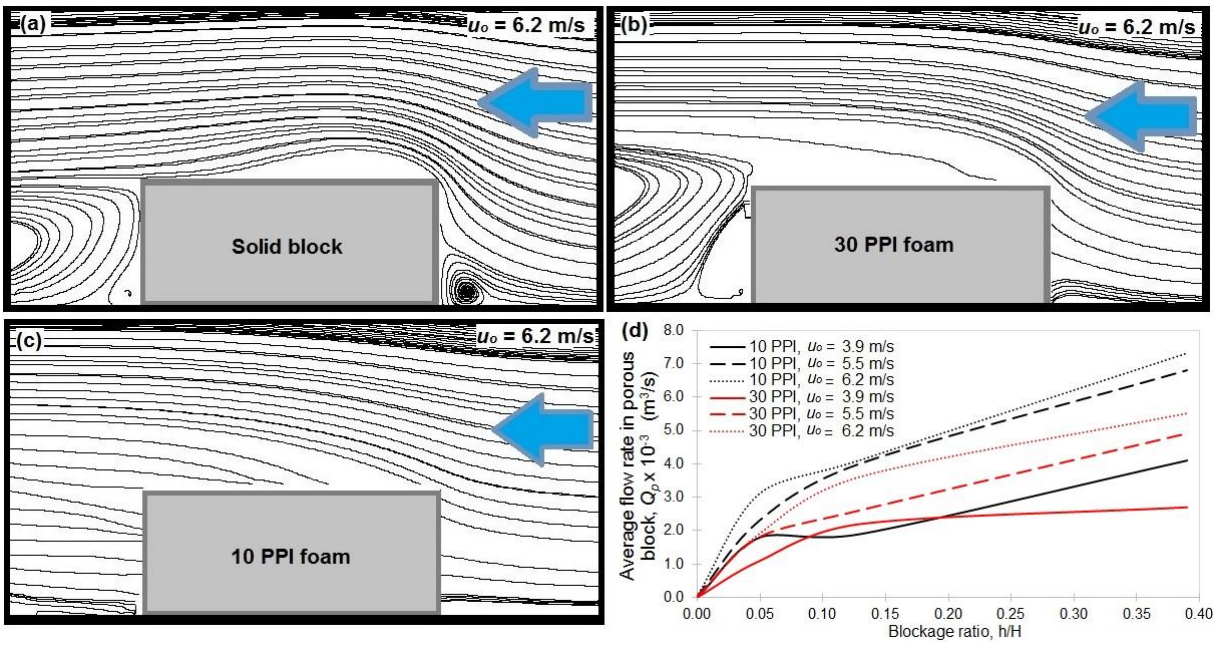

Figure 4.10 (a) – (c) Streamlines of partially channels with solid/metal foam block at u_o = 6.2 m/s (from PIV data) (d) Average flow rate across the foam block, Q_p

From **Figure 4.10 (b)** and **(c)**, it is clear that more significant flow is passing through the 10 PPI foam as compared to the 30 PPI foam of the same size. The average flow rates that passed through the foams are calculated using **Equations (4.8)** and **(4.14)**,

based on the concept of mass conservation and continuity equation explained in detail in the following section. **Figure 4.10 (d)** depicts the average flow rates for both 10 and 30 PPI foams with different blockage ratios. The 10 PPI foams have higher average flow rates, obviously seen with a significant blockage ratio. Also, these PPIs effects are more profound at the high inlet velocities, $u_o \geq 5.5$ m/s. For the low blockage ratios (h/H <0.20), especially with the lowest inlet velocity, the flow rates in the porous blocks are fluctuated and could attain a similar value, indicating the insignificant PPI effects in those conditions, as expected. The total flow rates of 30 and 10 PPI (shown in **Figure 4.10 (b)** and **(c)**) are 0.017 and 0.022 m^3/s, respectively with the maximum difference due to PPIs is about 25%.

4.3.3 Correlation of friction factor for partially filled channel

This study also proposed a correlation of friction factor for a channel partially filled with metal foam. The Buckingham π theorem was applied in our dimensional analysis by using key parameters such as hydraulic diameter, flow length, fluid properties (density and viscosity) as well as the average velocities. Since, there is no consensus in the literature on the characteristic length of the metal foam, the analyses were conducted by using a trial and error method [36]. Only the best conformity between the parameteric model and experimental data is presented. From a multiple linear regression analysis (95% confidence interval), our suggested variables (as shown in **Equation (4.7)**) show P-value <0.05 and the adjusted $R^2 = 0.98$. These results show that the suggested variables with the friction factor are statistically correlated.

Figure 4.11 shows the goodness of fit of linear regression for the predicted friction factor and the experimental data. The regression shows a strong agreement since $R^2 > 0.95$ with the deviation between the predicted friction factor and the experimental data being ±16%. Most probably, the deviation is caused by the velocity fluctuations in the free stream region, which are persistently present with thicker foam layers and at higher inlet velocity values. Using more data points throughout the foam length (streamwise direction) could represent the exact flow and the estimation of pore velocities and the friction factor would be more accurate.

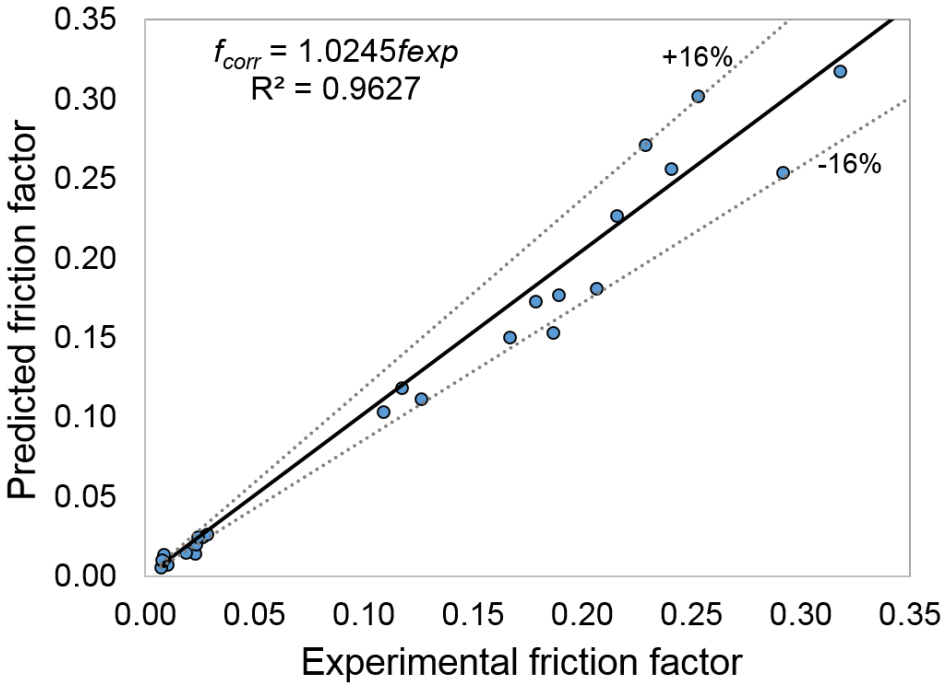

Figure 4.11 Experimental versus predicted friction factor

The correlation of friction factor for a partially filled channel with metal foam is expressed as follows:

$$f = 9.155\times10^{-5}(Re_{\mathrm{H}})^{-1.332}\left(\frac{\mathrm{Hf}}{\mathrm{H}}\right)^{-6.2966}\left(\frac{u_p}{u_{us}}\right)^{-0.401} \quad \textbf{(4.7)}$$

where, the pore velocity, u_p, in **Equation (4.7)** can be determined using the following equation:

$$u_p = \frac{u_{us}\mathrm{H} - u_f\mathrm{Hf}}{\varepsilon\mathrm{h}} \quad \textbf{(4.8)}$$

Due to the nature of aluminium foam, it is impossible to measure the pore velocity using the LDA or other conventional equipment. Hence, **Equation (4.8)** is adapted from the mass continuity theory, where the volume flow rate in the upstream region, Q_{us} is assumed to be equal to the flow rates in the downstream region, Q_{ds} and partially filled region, Q_{pf}. By assuming an incompressible flow, the relation between the flow rates is expressed as:

$$Q_{us} = Q_{ds} = Q_{pf} = Q_p + Q_f \quad \textbf{(4.9)}$$

where Q_p and Q_f are the flow rates in the porous and free stream regions, respectively. By referring to **Equation (4.9)**, the average velocity in the partially filled channel, can be written as:

$$\bar{u} = \frac{1}{\mathrm{H}} \int_0^{\mathrm{H}} u_{us} dy = \frac{1}{\mathrm{H}} \left[\int_0^{\mathrm{h}} u_p dy + \int_{\mathrm{h}}^{\mathrm{H}} u_f dy \right] \quad \textbf{(4.10)}$$

where H is the channel heights, h is the foam height, u_p is the pore velocity and u_f is the free stream region velocity. The free stream and porous regions (shown in **Figure 4.2**) were considered as two distinct regions. The volume flow rates in the upstream and free stream regions can be determined by integrating the measured velocity profiles using **Equation (4.11)** and **(4.12)**, respectively. Otherwise, the average velocity in those regions can also be multiplied by the cross-sectional area:

$$Q_{up} = \int_0^{\mathrm{W}} \int_0^{\mathrm{H}} u_{up}(y) dy dz \quad \textbf{(4.11)}$$

$$Q_f = \int_0^{\mathrm{W}} \int_{\mathrm{h}}^{\mathrm{H}} u_f(y) dy dz \quad \textbf{(4.12)}$$

For an estimation of the core velocity, the average flow rate in the free stream region can be obtained by averaging the measured velocities from three different locations (labelled as 2, 3 and 4 in **Figure 4.2**). The average volume flow rate in the porous region can be determined using **Equation (4.13)**. Instead of **Equation (4.8)**, the average pore velocity can be also estimated using **Equation (4.14)** as:

$$\overline{Q_p} = Q_{up} - \frac{\sum_{i=1}^{N} Q_f}{N} \quad \textbf{(4.13)}$$

$$\bar{u}_p = \frac{\overline{Q_p}}{\varepsilon A_f} \quad \textbf{(4.14)}$$

Figure 4.12 shows the relationship between the dimensionless velocity, u_p/u_{us}, (a ratio of pore velocity and upstream velocity) and the blockage ratio. Increasing the blockage ratio, the pore velocities plunge but this behavior is only observed at low velocities; i.e. $u_o \leq 6.5$ m/s. At a higher inlet velocity, such as 9.5 and 12.5 m/s, the foam velocities with h/H>0.16 would be increased again, as shown in 5 PPI foam. Based on 10 and 30 PPI foams, the foam velocities decrease with the blockage ratio when h/H < 0.20. In addition, the indistinct trends of 10 and 30 PPI foams show tortuous flows probably

occurred inside the foam when the inlet velocity is less than 6.2 m/s. Therefore, the flow paths inside the porous region may cause additional pressure losses; though its significance is possibly inferior to that of the frictional resistances due to the ligament constrictions.

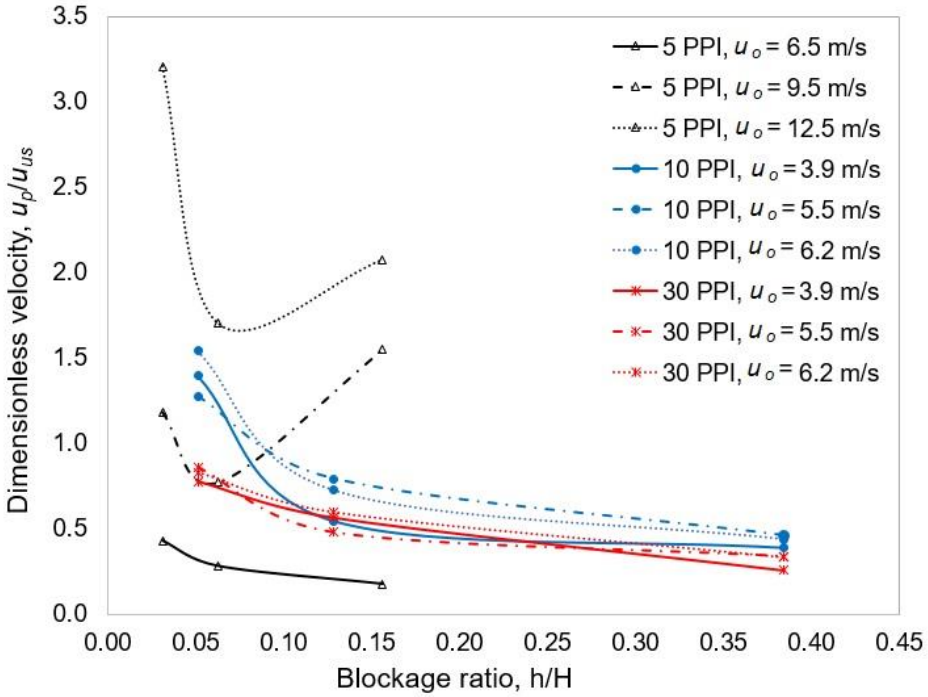

Figure 4.12 Dimensionless velocity, u_p/u_{us} versus blockage ratio

4.4 Conclusion

This study investigated velocity profiles of 5, 10 and 30 PPI with different blockage ratios, and inlet velocities. From a series of experiment in WT-1 and WT-2, the remarkable conclusions are listed as below:

(a) In the upstream and downstream regions, the velocity decreases towards the top wall, while the velocity behaviour near the bottom wall is rather complex, due to the presence of the metal foam block. A part of the air that enters the foam leaves it half-way through the foam interface at a high enough blockage ratio.

(b) The free stream velocity is increasing with the increase of the blockage ratio, resulting in a formation of recirculation zone at the downstream region. However, the effects of the lowest blockage ratio, h/H = 0.05 on the free stream velocity is insignificant. It is only noticeable with h/H = 0.13.

(c) The metal foam causes a higher pressure drop than the solid block of the same size. This even more pronounced with the higher blockage ratios, h/H>0.15. The 30 PPI foam with h/H = 0.39 shows a maximum increment in the pressure drop at u_o = 6.2m/s, with the value is about twice that of the solid block. At a lower inlet velocity, u_o = 5.5 m/s, the pressure drop of the metal foam is still higher compared to a solid block at u_o = 6.2m/s.

(d) The proposed friction factor model is in agreement with the experimental data with the deviation is about ±16%. The deviation might be attributed to the velocity fluctuations in the free stream region and within the porous structure of large pore foam, e.g., 5 PPI. Using a larger number of data points to compensate the fluctuated velocities near the interface and various foam samples could be helpful to enhance the model accuracy.

References

[1] C. T'Joen, P. De Jaeger, H. Huisseune, S. Van Herzeele, N. Vorst, and M. De Paepe, "Thermo-hydraulic study of a single row heat exchanger consisting of metal foam covered round tubes", *International Journal of Heat and Mass Transfer*, 53, 15–16, pp. 3262–3274, 2010.

[2] A. Chumpia and K. Hooman, "Performance evaluation of single tubular aluminium foam heat exchangers", *Applied Thermal Engineering*, 66, pp. 266–273, 2014.

[3] M. Odabaee and K. Hooman, "Application of metal foams in air-cooled condensers for geothermal power plants: An optimization study", *International Communications in Heat and Mass Transfer*, 38, 7, pp. 838–843, 2011.

[4] K. Hooman, "Thermohydraulics of porous heat exchangers: full or partial blockage?", in *Proceedings of the 5th International Conference on Porous Media and its Applications in Science and Engineering (ICPM5)*, Kona, Hawaii, 2014.

[5] F. Shikh Anuar, M. R. Malayeri and K. Hooman, "Particulate fouling and challenges of metal foam heat exchangers", *Heat Transfer Engineering*, 38, 7-8, pp. 730–742, 2017.

[6] N. Karimi, Y. Mahmoudi and K. Mazaheri, "Temperature fields in a channel partially filled with a porous material under local thermal non-equilibrium condition - An exact solution". *Proc. Inst. Mech. Eng. Part C J. Mech. Eng. Sci*., 228, 15, pp. 2778–2789, 2014.

[7] Y. Mahmoudi and M. Maerefat, "Analytical investigation of heat transfer enhancement in a channel partially filled with a porous material under local thermal non-equilibrium condition", *International Journal of Thermal Sciences*, 50, 12, pp. 2386–2401, 2011.

[8] M. Torabi, K. Zhang, G. Yang, J. Wang and P. Wu, “Heat transfer and entropy generation analyses in a channel partially filled with porous media using local thermal non-equilibrium model”, *Energy*, 82, pp. 922–938, 2015.

[9] D. Poulikakos and M. Kazmierczak, “Forced convection in a duct partially filled with a porous Material”, *Journal of Heat Transfer*, 109, pp. 653-662, 1987.

[10] M. E. Nimvari, M. Maerefat and M. K. El-Hossaini, “Numerical simulation of turbulent flow and heat transfer in a channel partially filled with a porous media”, *International Journal of Thermal Sciences*, 60, pp. 131–141, 2012.

[11] Y. Mahmoudi and N. Karimi, “Numerical investigation of heat transfer enhancement in a pipe partially filled with a porous material under local thermal non-equilibrium condition”, *International Journal of Heat and Mass Transfer*, 68, pp. 161–173, 2014.

[12] J. A. Ochoa-Tapia and S. Whitaker, “Momentum transfer at the boundary between a porous medium and a homogenous fluid-I. Theoretical development”, *Int. J. Mass Transf*., 38, 14, pp. 2635–2646, 1995.

[13] G. S. Beavers and D. D. Joseph, “Boundary conditions at a naturally permeable wall”, *Journal of Fluid Mechanics*, 30, 01, pp. 197-207, 1967.

[14] I. Ashtiani Abdi, K. Hooman and M. Khashehchi, “A comparison between the separated flow structures near the wake of a bare and a foam-covered circular cylinder,” *J. Fluids Eng*., 136, 12, pp. 121203, 2014.

[15] M. Khashehchi, I. Ashtiani Abdi, K. Hooman and T. Roesgen, “A comparison between the wake behind finned and foamed circular cylinders in cross-flow”, *Experimental Thermal and Fluid Science*, 52, pp. 328–338, 2014.

[16] M. Khashehchi, I. Ashtiani Abdi and K. Hooman, “A comparative analysis on the shed vortices from the wake of finned, foam- wrapped cylinders”, *Fluid Dynamics Research*, vol. 49, p. 045506, 2017.

[17] E. Sauret, I. Ashtiani Abdi and K. Hooman, “Fouling of waste heat recovery: Numerical and experimental results”, in *19th Australasian Fluid Mechanics Conference, Melbourne, Australia, 2014*.

[18] N. Dukhan, “Correlations for the pressure drop for flow through metal foam”, *Exp Fluids*, 41, pp. 665–672, 2006.

[19] M. Sener, A. Yataganbaba and I. Kurtbas, “Forchheimer forced convection in a rectangular channel partially filled with aluminum foam”, *Experimental Thermal and Fluid Science*, 75, pp. 162–172, 2016.

[20] Z.-B. Liu, Y.-L. He, Y.-F. Yang and J.-Y. Fei, “Experimental study on heat transfer and pressure drop of supercritical CO2 cooled in a large tube”, *International Journal of Heat and Mass Transfer*, 85, pp. 679–693, 2015.

[21] W. Lu, T. Zhang and M. Yang, “Analytical solution of forced convective heat transfer in parallel-plate channel partially filled with metallic foams”, *International Journal of Heat and Mass Transfer*, 100, pp. 718–727, 2016.

[22] P. Forooghi, M. Abkar and M. Saffar-Avval, “Steady and unsteady heat transfer in a channel partially filled with porous media under thermal non-equilibrium condition”, *Transport in Porous Media*, 86, pp. 177–198, 2011.

[23] H. J. Sung, S. Y. Kim and H. J. Min, “Forced convection from an isolated heat source in a channel with porous medium”, *Int. J. Heat Fluid Flow*, 16, pp. 527–535, 1995.

[24] S. Z. Shuja and B. S. Yilbas, “Flow over rectangular porous block in a fixed width channel: influence of porosity and aspect ratio”, *Int. J. Comut. Fluid Dyn*., 21, 7–8, pp. 297–305, 2007.

[25] Y. Addad, D. Laurence, C. Talotte and M. C. Jacob, “Large eddy simulation of a forward – backward facing step for acoustic source identification”, *International Journal of Heat and Fluid Flow*, 24, pp. 562–571, 2003.

[26] A. Kouidri and B. Madani, “Mechanics of materials experimental hydrodynamic study of flow through metallic foams : Flow regime transitions and surface roughness influence”, *Mechanics of Materials*, 99, pp. 79–87, 2016.

[27] J. Soria, A. R. Masri and D. R. Honnery, “An adaptive cross - correlation digital PIV technique for unsteady flow investigations”, in *Proceedings of the 1st Australian Conf. on Laser Diagnostics in Fluid Mechanics and Combustion*, Sydney, NSW, Australia, pp. 29–48, 1996.

[28] “China Beihai Building Material Co., Ltd.” [Online]. Available: http://www.chinabeihai.net/. [Accessed: 01-May-2015].

[29] “ELHI Thermal Solution Comm.V.” [Online]. Available: https://data.be/nl/bedrijf/Elhi-Thermal-Solutions-COMMV-0836107534.

[30] K. Hooman and N. Dukhan, “A theoretical model with experimental verification to predict hydrodynamics of foams”, *Transport in Porous Media*, 100, 3, pp. 393–406, 2013.

[31] V. Calmidi and R. Mahajan, “Forced convection in high porosity metal foams”, *Journal of Heat Transfer*, 122, pp. 557–565, 2000.

[32] N. Dukhan, M. A. Al-Rammahi and A. S. Suleiman, “Fluid temperature measurements inside metal foam and comparison to Brinkman-Darcy flow convection analysis”, *International Journal of Heat and Mass Transfer*, 67, pp. 877–884, 2013.

[33] Z. Zhang, LDA application methods - Laser Doppler Anemometry for fluids dynamics. Berlin, Heidellberg, 2010.

[34] G. C. Papageorgakis and D. N. Assanis, “Comparison of linear and nonlinear rng-based k-epsilon models for incompressible turbulent flows”, Numerical Heat Transfer, Part B: Fundamentals, 35, 1, pp. 1–22, 1999.

[35] E. Sauret, K. Hooman and C. S. Suvash, “CFD simulations of flow and heat transfer through the porous interface of a metal foam heat exchanger”, in *Proceedings of the ASME 2014 Power Conference*, 2014, pp. 1–6.

[36] A. Gancarczyk, M. Piątek, M. Iwaniszyn, P. Jodłowski, J. Łojewska, J. Kowalska and A. Kołodziej, “In search of governing gas flow mechanism through metal solid foams”, *Catalysts*, 7, 124, pp. 1–11, 2017.

Chapter 5: Partially Filled Channel with Open-Cell Metal Foam – Part II: Global-wise Measurement using Particle Image Velocimetry

The previous chapter explains how the effects of complicated structure on the external flow. Interestingly, the effects show different results as compared to the theory of porous media, numerically or analytically. Due to the complex nature of flow behaviours, instead of locally measured, a whole measurement would be more accurate. It is widely known that the measurements inside the pores are tricky and difficult to retrieve. This chapter, which is an extended study from Chapter 4 proposed an alternative to understand the flow behaviours inside the porous structure. Global-wise measurement techniques were employed to obtain a better understanding of the flow behaviours in the partially filled channel. Particle Image Velocimetry (PIV) was used to determine velocity fields in the clear region that includes the upstream, downstream and partially filled section. Meanwhile, a thermal imaging technique was used to investigate the flow pattern inside the porous foam block. Additionally, the airflow temperatures inside the channel were measured using a thermocouple at several locations across the channel; in both clear and porous regions. The effects of foam microstructural and geometrical properties on the flow behaviours, temperature and pressure drop, were discussed in details. The flow behaviours at the interface of fluid/foam are also described, qualitatively in this chapter. The content of this chapter is from:

F. Shikh Anuar, I. A. Abdi, and K. Hooman, **"Flow Visualization Study of Partially Filled Channel with Aluminium Foam Block**"*, International Journal of Heat and Mass Transfer*, 127, pp. 1197–1211, 2018.

Flow Visualization Study of Partially Filled Channel with Aluminium Foam

Fadhilah Shikh Anuar[a, b, 1], Iman Ashtiani Abdi[a, 1], Kamel Hooman[a]

[a]School of Mechanical and Mining Engineering, The University of Queensland, Queensland, Australia;

[b]Centre for Advanced Research on Energy (CARe), Fakulti Kejuruteraan Mekanikal, Universiti Teknikal Malaysia Melaka, Hang Tuah Jaya, 76100, Durian Tunggal, Melaka, Malaysia

Abstract

This experimental study investigated fluid dynamics of a channel partially filled with a metal foam block with various pore densities; 5, 10 and 30 PPI. The effects of foam heights, in a range of 0.004 – 0.050 m, and inlet velocities, from 3.9 to 12.5 m/s, on the flow field were investigated using Particle Image Velocimetry (PIV). For a more comprehensive analysis of the problem, detailed flow patterns inside the porous foam were visualized by applying a thermal imaging method. Results show that there are different flow behaviours in the partially filled channel depending on the key parameters. A boundary layer is formed on the horizontal fluid/foam interface, which is much more noticeable and thicker in high blockage ratio cases. The low-pore density foam allows the flow to pass through its porous structure while the higher pore density foam imposes more restrictions on the flow pushing the fluid away from the foam into non-porous region on the top of the foam block before reaching the foam end.

Nomenclature

d_f	ligament diameter (m)
d_p	pore diameter (m)
Da	Darcy number, K/H^2
f_1	friction factor of the empty channel
FOV	field of view
h	foam height (m)
H	channel height (m)
Hf	free stream height (m)
h/H	blockage ratio
k	resistance coefficient
K	permeability (m^2)

L	pressure taps distance (m)
L_c	channel length
Lf	foam length (m)
ΔP	pressure drop (Pa)
PPI	pore per inch
Re	Reynolds number
Δt	time between pulses (s)
T	temperature (K)
U	velocity (m/s)
u_s	streamwise velocity (m/s)
u_o	inlet air velocity (m/s)
wf	foam width (m)
W	channel width (m)
WT-1	wind tunnel with D_h = 0.088 m
WT-2	wind tunnel with D_h = 0.320 m
Y	Non-dimensional transversal coordinate, y/H

Subscripts

a	local air
c	channel
ds	downstream
Dh	channel hydraulic diameter
max	maximum
us	upstream

Greek Symbols

$\varnothing$	diameter (m)
ε	porosity
ρ	density (kg/m^3)
λ	laser wavelength (nm)

5.1 Introduction

Open-cell metal foams have been proved in many studies to have superior heat transfer performances but at the expense of higher pressure drop [1]. Hence, a partially filled channel is being considered as an alternative to a fully filled configuration

to minimize the pressure drop effects while keeping the same heat transfer enhancement over a non-porous channel [2]. Convection heat transfer through metal foams have been investigated in great details for fully filled channels [3-5]. Besides, numerical and analytical studies are reported to deal with filled configuration [6-11]. However, only several experimental studies have been conducted on channels partially filled with metal foams [12-15], and further experimental studies are required to identify the effects of foam heights, foam arrangement, and pore density on the flow field especially at the flow-foam interface [12].

Varying the inlet velocity from 1 to 5 m/s, Hamadouche et al. [12] investigated the heat transfer and pressure drop of a rectangular channel partially filled with three 40 PPI aluminium (porosity, $\varepsilon = 0.93$) foam blocks, which placed in staggered manner on top and bottom walls, and the results were compared with those pertinent to aluminium solid blocks of the same exterior size. According to those authors, the foam blocks dissipated about 2 times more heat compared to the identical solid blocks. It was also reported that the foams exhibited lower pressure losses because of their porous nature as opposed to impermeable solid blocks. Sener et al. [13] studied the heat transfer from 10 and 20 PPI aluminium foams in a fully developed rectangular channel over the Reynolds number range of $968 < Re_{Dh} < 29624$. Interestingly, they found that the 10 PPI foam has a better heat transfer capability than a 20 PPI in a partially filled channel while for the fully filled channel the converse is true. They also stated that the 10 PPI foam exhibits a relatively lower pressure drop compared to that of the higher PPI sample, for both partially and fully filled cases. Liu et al. [15] experimentally investigated heat transfer and pressure drop of supercritical CO_2 cooled in tubes partially filled with metal foam, using different pore densities of 20, 40 and 60 PPI, and with porosities ranging from 0.85 to 0.95. It was found that by decreasing the pore density, the heat transfer coefficient would be decreased to almost a constant value. By increasing the pore density, the pressure drop in the tube would be increased first before subsequently decreasing when plotted against bulk temperature. Tajik Jamal-Abad et al. [16] experimentally investigated the use of 30 PPI copper metal foam ($\varepsilon = 0.9$) to enhance the efficiency of a solar collector. They considered three different configurations of an absorber; partially filled, fully filled and without foam. It was concluded that addition of metal foam to the channel increases the efficiency at the expense of an increased pressure drop. Furthermore, it was

claimed that the foam induces a strong flow-mixing requiring a careful selection of the foam geometrical properties.

Buonomo et al. [14] experimentally studied natural convection in parallel plates horizontal channel with aluminium foam, through a visualization technique (He-Ne laser source) and wall temperature measurement, while the bottom wall was heated with a constant heat flux. It was reported that adding foam to the channel increases the heat transfer performance. Their flow visualization results indicated that the foam causes a secondary motion like Rayleigh-Benard cells, and the channel without foam induces mushroom-vortex flow. Sauret et al. [17] investigated a partially filled channel to determine the effects of inlet velocity and foam height on the pressure drop and velocity profile at the interface between porous and free stream region. Using a hot-wire anemometer, the authors questioned the accuracy of the velocity jump boundary condition at the interface as different interface velocities along the stream-wise direction were encountered. Hooman [18] argued that there is a possibility for a part of the fluid that enters a porous foam in a partially filled channel, to leave earlier from the interface before reaching the end of the foam, due to the formation of a recirculation region downstream of the foam. Through an analytical study for a partially porous-saturated channel, Kuznetsov [19] reported the existence of two momentum boundary layers for the porous medium; near the wall boundary and at the interface. It was assumed that the fluid velocity between the two boundary layers is constant.

Alkam and Al-Nimr [20, 21] studied the thermal performance of a partially filled pipe with an isotropic and homogenous porous medium. These numerical studies assumed axisymmetric, laminar and boundary layer flow with no internal heat generation. The interaction between a porous medium and clear fluid was stimulated by considering the Darcy-Brinkman-Forchheimer formula and the interface region was modelled using the continuity of velocity and shear stress. In Ref. [20], the authors stated that the mean velocity in the porous region is lower than the clear region because of the additional obstructions caused by the inertial and viscous forces of the porous structure. While the increase of the fluid velocity in the free stream region is due to the drafted fluid from the porous region. Later, Alkam and Al-Nimr [21] studied the pressure drop effects and found that the addition of the porous medium would increase the pressure drop of the partially filled pipe, up to 170 times due to the microscopic and macroscopic shear and drag forces. However, the study did not

include further explanation of Darcy number, PPI or permeability effects on the pressure drop performance. Considering the complex structure of a metal foam, a detailed experimental campaign providing accurate flow characteristics for such flows is called for. This will, obviously, assist the design engineer when it comes to analysing the trade-off between heat transfer augmentation and the excess pressure drop caused by metal foams in a partially foam-filled channel. Hence, the aim of this study.

Jin and Fan [22] proposed a thermal imaging technique using an infrared (IR) camera (FLIR 655 s; ±2% accuracy), and a macrolens that offering 50 μm resolution to investigate melting of paraffin filled in 15 PPI copper foam. The authors validate the thermal imaging results by comparing with temperature data obtained using a T-type thermocouple that located at the central point of a middle pore. Both techniques were employed simultaneously to measure the transient temperatures during the melting process. They conducted several precautions for the validation tests and found less than 4% deviation between those two data. This technique was also used in their extended study on the pore size effects [23] of 15, 30 and 50 PPI copper foams. In another study, Yao et al. [24] also observed the melting of paraffin at the pore scale level but employing a high definition camera in addition to the IR camera and thermocouples. They presented detailed phase changes and temperature fields on the complex melting phenomena.

The present study used the IR camera to visualize flows in a partially filled channel with an open-cell metal foam block. Particle Image Velocimetry (PIV) was also employed to analyse the flows in the non-porous regions that include the upstream and downstream of the foam block. This experimental study was conducted to investigate the effects of inlet velocity, foam height (or blockage ratio) and pore density of metal foam on the flow behaviour and pressure drop. Additionally, the fluid temperature in the partially filled channel were measured both in the porous and free stream regions to investigate the flow pattern within the porous media and at the interface.

5.2 Experimental Setup and Foam Samples

The present study relies on flow visualization and temperature measurements to investigate the effects of blockage ratio, pore density, and inlet air velocity on the overall fluid flow behaviours of a partially foam filled channel. This study conducted

two separate flow visualization experiments using (i) PIV and (ii) IR thermography. The experiments were conducted in two different wind tunnels. One of the wind tunnels, WT-1, has a test section with a size of 0.100 m (W) x 0.078 m (H) x 0.350 m (L_c) while the other one, WT-2, is larger; 0.320 m (W) x 0.320 m (H) and 1.20 m (L_c). The details of the WT-2 can be found in Ref. [17]. Meanwhile, the test section of WT-1 is shown in **Figure 5.1**. The ambient air is drawn into a blower (1.1 kW, ELMO-G) which then passes through a diffuser, an electric heater (3 kW) and a settling chamber before entering the rectangular test section. The air flow rate is controlled using a gauge valve, and the electric heater, which is located at 0.90 m upstream of the test section is only operated when measuring the air temperature and during the IR thermography experiment. The top and side walls of the test section is made of clear windows (Quartz glass) to provide better optical access for the flow visualization experiments. The Reynolds number (Re_{Dh}) in the empty test section of WT-1 ranges from 22,000 to 36,000 and that of WT-2 lies in the range of 135,000 to 265,000 corresponding to the inlet air velocity of 3.9 to 6.2 m/s (WT-1), and 6.5 to 12.5 m/s (WT-2), to study the effects of blockage ratio (ratio of foam height to channel height, h/H = 0.05 to 0.39) and pore densities (5 – 30 PPI) within the partly foam-filled channels. The metal foam properties are listed in **Table 5.1**.

Table 5.1 Metal foam microstructural and geometrical properties

Parameter	Value		
Pore density (PPI)	5	10	30
Ligament diameter, d_f (m)	0.0011	0.00044	0.00027
Pore diameter, d_p (m)	0.0058	0.0026	0.00087
Porosity, ε (-)	0.92	0.82 – 0.91	0.88 - 0.94
Permeability, K x 10^{-7} (m^2)	2.61	1.54 – 1.65	0.35 – 0.37
Foam height, h (m)	0.02, 0.05	0.004, 0.01, 0.03	
Blockage ratio, h/H	0.06, 0.16	0.05, 0.13, 0.39	
Foam length, Lf (m)	0.27	0.09	
Foam width, wf (m)	0.32	0.10	
Hydraulic diameter, Dh_{foam} (m)	0.038, 0.087	0.008, 0.018, 0.046	

The 10 and 30 PPI foams were used in WT-1 and 5 PPI foam was used in WT-2. The experimental results are anticipated to be independent of the wind tunnel and sample sizes once proper scaling parameters are used. This will, however, be tested, using the blockage ratio and the Reynolds number.

Experiments using Particle Image Velocimetry (PIV) were conducted in both of the wind tunnels to identify the flow characteristics in the two test sections. To run the PIV, airflow was exposed to oil droplet injection (an average particle diameter of, $\varnothing$ = 3 µm) by using a seeding generator. A pulsed dual cavity Nd:YAG laser (Litron -130 mJ) was used to provide 3 mm laser light sheet (λ = 532 nm) from a mirror arm that consists of cylindrical and spherical lenses. The laser sheet from the top wall (**Figure 5.1**) illuminated the oil droplets and the scattered lights would be captured by CCD cameras. Two cameras in a translational configuration were used in the experiment, which were placed next to the side wall of the test section. The resolution (HiSense MK-II) of the cameras is 1344 x 1024 pixels; 12 bits/pixel with a trigger rate of 4.5 Hz. Each camera was fitted with an optical filter for more uniform in-plane distribution of the mean image intensity. The system was controlled using a synchronizer, and the acquisition processes were conducted using a commercial software; DynamicStudio. For each experiment, 2000 images were captured with the time between laser pulses (tbp), Δt = 100 µs. The tbp is set based on the incoming air flow velocity as well as the experimental setup.

Note that when using the PIV, extra image noises may appear for a high shear region [25], and near a surface [26] due to the small particle displacements. Considering our experimental setup, a direct velocity measurement near the foam surface (interface region) is difficult due to the existence of undesirable effects such as light reflection and sharp local velocity gradients. To minimise the reflection of the laser sheet from the on the foam block interface, the foam samples were painted with a thin layer of flat black. For WT-1, the presence of the foam block inside the field of view (FOV) could interfere with the computation of the spatial correlation of the velocity field. This was resolved by applying a number of image processing steps such as background subtraction using min/max filter, masking and moving average validation method. The image analyses included an adaptive correlation algorithm [27], with an interrogation window size of 128 x 128 pixels in the initial pass, 32 x 32 pixels in the final pass and 50% overlap between the adjacent interrogation areas.

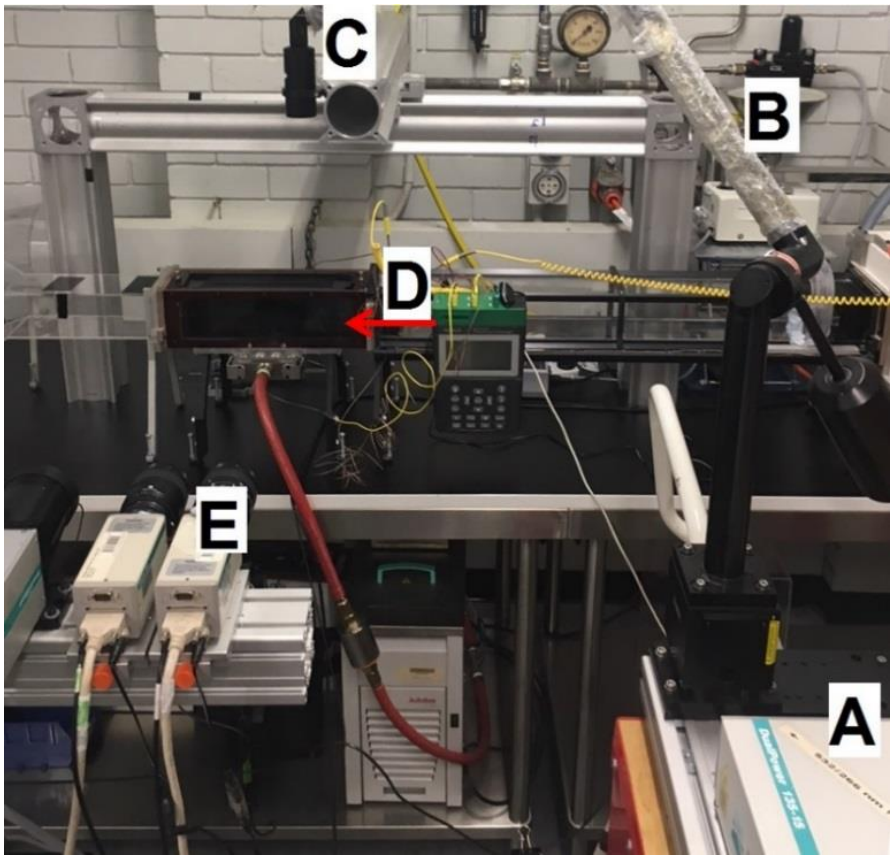

Figure 5.1 Experimental setup for planar PIV measurement (WT-1): (A) Dual-pulsed laser (B) Arm (C) Laser sheet optics (D) Entrance of test section with airflow direction (E) CCD cameras

Due to different sizes of the test sections and the limitation of the camera FOV, a whole clear region could only be captured simultaneously in the WT-1. The total FOV in WT-1 is 68 x 178 mm^2 with 2 mm overlap using two side by side cameras. Meanwhile, several FOVs are required in the WT- 2 to acquire a clear region as schematically shown in **Figure 5.2**. To obtain an insight of flow behaviour across the porous structure of the metal foam, two cameras were also positioned on the top of the test section to acquire FOV 6 and 7 (**Figure 5.3**). For these FOVs, the laser was shot through a lateral plane, located 0.005 m above the fluid/foam interface.

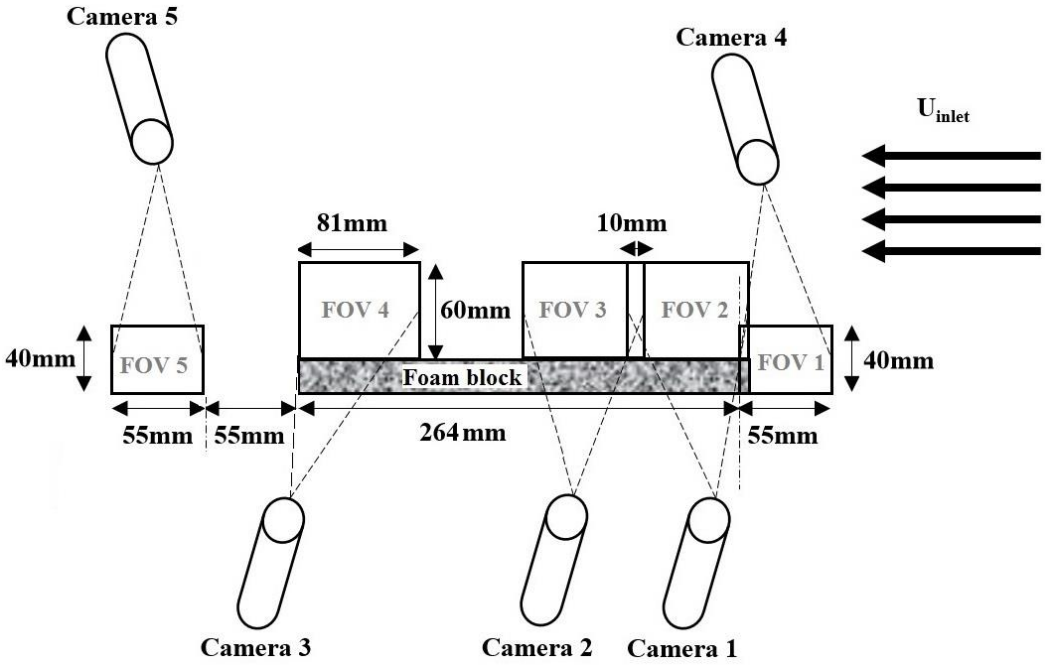

Figure 5.2 FOVs (FOV 1 to 5) from the side of partially filled channel (WT-2)

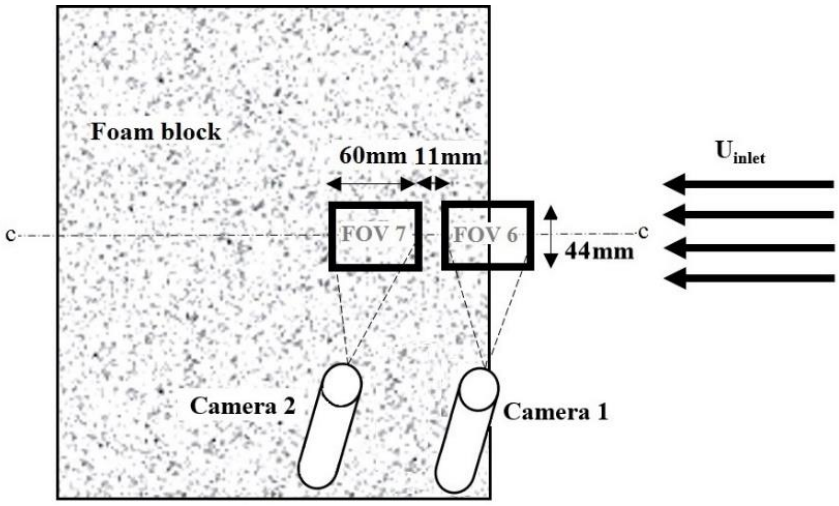

Figure 5.3 FOV 5 and 6 from the top of partially filled channel (WT-2)

This study also applied an infrared thermography technique (IRT) to investigate the flow characteristics inside the foam block. The experiment was performed in the WT-1 with 10 and 30 PPI foam blocks. The incoming air flow was heated to 60°C, using the electric heater. The maximum and minimum inlet air velocities (3.9 and 6.2 m/s) were used to perform this experiment. A refrigerated/heating circulator unit (Julabo F25) was used to circulate the coolant (a mixture of 50:50 water/ethylene glycol) at 20°C, at the bottom of the test section. The constant temperature at the bottom surface facilitates in-depth analysis of heat and fluid flow through the foam.

The coolant flow rate was set to 5 litre/minute using a digital flow sensor (SM 6000-Efector 300). A thin layer of thermally conductive silicone paste (Omegatherm -201**;** 2.3 W/m·K) was carefully applied at the bottom surface of the foam block to reduce thermal contact resistances. A FLIR T650sc infrared (IR) camera is also used to investigate the flow characteristics based on the thermal patterns. To obtain meaningful data, we heated the incoming air and kept the foam block base at a constant temperature. After reaching the steady state condition where the temperature readings were constant, the thermal images were captured. In this technique we have tried to cross correlate the isotherms with the velocity field data, and estimate the behaviour of flow within the foam block. The spectral range of the camera is 7.5 – 14 μm with focal length of the lens and resolution being 25 mm and 640 x 480 pixels, respectively. Basically, the camera captures the infrared radiation emitted by the test section wall and converts it to an electronic signal to present the results as 2-D temperature field. The camera was placed 0.40 m away from the side wall of the test section, in a similar position as the CCD camera in **Figure 5.1**. The experiment involved in-situ visualization and acquisition of thermal images using FLIR Tools software.

In addition, the airflow temperature inside the partially filled channel was measured using a Type-K thermocouple to understand the thermal effects induced by a foam block. The measurements covered three different locations, (1) upstream, (2) downstream, and (3) partially foam-filled section. Each location in the partially filled section (Pf1, Pf2 and Pf3) was 0.023 m apart, with Pf2 located in the middle of the foam block (**Figure 5.4**). The upstream and downstream temperatures were measured at 0.080 m from the leading and rear edges of the foam block. The thermocouple was fixed on a moveable rail on the top of the test section to measure normal points along each location. The thermocouple was calibrated using ice-mixed water with ±0.5°C maximum error. This measurement technique (with in-house manufactured rail) allowed a stable position of the thermocouple when traversing in the vertical direction from point 1 to 12 (see **Figure 5.4**).

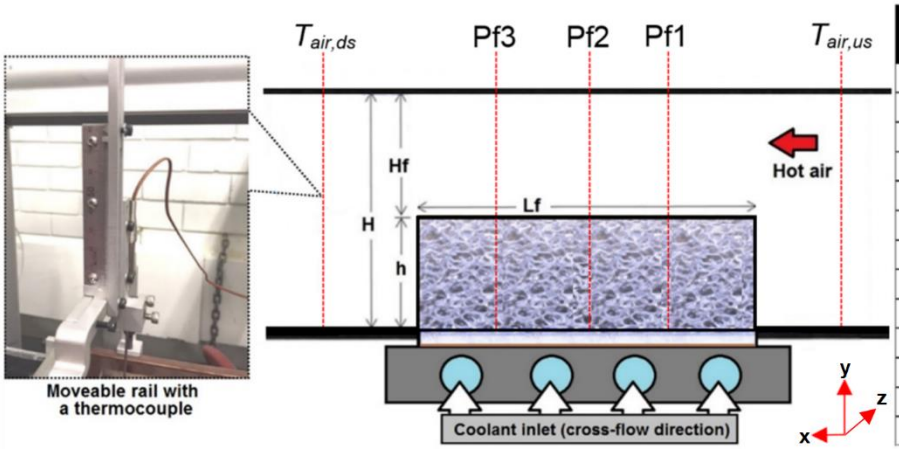

Point	Location (m)
1 (top wall)	0.078
2	0.075
3	0.070
4	0.060
5	0.050
6	0.040
7	0.030
8	0.025
9	0.020
10	0.015
11	0.010
12	0.005
13 (bottom wall)	0

Figure 5.4 Schematic diagram of WT-1 with measurement locations

The top wall (point 1) temperature was measured using a surface thermocouple (Omega SA1XL, accuracy: 1.1°C). All the measurements data were recorded using a data logger (Omega RDXL8). At the beginning of each experiment, the test facility was run idle with the incoming heated airflow for at least 0.5 hour to achieve steady state condition. This is when the temperature readings from the surface thermocouples on the walls stopped changing with time. Pressure drops were measured by placing pressure taps (Sensirion, SDP600 series) at the upstream and downstream of the foam block. In WT-1, the pressure taps were placed 0.25 m apart. While, the total pressure drop in WT-2 was measured with the, 0.41 m apart, taps positioned at 0.07 m from the leading and rear edges of the foam block. The uncertainties of the main parameters in this study are limited to the accuracy of the measurement device as shown in **Table 5.2**.

Table 5.2 Uncertainty in measurement

Parameters	Measurement device	Uncertainty	Ref.
Air velocity	Particle Image Velocimetry (PIV)	0.2 to 2% of full-scale reading	[28]
Air temperature	Type-K thermocouple	±0.5°C	[29]
Air flow rate (WT-1)	Calibrated gauge valve	±5%	[30]
Coolant flow rate	Digital flow sensor (SM 6000-Efector 300)	±2.0%.	[29]
Pressure drop	Differential pressure sensors (Sensirion, SDP610-125Pa)	±3% of reading	[29]
Wall temperature	FLIR T650sc Infrared camera	±1°C for limited temperature range for measuring object (+5°C to +120°C)	[31]

5.3 Results and Discussion

In this study, PIV was utilised primarily as a state of the art flow visualization technique to investigate the flow behaviour in the clear (of metal foam) region of partially porous-filled channel. The results of the PIV experiment are presented as normalized velocity fields (streamwise velocity divided by inlet velocity). Note that, a grey box in the flow fields indicates the foam block. With the presence of the metal foam block in the channel, the full-scale range of the PIV measurement in the non-porous region is 12.0 m/s. By significantly increasing the blockage ratio (h/H = 0.39) in the channel, formation of boundary layer on the top of the horizontal interface could be clearly observed as shown in **Figure 5.5**. The stream-wise velocity adjacent to the interface is reduced significantly as compared to the free stream velocity. The drag due to the foam ligaments is significant particularly along the solid-pores boundaries. Flow separation is initiated from the top of the foam, and the separation extends to at least about one-third of the foam length in the downstream region. The boundary layer could not follow the sharp corner of the porous block thereby causing yet another separation and forming recirculation in the downstream region of the 30 PPI foams.

The negative velocities in the downstream region could be seen in **Figure 5.5 (a)** and **(b)**. However, the mentioned effect and the formation of recirculation zone does not occur when introducing a foam with a larger pore size at the same blockage ratio, e.g., 10 PPI foam, h/H = 0.39 as **Figure 5.5 (c)** and **(d)** shows. As the fluid is flowing inside the 10 PPI foam block, it experiences the resistances caused by ligaments. Hence losing the momentum, the air leaves the foam towards the end of the foam at the downstream region. In this experiment with 0.09 m foam length, the flow has successfully passed through the porous structure of 10 PPI foam towards the rear end, at a very low velocity. However, using a longer foam (Lf > 0.09 m) is not necessarily will exhibit the similar flow behaviours, even though the same blockage ratio and PPI are applied. Instead, the longer foam will provide a higher amount of resistance in the streamwise direction, which may also deteriorate the fluid momentum. From this point, the flow in the 10 PPI foam could eventually experience the similar effects like the 30 PPI foam, with the existence of a recirculation zone or wakes at the downstream region. Therefore, an optimum foam length is also crucial to keep the flow inside the porous region. According to **Figures 5.5** and **5.6**, the downstream flow patterns of different foams could be different depending on the pore

density and blockage ratio. The downstream velocity pertinent to the 10 PPI and 30 PPI foams, with h/H = 0.39, is about 1.6 and 1.8 times higher than that at the inlet. Nevertheless, the flow separation with a high blockage ratio may induce wakes further downstream leading to drastically higher pressure drops. The difference in the free stream velocities and wake patterns for different foam samples also raise a question on the effect of PPI on the pressure drop, which will be discussed later in this section.

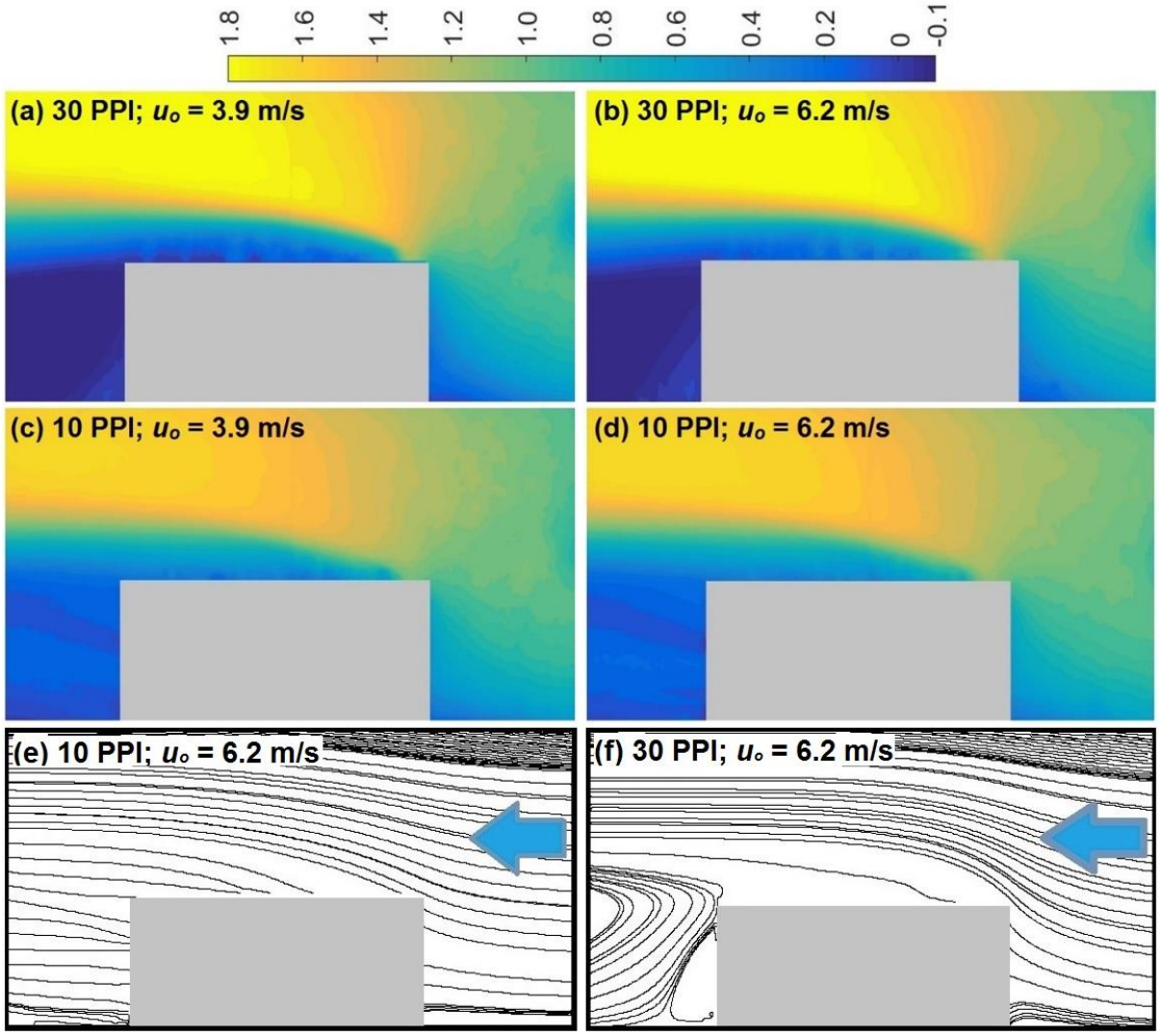

Figure 5.5 Contours of normalized stream-wise velocity, u_s/u_o with h/H = 0.39 at different inlet velocities (a) 30 PPI; u_o = 3.9 m/s (b) 30 PPI; u_o = 6.2 m/s (c) 10 PPI; u_o = 3.9 m/s (d) 10 PPI; u_o = 6.2 m/s and streamlines (e) 10 PPI (f) 30 PPI

One would also expect a circulation zone upstream of a high porosity foam block (ε = 0.97, Darcy number, $Da = 10^{-6}$) in a partially filled channel, as reported by Ghorab [32]. However, our high porosity (ε >0.9) foams exhibit a rather different flow pattern there. As seen, the high porosity of the foam, for 10 PPI with a high blockage

ratio, allow for a smooth passage of the air to the foam without a notable circulation region being form at the entrance to the foam. **Figure 5.6** shows a comparison of velocity profiles between the present study and Sauret et al. [17] at a similar inlet velocity, u_o ~ 6.0 m/s and foam arrangement. The study investigated velocity profiles near the interface and within 10 PPI foam (K = 5.3 x 10^{-7}). Their model considered the standard k-ε turbulence for the non-porous region, Hazen-Dupuit-Darcy law for the isotropic porous medium, and continuity in shear stress for the interface region. As shown in **Figure 5.6**, the simulation data shows negative velocities that represent a recirculation zone at the end of the foam block, which is different than their experimental profile. Interestingly, our 5 PPI trend at the end of the foam is in good agreement with their numerical result of 10 PPI, comparing at the same foam length and blockage ratio. The difference in the velocity probably due to the variations in the permeability and inlet velocity. Even though the plotted velocities are difference, our profiles at the foam inlet are in agreement with their numerical result, in which the velocities near the interface region could be decreased sharply, regardless of PPI and blockage ratio.

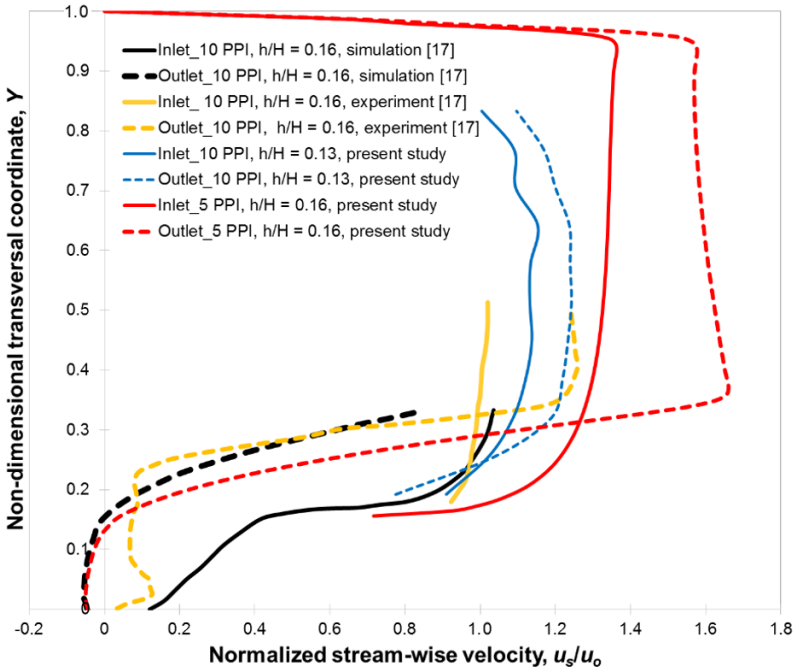

Figure 5.6 Comparison of velocity profiles at the beginning and end of the foam blocks in the partially filled channels

For a low blockage ratio foam such as h/H = 0.05 and 0.13, the result shows insignificant influence on the velocity field in the free stream region, with a small

increment of velocity ($u_s/u_{o,\,max} \leq 1.2$) regardless of the inlet velocity. The effect of the smallest blockage ratio, h/H = 0.05, at the specified inlet velocities is negligible. For the blockage ratio of 0.13, the effect of flow disturbances caused by the ligaments on the foam surface roughness at the horizontal interface plane becomes pronounced in a close proximity to the foam/fluid interface and in the downstream region regardless of the PPI. Low velocity in those regions also suggests the formation of boundary layer and a recirculation zone, which could be visually observed in **Figure 5.7 (b)** and **(d)**. Away from the foam/fluid interface, there is almost no disturbance to the air flow. **Figure 5.7 (a)** shows that the data on the interface region of 30 PPI could not be retrieved using the PIV, possibly due to the flow complexity in that region which influences the intensity of the seeding particles.

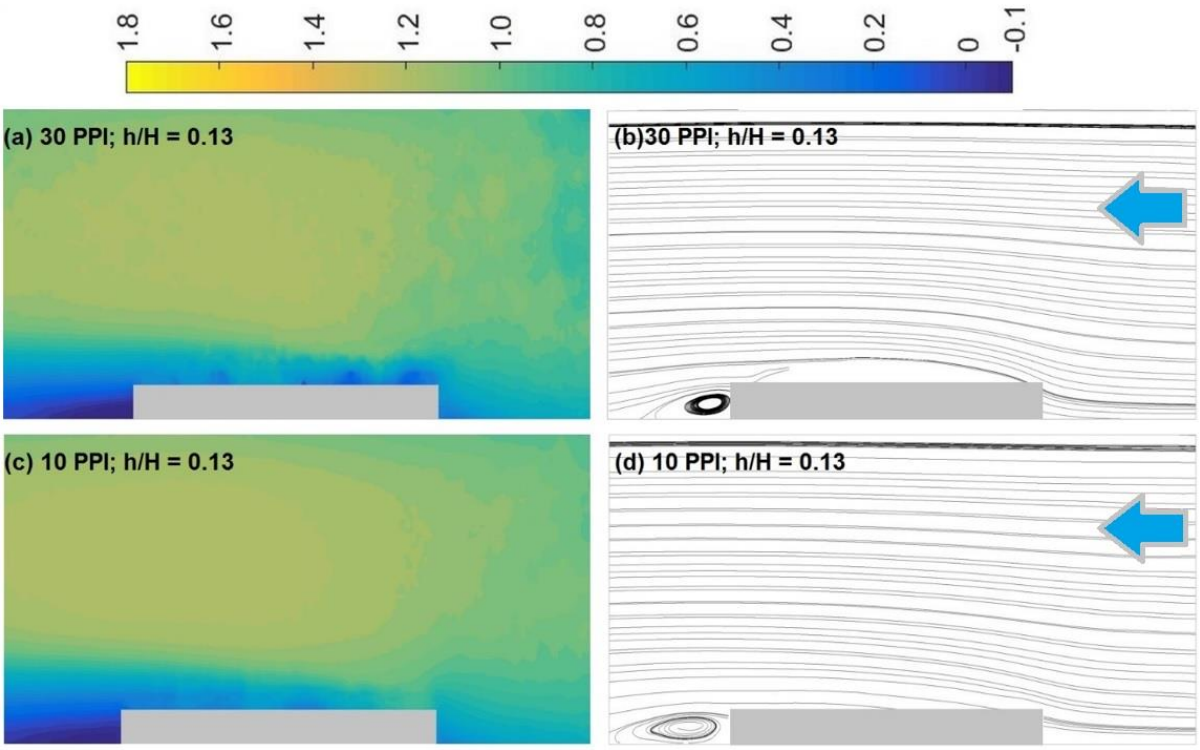

Figure 5.7 Contours of normalized stream-wise velocity, u_s/u_o and streamlines at u_o = 6.2 m/s (a) & (b) 30 PPI; h/H = 0.13 (c) & (d) 10 PPI; h/H = 0.13

Interestingly, a smaller recirculation zone appears at the downstream of the 30 PPI foam compared to the 10 PPI foam. This can be attributed to the tendency of the air inside the 30 PPI foam (with a higher restriction) to leave the foam towards the free stream before reaching the end of foam block. The air is directed and pushed to the foam but once inside, choses the path with lower resistance. That is, it will leave the foam sooner before reaching the end which face the extra resistance posed by the

wake at the back of the foam (depicted by **Figure 5.7 (c)** and **(d)**). Nevertheless, the slight effect of the low blockage ratio (h/H ≤ 0.13) on the whole flow field suggests the requirement of defining a minimum blockage ratio in the design of a partially filled channel to benefit from this unique porous structure.

Figure 5.8 shows the normalized stream-wise velocity in WT-2 with the 5 PPI foam. As seen, a boundary layer forms on the interface of the foam block, similar to the WT-1 case. The formation of the boundary layer is even more pronounced with a higher blockage ratio, h/H = 0.16 m. Interestingly, for the lower blockage ratio, h/H = 0.06, when the inlet velocity is halved (compared to the 12.5 m/s case), to 6.5 m/s, a similar boundary formation pattern is observed as illustrated by **Figure 5.8 (c)**. The inlet velocity in the range of 6.5 to 12.5 m/s leads to indifferent flow pattern effects.

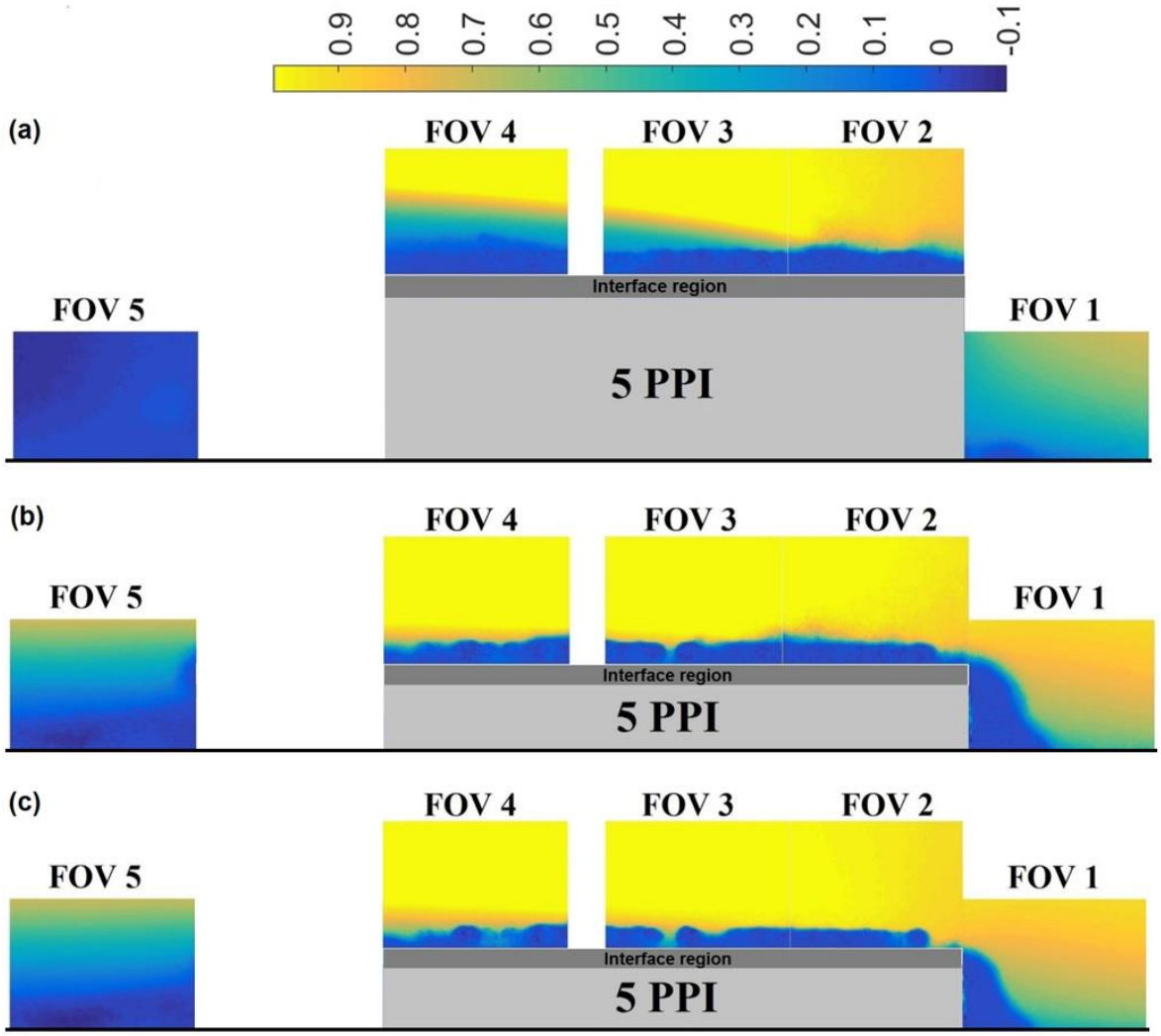

Figure 5.8 Contours of normalized stream-wise velocity, u_s/u_o in WT-2 with 5 PPI foam (a) u_o = 12.5 m/s; h/H = 0.16 m (b) u_o = 12.5 m/s; h/H = 0.06 (c) u_o = 6.5 m/s; h/H = 0.06 (flow direction from right to left)

However, downstream the foams, the effects of blockage ratio on local air flow distribution and patterns is notable. Very low velocity in the downstream region, just after the foam, (**Figure 5.8 (a)**) could be attributed to the formation of a recirculation zone. A slight decrease in the velocity is found close to the leading edge of the foam where the fluid comes across the foam block (FOV2), and the flow splits into two streams, one goes into the free stream and the other goes into the porous region. Furthermore, investigating the FO3 and FOV4 reveals that the fluid velocity in the free stream region, further away from the foam, regains the same value as the inlet velocity. Predominantly, this is the effect of surface roughness, or possibly other factors which could not be discovered with only the FOV from the side wall. The flow pattern of the partially filled section will be discussed further, considering another FOV position and the thermal imaging method later in this section (see **Figure 5.11 – Figure 5.13**).

Figure 5.9 shows the pressure gradient of an empty channel or blockage ratio, h/H = 0, with different inlet velocities. The highest pressure gradient of the empty channel is achieved at the maximum inlet velocity in this study, u_o = 12.5 m/s, as expected. Without the foam block and comparing at a similar inlet velocity, u_o ~ 6.0 m/s, the results show similar pressure gradients for both WT-1 and WT-2 with $\Delta P/L$ < 3 Pa/m, which confirmed the similar test conditions. **Figure 5.9** also shows the pressure gradient for all the foam samples. Due to the presence of the foam block, particularly for high blockage ratio, pressure difference between the upstream and downstream regions are noted. The pressure gradient increases with the blockage ratio, while the pressure drop is affected by the foam PPI for h/H > 0.15, at h/H = 0.39, the pressure drop of 30 PPI foam is higher than that of the 10 PPI foam, regardless of the inlet velocity. On the other hand, the 5 PPI foam with the highest velocity, u_o = 12.5 m/s, shows the highest pressure gradient compared to the other cases. However, at a similar blockage ratio of 0.06, and inlet velocity of 6.5 m/s, the pressure gradient of 5 PPI is higher than those of 10 and 30 PPI foams. The wake formed owing to high PPI foams is big enough to induce significant flow resistance. For low PPI foams, nonetheless, velocity fluctuation at the interface and inside the porous region adds to the complexity of the problem and a unified trend in pressure drop versus PPI cannot be deduced.

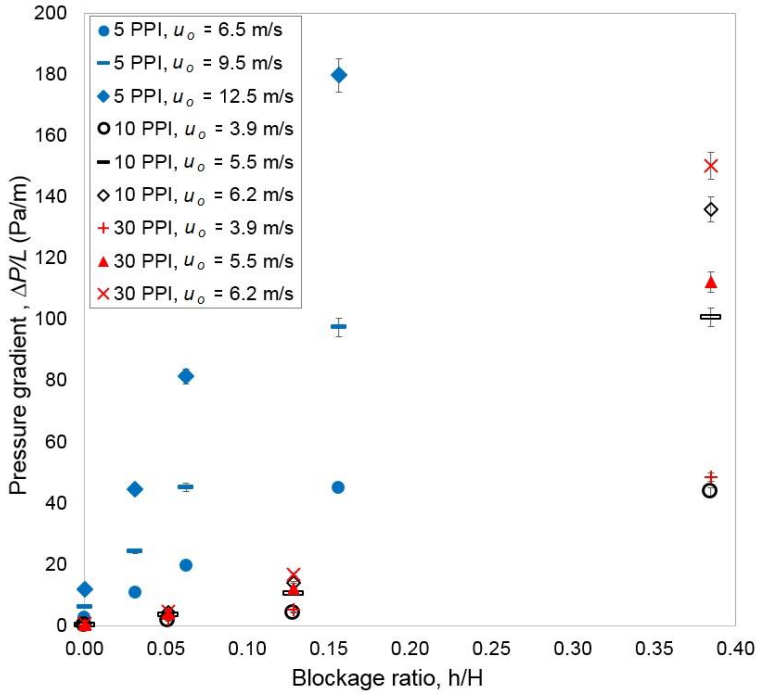

Figure 5.9 Pressure gradient versus blockage ratio

As shown by **Figure 5.4**, the pressure taps were used to measure the pressure drop in the test section with contribution from (1) channel wall frictional losses, (2) flow acceleration due to the reduced cross-sectional area (3) flow deceleration due to the enlarged cross-sectional area and (4) form and skin-friction drags due to the ligaments (core) and also additional losses at the top surface of the metal foam. The measured pressure drop in **Equation (5.1)** can be formulated using head loss and resistance coefficient equations from Ref. [33]:

$$\Delta P = \left(k_{\text{channel}} + k_{\text{entrance}} + k_{\text{exit}} + k_{\text{foam}}\right)\frac{\rho u_o^{\,2}}{2} \qquad \textbf{(5.1)}$$

The first term in the parenthesis, $k_{\text{channel}} = f_1(L/D_h)$ is the channel resistance coefficient which can be modelled using the Darcy-Weisbach equation, where f_1 is the friction factor of the empty channel available in the literature from existing experimental data. The calculated frictional losses are based on the channel walls. However, a part of the channel bottom wall would be replaced by a foam block, yet its effect on the total pressure loss is expected to be very small and negligible. The last term in the parenthesis, k_{foam}, represents the resistance coefficient for the partially filled section. This term, k_{foam}, accounts for the actual porous medium resistance (form, shear and viscous drag terms) as well as minor losses above the foam in the clear (from foam) flow region of the partially filled section.

The resistance coefficients are referring to the pressure difference between the beginning and end of the foam block. The minor losses at the upstream and downstream region are deducted from the total pressure drop, presented as k_{foam}*Dh/Lf, which is the resistance coefficient of the partially filled section, k_{foam}, multiply by the normalized lengths, to consider data from different setups and foam properties. In this study, the foam is considered as a solid block since most of the fluid tends to flow into the free stream region, especially for the low blockage ratios and high PPI foams. By substituting the entrance effects, yet depending on the experimental data, the presented resistance coefficients are slightly overestimated the real condition. These overestimation values are much safer in designing a partially filled heat exchanger, taking account the effects of pressure drop and pumping power. Note that the resistance coefficients reflect the complex constituents that exist in the partially filled section, such as (i) the effects of the air does not flow through the foam block, (ii) the early formation of flow separation or recirculation zone, (iii) the mixing flow inside the porous region and at the interface region of a very high/low PPI foam and (iv) the frictional effects from the interface and internal side of the porous region. These contributions to the resistances are grouped together merely due to difficulty in identifying each constituent.

In a fully filled configuration, the entrance and exit losses are negligible compared the viscous and form drag posed by the metal foam [34]. However, for a partially filled configuration, the pressure drop is always affected by the entrance and exit losses which are comparable to the foam resistance. Thus, a planar restriction or an orifice plate model could be used to identify the pressure losses at the inlet and outlet [35]. For the sake of simplicity, in this study, the entrance and exit losses are simplified by using formulas of resistance coefficient for a sudden contraction and expansion, as shown in **Equations (5.2)** and **(5.3)** [33]:

$$k_{\text{contraction}} = \frac{1}{2}\left[1-\left(\frac{\mathrm{H}-\mathrm{h}}{\mathrm{H}}\right)^2\right]^2 \qquad \textbf{(5.2)}$$

$$k_{\text{expansion}} = \left(1-\frac{(\mathrm{H}-\mathrm{h})}{\mathrm{H}}\right)^2 \qquad \textbf{(5.3)}$$

Thus, **Equation (5.4)** is developed to estimate the resistance coefficient for a foam block, k_{foam}, (including the effect from the free stream region).

$$k_{\text{foam}} = \frac{2\Delta P}{\rho u_o^{\,2}} - f_1 \frac{L}{Dh} - 0.5\left[1-\left(\frac{\text{hf}}{\text{H}}\right)^2\right]^2 - \left(1-\frac{\text{hf}}{\text{H}}\right)^2 \quad \textbf{(5.4)}$$

Figure 5.10 shows the comparison of normalized resistance coefficients for each partially filled section, k_{foam}*Dh/Lf, at different PPIs. Generally, the resistance coefficient increases with the blockage ratio. The highest calculated k_{foam}*D_h/L_f in this study is 1.3, attained by 30 PPI with h/H = 0.39, and u_o = 6.2 m/s. With a significant blockage ratio, the 30 PPI foam shows a higher resistance coefficient compared to the 10 PPI foam, for all different inlet velocities. However, under the same test conditions (h/H = 0.15; u_o = 6.2 m/s), the resistance coefficient of 5 PPI foam block is higher than those of 10 and 30 PPI foam blocks. The resistance coefficient tends to vary with the block size. The resistance coefficient is also increasing with the inlet velocity. This is more pronounced at higher blockage ratios; i.e. when h/H > 0.15.

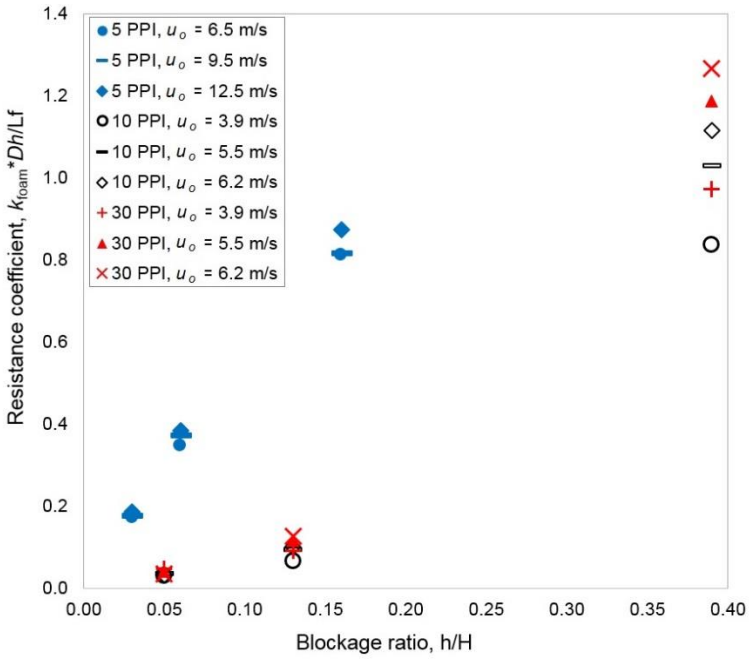

Figure 5.10 Resistance coefficient for the partially filled section versus blockage ratio

This interesting phenomenon (for low PPI foams, e.g., 5 PPI) is well-explained through the results of PIV experiments shown in **Figure 5.11**, which shed light on the flow behaviour at the foam-freestream interface. The results show the flow pattern on a horizontal plane 0.005 m away (in the normal direction) from the interface. FOV 6 presents the incoming flow toward the foam for different inlet velocities. Interestingly, after a certain foam length (approximately, 0.070 m), the magnitude of the stream-

wise velocity drops to zero, as is recognisable in FOV 7. On the specified plane, where the stream-wise velocity is zero, a span-wise velocity component is formed, it is expected that either the flow (1) goes into the porous region or (2) leaves the foam block into the free stream regions. This phenomenon could be observed from **Figure 5.12**, which shows instantaneous images from the PIV experiment. In principal, the submicron seeding particles will accurately follow or represent the fluid flow inside the channel. **Figure 5.12 (a)** displays some of the seeding particles which are entering the foam block, while **Figure 5.12 (b) and (c)** shows the seeding particles are also coming out from the foam interface into the free stream region and flow over the sharp corner of the foam, respectively.

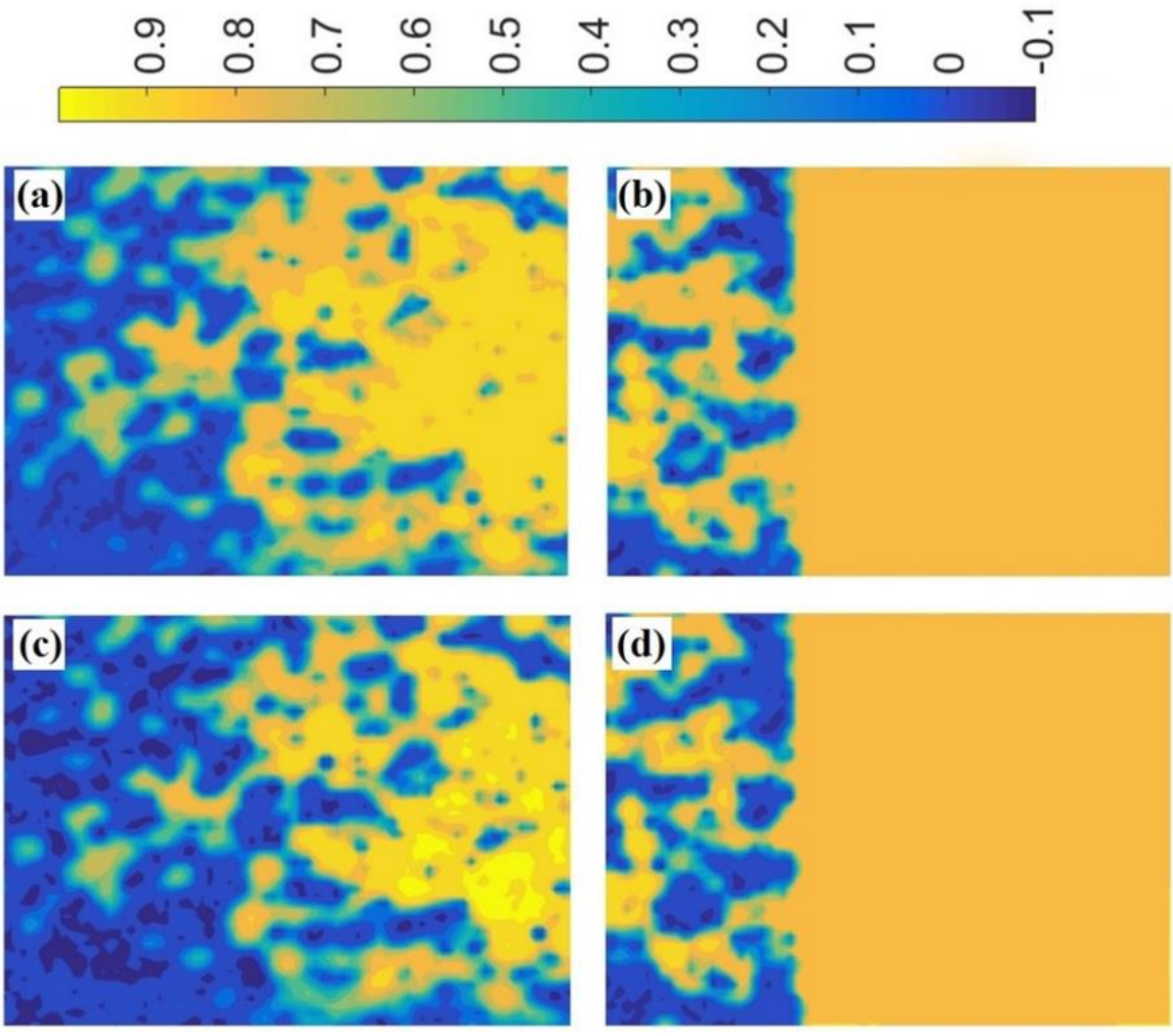

Figure 5.11 Contours of normalized stream-wise velocity, u_s/u_o of 5 PPI foam; h = 0.020 m (a) FOV 7; u_o = 6.5 m/s, (b) FOV 6; u_o = 6.5 m/s, (c) FOV 7; u_o =12.5 m/s and (d) FOV 6; u_o =12.5 m/s (flow direction from right to left)

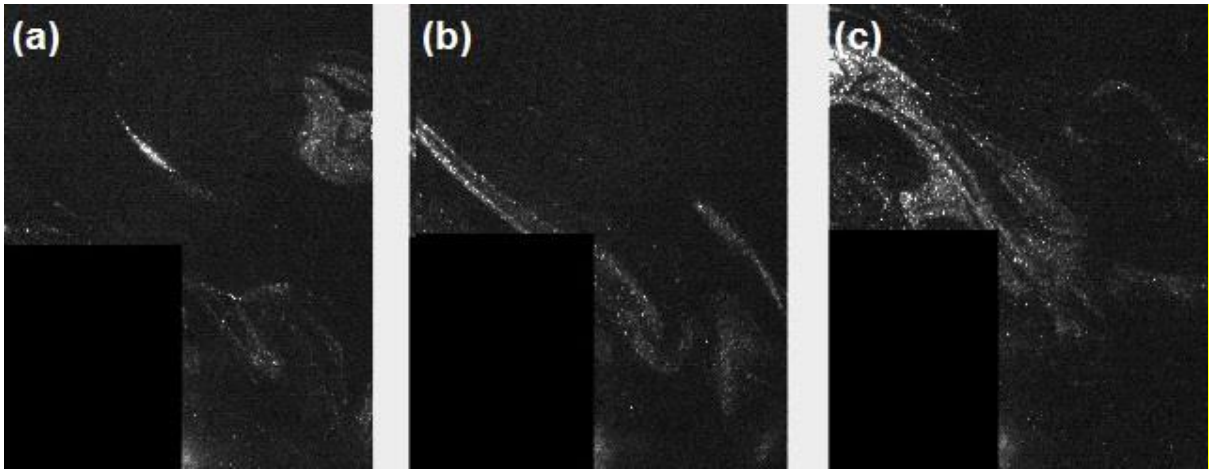

Figure 5.12 Instantaneous images from the PIV experiment (flow direction from right to left)

The spatial fluctuating flow at the interface of 5 PPI foam contributes to a higher pressure drop and resistance coefficient. Thus, we may divide the resistance of a partially filled channel into (1) frictional drag due to the shear stress at the interface and porous structure, as well as (2) pressure drag due to the blockage (considerable shape and size) of the foam block. The details of friction effect and foam surface roughness on the pressure drop and flow regimes have been discussed by Kouidri and Madani [36]. According to those authors, the influence of surface roughness on the pressure drop is significant. Thus, these effects should not be neglected, especially for a partially filled channel with the foam surface exposed to flowing fluid in the free stream region.

Furthermore, **Figure 5.13** clearly demonstrates the flow fluctuation inside the porous structure of the 5 PPI foam. The raw images (**Figure 5.13 (a)** and **(b)**) shows that some of the cells (marked with red circles; Pores ‘a’ in FOV 7 and Pores ‘b’ in FOV 6) which are stretched all the way to the interface provide a passage for the airflow to leave the porous region into the free stream region. The same “escape” phenomenon is not observed in the neighbouring regions due to further restrictions by the ligaments. The pore-ligament layout causes an additional frictional effect from both inside and top surface of the metal foam (surface roughness effects). However, the significance of those two areas is difficult to distinguish at this current stage. As seen, a different flow field and behaviour is observed with high and low PPI foams. For a low PPI foam with a short enough length, at high enough blockage ratio, the large cell size leaves more momentum for the air flow once pushed to the foam end. However, with

a high PPI foam which consists of very small pores, the flowing air tends to choose the less-restricted flow area, e.g., free stream region; and a stagnation region with the trapped air could appear inside its microstructure. In a way, with larger pores the flow retains more momentum to reach the end of the foam once pushed in whereas with smaller pore sizes, higher PPI values, the air in the foam is left with enough momentum only to find the shortcut and move upwards to the interface. This phenomenon involving the porous region is better explained with the results of thermal images.

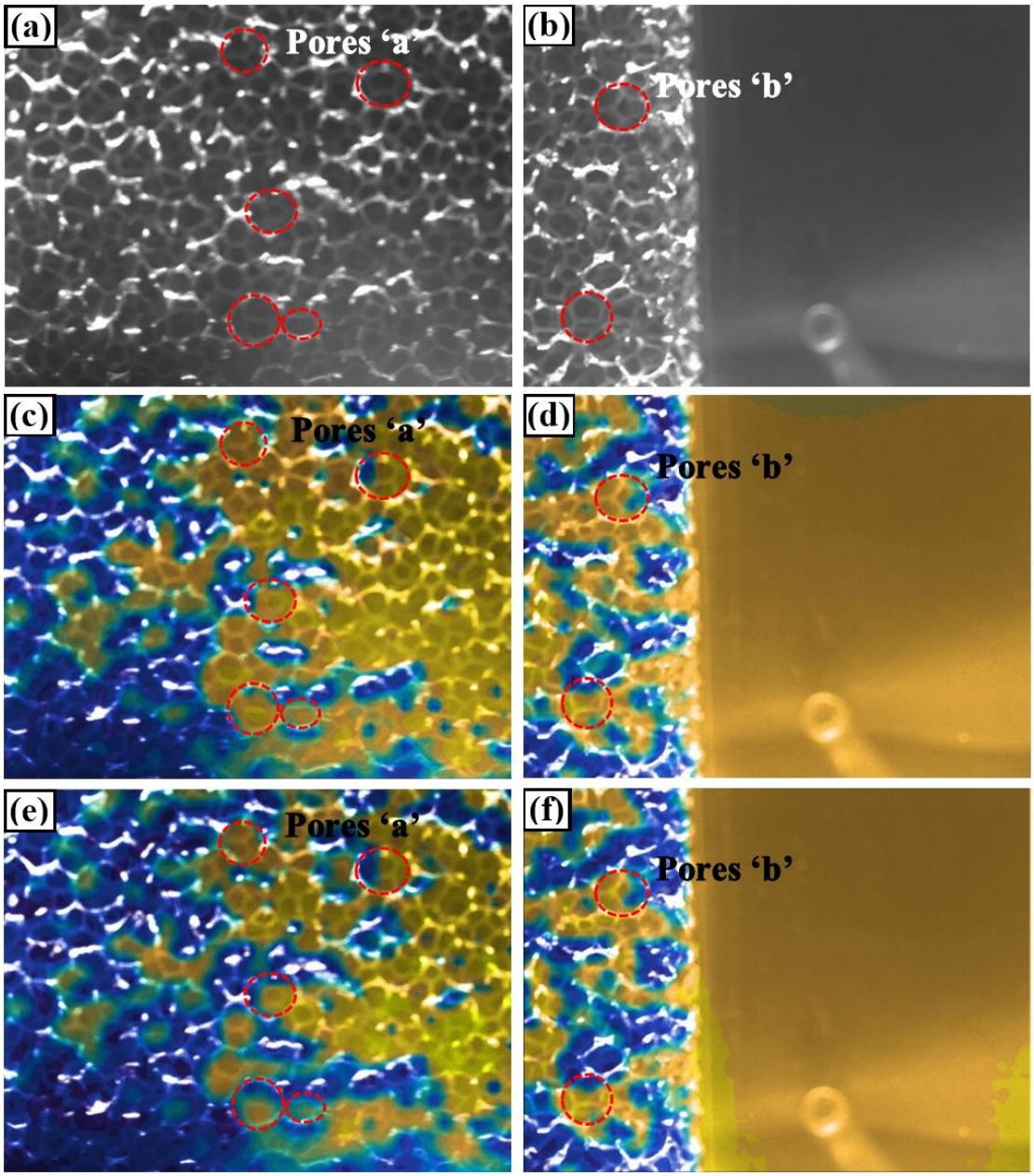

Figure 5.13 Raw images of 5 PPI with h = 0.020 m (a) FOV 7 (b) FOV 6; Overlapped images (c) FOV 7; u_o = 6.5 m/s, (d) FOV 6; u_o = 6.5 m/s, (e) FOV 7; u_o =12.5 m/s, (f) FOV 6; u_o =12.5 m/s (flow direction from right to left)

To comprehend the complex flow behaviour we encountered, the IR thermography was employed to acquire 2-D thermal images which could shed some light on the flow behaviour inside the partially filled channel. The hypothesis is that there would be different temperature distributions in the channel, which are affected by the presence of a metal foam block, depending on the metal foam microstructural and geometrical properties. The hot flow that passes through both the clear and porous regions causes various temperature contours as shown in **Figure 5.14**. However, it is important to note that the temperature distributions are not presenting the exact fluid temperature, but mainly determined by the surface temperature of the foam block. In this case, those areas (neighbouring ligaments) that exposed to the fluid pathways would be heated, distinguishing itself from the unfavourable paths.

Our particular interest is focused on the effects of pore density and blockage ratio, where the thermo-fluid dynamics are studied based on the wall temperature fields. The high emissivity value of the Quartz glass, ~ 0.95, ensures high sensitivity of the IR measurement to provide the thermal images. A region with a higher temperature inside the channel would emit a greater intensity of infrared energy, and vice versa. Besides, our short camera-to-object (wall) distance, [37] allowed us to neglect the influence of ambient on the temperature distributions. The IR image acquisitions were also carried out once the wall temperature (measured using the surface thermocouple) was constant. Thus, the emitted heat radiation from the wall temperature is predominantly due to the effect of the heated flow and the foam block. Interesting flow-features are disclosed based on the temperature distributions throughout the porous structure and interface as shown in **Figure 5.14**.

Clearly, the blockage ratio and the pore density influence the amount of fluid entering the porous structure of the metal foam. There are insignificant differences in the flow pattern for $h/H < 0.15$, regardless of pore density. As the coolant is running on the bottom side of the foam (non-contact and cross-flow direction), those foam temperatures are affected by the coolant temperature. For the insignificant foam heights, most of the flow that coming in contact with the foam block would prefer the non-porous region, causing a stagnant region inside the foam block. With the lowest foam height of 0.004 m (**Figure 5.14 (a)** and **(b)**), the foam itself is insignificant to influence or be affected by the incoming flow, suggesting a need for a minimum foam height in this setup. By increasing the blockage ratio (foam height), the effect of pore

density on the flow pattern within the porous block becomes more obvious. At the highest blockage ratio, h/H = 0.39 in this study, two different flow patterns, pertinent to the two different PPI values, emerge. Smaller pore sizes of the 30 PPI foam make it more difficult for the air to flow through the foam compared to bigger pores of the 10 PPI foam as shown in **Figure 5.14 (e)** and **(f)**, respectively. Interestingly, we can also see how the heated flow of the 30 PPI, h/H = 0.39, tends to leave the porous region, into the free stream region before reaching the end of the porous block. Similarly, for the 10 PPI foam, with the same blockage ratio, the heated flow is able to pass through, until the rear edge of the foam block. The temperature variation on the interface region (**Figure 5.14 (e) and (f)**) confirm that slip velocity exists at the interface between the porous block and the free stream region. This effect is obviously seen with the 30 PPI foam. At a higher vertical distance from the interface, the effect of the foam block (PPI) on the temperatures is almost insignificant. However, different isotherm patterns are noted in **Figure 5.14 (e)** and **(f)**. For the 30 PPI foam, the high amount of heat accumulated at the upstream near the leading edge, shows a massive flow obstruction due to the ligaments. Meanwhile, the highest temperature exists deeper inside of the porous structure in the 10 PPI foam. Furthermore, a stagnation region appears inside the 30 PPI foam with the highest blockage ratio (see **Figure 5.14 (f)**). This proved our theory that a higher PPI foam with greater inner resistances causes the fluid to lose its momentum and exit the porous block before reaching the end. From these two visualization experiments (using PIV and thermal camera), the results show consistency on how the flow would successfully pass through a more porous structure or exiting through the interface when encountering a smaller pore structure at a high enough foam height. The amount of the fluid in the porous region significantly depend on the fluid momentum and the ligament restrictions either in the streamwise or transverse direction. With long enough foam, a stagnant region may appear in the porous structure, regardless of the PPIs. However, introducing a higher fluid velocity may enforce a longer flow distance throughout the significant blockage ratio (foam heights). In another hand, using a very large pore size, for instance, 5 PPI with insufficient foam heights may naturally cause the flow inside the pores to escape through the interface. All these conditions may significantly influence and vary the pressure drop of the systems, including the merit of using a porous structure. Hence,

optimum parameters (considering the blockage ratio, PPI, and air velocity) are crucial for the partially filled channel with metal foam.

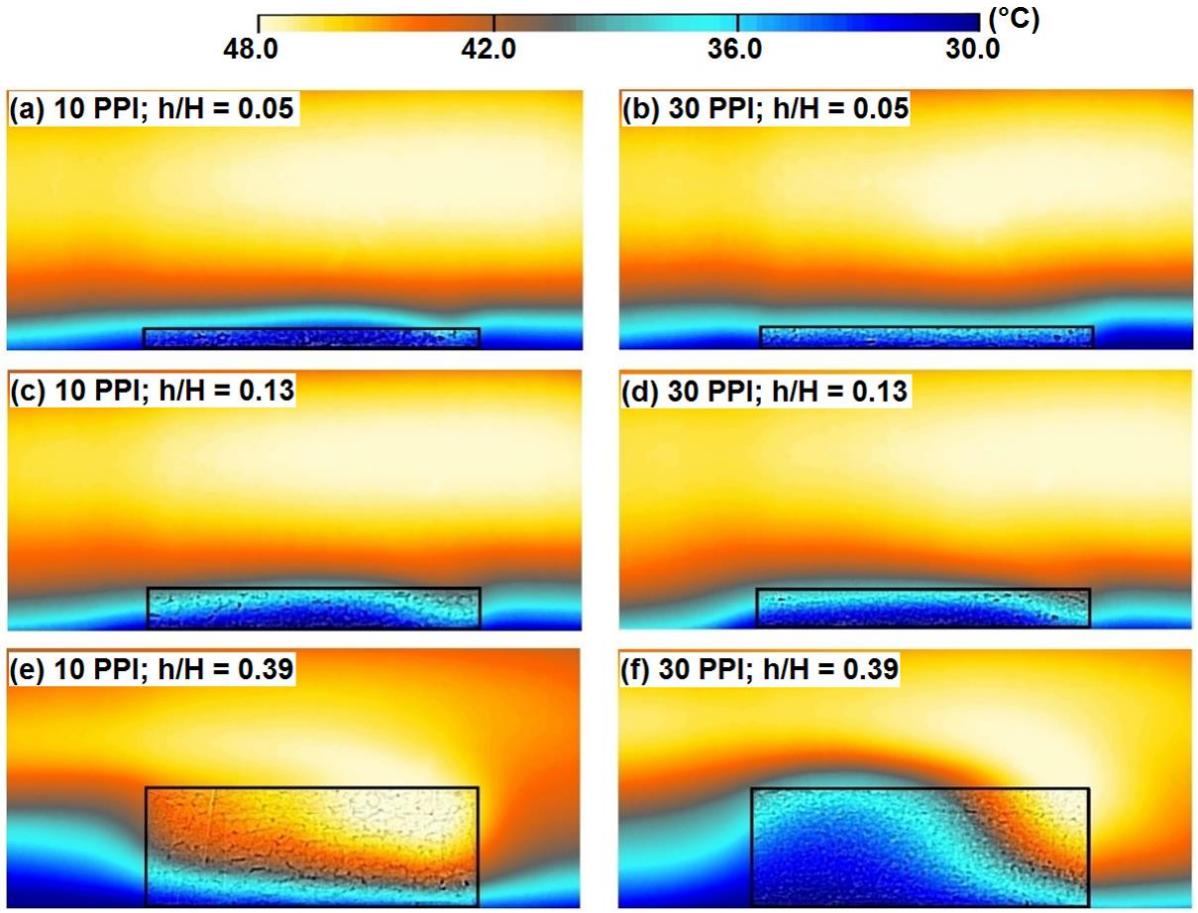

Figure 5.14 Disclosed flow-features based on the temperature fields with 10 and 30 PPI foams at u_o = 3.9 m/s for various blockage ratio (a) 10 PPI; h/H = 0.05 (b) 30 PPI; h/H = 0.05 (c) 10 PPI; h/H = 0.13 (d) 30 PPI; h/H = 0.13 (e) 10 PPI; h/H = 0.39 (f) 30 PPI; h/H = 0.39 (flow direction from right to left)

To understand the flow pattern influenced by the presence of the metal foam using temperature profiles, the temperatures that measured at the normal centreline (see **Figure 5.4)** of the channel (WT-1) are presented in **Figure 5.15**. It shows a dimensionless temperature profile in the partially filled channel, which includes the partially filled section, upstream and the downstream regions, for both 10 and 30 PPI with h/H = 0.39 m/s at the maximum and minimum inlet velocities. An asymmetric temperature profile due to the presence of the metal foam is observed. The pore density influences the temperature profile, especially within the porous region and downstream region, right behind the foam block. As expected, the temperature

distribution is higher inside the 30 PPI foam, particularly with a lower velocity value (**Figure 5.15 (c)**) due to the presence of a stagnation region. The temperature inside the porous region is decreasing in the stream-wise direction for all foam samples and inlet velocities, but obviously observed within the 30 PPI foam.

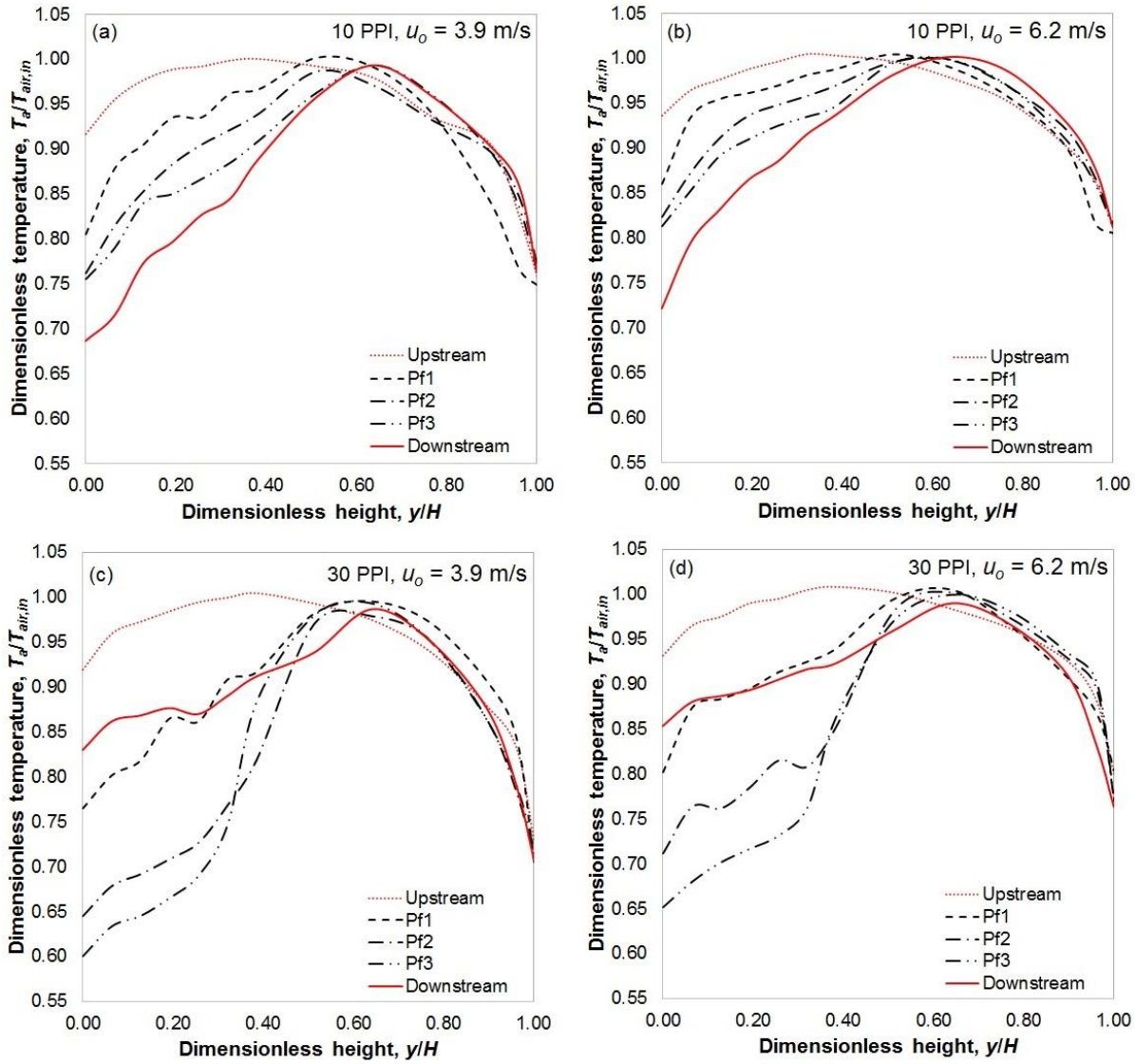

Figure 5.15 Temperature profile in the partially filled channel with metal foam

This is in agreement with the IR images, where more areas with low temperatures are seen in the 30 PPI foam block than the 10 PPI foam. For the temperatures in the proximity of fluid/foam interface, the profiles show that the 30 PPI foam causes irregular temperature trend due to small-pores morphology, while the 10 PPI foam shows a more stable trend; a decreasing temperature (Pf1> Pf2> Pf3) with the increase of the foam length. Far away from the interface (in the free stream region, y/H > 0.6), the temperature profiles are almost similar, regardless of the stream-wise

measurement locations. It is only the free stream temperature profile of the 10 PPI foam at Pf1 (**Figure 5.15 (a)**) that shows slightly lower values, particularly at a lower inlet velocity, u_o = 3.9 m/s. The reason could be due to the porous structure, where a higher amount of the flow goes into the porous region, rather than into the free stream area. This finding shows different temperature effects with different PPIs. In summary, it is important to note that, the influences of the porous block on the temperature distribution is only substantial with a high blockage ratio.

5.4 Conclusion

This study mainly used PIV and IR thermograph as two flow visualization techniques to understand the fluid flow behaviour of partially filled channel with metal foam block. Various pore densities and blockage ratios were considered, and the remarkable conclusions are presented as follows:

(a) A part of the incoming flow goes into the porous foam, but the flow also tends to leave into the free stream region after a certain foam length. This phenomenon occurs only with high enough PPI, foam length and blockage ratio. The results on the interface of fluid/foam suggest a complicated phenomenon, e.g., fluctuating flow velocity and changing in the flow direction, which affects the total pressure drop and resistance coefficient.

(b) The effect of friction inside a porous structure is also significant on the pressure drop of a low PPI foam. This study found that the 5 PPI foam could exhibit a higher pressure gradient as compared to the 10 and 30 PPI foams at a same condition. While the 30 PPI foam would have a higher pressure drop than the 10 PPI foam at a high enough blockage ratio. Thus, optimum pore density, foam length and blockage ratio should be identified for a partially filled channel design.

(c) Variation induced in the temperature distribution of partially filled channel under several variable parameters (blockage ratio, and pore density) have been obtained, qualitatively and quantitatively. A partially filled channel with high blockage ratio significantly influences the temperature distributions. An infrared thermography could be used to disclose interesting flow-features of the partially filled channel with metal foam, under a specific experimental setup.

(d) The development of boundary layer on the foam interface has been observed in this study but it remains as a point for further research, where the effects of various operating conditions and foam properties could be determined. Point-wise measurement, e.g., hot-wire anemometer could be used as an alternative in measuring the velocity near the foam interface.

References

[1] F. Shikh Anuar, M. R. Malayeri and K. Hooman, “Particulate fouling and challenges of metal foam heat exchangers”, *Heat Transfer Engineering*, 38, 7-8, pp. 730–742, 2017.

[2] I. Kurtbas and N. Celik, “Experimental investigation of forced and mixed convection heat transfer in a foam-filled horizontal rectangular channel”, *International Journal of Heat and Mass Transfer,* 52, 5–6, pp. 1313–1325, 2009.

[3] S. Mancin, C. Zilio, A. Cavallini and L. Rossetto, “Heat transfer during air flow in aluminum foams”, *International Journal of Heat and Mass Transfer*, 53, 21–22, pp. 4976–4984, 2010.

[4] S. Mancin, C. Zilio, A. Diani and L. Rossetto, “Air forced convection through metal foams: Experimental results and modeling” *International Journal of Heat and Mass Transfer*, 62, pp. 112–123, 2013.

[5] N. Dukhan and K. Patel, “Effect of sample’s length on flow properties of open-cell metal foam and pressure-drop correlations”, *Journal of Porous Materials*, 18, pp. 655–665, 2011.

[6] W. Lu, T. Zhang and M. Yang, “Analytical solution of forced convective heat transfer in parallel-plate channel partially filled with metallic foams”, *International Journal of Heat and Mass Transfer*, 100, pp. 718–727, 2016.

[7] Y. Mahmoudi and N. Karimi, “Numerical investigation of heat transfer enhancement in a pipe partially filled with a porous material under local thermal non-equilibrium condition”, *International Journal of Heat and Mass Transfer*, vol. 68, pp. 161–173, 2014.

[8] Y. Mahmoudi, N. Karimi and K. Mazaheri, “Analytical investigation of heat transfer enhancement in a channel partially filled with a porous material under local thermal non-equilibrium condition: Effects of different thermal boundary conditions at the porous-fluid interface”, *International Journal of Heat and Mass Transfer*, vol. 70, pp. 875–891, 2014.

[9] Y. Mahmoudi and M. Maerefat, “Analytical investigation of heat transfer enhancement in a channel partially filled with a porous material under local thermal non-equilibrium condition”, *Int. J. Therm. Sci.*, 50, 12, pp. 2386–2401, 2011.

[10] N. Karimi, Y. Mahmoudi and K. Mazaheri, “Temperature fields in a channel partially filled with a porous material under local thermal non-equilibrium condition - An exact solution”, *Proc. Inst. Mech. Eng. Part C J. Mech. Eng. Sci*., 228, 15, pp. 2778–2789, 2014.

[11] B. Buonomo, A. Diana, O. Manca and S. Nardini, “Numerical investigation on natural convection in horizontal channel partially filled with aluminium foam and heated from above”, *J. Phys. Conf. Ser*., 923, 012049, 2017.

[12] A. Hamadouche, R. Nebbali, H. Benahmed, A. Kouidri and A. Bousri, “Experimental investigation of convective heat transfer in an open-cell aluminium foams”, *Exp. Therm. Fluid Sci*., 71, pp. 86–94, 2016.

[13] M. Sener, A. Yataganbaba, and I. Kurtbas, “Forchheimer forced convection in a rectangular channel partially filled with aluminium foam,” *Exp. Therm. Fluid Sci*., 75, pp. 162–172, 2016.

[14] B. Buonomo, M. Oronzio, S. Nardini and L. Guy, “Experimental investigation on mixed convection in horizontal channels heated below and partially filled with aluminium foam”, in *8th World Conference on Experimental Heat Transfer, Fluid Mechanics and Thermodynamics*, Lisbon, Portugal, 2013.

[15] Z.-B. Liu, Y.-L. He, Y.-F. Yang and J.-Y. Fei, “Experimental study on heat transfer and pressure drop of supercritical CO_2 cooled in a large tube”, *Int. J. Heat Mass Transf*., 85, pp. 679–693, 2015.

[16] M. Tajik Jamal-Abad, S. Saedodin and M. Aminy, “Experimental investigation on the effect of partially metal foam inside the absorber of parabolic trough solar collector”, *Int. J. Eng*., 30, 2, pp. 281–287, 2017.

[17] E. Sauret, I. Ashtianti Abdi and K. Hooman, “Fouling of waste heat recovery: Numerical and experimental results”, in *19th Australasian Fluid Mechanics Conference, Melbourne, Australia*, 2014.

[18] K. Hooman, “Thermohydraulics of porous heat exchangers: full or partial blockage?”, in Proceedings of the 5th International Conference on Porous Media and its Applications in *Science and Engineering* (ICPM5), Kona, Hawaii, 2014.

[19] A. V. Kuznetsov, “Analytical investigation of the fluid flow in the interface region between a porous medium and a clear fluid in channels partially filled with a porous medium”, *Appl. Sci. Res*., 56, 1, pp. 53–67, 1996.

[20] M. K. Alkam and M. A. Al-Nimr, “Transient non-Darcian forced convection flow in a pipe partially filled with a porous material”, *International Journal of Heat Mass Transfer*, 41, 2, pp. 347–356, 1998.

[21] M. K. Alkam and M. A. Al-Nimr, “Solar collectors with tubes partially filled with porous”, *J. Sol. Energy Eng. Trans. ASME*, 121, pp. 20–24, 1999.

[22] L.-W. Fan and H.-Q, Jin, “Local thermal non-equilibrium during melting of a paraffin filled in an open-cell copper foam: A visualized study at the pore-scale”, *J. Heat Transf*., 139, 3, pp. 034505, 2016.

[23] H.-Q, Jin, L. –W. Fan, M.-J. Liu, Z.-Q. Zhu and Z.-T. Yu, “A pore-scale visualized study of melting heat transfer of a paraffin wax saturated in a copper foam: Effects of the pore size”, *International Journal of Heat and Mass Transfer,* 112, 39 – 44, 2017.

[24] Y. Yao, H. Wu, Z. Liu and Z. Gao, “Pore-scale visualization and measurement of paraffin melting in high porosity open-cell copper foam”, *Int. J. Therm. Sci*., 123, 73-85, 2018.

[25] M. W. Brandon and L. S. Barton, “Uncertainty on PIV mean and fluctuating velocity due to bias and random errors”, *Measurement Science Technology*, 24, 035302, 2013.

[26] A. Sciacchitano and F. Scarano, “Elimination of PIV light reflections via a temporal high pass filter”, *Measurement Science Technology*, 25, 084009, 2014.

[27] J. Soria, “An adaptive cross-correlation digital PIV technique for unsteady flow investigation”, in *1st Australian Conference on Laser Diagnostics in Fluid Mechanics and Combustion*, Sydney, NSW, pp. 29–45, 1996.

[28] R. J. Adrian and J. Westerweel, Particle Image Velocimetry. New York: Cambridge University Press, Cambridge, 2011.

[29] M. P. Orihuela, F. Shikh Anuar, I. A. Abdi, M. Odabaee and K. Hooman, “Thermohydraulics of a metal foam-filled annulus”, *Int. J. Heat Mass Transf*., 117, pp. 95–106, 2018.

[30] M. Odabaee, S. Mancin and K. Hooman, “Metal foam heat exchangers for thermal management of fuel cell systems – An experimental study”, *Exp. Therm. Fluid Sci*., 51, pp. 214–219, 2013.

[31] “FLIR T600sc-Series Infrared Camera.” [Online]. Available: http://www.flir.com.au/science/display/?id=46818. [Accessed: 11-Jan-2018].

[32] M. G. Ghorab, “Modeling mixing convection analysis of discrete partially filled porous channel for optimum design”, *Alexandria Engineering Journal*, 54, 4, pp. 853–869, 2015.

[33] “Flows of fluids,” Crane Company, United States, 2010.

[34] V. V. Calmidi, “Transport phenomena in high porosity fibrous metal foams”, Thesis, University of Colorado, 1998.

[35] C. Naaktgeboren, P. S. Krueger and J. L. Lage, “Inlet and Outlet Pressure-Drop Effects on the Determination of Permeability and Form Coefficient of a Porous Medium”, *J. Fluids Eng*., 134, pp. 1–8, 2012.

[36] A. Kouidri and B. Madani, “Mechanics of materials experimental hydrodynamic study of flow through metallic foams: Flow regime transitions and surface roughness influence”, *Mechanics of Materials*, 99, pp. 79–87, 2016.

[37] M. Imran, M. N. Hamidreza and J. S. Ruud, “Application of infrared thermography for temperature distributions in fluid-saturated porous media”, *Arab J Geosci*, 9, 318, 2016.

Chapter 6: Experimental Study of Particulate Fouling in Partially Filled Channel with Open-Cell Metal Foam

This study experimentally investigates particle transport and deposition processes in a partially filled channel with an open-cell metal foam. Various blockage ratio (a ratio of foam height and channel height) in range of 0.05 to 0.39, and pore density (10 and 30 PPI) were used to determine the effects of the foam microstructure and exterior shape on the propensity of fouling. In-situ observations were conducted using a high-speed camera to determine the particle trajectory and velocity in the partially filled channel. Result shows a complex transport and deposition process, which significantly influenced by the particle size and pore diameter. If merely consider the exterior shape of the foam, a higher blockage ratio causes more deposition in the upstream region. While, a low blockage ratio causes more deposition on the top surface of the foam block, regardless of pore density. These results demonstrate that the foam arrangement and heights play primary roles in influencing the preferential deposition areas, which originally associated with flow behaviours in the partially filled channel. Interestingly, the microstructure of the metal foam is not only blocked and trapped the particles, yet causing the breakage of particle clusters. These particles either disperse within the incoming flow or causing more depositions on the foam surfaces. The building up deposits would increase the pressure drops, as expected, but the effects of pore density become insignificant over time.

Nomenclature

d	diameter (m)
D50	50% of the particles in the sample > $\overline{d_p}$
$\overline{d_p}$	average particle diameter (m)
f#	lens f-number
FOV	field of view
fps	frame per seconds
h	foam height (m)
H	channel height (m)
h/H	blockage ratio

k	thermal conductivity (W/m·K)
L	pressure taps distance (m)
Lf	foam length (m); Lf = 0 = leading edge
lpm	litre per min
N	number of sample size
ΔP	pressure drop (Pa)
PPI	pore per inch
Re	Reynolds number
ROI	region of interest
t	recording duration (s)
u	velocity (m/s)
u_o	inlet velocity (m/s)
$\bar{u}$	average velocity (m/s)
wf	foam width (m)
x	streamwise position (m)
X	FOV streamwise length (m)
y	transversal position (m)
Y	FOV transversal length (m)
Subscripts	
p	particle
Dh	hydraulic diameter (m)
Greek symbols	
ε	porosity
ρ	density (kg/m^3)

6.1 Introduction

Open-cell metal foam heat exchangers have been studied extensively as their porous structures demonstrate a tendency to overwhelm the existing heat exchanger thermal performances. Their superior performances under a clean environment have been discussed in many literatures [1], [2], attributed to their pore-ligament constructions that provide large heat transfer area per unit of volume, excellent flow mixing and high thermal conductivity material. The foam microstructures provide tortuous flow path [2] and may act as turbulence promoters [3] which could either (i) reduce fouling from particle re-entrainment or (ii) increase fouling rates because of turbulence impactions. To explore these possibilities, the metal foam performances

are investigated further under a fouled condition such as exhaust gas recirculation (EGR) cooler [4], and air-cooled heat exchanger [5–7]. Until recently (2018), most of the published literature on the fouling of metal foam were performed numerically [5], [7–9] and analytically [3], [10]. While, the existing experimental studies [4], [11], [12] did not elaborate on the underlying mechanisms of fouling in details. However, there exists an attempt to understand fluid-particle physics and the propensity of fouling for the complicated foam microstructures by applying an idealized porous media [13].

Muley et al. [14] in their study on the metal foam as an alternative to a conventional wavy plate-fin heat exchanger in the EGR application found that the foam could have better thermal effectiveness but at the expenses of high pressure drop. The authors also suggested for further investigations under a fouled condition, as the inherent random cell structures of the metal foam may susceptible to fouling. However, Hooman and Malayeri [4] positively argued that an appropriate foam design could achieve a superior thermal performance at a reasonable pressure drop as compared to no-foam cases. They found that the low pore density foam; 20 PPI would have a higher pressure drop than 40 PPI foam, before reaching a similar value after four hours soot injection. While, a thicker foam (foam height, h = 4 mm) would only have a higher pressure drop than 3 mm foam after two hours exposure. Besides, they found the heat transfer of the same PPI foams with different heights remain the same, but the 20 PPI foam would perform better than 40 PPI foam. Odabaee et al. [5] used ANSYS software to model a uniform deposition layer on a metal foam-wrapped tube bundle. Their result shows that the pressure drops of the fouled metal foam would increase up to 44% as compared to its clean condition even with only 0.01 mm deposition thickness. However, they only found remarkable increments of thermal resistances at a higher deposition thickness, e.g., 0.1 and 0.2 mm, while the thermal resistance of 0.01 mm deposition layer is insignificant, regardless of inlet velocity from 1 to 7 m/s. Hooman et al. [3] considered a cubic cell model in investigating the effects of particle deposition in a metal foam heat exchanger. Their result shows that the pressure drop of a fouled metal foam could be increased up to three-order magnitude higher than its clean condition, which is more evident with the high pore density foam. The authors [3, 5] stated that the dominant mechanisms in their studies are the gravitational force and inertial impaction because of the large particle size (10 - 400 μm) and the ligament restrictions. Even though their studies assumed a uniform distribution of particle

deposition, they suggested for further investigations as the metal foam imposes continuous changes of pressure, velocity and temperature profiles.

Like Odabaee et al. [5], Sauret et al. [6] also numerically studied the particle deposition on a single-row metal foam-wrapped tube bundle based on the same geometry of a real metal foam [15]. However, Sauret et al. [6] injected 5000 soot particles (ρ = 2000 kg/m^3, 10 μm ≤ d_p ≤ 250 μm) rather than assuming a uniform particle deposition. The authors applied a Lagrangian particle-tracking model and considered the possibilities for the particles to rebound and stick to the tube wall. The result shows that the heat transfer coefficient decreases with the increase of pore density (5 to 50 PPI), but showing different values at the front tube (up to 15 W/m^2.K) and rear region (3.0 W/m^2.K). Consequently, a higher deposition and particle volume fraction are observed at the front tube as compared to the rear region. Besides, a large recirculation zone and weak backward velocity at the rear region causes difficulty carrying the particles back to the rear wall. Sauret et al. [9] extended their study [6] by investigating the effects of different particle size distribution and preferential particle deposition area in the same foam configuration. Similarly, more particles deposit in the front region and only small particles (d_p< 20 μm) deposited in the rear regions. They also found most of the particles trapped within the porous structure, rather than moving towards the tube wall.

It is worthy to mention that Kuruneru et al. [7], [16–18] have reported most of the fouling studies on the metal foam heat exchangers. However, their works mostly involved numerical approaches or experiments with idealized metal foams. For example, Kuruneru et al. [16] investigated 500 μm wood-dust deposition in five idealized porous channel configurations with different porosities, ε from 72 to 93%. Their result shows that the deposition could be increased by decreasing the porosity. They also found a higher particle deposition at the leading edge of obstacles (idealized ligaments) than the trailing edge. They stated that the inertial impaction is more profound at the leading edge as compared to the gravitational effects. Also, their numerical result of velocity vector using ANSYS Fluent agrees with the preferential deposition areas in the experiment. In another study, Kuruneru et al. [17] used OpenFOAM software and soft-sphere discrete element method to study the transport mechanisms of the sandstone and sawdust ($\overline{d_p}$= 35 ± 10 μm) in circular obstructions (ε = 0.9). The sandstone particles show a higher deposition fraction and pressure drop,

while the sawdust deposition is insignificant and could be neglected. Their numerical pressure drop shows a good agreement with a modified Darcy equation. The inertia and gravitational sedimentation are the dominant mechanisms for the high density particle; sandstone, while particle interception is more profound with the sawdust because of its lower inertia.

Kuruneru et al. [18] used a finite volume method and discrete element method (FVM-DEM) to study fouling on an array of a circular cylinder. They assumed a laminar and isothermal condition, where only drag and gravitational forces were considered as the transport mechanisms for 50 and 70 µm particles. The result shows no deposition for the smaller particles, regardless of the injection rate, while the larger particles tend to clog the pores. A higher injection rate causes more clogging within the porous structure, particularly for 70 µm, which results in a lower porosity than 50 µm. The findings show that the deposition fraction and pressure drop increase linearly, and they justified the variation of data over time due to fouling layer thickness and surface area of the particle itself. Using idealized Weaire-Phelan metal foam geometry, Kuruneru et al. [7] attempted to model a real metal foam. The findings show only the pressure drop at low inlet velocity (u_o< 1.0 m/s) is successfully modelled through this method. They also assured that regardless of different porosities (ε = 0.95 and 0.98) and ligament thickness (0.09 and 0.17 mm), the foam microstructures are always susceptible to fouling.

Therefore, understanding the underlying mechanisms is important to come out with a proper foam design. This experimental study is conducted to shed light on the particle transport and deposition processes in a partially filled channel with metal foam. This includes the determination of particle preferential deposition area in that configuration. The fouling effects on the pressure drop performance are also determined. This study focuses on the influence of foam itself, while the other contributing factors, e.g., inlet velocity, temperature gradient, and particle injection rate are kept constant.

6.2 Experimental Setup

6.2.1 Test rig and measurements

A series of experiments were performed in a small blown-type wind tunnel, consists of (1) blower, (2) heater, (3) particle injector (4) test section (5) filter and (6) flexible exhaust duct

as shown schematically in **Figure 6.1**. The ambient air was sucked through the blower, to pass through the heater and the settling chamber before entering the test section. The test section size is 0.078 m (H) x 0.10 m (W) x 0.35 m (L_c), which partially filled with an open-cell metal foam block (Figure 2). The test section walls are made of transparent glass (Quartz) that provide optical access to the flow. The incoming air velocity is set to 6.2 m/s by downsizing the size of the inlet tube using a gauge valve [19] with the Reynolds number (Re_{Dh}) of an empty channel is 35,000. Accordingly, the experiments were conducted in a turbulent flow. The details of the wind tunnel can be found in Ref. [20]. A fouled condition was created by injecting solid particles (see Section 2.2) at 1.67 x 10^{-5} kg/s using a vibratory feeder (Fritsch – Laborette 24). To make sure the particle can be dispersed uniformly across the partially filled section, the particle injector is positioned about 1.0 m far away from the test section, right before the settling chamber. In addition, the tip of the injector was inserted exactly at the middle of the cross-sectional area of the rectangular channel. The injected particles travelled from the beginning of the settling chamber and passed through the test section. Some of them could be caught in the filter at the end of the exhaust duct, while the others may deposit on the neighbourhood surfaces, e.g., foam block and test section/channel walls.

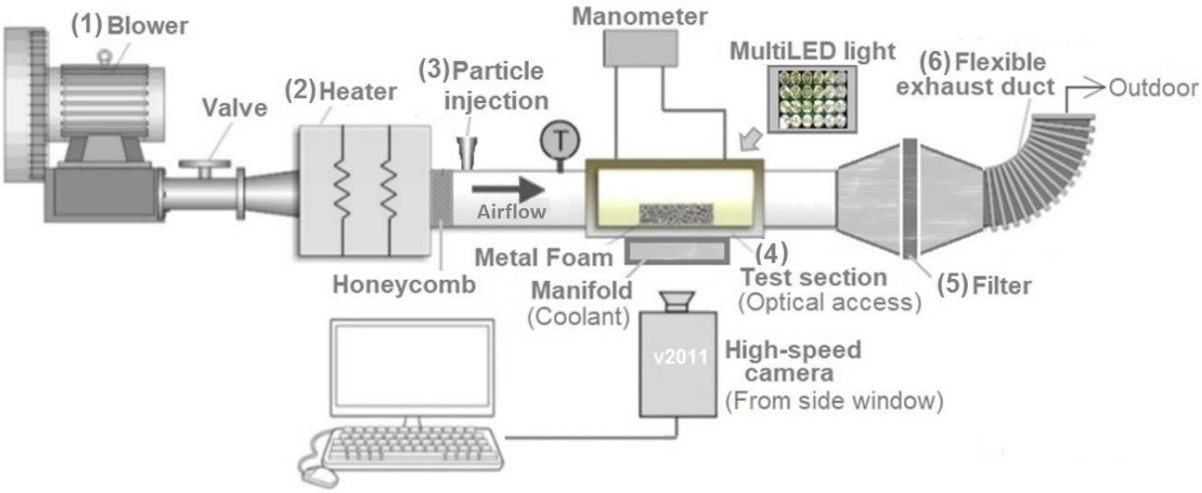

Figure 6.1 Test rig with high-speed camera setup

The most difficult task in conducting the fouling experiment is to conduct the same experiment multiple times due to massive time and cost consumptions. In this study, the settling chamber and the channel are purposely made of glass material. It is also designed to be easily dismantled, with an opening on the top wall of the test section. These designs allow us to clean all the particles in the settling chamber and the test section before repetitive experiments could be conducted. Three repetitive experiments were conducted for the highest and lowest blockages. A new foam sample was used for each experiment. However, it is important to note that it is

impossible to have the first deposition on the same place within the porous structure. However, taking into account the whole deposition processes under the same operating conditions, the particle preferential deposition areas are still the same, regardless of the blockage ratios. Also, the statistical analysis to ensure the repeatability of the experiments was conducted in term of pressure drop comparison, with less than ±6% deviation is found between those three repetitive experiments at the maximum injection period, t = 240 min.

A high-speed camera (Phantom v2011) was used to follow and study the particles movements when they were crossing the test section. Using the camera with Nikon mount lens (f = 50 mm, and maximum aperture, f/2.8), video recordings were acquired at 10,000 fps, with a resolution of 1024 x 768 pixels and exposure time of 30 µm. The recordings capture the particle movements over a two-dimensional plane of 0.195 m x 0.070 m field-of-view that is perpendicular to the camera position (located at one side of the test section). The camera was connected to a host computer, and Phantom Camera Control Software (PCC) was used to control the camera operation. Two multi-LED lights were mounted from both sides of the camera to obtain a clear view inside the test section. In this study, the particle movements are expected to be primarily one-dimensional, following the main flow direction [21]. A short period of recordings (less than 30 minutes) was considered to avoid visual restrictions due to deposition of particles on the walls.

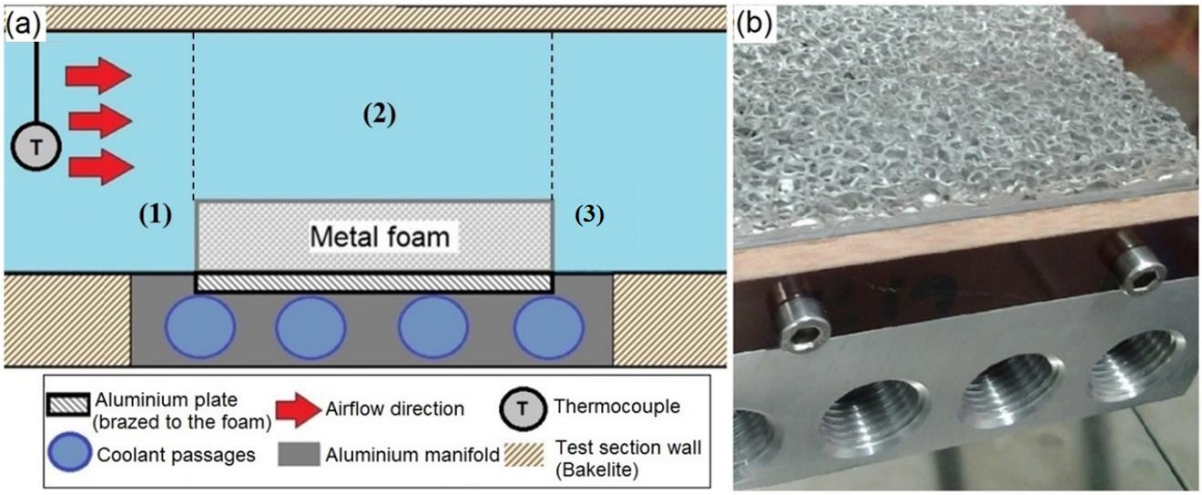

Figure 6.2 (a) Cross-section of the test section with three ROIs (b) Partially filled section with a foam block - ROI 2

A refrigerated circulator (Julabo F25) was used to circulate coolant (50:50 water/ethylene glycol; 20°C) in a closed loop at the bottom of the foam block to cause a thermophoretic deposition. The air gaps between the foam and aluminium manifold were eliminated by applying a thin layer of thermal conductive silicone paste (Omegatherm-201; k = 2.3 W/m·K). The heater (3.0 kW) was also operated to increase the flow inlet temperature, $T_{air,in}$ from room temperature to 60°C. All thermocouples (Type-K) were connected to a data logger (Omega RDXL8; accuracy: ±0.5°C). The particles were only injected after a steady state has been reached. It is when the temperature readings did not vary more than 0.5°C during five-minute intervals. This took approximately 20 to 30 minutes depending on the flow velocity. Besides the in situ observation experiment, this study also conducted pressure drop measurements to understand the effects of fouling over time. Pressure taps (Sensirion, SDP-600 series; accuracy: ±3%) were installed at the upstream and downstream of the foam block (L = 0.25 m). The measurements were taken at 30-minute intervals up to 240 minutes. The data are presented as a normalized pressure drop, $\Delta P_{fouled}/\Delta P_{clean}$, which is defined as pressure drop time-dependent values divided by the pressure drop under a clean condition. The pressure drop data under the clean condition is obtained from our previous study [22].

Ideally, a very long period experiment or an asymptotic fouling condition could not be used to distinguish the effects of a porous structure. Furthermore, the foam structures are expected to be completely covered with the particles, as found in Ref. [12]. In that case, understanding the morphology of the outer deposits layers are more important, instead of what buried inside for any possibility of mitigation and re-entrainment. Nevertheless, the present study was also conducted with the aims to determine the particle preferential deposition areas from the beginning of the fouling process and monitoring the process of particle removal, if there is any. The recorded videos are imported, and the particle size, trajectory, and velocity through those three regions; ROI 1, 2 and 3 (see **Figure 6.2** (a)) are determined using Trackers software. This study considered the upstream (ROI 1) and downstream (ROI 3) regions are about 0.02 m and 0.07 m from the leading and rear edges of the foam block, respectively. These limited distances provided an acceptable resolution to obtain more accurate data, e.g., the particle size and particle travelled distance. The partially filled

section (see **Figure 6.2** (b)), where a foam block was positioned is called as ROI 2 in this study.

Note that, one of the main uncertainties in using the high speed camera is particle-position uncertainty [23], which would affect the results of particle trajectory and velocity. This study calibrated the video recordings/images using an image of a known object dimension [21]; a millimetre-ruler in this case. The image was used to determine the representative length of a pixel. The analyses were started with the adjustment of image sequences' brightness and sharpness to clearly identify individual particles. The two-dimensional velocity was also calculated based on the difference in a particle's position in two consecutive video frames, divided by the time interval between the frames. At least 100 particles were analysed for a statistical determination of the average particle velocity [23]. This study attempts to understand the effects of upward flow from the high blockage ratio and high PPI foam [20] on the particle velocity in the free stream region. In that case, Lf = 0.030 m is selected as a reference point. This study used an average sample size, N = 50 for every 0.010 m increments in the transverse direction. Also, the maximum uncertainty of the particle velocity is ±1.2 m/s when using propagation of errors for those data obtained between two frame rates [23]. For a better understanding of the particle transport, some overlapping trajectories are purposely omitted, presenting only the average size particles of 300, 500 and 700 µm (±100 µm).

6.2.2 Foulant and metal foam properties

This study used calcium carbonate ($CaCO_3$) to investigate the particulate fouling in the porous structure. These particles were selected for their speckling and brightness features to match the grayscale images of the high-speed camera. They were supplied by Omya Australia Pty. Limited [24] and their particle size distribution, and SEM image are shown in **Figure 6.3 (a)** and **(b)**, respectively. The particle size is ranging from 0.5 to 8 µm with the mean diameter, $\overline{d_p}$ is 1.8 µm (D50) [24]. However, it was noted during experiments the particles can easily agglomerate as moving through the particle feeder and the settling chamber. Our on-line data (video recordings) shows a larger particle size distribution in the air motion, up to 700 ± 100 µm. These equivalent particle sizes were determined from their projected area diameter [25] in the two-dimensional plane. For the sake of simplicity, the particle shape was assumed

spherical, where the effects of particle polydispersity and irregularities (**Figure 6.3 (b)**) are neglected in this study.

Note that there are also fine particles in the test section. However, quantitative analyses are difficult because of their low intensity and brightness in the video recordings. The fine particles were assumed to accurately follow the fluid streamlines while the other particles with their sizes in between 100 to 800 µm were characterized to determine their trajectories and velocities. The metal foams were purchased from China Beihai Building Material Co., Ltd. [30], with the details in listed in **Table 6.1**. In this study, different pore densities (10 and 30 PPI) were used to investigate the influence of porous structure on the propensity of fouling.

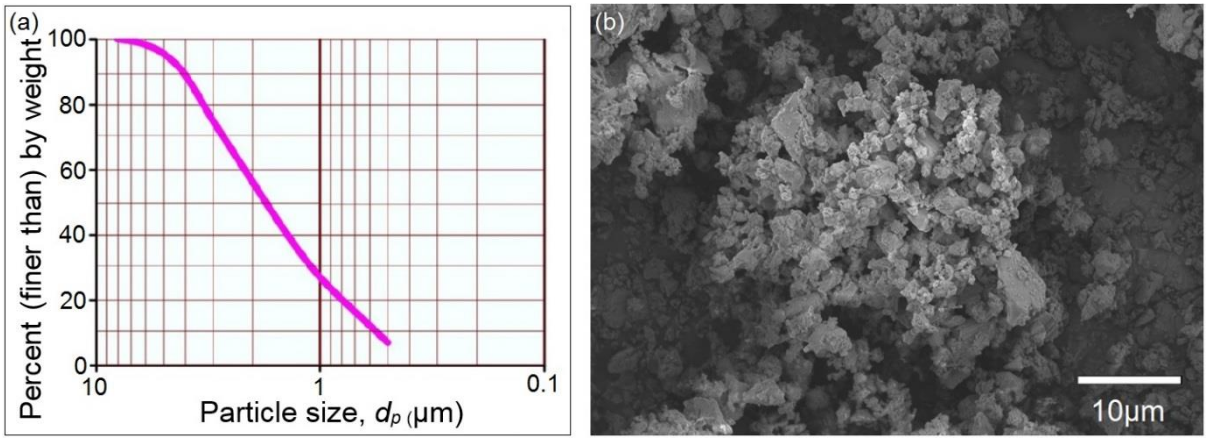

Figure 6.3 (a) Particle size distribution in range of 0.5 to 8.0 µm [24] and (b) SEM image of $CaCO_3$

Table 6.1 Metal foam microstructural and geometrical properties

Parameter	**Value**	
Pore density (PPI)	10	30
Ligament diameter, d_l (m)	0.00044	0.00027
Pore diameter, d_p (m)	0.00256	0.00087
Porosity, ε (-)	0.82 – 0.91	0.88 - 0.94
Permeability, K x 10^{-7} (m^2)	1.54 - 1.65	0.35 - 0.37
Foam height, h (m)	0.004, 0.01, 0.03	
Blockage ratio, h/H	0.05, 0.13, 0.39	
Foam length, Lf (m)	0.09	
Foam width, wf (m)	0.10	

6.3 Results and Discussion

6.3.1 Particle trajectories and velocities

As expected, there are fewer particles found in the regions close to the top wall. Thus, this study combined at least 50 particles (of the same size) from adjacent transverse positions to have a statistically sufficient database [26]. The particle trajectories over the two-dimensional planes along the partially filled channel with different PPIs are obtained from the particle tracking analyses. In general, the particle trajectories are influenced by their densities, which could be also different from the fluid (air) elements. **Figure 6.4** shows some of the particle trajectories are consistent with the flow motion [24], while the others would deviate from the mean streamlines, revealing their complex motion.

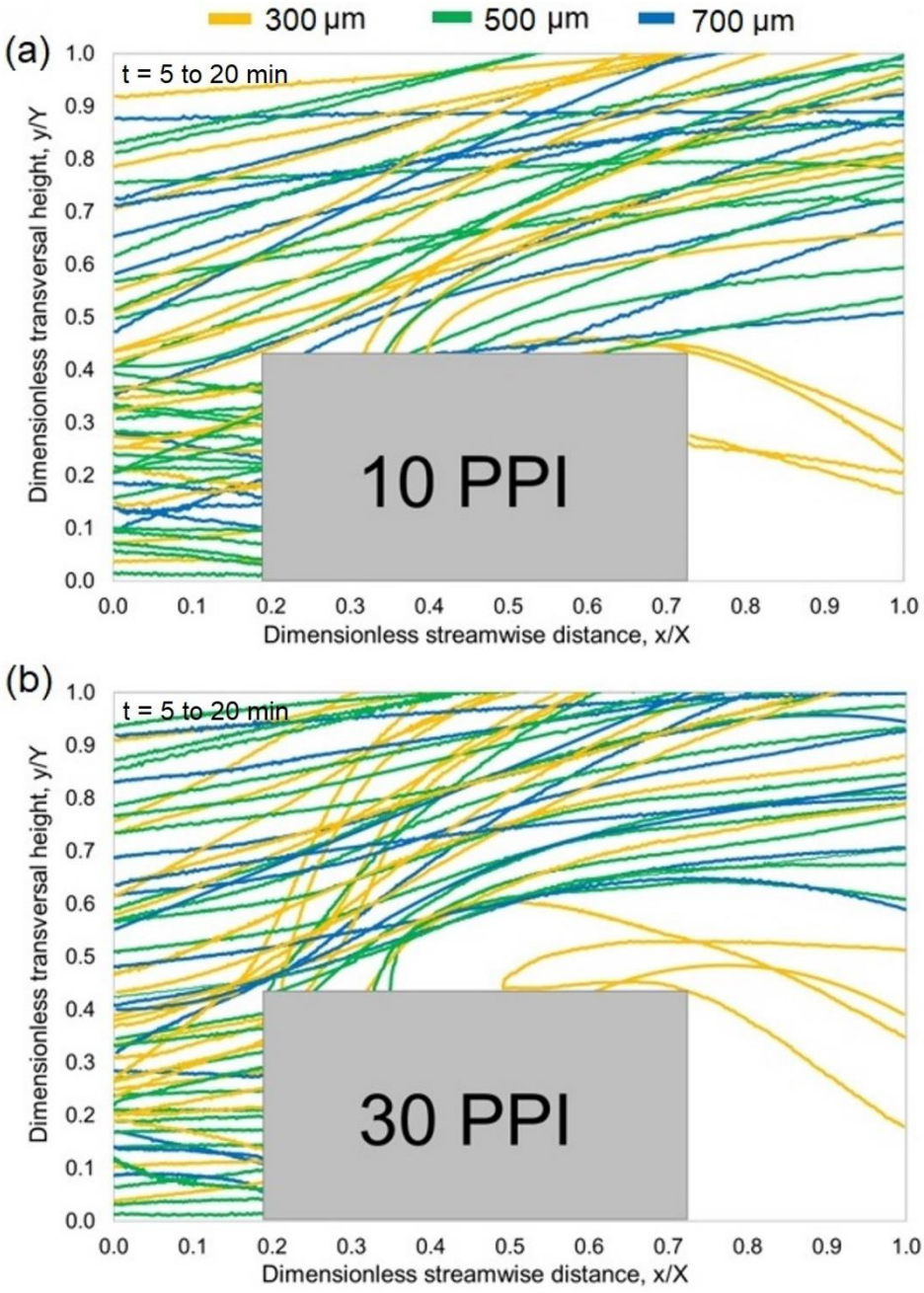

Figure 6.4 Particle motion trajectories in the partially filled channel (flow direction from left to right)

Regardless of pore density, four main situations occur in the partially filled channel; (1) particle collision and deposition on/within the foam block, (2) particles breakage, (3) particles exit through the fluid/foam interface, and (4) particles transport through the ROIs without any deposition. For the experiments with a low blockage ratio, h/H ≤0.13, most of the particles would move towards the end of the test section, supporting our findings on the insignificant effects of low blockage ratio [24]. However, the partially filled channel with a significant blockage ratio, h/H = 0.39, would restrict

the particle movements in the lower region, as expected (see **Figure 6.4 (a**) and **(b)**). As the particle-laden flow passes through ROI 1, direct particle impaction with the frontal area (ligament surfaces) of the foam block is possible. Consequently, some of them tend to get deposited on the bottom surface of ROI 1, while the others could successfully enter the porous region, depending on the particle and the subjected pore sizes.

Also, some of the particles tend to avoid the foam block, following the fluid streamlines into the non-porous region, which mostly involved the smaller particles, $\bar{d}_p \leq 500$ µm. Interestingly, **Figure 6.4 (a)** shows the bend degree (curvilinear motion) of the particle trajectories with 10 PPI foam are stronger than 30 PPI foam as the particle is moving away from the fluid-foam interface. This suggests the horizontal flow in the free stream region of 10 PPI is significant. Meanwhile, **Figure 6.4 (b)** shows some trajectories ($\bar{d}_p < \bar{d}_{pore}$) with 30 PPI foam have upward deviations from the fluid streamlines in a region near to the leading edge. Unlike the 10 PPI foam that allows more particles to come out along the interface, the particle trajectories with 30 PPI could be only seen in the regions near to the leading and rear edges. This phenomenon could be influenced by the flow behaviours in the partially filled channel. For the 30 PPI foam with higher restrictions, it is known that the flow inside its porous structure could lose its momentum and exit through the interface, specifically a region about one-third from the leading edge [20]. Our previous study [20] also found a large recirculation zone behind the foam block, originating from the foam itself. Thus, the present particle laden flow shows the similar flow behaviours, forcing the particles to transport in the same manner.

In another opinion, the particles trajectories on the interface may also represent the detachment of the deposited particles as the flow is passing through. Because of its larger pores, 10 PPI shows different size particles up to 700 µm are exiting through the interface. While, the smaller particle size (less than 500 µm) is found with the 30 PPI foam. Most likely, this phenomenon is experienced by the naturally small particles ($\bar{d}_p < \bar{d}_{pore}$), or a result of particle breakage episode in the porous structure. Note that it is impossible for those particles with a larger size than the pore diameter ($\bar{d}_p > \bar{d}_{pore}$) to penetrate into the porous region. Unless the particle breakage incident is happening, as they hit the foam-ligament surfaces. Interestingly, this study noticed that the particle breakage could be a natural event in this case, considering the nature

of our particle characteristics and the interconnected pore-ligament networks. This topic will be discussed further in the following section.

It is also noticeable in **Figure 6.4 (a)** on how the particle keeps its inertia and passing linearly through both porous and non-porous (free stream) regions. This, probably due to a small disturbance in the free stream region as more flow prefers to enter the porous structure of 10 PPI. If considering the flow behaviors inside the porous structures [20], the 10 PPI foam seems to have a higher capability to accommodate more particles. These higher amounts of incoming flows into the porous region is also a good indicator that the deposited particles could be carried away out of the porous region. However, very few particles exit the rear ends of the 10 PPI foam, and there is no particle (visible size from the on-line data) is coming out from the 30 PPI foam. In that case, the 30 PPI foam with smaller pores could have blocked or trapped the particles, and the very low velocity at the downstream region (due to the existence of a recirculation zone) could not bring back the particles towards the foam, as shown in ROI 3, **Figure 6.4 (b)**. It is also possible because of a stagnant region in the high PPI foam [20]. However, the 10 PPI foam with larger pores may only allow the particle to pass through its porous structure up to a certain period. In summary, those two PPIs show different particle movements in ROI 2 (the non-porous region) and ROI 3.

Figure 6.5 depicts normalized particle velocity with different PPIs, measured on the top of the foam block at Lf = 0.030 m. The average particle velocity is normalized by the inlet velocity, u_o. Because of the limited visual inside the porous region, the foam interface is considered as the starting point for the particles. Also, note that **Figure 6.5** is based on the field-of-view of the camera. Based on the decreasing profiles in adjacent regions near to the top wall (**Figure 6.5 (a)**), we could assume a no-slip condition for the particle velocity on that surface. Only small friction effects are expected because of the smooth material of the top wall. In general, we can observe the particles accumulate in the low-speed streaks that near to the foam interface. The lower velocity is possibly due to different flow regime [20], where a boundary layer appears on the foam interface, regardless of pore density. As expected, the smallest particle, $\bar{d}_p$= 300 µm shows a lower velocity as compared to those two larger particles, especially in the adjacent region to the interface. The rests in **Figure 6.5 (a)** show similar profiles with only a small difference in value. The largest particle, $\bar{d}_p$= 700 µm,

which supposed to have the highest density is moving a little bit faster as compared to the others.

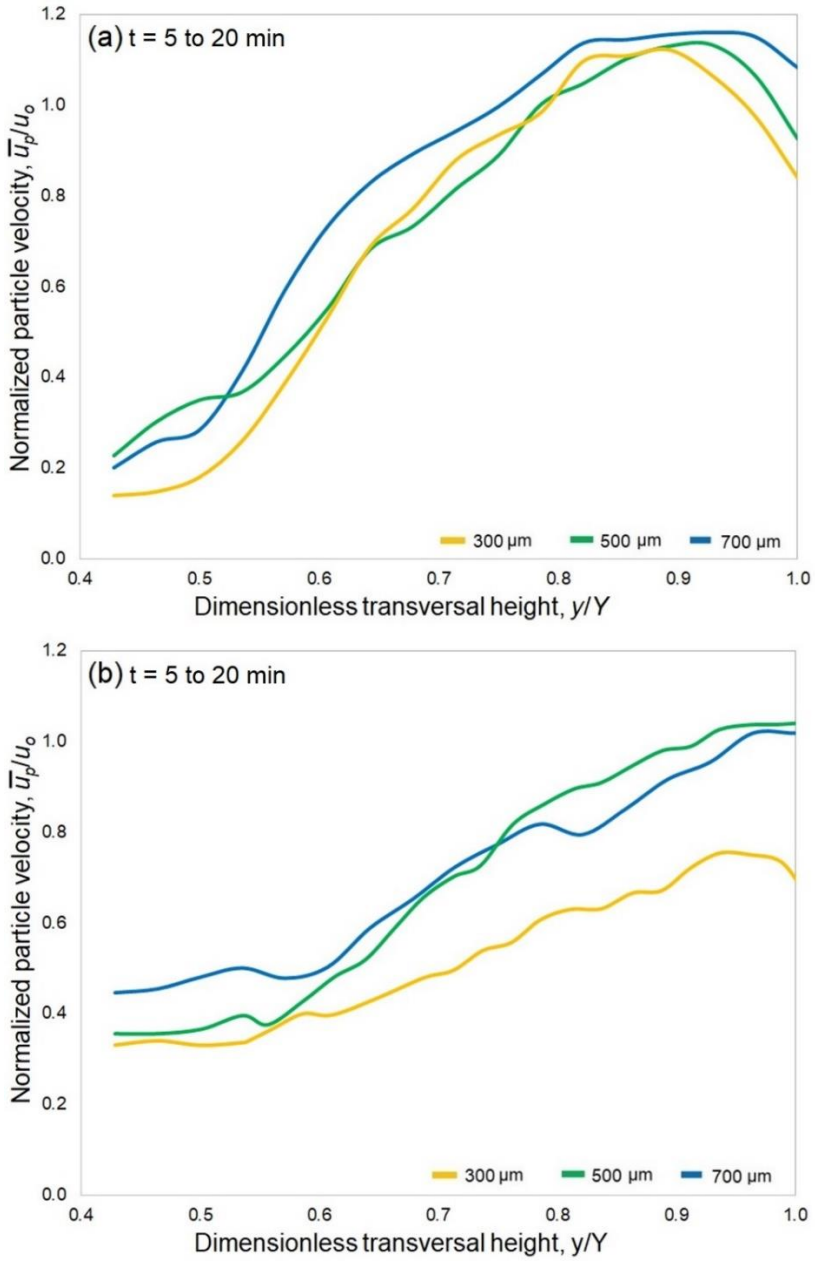

Figure 6.5 Normalized particle velocity in ROI 2 with h/H = 0.39 (a) 10 PPI and (b) 30 PPI

Meanwhile, **Figure 6.5 (b)** with the 30 PPI foam shows virtually a linear velocity increment, starting from y/Y = 0.6 for those two larger size particles. Interestingly, their velocity is slightly lower as compared to those particles with 10 PPI foam. Those large particles are probably trying to keep their inertia towards the top wall, but declining in speed due to the effect of secondary flow that only appear in the free stream region of 30 PPI foam [20]. Even though the large particles might keep their directions, the

upwards flow motion may have some influences on their velocity and momentum. In a case with the smallest particle, $\bar{d}_p$ = 300 µm, the upwards flow motion influences both the trajectories (see **Figure 6.4 (b)**) and velocity. Most of the smallest particle at the point of interest, (Lf ~ 0.030 m) show a tendency to move upwards and to verge slowly in the streamwise direction. This, however, contributes to a lower velocity (based on the particle distance between two frames). Their upward motions also suggest insignificant drag effects and the existence of slip velocity around these small size particles. The variations in the trajectories and velocity are expected to cause a complicated deposition process within the porous structure of the metal foam.

6.3.2 Particle preferential deposition areas, transport and deposition mechanisms

Our findings support the ideas by Hooman et al. [3] that small particles could pass through the pore network with some of them may deposit on the ligaments and partially block the pathways, while large particles tend to sit and clog the pores. However, our results also show those phenomena are subjected to the type of particles or foulant, besides the interconnected pores. To have a clear view on the relationship between the particle and the porous structure, a series of raw images (**Figure 6.6**) that describes the process of particle transport from the upstream region towards the foam block is also included. Note that the time, (t) in **Figure 6.6** is the travelling period from one point to another point in 30 fps video recordings, which is not the real-time of particle motion during the experiment.

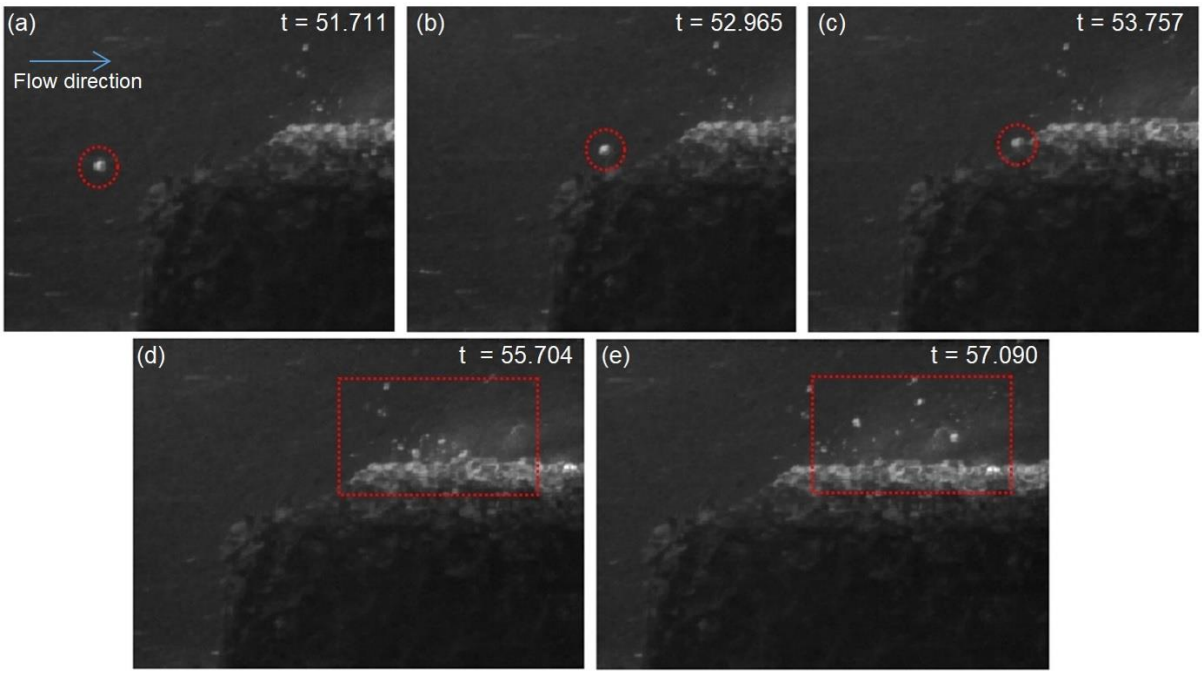

Figure 6.6 Particle transport, breakage and dispersion

Figure 6.6 (a) to **(c)** shows how the particle is approaching the foam block. The particle enters the porous structure of the foam and disappears for a while before coming out from the top surface (**Figure 6.6 (d)**). Even though the carrier (particle laden flow) is passing through the porous structure, the particle collides with the ligaments and breaking into several pieces. A part of those pieces is being carried away by the incoming flow and dispersed into the free stream region. While some of them may deposit on the foam surface. Also note, the detachment of the deposits by the impact of the incoming flow is also possible, suggesting this as one of the important transport mechanism in the partially filled channel. This phenomenon offers a high possibility to make use of the porous structure to remove the unwanted particles. The particle/agglomerate rigidity and flow impact must be taken into account when considering the metal foam under a fouled condition. Most prominently, due to randomness and interconnected pores, the penetrated particles could be caught inside the porous region. Without proper design, the foam itself could act as a trap or filter to the particles.

As one would expect, the preferential deposition areas are significantly depending on the foam arrangement and its geometrical design. The effects of our arrangement on the deposition process are schematically described in **Figure 6.7**. For the low blockage ratio case (**Figure 6.7 (a)**), for example, h/H = 0.13, it is found that

the preferential deposition area is located at the top surface of foam block, as most of the particle-laden flow could successfully pass through the partially filled section (ROI 2). The horizontal flow encourages the shear effect on the foam interface. Even though this shear may also contribute to the detachment of particles, the deposition rate is undisputable higher in this case. The depositions could further be increased because of the gravitational forces. While, the preferential deposition area for the high blockage ratio (**Figure 6.7 (b)**) is right in front of the foam block, within ROI 1. Note that the specific size particles ($\bar{d}_p < \bar{d}_{pore}$) may either penetrate into the porous region, or colliding with the ligament restrictions, get deposited on the foam surfaces or the bottom of RO1 region.

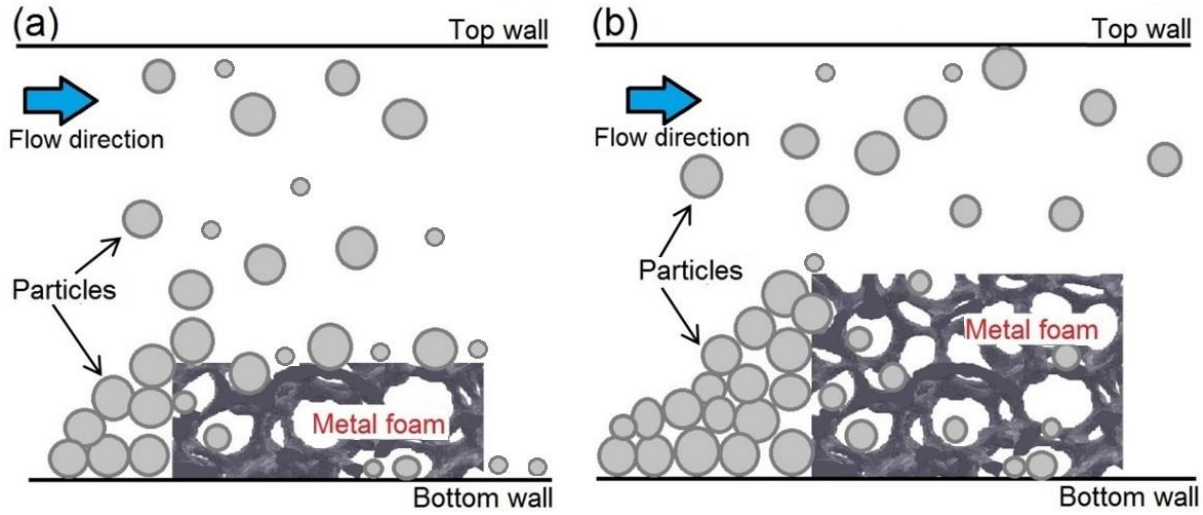

Figure 6.7 Illustration of particle deposition across the partially filled section (a) low blockage ratio and (b) high blockage ratio

Due to the prolongs injection time, the deposited particles started to accumulate in ROI 1, resulting in completely blocked passages (frontal area of the foam block) into the porous region. These accumulated particles form a slope or triangular-shaped deposits right in front of the foam block, which obviously seen with the high blockage ratio. From that point, the flow tends to choose the free stream region. Note that the deposits in ROI 1 could either (1) stick there for a very long time or (2) detaching from that slope due to lifting or rolling effects because of the impact of the incoming flow. Within this injection period, we could conclude that the upstream region (ROI 1) and the leading edge are the preferential deposition areas for the high blockage ratio, regardless of pore density (PPI). In this study, most of the large particles do not follow the fluid streamlines. Thus, the inertial impaction is the dominant mechanism for the

high blockage ratio. However, the thermophoresis is unlikely important for the high blockage ratio, due to the presence of a local thermal equilibrium between the upper region of the foam block and fluid phase [20].

At the microscopic level (**Figure 6.8**), we could see that those particles either get deposited on the bottom surface of the aluminum plate or stick on the ligaments. Different size particles found on the bare plate (see **Figure 6.8 (a)**) and with a close observation on **Figure 6.8 (b)**, one can realise that the depositions on the ligament surfaces are non-uniform and they are subjected to the orientations of the ligament surface. Those exposed areas to the flow (circled in red colour) could have a thicker deposition as compared to the hidden areas at the beginning of the fouling process. This proved that the assumption of uniform deposition layers in the porous structure [3, 5] is not always true in a real practice. Even though the deposition layer is building up and filling up the pores, the structure of the deposition layers itself are non-uniform, at least in this case. It is worthy to note that these initial depositions are important as they are more likely to influence the subsequent deposition processes, by providing a higher adhesion force and more restrictions to the other particle motions. This, however, could be better observed after more particles are injected into the system, as shown in **Figure 6.9**.

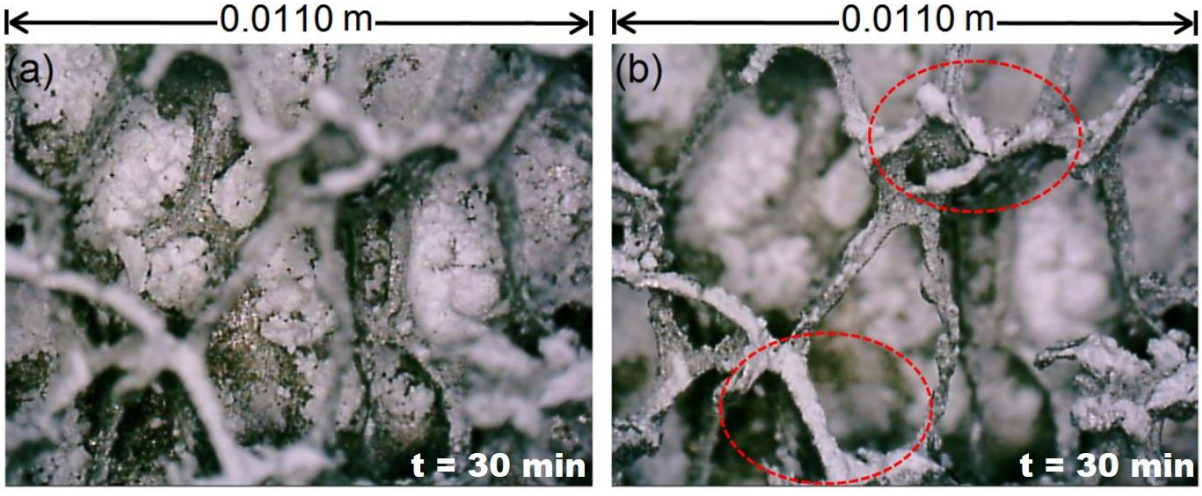

Figure 6.8 Microscope images of 10 PPI foam at the same location (a) Deposition on the bare plate (b) Deposition on the ligaments (Flow from the right to left direction)

In term of PPIs, the 30 PPI foam is blocked faster due to its more restrictions and smaller pores than 10 PPI foam. **Figure 6.9 (a)** shows that the high PPI foam is easily filled with the particles, but more unclogged areas with 10 PPI foam, as shown

in **Figure 6.9 (b)**. It also clearly seen with the 10 PPI foam that there exists strong adhesion between particles, as the particles tend to deposit on the same spot. Another possibility is the effects of internal or tortuous flows, where the 10 PPI foam allows more flow to pass through its pores, avoiding or detaching the deposits. This study agreed with the findings from another literature [12], that more deposition of the fine particles, e.g., soot particles on the upper ligament surface (on the interface) as compared to the lower ligaments of a more porous foam. In this case with the low blockage ratio, h/H = 0.13, there is a high possibility that the dominant deposition mechanism is thermophoresis. This transport mechanism is possible as our particle could be as small as 0.5 µm (see **Figure 6.3 (a)**). The particles tend to deposit on the ligament surfaces, obviously seen with the 10 PPI foam. Our previous study [20] found that the coolant at the bottom of foam block (h/H = 0.13) caused a low temperature region in the entire foam block. In that case, the fluid molecules from the hot sides (upstream and free stream regions) have a higher velocity than fluid molecules near or inside the foam block. Consequently, the fine particles may experience a thermophoretic force, while the large particles would keep their inertia and move towards the downstream region of this setup.

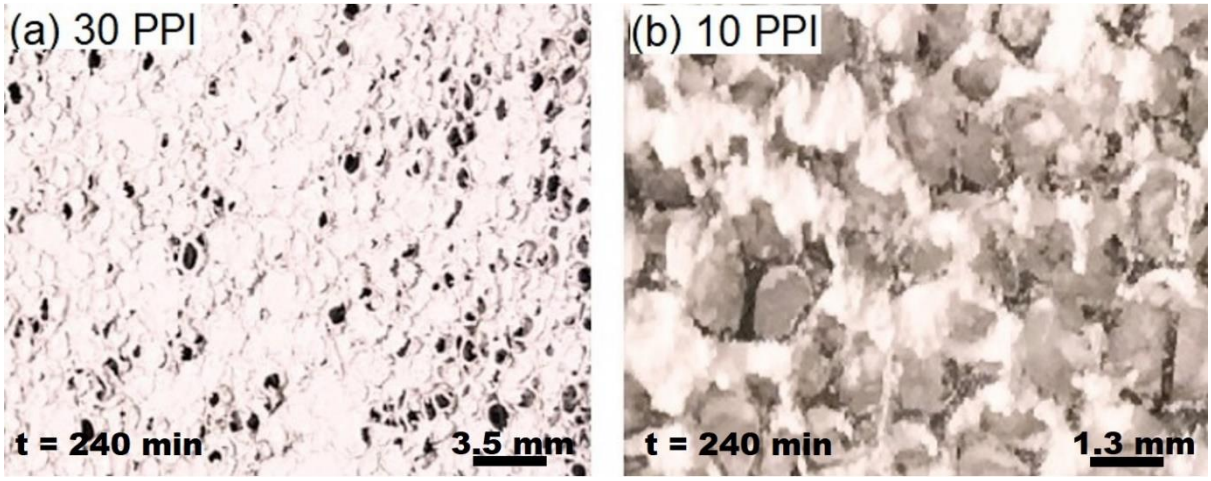

Figure 6.9 Particle deposition on the top surface of the foam block (h/H = 0.13) with different pore densities

6.3.3 Pressure drop performances

Figure 6.10 depicts normalized pressure drops for different PPIs and blockage ratio, h/H = 0.05 to 0.39 in the test section at inlet velocity, u_o = 6.2 m/s. Our result with h/H = 0.39 is also compared with another literature [4] that considered 20 and 40 PPI metal foams as a potential EGR cooler. Regardless of the PPIs and blockage ratio,

the normalized pressure drops are increasing with the injection time up to 240 minutes. However, it is noticeable that the pressure drop values are fluctuated before subsequently reaching a similar value, regardless of PPI and blockage ratio. It was expected as the experiment deals with unpredicted deposition process over the complicated structure of the metal foam. Later, the 10 and 30 PPI foams show similar pressure drops beyond 200 minutes of particle injection, suggesting significant depositions in the porous structure at that time. Interestingly, at the beginning of the fouling process, the pressure drops of 10 PPI foam is mostly higher than 30 PPI foams, except for h/H = 0.05 (**Figure 6.10 (a)**).

One would expect to see the pressure drop of 30 PPI is higher than 10 PPI foam, as a result of its more substantial pore-ligaments restrictions, which should have a higher tendency to trap more particles. However, due to the more porous structure of the 10 PPI foam, it could accommodate more particles further inside (streamwise direction). Meanwhile, the 30 PPI foam could have more depositions over its frontal area. This effect may cause fluctuated, and disturbance flows in the 10 PPI foam, producing a higher pressure drops at the beginning of the fouling process as compared to 30 PPI foam. Also, the 10 PPI foam with larger pores causes more particles (various sizes) to enter and escape its porous structure (**Figure 6.4 (b)**). Those trapped particles inside the porous structure, however, may influence the internal surface roughness and frictional effects on the pressure drops. Interesting, the pressure drops also decrease for a while, around 80 to 120 minutes before increasing again. Probably, as the frontal area of the foam blocks is blocked, the foams mimic a solid block behaviour with no internal friction effects. As the injection continued, more particles could be pushed further into the foam block that increase the pressure drops again. The deposition within the porous region may reduce the permeability of the porous structure and affect the internal flow behaviours. However, this probably more dominant with the 10 PPI foam. Also noted, both PPIs are subjected to a non-uniform distribution of the particles within their porous structure as a results of their internal flow behaviours [20]. These could be the reasons for these fluctuation values of the pressure drops, among the other factors which are not yet discovered at this point of research.

Interestingly, the normalized pressure drops with h/H = 0.13 show the highest values as compared to the other blockage ratio, h/H = 0.05 and 0.39. The high

blockage ratio setup has more deposition in the upstream region and the adjacent regions to the leading edge, but lesser particles in the rear region (according to the trajectories in **Figure 6.4**).

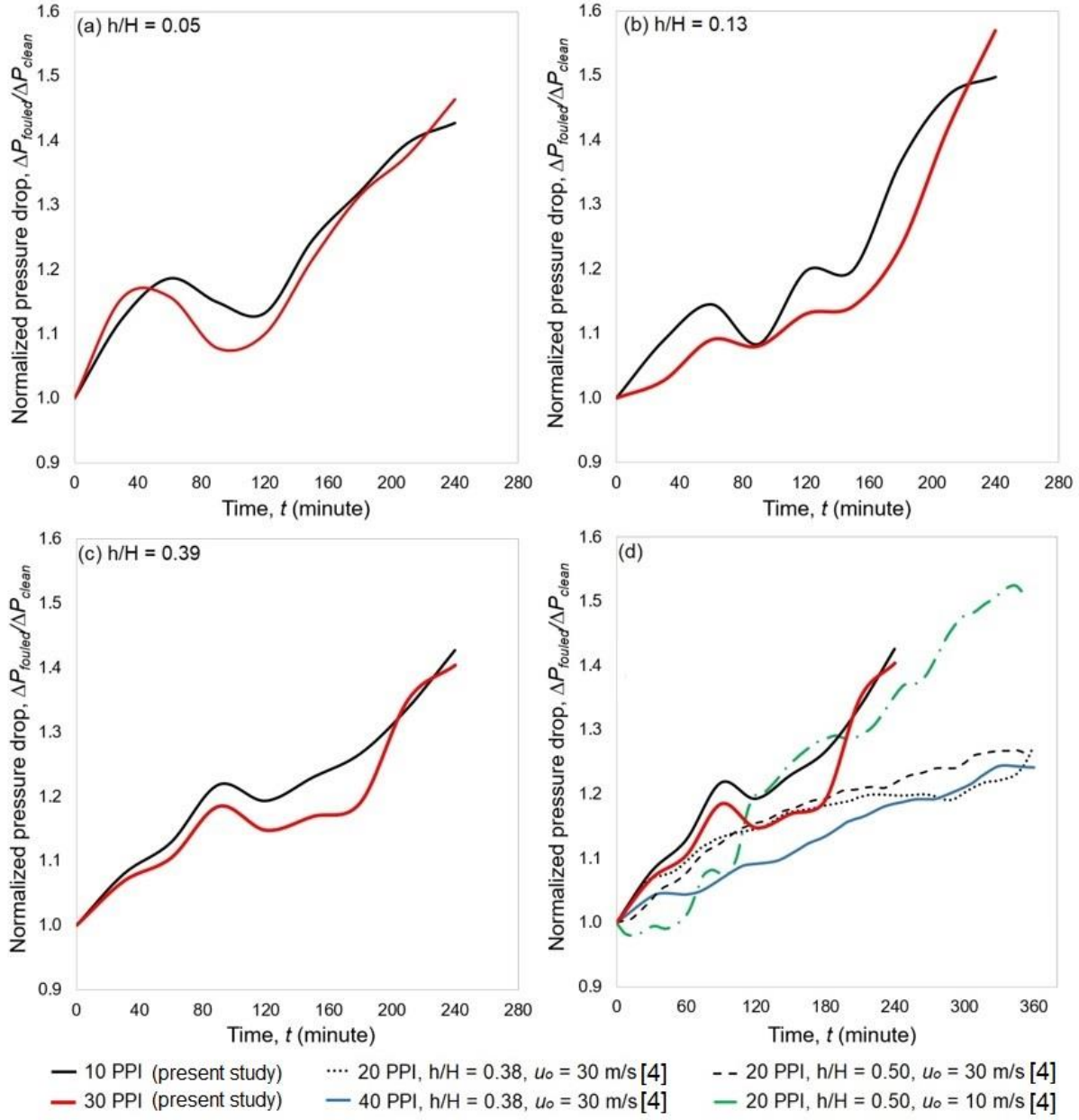

Figure 6.10 Normalized pressure drop of partially filled channel with different PPIs and blockage ratio (a) h/H = 0.05, (b) h/H = 0.13, (c) h/H = 0.39 and (d) Comparison of present data with existing literature [4]

Meanwhile, the low blockage ratio is subjected to more deposition on the top surface and inside the pores. Hence, the significant fouled structure tends to cause a substantial increase in the pressure drop. However, as the fouling layers intensify over time, the microstructural effects become insignificant, resulting in similar pressure drop

values. Comparing our results, h/H = 0.39 with Ref. [4], the normalized pressure drops are quite similar, except the significant drops in the pressure drop at a specified period. Most probably, since our total pressure drop are affected by the minor losses at the upstream and downstream, the pressure drops could be easily affected by the presence of the deposits at the upstream region. Thus, mimicking the lower pressure drop value of a solid block [22], at one time before experiencing an increase of pressure drop due to the deposition.

6.4 Conclusion

In this study, particle transport and deposition processes were studied in a partial filled channel by means of direct observation using video recordings. The remarkable findings from this study are summarized as follows:

(a) The particle size is one of the important parameters in characterizing the particle trajectories in the partially filled channel. The large particles keep their inertia, and tend to hit the obstacle in the pathways, if there is any. While the fine particles follow the fluid streamlines.

(b) The particle deposition on/within the porous structure are also highly dependent on the particle size or in the opposite view, subjected to the pore and ligament sizes. The high blockage ratio causes more depositions in the upstream region, regardless of PPIs. However, there almost no deposition behind the block, probably due to very low velocity in that region.

(c) Inertial impaction is the dominant mechanism for the high blockage ratio. The preferential deposition area for the low blockage ratio is the top surface of the foam block, attributed to the effects of thermophoresis and drag forces.

(d) Some particles detach or exiting into the free stream region through the fluid-foam interface. They tend to follow the fluid behaviours, with some of them could break into smaller pieces as colliding with the pore-ligament networks.

(e) Deposition causes a fluctuated pressure drop at the initial stage before reaching a similar value, regardless of PPIs. The deposition within the porous structure and over the frontal area of the foam block could be the main reasons for these fluctuating values.

References

[1] F. Shikh Anuar, M. R. Malayeri and K. Hooman, “Particulate fouling and challenges of metal foam heat exchangers”, *Heat Transfer Engineering*, 38, 7-8, pp. 730–742, 2017.

[2] X.-H. Han, Q. Wang, Y.-G. Park, C. T’Joen, A. Sommers and A. Jacobi, “A review of metal foam and metal matrix composites for heat exchangers and heat sinks”, *Heat Transfer Engineering,* 33, 12, pp. 991–1009, 2012.

[3] K. Hooman, A. Tamayol and M. R. Malayeri, “Impact of particulate deposition on the thermohydraulic performance of metal foam heat exchangers: A simplified theoretical model”, *J. Heat Transfer*, 134, 9, pp. 092601, 2012.

[4] K. Hooman and M. R. Malayeri, “Metal foams as gas coolers for exhaust gas recirculation systems subjected to particulate fouling”, *Energy Convers. Management,* 117, pp. 475–481, 2016.

[5] M. Odabaee, M. De Paepe, P. De Jaeger, C. T’Joen and K. Hooman, “Particle deposition effects on heat transfer from a metal foam-wrapped tube bundle”, *Int. J. Numer. Methods Heat Fluid Flow*, 23, 1, pp. 74–87, 2013.

[6] E. Sauret, S. C. Saha and Y. Gu, “Numerical simulations of particle deposition in metal foam heat exchangers”, *Int. J. Comput. Mater*. Sci. Eng., 2, 3&4, pp. 1350016, 2013.

[7] S. T. W. Kuruneru, E. Sauret, S. C. Saha and Y. T. Gu, “Numerical investigation of the temporal evolution of particulate fouling in metal foams for air-cooled heat exchangers”, *Appl. Energy*, 184, pp. 531–547, 2016.

[8] S. T. W. Kuruneru, E. Sauret, K. Vafai, S. C. Saha and Y. T. Gu, “Analysis of particle-laden fluid flows, tortuosity and particle-fluid behaviour in metal foam heat exchangers”, *Chem. Eng. Sci*., 172, pp. 677–687, 2017.

[9] E. Sauret and K. Hooman, “Particle size distribution effects on preferential deposition areas in metal foam wrapped tube bundle”, *International Journal of Heat and Mass Transfer,* 79, pp. 905–915, 2014.

[10] P. Clark, K. A. Koehler and J. Volckens, “An improved model for particle deposition in porous foams”, *J. Aerosol Sci*., 40, 7, pp. 563–572, 2009.

[11] H. D. Ackermann, “Experimental Investigation of Fouling in various Exhaust Gas Recirculation Coolers”, ITW-Thesis, University of Stuttgart, Germany, 2012.

[12] J. Kahle, “Experimental investigation of deposit formation in foam structured EGR coolers”, ITW-Thesis, University of Stuttgart, Germany, 2012.

[13] S. T. Wickramasooriya Kuruneru, E. Sauret, S. C. Saha and Y. T. Gu, “A novel experimental method to assess particle deposition in idealized porous channels”, *Heat Transfer Engineering,* 38, 11–12, pp. 1008–1017, 2017.

[14] A. Muley, C. Kiser, B. Sundén and R. K. Shah, “Foam Heat Exchangers: A Technology Assessment”, *Heat Transfer Engineering,* 33 1, pp. 42–51, 2012.

[15] C. T’Joen, P. De Jaeger, H. Huisseune, S. Van Herzeele, N. Vorst, and M. De Paepe, “Thermo-hydraulic study of a single row heat exchanger consisting of metal foam covered round tubes”, *International Journal of Heat and Mass Transfer*, 53, 15–16, pp. 3262–3274, 2010.

[16] S. T. W. Kuruneru, E. Sauret, C. S. Suvash, Y. T. Gu and K. Hooman, “A novel experiment method to assess industrial aerosol deposition in idealised porous channels”, *17th IAHR Int. Conf. Cool. Tower Heat Exch*., QLD, Australia, 2015.

[17] S. T. W. Kuruneru, E. Sauret, C. Saha and Y. Gu, “Poly-disperse particle transport and deposition in idealized porous channels”, in *2nd Australasian Conference on Computational Mechanics*, QLD, Australia, 2015.

[18] S. T. Wickramasooriya Kuruneru, E. Sauret, C. S. Suvash and Y. T. Gu, “An FVM-DEM assessment of particle deposition in low-porosity foams with circular strut cross sections for electronics cooling applications”, *R. Aust. Chem. Institute, Chemeca Conference,* pp. 23–26, Victoria, Australia, 2017.

[19] M. Odabaee, S. Mancin and K. Hooman, “Metal foam heat exchangers for thermal management of fuel cell systems – An experimental study”, *Exp. Therm. Fluid Sci*., 51, pp. 214–219, 2013.

[20] F. Shikh Anuar, I. Ashianti Abdi and K. Hooman, “Flow visualization study of partially filled channel with aluminium foam block”, *International Journal of Heat and Mass Transfer*, 127, pp. 1197–1211, 2018.

[21] R. Lindeboom, G. Smith, D. Jeison, H. Temmink and J. B. van Lier, “Application of high speed imaging as a novel tool to study particle dynamics in tubular membrane systems”, *J. Memb. Sci*., 368, 1–2, pp. 95–99, 2011.

[22] F. Shikh Anuar, I. Ashtiani Abdi, M. Odabaee and K. Hooman, “Experimental study of fluid flow behaviour and pressure drop in channels partially filled with metal foams”, *Experimental Thermal and Fluid Science*, 99, pp. 117-128, 2018.

[23] Y. Feng, J. Goree and B. Liu, “Errors in particle tracking velocimetry with high-speed cameras”, *Review of Scientific Instruments,* 82, pp. 053707-1-7, 2011.

[24] Omya Australia Pty. Limited, “Cement Based Products.” [Online]. Available: https://www.omya.com/Pages/au/en/cement_based_products.aspx. [Accessed: 26-Feb-2018].

[25] W. Pabst and E. Gregorova, “Characterization of particles and particle systems”, ICT Prague, pp. 1–122, 2007.

[26] D. Kaftori, G. Hetsroni and S. Banerjee, “Particle behavior in the turbulent boundary layer. II. Velocity and distribution profiles”, *Phys. Fluids*, 7, 5, pp. 1107–1121, 1995.

Chapter 7: Conclusion and Suggestion for Future Work

7.1 Conclusion

It is well-known that the complex microstructure of the metal foams required additional attention to obtain generally accepted metal foam heat exchangers in the market. Both the geometrical and microstructural properties of the metal foams play important roles in influencing the metal foam heat exchangers performances. In this study, two different configurations of metal foam were studied: the metal foam-filled annulus and partially channels with metal foam blocks. A series of experiments were conducted to gain insights on the fluid behaviors across the complicated structure of the metal foam and better understanding of their thermohydraulic properties. Fundamental knowledge on the thermohydraulic of metal foams in a clean condition could be helpful in disclosing any unexplained fouling phenomenon of a similar setup.

Detailed experimental and numerical results on the thermohydraulic of metal foam-filled annulus were discussed in Chapter 3. The experimental work in this chapter focused on the accurate measurement of the pressure drop and temperature fields in the foam structure of 5 and 20 PPI foams. Three different airflow rates (20, 85 and 150 SLPM) were considered to investigate the effects of pressure drop and thermal-fluid behaviors in different pore densities. The results show that the pressure drop is increasing with the metal foam length and pore density. However, a significant amount of heat transfer only takes place in the first half of the foam, with the higher PPI foam would have a better performance than the lower PPI foam. Thus, a longer metal foam than 0.05 – 0.06 m, for example in the case of 20 PPI at 20 SLPM may be unworthy since the pressure drop continues rising considerably while the changes of temperatures are insignificant. A significant increment in the pressure drop could be seen by changing the air flow rates, for example at a higher flow rate of 150 SLPM, the pressure drop is about three time of the pressure drop of 20 SLPM, regardless of the pore size.

In Chapter 4, the investigations on the fluid behaviors in the partially filled section using point-wise measurements, e.g., the hot-wire and laser Doppler anemometer show different flow behaviours could be observed at the foam-fluid

interface, upstream and downstream regions. As expected, the velocity profile decreases towards the top wall (non-porous region), while the velocity behaviour near the bottom wall is rather complex, due to the presence of the metal foam block. However, the use of lowest blockage ratio (h/H=0.05) shows insignificant effects on the average velocities in the channel, regardless of the pore density, and the presence of the foam block is only noticeable with h/H=0.13. The velocity profiles also show a high possibility of recirculation or dead zones formations at the interface and downstream regions based on the fluctuated velocity profiles. Interestingly, the study also found the pressure drops of the metal foams are also higher than the pressure drop of solid blocks of the same size. These effects probably because of the internal friction inside the porous structure of the metal foam block and also the existence of a recirculation zone at the downstream region. By fitting different set of experimental data from various foam samples and operating conditions, a friction factor model of the partially filled channel is proposed. The proposed model is in agreement with the experimental data with deviation is about ±16%.

The findings on the flow behaviours in the partially channel are more clear in Chapter 5 with the results from global-wise measurements (using particle image velocimetry and infrared camera). The result shows that the flow inside the porous structure could exit into the free stream region through the interface for certain blockage ratios and pore densities, for example, 30 PPI foam with h/H = 0.39. However, the existing model and numerical studies in the literature on this similar setup have possibly oversight these critical findings. Furthermore, the formation of a recirculation zone at the downstream region only occurs with the 30 PPI foam, while a portion of the flows is successfully exiting through the rear end of the 10 PPI foam block. Also, only the partially filled channel with high enough blockage ratio would significantly influence the temperature distributions and flow behaviors. Once high enough blockage ratio is considered, the effects of foam microstructure or pore density on the flow behaviors become noticeable. Even though the high pore density foams are expected to cause high pressure drop, the partially filled configuration tend to show the opposite result. The low PPI foam, e.g., 5 PPI could exhibit a higher pressure gradient as compared to the 10 and 30 PPI foams at the same condition. While the 30 PPI foam would have a higher pressure drop than the 10 PPI foam only at a high

enough blockage ratio. Thus, optimum pore density, foam length, and blockage ratio should be identified for a partially filled channel design.

With the addition of particles (foulant) in the partially filled channel (Chapter 6), the particle transport and deposition processes have been investigated by means of direct observations using video recordings. The result shows that the particle size is one of the important parameters in characterizing the particle trajectories, as large enough particles (several hundred micron-size particles in this case) tend to keep their inertia, and depositing on any obstacle in the pathways. While the fine particles follow the fluid streamlines. However, if the large particle is travelling towards the pore instead of hitting the ligament surface, the particles would deposit deeper into the porous region. However, because of the interconnected pore-ligament structure, the preferential deposition area for the high blockage ratio (h/H = 0.39) is the frontal area and upstream region, regardless of the PPIs. As the deposition is building up over time, a longer foam or deeper porous structure into the streamwise direction is meaningless. Meanwhile, the low blockage ratio setup would be easily covered with the deposition layer as the particles are travelling through the partially filled section. The top surface of the foam block becomes the preferential deposition area for the low blockage ratio. Due to the nature of the particle itself, some of them could break into smaller pieces as colliding with the pore-ligament networks, detaching or exiting into the free stream region through the fluid-foam interface. As the particle injection continued for several hours, the effects of metal foam microstructure on the pressure drop become insignificant.

This study proved the importance of experimental studies in understanding the fluid flow behaviors in the porous structure of metal foams. The effects of the complicated porous structure could not be seen easily through modelling and numerical studies. The fundamental knowledge of flow characteristics is crucial to explore the possibility of using the metal foam under a fouled condition, for example, an exhaust gas recirculation cooler for diesel engine application. The low velocity and stagnant region in the vicinity or inside of the metal foam are unfavorable as any fouling tendency must be avoided in the heat exchanger design. This study on the thermohydraulic and flow behaviors in one kind of porous media (open-cell metal foam) will contribute to the area of thermal engineering, particularly in developing a metal foam heat exchanger for different applications.

7.2 Future Work

This study noticed many areas that required further investigations in designing a proper and high-performance metal foam heat exchanger. For the partially filled channel design, a minimum blockage ratio should be carefully selected to make use of the foam pore density. There are still inconclusive findings on their thermohydraulic performance, which required further optimization studies and validation tests, particularly on the foam geometrical and microstructural properties. This study also found that the existing concept of porous media could not represent the exact flow behaviours in the partially filled channel, due to fluctuated flows across the porous structure of the metal foam and at the interface region. The characteristics associated with both the porous metal foam and fluid region are not fully understood at the current stage, with a lack of proper mathematical treatments in the literature for different regions across the foam structure, including the fluid/foam interface. An accurate analytical model and further numerical studies are required to validate the results and providing more comprehensive explanations. Also, the existence of stagnant and wakes in the partially filled channel required more attention and additional studies for validation.

The laser-diagnostic equipment, e.g., the PIV and LDA have their own limitations in taking measurement near a boundary, thus the intrusive point-wise measurement, e.g., the hot-wire anemometer could be used as an alternative in measuring the velocity near the foam interface. However, a larger number of data points is required to compensate the fluctuated velocities to improve the accuracy of the proposed friction factor model. Additionally, it is really important to use various foam samples (different geometrical and microstructural properties) and a wide range of inlet velocities to obtain an established pressure drop performance and a more generalized conclusion. This is also helpful in identifying the individual pressure losses in the partially filled channel. In another aspect, a useful correlation to estimate the effective length of a metal foam-filled annulus heat exchanger based on different parameters is also required. Although a numerical model has been used to simulate the actual heat exchanger in our experiment, there was a slight deviation due to the limitations of the porous media model in the Fluent software. The existing model is only useful for a qualitative analysis yet an improved model would be useful to avoid the time-consuming experimental measurements.

Also note that this study only conducted two-dimensional imaging studies, either from the PIV, infrared camera or high-speed camera. Therefore, span-wise measurements are called for. The three-dimensional measurements could provide a full understanding of the flow behaviours and better insights into the process of particle transport and deposition in the partially filled channel. Since the high pore density foam seems to act as a filter, a highly compact metal foam heat exchanger could be unsuitable for a dusty environment, expecting severe fouling and difficulty in the cleaning processes. However, a proper foam arrangement with a suitable pore diameter and flow velocity could be a promising design to enhance the particle removal process. This, however, also depend on the particle characteristics. The weighted on how good the interconnected pore-ligament network to mitigate fouling should be explored. Nevertheless, a further understanding of the particle-detachment process is fundamental to the development of fouling-metal foam models and their predictive capabilities.

Appendix A: Laser Doppler Anemometry (LDA)

Working Principle and Measurement Setup:

LDA is an established non-intrusive technique for fluid dynamics investigations in many gases and liquid experiments or applications. The LDA could be used to measure the flow velocity in a range of 0 to supersonic and up to three velocity components simultaneously. However, the measurement is limited to one specific location per time (point-wise measurement technique). The main advantages of the LDA system are: (1) no calibration is required (2) high spatial and temporal resolutions and (3) provide instantaneous and time-averaged data. Generally, the LDA system consists of the following components:-

- Laser
- Beam splitter (e.g., a brag-cell)
- Transmitting or receiving optics
- Photodetector
- Signal processor
- Data analysis system (software)

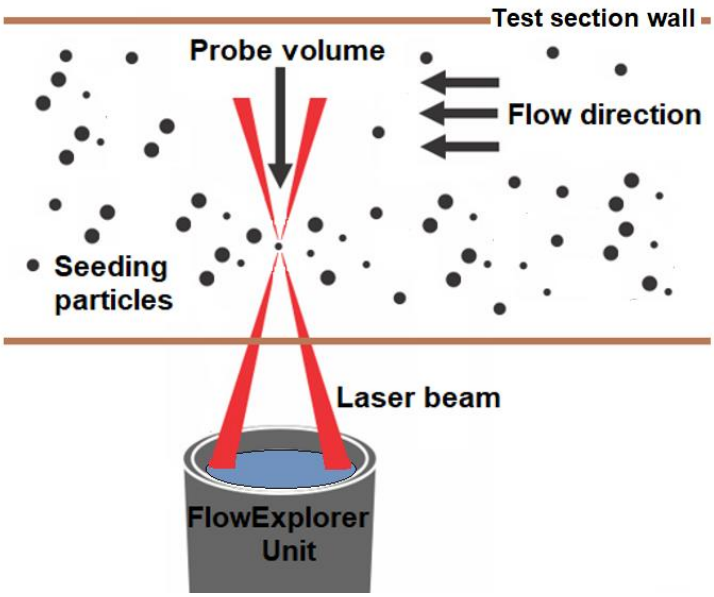

Figure A-1 Laser beam and probe volume

In this study, the LDA system (from Dantec Dynamics) has only three main components: (1) FlowExplorer unit, which consists of an optical probe (2) Burst Spectrum Analyzer (BSA) signal processor and (3) Windows software package (BSA

Flow Software). Therefore, the laser, beam splitter, transmitting or receiving optics as well as photodetector are embedded in the FlowExplorer Unit. The additional components include a seeding generator (Flow Tracker 700 CE) and a 3D traverse system. This study used the seeding generator to inject the seeding particles (oil droplets with approximately 3.0 μm diameter) into the test section. The location of the seeding generator is about 2 m from the upstream of the foam block.

In the FlowExplorer unit, two beams (diameter, ∅ = 2.6 mm) with the same intensity are created by splitting a continuous laser light (λ = 660 nm; 785 nm) using the beam splitter, making an intersection outside of the unit, as shown in **Figure A-1**. This crossing region is called as probe volume. Once these two lasers cross in a very small region, an interference pattern is generated and light and dark stripes (also known as fringes) form inside the probe volume. To measure the flow velocity, the seeding particles will be required. The particles should be small enough to accurately follow the flows and also large enough to scatter sufficient light for signal detection. The seeding particles that move through the probe volume would scatter the laser light. The scattered light would be collected by a receiver lens and focused on a photodetector. The difference between the incident and scattered light frequencies is called the Doppler shift. Note that the frequency of the scattered light is shifted by an amount proportional to the particle velocity. Hence, the flow velocity can be estimated by observing the frequency shift, where the Doppler-equivalent frequency of the scattered laser light was analysed.

Specifically, the LDA was used to measure the local velocities in the clear region of the partially filled channel, as shown in **Figures A-2 (a)** and **(b)**. The clear region can be divided into three sections; (1) upstream, (2) downstream and (3) free stream region (which is a non-porous region on top of the metal foam). The measurement locations in these experiments are located within the free stream (outside of the porous structure). The intersected laser beam is adjusted to be at the middle plane of the test section/foam width and the laser is moved vertically on the selected locations (see **Figure A-2 (b)**). The selected locations are labelled as numbers 1 – 5, which represent the measurement locations for flow velocities in the y-axis direction. Each location contains 14 data points (0.005 m apart). The upstream and downstream velocities (labelled as numbers 1 and 5) were measured 0.015 m and 0.030 m from the foam edges, respectively. While location number 2 and 4 are

positioned exactly on the top of the front and rear edges of the foam, respectively. Lastly, location number 3 is actually at the middle of the free stream region. The movement of the laser through the data points or 'dash line' was automatically controlled by the traverse system. To ensure the accuracy of the measurements, at least 100 data samples were obtained for each data points.

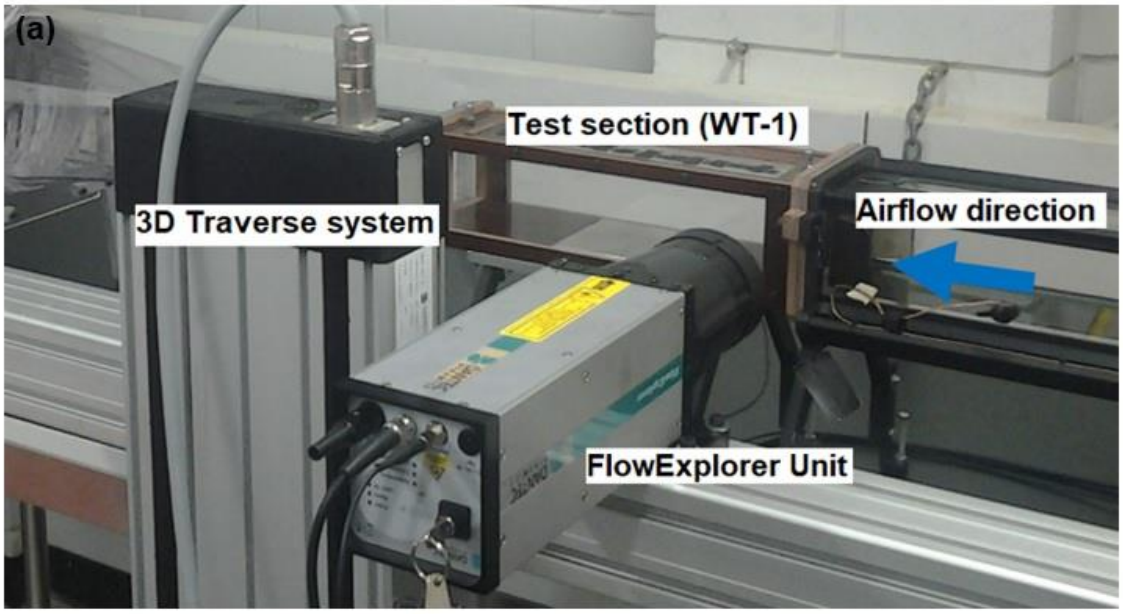

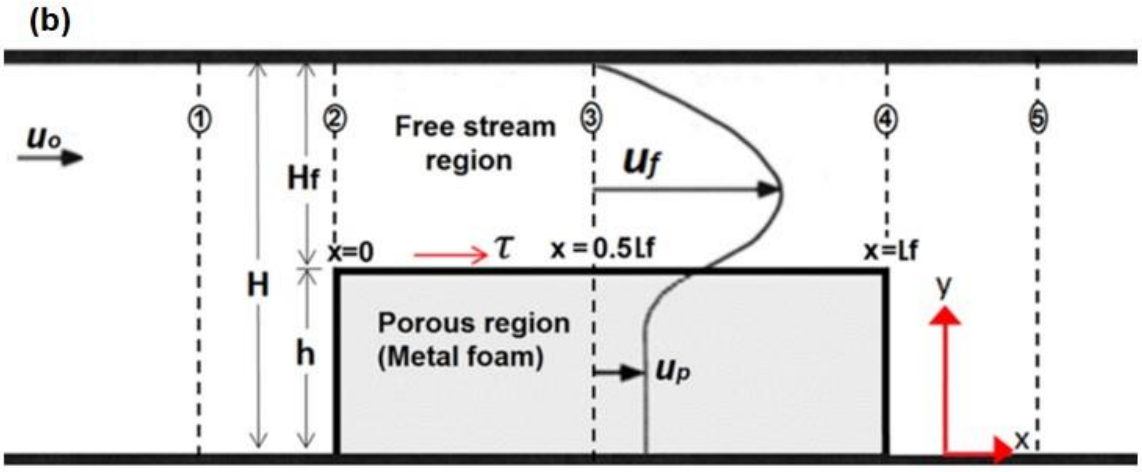

Test section dimension (m)	WT-1
Height, H	0.078
Width, W	0.10
Length, L_c	0.35

Note:
Vertical dashed lines represent the velocity measurement locations
① upstream, ② x = 0, ③ x = 0.5Lf, ④ x = Lf, and ⑤ downstream

Figure A-2 (a) LDA setup (b) Schematic test section with measurement locations

Appendix B: Particle Image Velocimetry (PIV)

Working Principle and Measurement Setup:

The PIV is also a non-intrusive measuring device. However, unlike the LDA that only collecting the velocity data at one specific point per time, the Particle Image Velocimetry (PIV) measurements could obtain an instantaneous whole-flow-field in the test section. Specifically, the whole measurement area in **Figure A-2 (b)**, starting from measurement location numbers 1 to 5 could be captured simultaneously. This technique allows the identification of any coherent structure in the flow if there is any. Basically, the PIV system (from Dantec Dynamics) used in this study consists of:

- Double pulsed Nd:YAG laser (Litron-130 mJ)
- Synchronizer
- Articulating arm (laser optics)
- Charge-coupled device (CCD) camera
- Seeding particle and pressurized seeding generator

In this study, the PIV is used to measure instantaneous, two-dimensional velocity vectors in two different channels. The major difference between those two channels is their channel size, where the WT-1 and WT-2 cross-sectional areas are 0.008 m^2 and 0.102 m^2, respectively. The flows inside the channels were uniformly seeded with oil droplets (approximately, 3.0 μm diameter) using the seeding generator. For WT-1, the seeding particles were injected 2 m from the test section (**Figure A-2 (a)**), while the seeding particles in WT-2 were injected starting from the bell-mount entrance (**Figure C-1**). The oil droplets in the test sections were illuminated with a light source, in this case, the doubled pulsed Nd:YAG laser (λ = 532 nm). To produce a very thin light sheet, approximately 3 mm thick, an articulating arm that consists of laser optics (spherical and cylindrical lens) was used. The arm is positioned about 0.40 m above the top surface of the test section (**Figure B-1**), shotting at the middle of the section (span-wise direction of the flow). The light sheet illuminated the seeding particles in the measurement area.

The scattered light from the seeding particles was captured by two or three CCD cameras (HiSense MK-II, resolutions of 1344 x 1024 pixels, 12 bits/pixel with a trigger rate of 4.5 Hz). Two cameras were used in WT-1, while three cameras for WT-2 due to its larger test section (measurement) area. By using more than one camera,

the field of view could be increased. The total field of view (FOV) is 68 mm x 178 mm (after omitting 5 mm overlapping between two cameras and mapping out the test section wall or any reflection) with the detailed FOV locations in the partially filled channels have been discussed in **Chapter 5**. The cameras also were fitted with 50 mm Nikon lens with f-stop was set at 4. Note that the cameras must be positioned perpendicular to the light sheet in order to obtain a global and sequential image of the illuminated particles. Each camera is able to capture each light (laser) pulse in separate image frames, as shown in **Figure B-1**. The CCD chip includes 1.344 by 1.024 light sensitive cells (or storage cell). The first laser pulse exposes the CCD, and the resulting charge is immediately being transferred to the storage cells after the first pulse. This stored as the first image frame. Then, the second laser pulse is fired to expose the second frame, resulting in two image frames in the storage cell. The particles are expected to travel some distances in the short period (between two laser pulses). Each of the cameras can be externally triggered to capture 2000 image pairs (per each camera) for each foam sample to guarantee statistical convergence.

The image acquisitions can be done using a commercial software, DantecStudio. The software also allows us to control the synchronizer and timing of the laser and the cameras. The time between laser pulses (tbp), Δt = 100 μs, based on the incoming airflow velocity as well as the experimental setup. The images pre- and post-processing can be also done using the same software. Once a sequence of two laser pulses is recorded, each image frames are divided into small subsection called as interrogation window. The velocity vectors were derived from the interrogation windows by measuring the movement of the particles (in image frame 1 and 2 of **Figure B-1**) between two laser pulses, dt. Specifically, the interrogation window from each image frame was cross-correlated with each other. The analyses were conducted using an adaptive correlation algorithm. The correlation produced a signal peak, identifying the common particle displacement, dx in the interrogation window. Before executing the analysis, the initial and final pass was set to 128 pixels and 32 pixels, respectively and the overlap between the adjacent interrogation window was set to 50%. The particle displacement, dx was then divided by the time separation between the laser pulses, dt to obtain the local velocity, v = dx/dt. By repeating the cross-correlation for each interrogation window in the two image frames, a velocity

vector map over the measurement area could be obtained. Note that, all the analyses in this study were also conducted using the DantecStudio software.

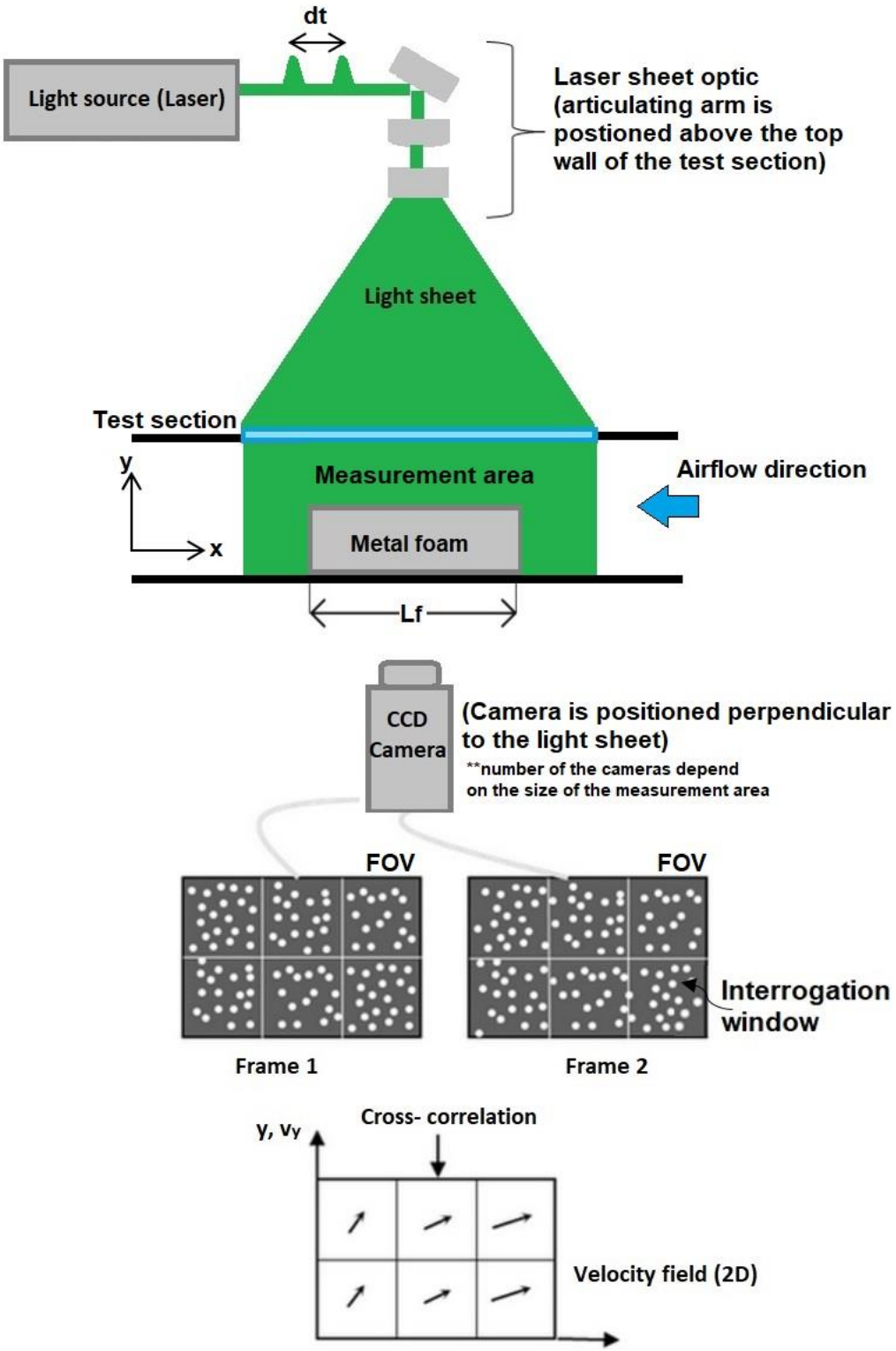

Figure B-1 Partially filled channel with the PIV system

Appendix C: Hot-Wire Anemometry (HWA)

Working Principle and Measurement Setup:

The hot-wire measurements were conducted in a suction wind tunnel (WT-2). The wind tunnel schematic is shown in **Figure C-1** with the size of the square test section is 0.32m (H) × 0.32m (W) × 2.0m (L_c). The square test section was partially filled with foam blocks of different heights, 0.010, 0.020 and 0.050 m, and three inlet velocities (6.5, 9.5 and 12.5m/s) were used in these measurements. To measure the air velocities in the test section (at the leading edge x = 0, centre of foam, x = 0.5Lf and the rear edge of the foam x = Lf), the x and y-axes were considered as stream-wise and the transverse directions, respectively. The test section walls have made of transparent Plexiglas. Air is drawn into the intake bell-mount by a fan rotor driven by an electric motor (17 kW). The intake consists of a fine mesh screen followed by a honeycomb section with 1700 cardboard cylinders. The maximum free-stream turbulence intensity in the absence of the foam block is 0.5% for the stream-wise fluctuating velocity and 0.75% for the transverse fluctuating velocity.

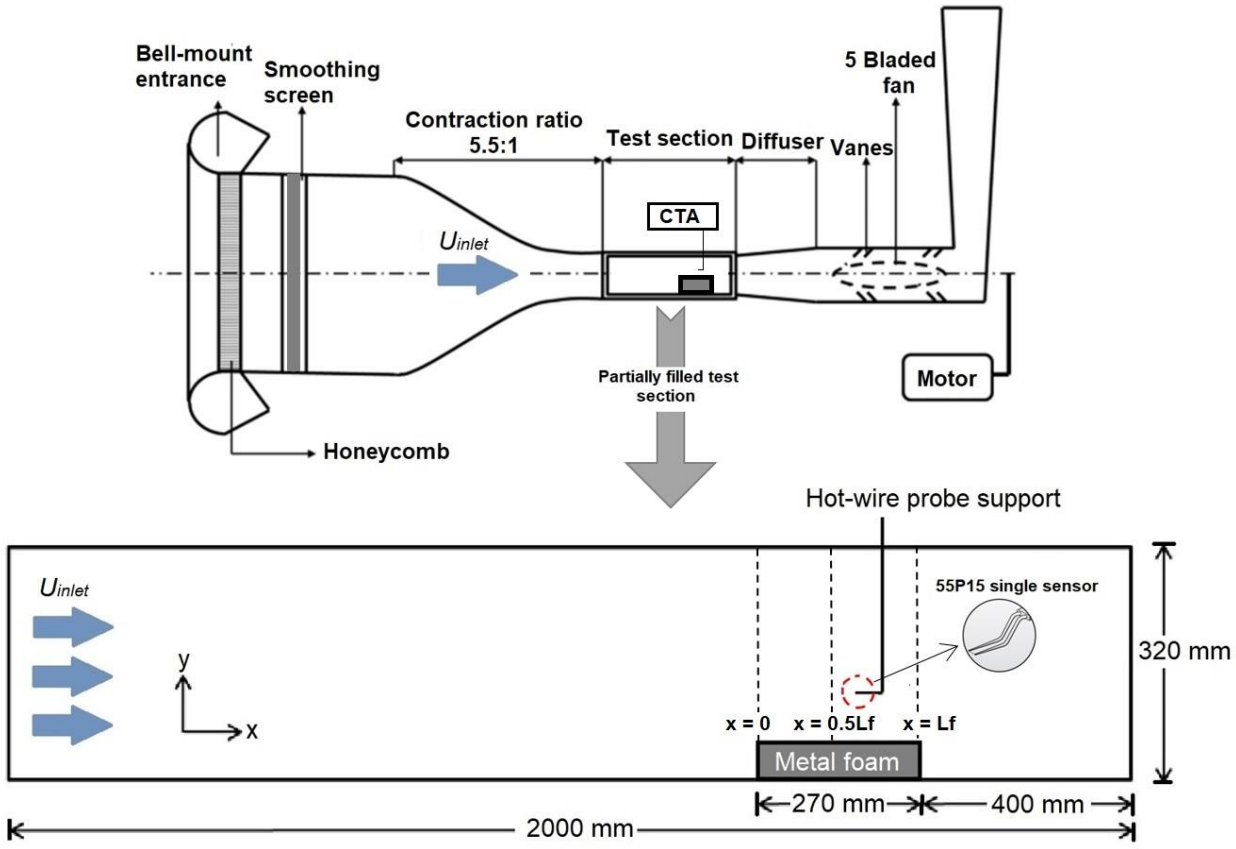

Figure C-1 Wind tunnel schematic

Generally, the hot-wire anemometer can be used to measure turbulence and velocity up to very high frequencies fluctuations. The hot-wire anemometer consists of two probes with a very thin wire stretched between them. In this study, a Dantec 55P15 single-sensor hot-wire probe was used. The wire is made of platinum-plated tungsten, with its diameter and length is 5 μm and 1.25 mm, respectively. It is welded directly to the prongs, where the entire wire length acts as a sensor. This specific sensor is designed to take measurements within boundary layers. Thus, the shape of the prongs itself facilitates the measurement in close proximity to the metal foam surface.

In principle, an electric current is sent through the wire to increase the wire temperature. As the fluid (air in this case) flows over the wire, the heated wire is cooled down as some of the heat energy is removed from the wire. To describe this phenomenon (heating and cooling process of the wire), an energy balance equation can be used, which then solved to determine the velocity of the flowing fluid. As the wire has a small time constant, it is really sensitive to the velocity fluctuations. There are two modes of hot-wire operation: (1) constant current and (2) constant temperature (CTA). In this study, the hot-wire probe was operated in constant temperature mode with an over-heat ratio was set to 1.8. Note that the CTA from Dantec used Wheatstone bridge configuration to obtain more accurate data.

The Wheatstone circuit is composed of four resistors (two fixed resistors, one variable resistor and the hot-wire probe as the fourth resistor). The increased or decreased fluid speed over the wire caused the changes in the temperature of the wire and the resistance. This results in a voltage difference, which can be detected by a servo amplifier. The amplifier keeps the bridge in balance by re-adjusting the current to maintain the constant temperature of the wire. These changes in the current can be used to calculate the fluid velocity over the wire. This study used Dantec 54T29 reference velocity probe to calibrate the hot-wire probe. The calibrator requires a normal pressurized air supply to produce a free jet (where the probe is placed during calibration). To facilitate the measurements, the probe was mounted to a 3D traverse system (controlled by a computer). The streamwise velocity fluctuations in the test section were acquired at logarithmically spaced points with a resolution of 10 μm at three different locations (the vertical dash lines in **Figure C-1**). Sufficient sampling frequency of 10 kHz and long sample lengths approximately 120 seconds was considered at each measurement points for statistical convergence.